HACETTEPE ÜNİVERSİTESİ
FEN BİLİMLERİ ENSTİTÜSÜ

NEMRUT VOLKANI'NIN YAPISAL - VOLKANOLOJİK İNCELENMESİ VE DOĞAL RİSK POTANSİYELİNİN BELİRLENMESİ

İNAN ULUSOY

Hacettepe Üniversitesi
Lisansüstü Eğitim-Öğretim ve Sınav Yönetmeliğinin
JEOLOJİ Mühendisliği Anabilim Dalı İçin Öngördüğü
DOKTORA TEZİ
olarak hazırlanmıştır.

2008

Numéro d'Ordre: D.U. 1855

UNIVERSITE BLAISE PASCAL – CLERMONT FERRAND II

U.F.R. Sciences et Technologies

ECOLE DOCTORALE DES SCIENCES FONDAMENTALES N° 577

THESE

présentée pour obtenir le grade de

DOCTEUR D'UNIVERSITE

Spécialité : Volcanologie

Par

ULUSOY İnan

Master

Etude volcano-structurale du volcan Nemrut (Anatolie de l'Est, Turquie) et risques naturels associés

Soutenue publiquement le 18 Septembre 2008, devant la commission d'examen

Président :	**LENAT Jean-François**	Université Blaise Pascal - Clermont-Ferrand
Examinateur :	**YÜRÜR Tekin**	Université Hacettepe - Ankara
Rapporteur :	**LESAGE Philippe**	Université de Savoie - Le Bourget du Lac
Rapporteur :	**BOZKURT Erdin**	Univ. Technique de Moyen Orient - Ankara
Directeur de thèse :	**AYDAR Erkan**	Université Hacettepe - Ankara
Co-directeur de thèse :	**LABAZUY Philippe**	Université Blaise Pascal - Clermont-Ferrand

NEMRUT VOLKANI'NIN YAPISAL – VOLKANOLOJİK İNCELENMESİ VE DOĞAL RİSK POTANSİYELİNİN BELİRLENMESİ

VOLCANO – TECTONIC INVESTIGATION OF NEMRUT VOLCANO AND DETERMINATION OF ITS NATURAL RISK POTENTIAL

İNAN ULUSOY

Hacettepe Üniversitesi

Lisansüstü Eğitim – Öğretim ve Sınav Yönetmeliğinin

JEOLOJİ Mühendisliği Anabilim Dalı İçin Öngördüğü

DOKTORA TEZİ

olarak hazırlanmıştır.

2008

Résumé

Le volcan actif Mont Nemrut, situé à l'ouest du lac Van, est l'un des volcans les plus importants d'Anatolie orientale. Il possède une caldeira sommitale de 8.5×7 kilomètres de diamètre. L'activité volcanique du Nemrut a commencé il y a ~1 Ma et s'est poursuivie jusque dans les périodes historiques. Les éruptions les plus récentes ont été signalées en 1441, 1597 et 1692 A.D. Parmi les volcans anatoliens orientaux; le Nemrut est le volcan le plus dangereux, compte tenu de sa proximité avec des sites urbanisés environnants ; il menace directement 135.000 habitants. Les manifestations actuelles de l'activité volcanique sont représentées par une activité hydrothermale et fumerollienne au sein de la caldeira.

L'évolution structurale du volcan se subdivise en deux stades principaux (pré-caldeira et post-caldeira) séparés par l'effondrement catastrophique de la caldeira. Les produits de l'activité anté-caldeira sont majoritairement représentés par des écoulements et des dômes de lave felsiques. Les séries ignimbritiques du Nemrut et de Kantaşı, manifestations majeures de l'activité de la caldeira, sont constituées d'unités pliniennes et d'écoulements ignimbritiques. L'activité post-caldeira est représentée par une activité phréatomagmatique explosive et une activité effusive basaltique-rhyolitique bimodale, concentrées au sein de la caldeira et au niveau de la zone de rift récente du Nemrut, sur le flanc nord.

L'analyse des données multisources (études de polarisation spontanée, modèles numériques de terrain et bathymétrie ainsi que leurs produits dérivés, images Landsat et ASTER) a permis de caractériser la structure de la caldeira du Nemrut et les circulations hydrothermales associées. La synthèse de ces approches pluri-thématiques et des interprétations correspondantes permet de proposer que la caldeira est constituée de trois blocs principaux, conséquence des processus de fragmentation générés lors des phases d'effondrement. Les frontières délimitant ces blocs et la frontière structurale principale de la caldeira contrôlent les principales activités hydrothermales intra-caldeira.

Le régime tectonique régional de compression-extension existant au Pliocène est structuralement enraciné et est responsable du déclenchement du volcanisme du Mont Nemrut. Le jeu de systèmes décrochants surimposés aux structures pré-existantes a provoqué l'apparition d'une zone de faiblesse localisée au sein de laquelle le système volcanique du Nemrut s'est préférentiellement mis en place.

La surveillance de l'activité du volcan Nemrut a été initiée avec l'installation d'un ensemble de trois sismomètres, ce qui constitue le premier réseau de surveillance sismo-volcanique sur un volcan en Turquie. Les données temps réel sont acquises, traitées et archivées depuis octobre 2003. L'interprétation des signaux volcaniques acquis dans le cadre de cette surveillance sismologique, couplée aux résultats de l'étude du système hydrothermal, confortent clairement l'existence d'une chambre magmatique active localisée aux environs de 4-5 kilomètres de profondeur. La surveillance à long terme de ce volcan potentiellement actif est essentielle pour la prévention des risques associés et fournira de plus une base de données essentielle pour une meilleure connaissance et compréhension du mode de fonctionnement de ce volcan.

Mots Clés: Nemrut, Lac Van, Anatolie de l'Est, Turquie, Polarisation spontanée, ASTER, Imagerie Infrarouge thermique, système hydrothermal, Surveillance Sismologique, Collision Continentale, Extension, Ignimbrites.

Directeur de thèse : Prof. Dr. Erkan AYDAR, Hacettepe Üniversitesi Jeoloji Mühendisliği Bölümü, Mineraloji – Petrografi Anabilim Dalı.

Co-directeur de thèse : Dr. Philippe LABAZUY, Blaise-Pascal Univ., Laboratoire de Magmas et Volcans.

Öz

Van gölünün batısında yeralan Aktif Nemrut volkanı, Doğu Anadolu'da yeralan volkanların en önemlilerinden biridir. Zirvesinde 8.5x7 km çapında bir kaldera yeralmaktadır. Nemrut dağının volkanik faaliyeti ~1 My önce başlamış ve tarihsel çağlara kadar devam etmiştir. Volkanın en genç patlamaları M.S. 1441, 1597 ve 1692'de gerçekleşmiştir. Doğu Anadolu'da yeralan volkanlar arasında Nemrut dağı, çevresi için en tehlikeli volkandır ve etrafında yaşayan 135.000 kişiyi tehdit etmektedir. Güncel volkanik faaliyet, kaldera içindeki hidrotermal faaliyet ve buhar çıkışları ile belirgindir.

Volkanın yapısal gelişimi, katastrofik kaldera çökmesi ile ayrılan iki ana evrede (kaldera öncesi ve kaldera sonrası) incelenmiştir. Kaldera öncesi ürünler esas olarak felsik lav akıntıları ve domlardan oluşmaktadır. Pliniyen üniteler ve ignimbirit akıntılarından oluşan Nemrut ve Kantaşı ignimbirit serileri kaldera oluşturan faaliyeti temsil etmektedir. Kaldera sonrası faaliyet ise kaldera içindeki patlayıcı hidrovolkanik ve riyolitik lav akıntıları/domları ile Nemrut rift zonundaki bimodal bazaltik-riyolitik efüzif faaliyet ile temsil edilmektedir.

Nemrut kalderası içindeki hidrotermal akışkan hareketleri ve kaldera'nın yapısallığı, doğal-potansiyel ölçümleri, batimetri verisi, SAM (Sayısal Arazi Modeli) türevleri ve Landsat - ASTER uydu görüntüleri yardımıyla açığa çıkarılmıştır. Kaldera'nın üç ana bloktan oluştuğu ve parçalı tipte çökme ile oluştuğu düşünülmektedir. Bu blokların arasındaki yapısal sınırlar ve ana kaldera sınır fayı kaldera-içi hidrotermal faaliyeti kontrol etmektedir.

Pliyosen'de sıkışma-açılma tektonik rejiminin başlaması Nemrut volkanizmasını tetiklemiş ve yapısal anlamda köklerini oluşturmuştur. Daha önceden var olan yapılara doğrultu-atımı bileşeninin dahil olması, Nemrut volkanının oluşumuna olanak tanıyan yerel açılmalara izin vermiştir.

Nemrut volkanının gözlemlenmesi amacıyla üç adet sismometre ile yerel bir sismik ağ kurulmuştur. Bu ağ, Türkiye'de bir volkanın etrafına kurulan ilk sismik volkan gözlem ağıdır ve 2003 yılından beri gerçek-zamanlı veri sağlamaktadır.

Hidrotermal durum ve gözlenen volkanik kökenli sinyaller, 4-5 km derinlikte bir aktif magma odasına işaret etmektedir. Sessiz bir dönemde olan bu aktif volkanın uzun süreli gözlemlenmesi elzemdir ve volkan hakkındaki bilgilerimizi artıracaktır.

Anahtar Kelimeler: Turkiye, Doğu Anadolu, Nemrut, Doğal-potansiyel, hidrotermal sistem, ASTER, Gece termal kızılötesi, Sismik gözlem, Kıtasal çarpışma, Açılma, İgnimbiritler, Van Gölü.

Danışman: Prof. Dr. Erkan AYDAR, Hacettepe Üniversitesi Jeoloji Mühendisliği Bölümü, Mineraloji – Petrografi Anabilim Dalı.

Eş Danışman: Dr. Philippe LABAZUY, Blaise-Pascal Univ., Laboratoire de Magmas et Volcans.

Abstract

Active Mt. Nemrut volcano, situated at the west of Lake Van, is one of the most important volcanoes of the Eastern Anatolia. It has a summit caldera with 8.5×7 km diameter. Volcanic activity of Mt. Nemrut started ~1 Ma ago and has continued in historical times. The most recent eruptions of the volcano were in 1441, 1597 and 1692 A.D. Amongst the Eastern Anatolian volcanoes; Mt. Nemrut is the most hazardous volcano for its vicinity, threatening 135,000 habitants living nearby. The present volcanic activities are represented by hydrothermal and fumarolic output within the caldera.

Structural evolution of the volcano is mainly investigated in two stages (pre-caldera and post-caldera) separated by catastrophic caldera collapse. Pre-caldera products are dominated by felsic lava flows and domes. Nemrut and Kantaşı ignimbrite series represent the caldera forming activity, of which sequences are comprised of plinian units and ignimbrite flows. Post-caldera activity is represented by bimodal basaltic - rhyolitic effusive and explosive hydrovolcanic activity concentrated in the caldera and on Nemrut rift zone.

Hydrothermal fluid circulation paths in Nemrut caldera and the structure of the caldera have been revealed using self-potential surveys, bathymetry data, derivatives of DEMs, Landsat and ASTER images. It is proposed that the caldera consists of three main blocks and has collapsed in a piecemeal manner. Boundaries delimiting these blocks and the main structural boundary of the caldera control the intra-caldera hydrothermal activities.

Initiation of compressional-extensional tectonic regime in Pliocene structurally rooted and triggered the volcanism of Mt. Nemrut. Addition of strike-slip component to the pre-existing structures has led localized extensions where Nemrut volcanic system has been preferentially emplaced.

To monitor the Nemrut volcano, three seismometers were installed. This is the first volcano-seismic monitoring network around a Turkish volcano and real-time data are being collected since October 2003. Hydrothermal signature as well as

acquired volcanic signals clearly refer to an active magma chamber emplaced around 4-5 km depth. Long term monitoring of this active-quiescent volcano is vital and will yield more knowledge about this volcano.

Keywords: Turkiye, Eastern Anatolia, Nemrut, Self-potential, hydrothermal system, ASTER, night-time thermal infrared, Seismic surveillance, Continental collision, Extension, Ignimbrites, Lake Van.

Advisor: Prof. Dr. Erkan AYDAR, Hacettepe Üniversitesi Jeoloji Mühendisliği Bölümü, Mineraloji – Petrografi Anabilim Dalı.

Co-advisor: Dr. Philippe LABAZUY, Blaise-Pascal Univ., Laboratoire de Magmas et Volcans.

Acknowledgements

This work was supported by Hacettepe University Scientific Research Foundation research grant (Project No.: 0101602021), by UMR-CNRS 6524 and an integrated PhD grant from the French Ministry of Foreign Affairs. During the period of my PhD study, I have had enormous support and help from the following exceptional people and I am very grateful for all the encouragement that I have received.

My gratitude to my advisor Prof. Dr. Erkan Aydar could never be sufficient in regards to his guidance, support and his faith in me throughout the years; he guided me into new horizons. I will always be proud for having the possibility to work in his group.

I am sincerely grateful to my co-advisor Dr. Philippe Labazuy, for his support and supervision. He always encouraged me for in-depth learning and braced me up. He helped me to built-up the basis of my geophysics and remote-sensing knowledge.

To work with Dr. Evren Çubukçu, Dr. Orkun Ersoy and Dr. Erdal Şen, has always been always challenging, I always enjoyed and benefited to work with them. I will never forget their friendship.

I always felt the caring support from both Prof. Dr. Hasan Bayhan and Prof. Dr. Alain Gourgaud over the years. Without their contribution, it would have been impossible to overcome this project.

I would like to thank Assist. Prof. Dr. Levent Tezcan. I will always consider myself lucky to be able to benefit from his broad knowledge of GIS. I would also like to thank to Prof. Dr. Jean-François Lénat for his courtesy for allowing me to use his code to generate the Ce map.

I would like to express my gratitude to Prof. Dr. Jean-François Lénat, Prof. Dr. Erdin Bozkurt, M. Conf. Dr. Philippe Lesage and Assoc. Prof. Dr. Tekin Yürür for

honoring me by accepting to be the members of the thesis committee. Their guidance significantly improved this report.

I would like to thank the Governor Generalship and General Command of Gendarmerie of Bitlis City, Tatvan, Güroymak and Ahlat villages; during fieldworks and installation/maintenance process of seismic stations, their help was very valuable. I owe special thanks to Major Oktay Polat for his kind support.

Our driver in fieldtrips, Dursun Kıncal deserves our special thanks here; he is one of the best guides in the region. I am thankful to photographers Adem Sönmez and Oktay Subaşı for letting me use their photographs.

Finally, I am grateful to my parents Filiz and Mahir Ulusoy for all their efforts during my education. It was their support that carried me to this point. I always felt that my wife Ayşe Ulusoy and my sister Gülen Ulusoy have been there for me and kept my moral during hard times. Throughout these years, all the constructive discussions in the family contributed to my academic intelligence.

“Damla bile değil idim

Göle çevirdiler beni”

S. Miskini

TABLE OF CONTENTS

1. INTRODUCTION 13

1.1. TECTONICS AND VOLCANISM IN ANATOLIA 15
1.2. NEMRUT CALDERA 22
1.3. PREVIOUS STUDIES 26
1.4. STRUCTURAL APPROACH AND NATURAL RISK OF THE NEMRUT CALDERA 27
1.4.1. Methodology 28

2. GEOLOGY, CALDERA FORMING ERUPTIONS 30

2.1. PRE-VOLCANIC BASEMENT 33
2.1.1. Bitlis Metamorphics 35
2.1.2. Çatak Ophiolites 35
2.1.3. Tertiary Sediments (Ahlat formation) 35
2.2. VOLCANISM IN THE VICINITY OF MT. NEMRUT 36
2.2.1. Süphan Volcano 36
2.2.2. Bilican volcano and Kolango dome 37
2.2.3. İncekaya Tuff Cone 38
2.3. GEOLOGICAL EVOLUTION OF NEMRUT VOLCANO 39
2.3.1. Pre-caldera activity 43
2.3.2. Caldera forming eruptions (Sub-stage V) 49
2.3.3. Post-caldera activity 81
2.4. SYNTHESIS 87

3. HYDROTHERMAL ACTIVITY AND FLUID CIRCULATION 89

3.1. IMAGE BASED RETRIEVAL AND CORRECTION OF ALTITUDE AND ASPECT EFFECTS ON NIGHTTIME TIR IMAGERY 92
3.2. STRUCTURE OF THE NEMRUT CALDERA (EASTERN ANATOLIA, TURKEY) AND ASSOCIATED HYDROTHERMAL FLUID CIRCULATION 109

4. SEISMIC MONITORING OF NEMRUT VOLCANO 125

4.1. SEISMIC NETWORK 127

4.1.1. Limitations, problems faced and efficiency of the network 129

4.2 DATA PROCESSING.....132

4.3. SEISMICITY OF THE VOLCANO.....134

4.3.1. Seismicity between October 2003 and October 2005 140

4.4. SYNTHESIS 149

5. DISCUSSION AND CONCLUSIONS.....150

5.1. STRUCTURE OF NEMRUT CALDERA 151

5.1.1. Tectonic evolution and initiation of Nemrut volcanism.....158

5.1.2. On the formation of Lake Van 168

5.2. NATURAL RISK POTENTIAL OF NEMRUT VOLCANO 170

5.2.1. Small scale cold lahars.....171

5.3. SUGGESTIONS.....173

5.4. ONGOING WORKS 174

5.4.1. On the calculation method of Ce Map 174

5.4.2. Lightweight multi-electrode resistivity cabling system 181

REFERENCES CITED 183

APPENDIX – A 196

APPENDIX – B 202

E-APPENDIX – 1: *EVOLUTION OF NEMRUT VOLCANO* 215

E-APPENDIX – 2: *STRATIGRAPHICAL SECTIONS*.....215

E-APPENDIX – 3: *"STCORR" AND SHORT USER GUIDE.* 215

E-APPENDIX – 4: *"NEMTRIG" AND SHORT USER GUIDE*.....215

Chapter 01

Introduction

“Change is the only constant.”

Heraclites

1. Introduction

Turkey forms one of the most actively deforming regions in the world and has a long history of devastating earthquakes (Bozkurt, 2001). Run of disasters (Kocaeli, M: 7.4; Düzce, M: 7.2) at the end of 1999 aroused interest on active tectonics of Turkey once again. Close location of earthquakes to one of the most crowded cities in the world also attracted interest of the public. Earthquakes, their genesis and results became a popular discussion subject. The popularity of the discussion also banished the subject from its scientific basis which must originally be the root of the following research, construction and reconstruction. After the catastrophic events, large amount of research budget on tectonics (worldwide) were directed into the research under Marmara Sea. Participation and support of local civil authorities to the ongoing research was also polemical. Politicians disregarded the importance of the research needed for future protection. In summary, even the disaster was catastrophic, both funding and interest of civil authorities for future research are not seem to be adequate.

In addition to the active tectonic regime, volcanism played an important role in the geological evolution of Anatolia. Research on volcanism and the natural risk associated with the volcanoes in Turkey is much more complex when compared to active tectonism. In the primary and secondary education of Turkey, it is said that volcanoes of Turkey are all extinct. On the other hand, Global volcanism program indexes 13 volcanoes have had Holocene activities (Table 1.1). Some of these volcanoes have historical records. Thus there are some questions awaiting answer: Can we classify these volcanoes as extinct volcanoes? In a zone where tectonic regime is dominantly active, can the natural risk of the volcanoes be disregarded? Present study concerns with the structural investigation of Mt. Nemrut, one of the youngest volcanoes in Eastern Anatolia and will be focused on the natural risk possibly associated with the volcano.

Name	Status	Type	Last known eruption	Dating technique	Eruptive characteristics
Kula	Holocene	Cinder cones	Unknown		
Karapınar Field	Holocene	Cinder cones	Unknown		
Mt. Hasan	Anthropology	Stratovolcano	6200 BC (in or before)	Anthropology	
Göllüdağ	Holocene?	Lava dome	Unknown		
Acıgöl-Nevşehir	Anthropology	Caldera	2080 BC ± 200 years	Anthropology	Explosive eruption
Karacadağ	Holocene	Shield volcano	Unknown		
Mt. Erciyes	Holocene?	Stratovolcano	253 AD (in or before)	Eruption is UNCERTAIN	Flank (excentric) vent, Explosive eruption (?)
Mt. Süphan	Holocene	Stratovolcano	8050 BC (?)	Tephrochronology	Flank (excentric) vent, Explosive eruption (?)
Girekol	Holocene	Unknown			
Mt. Nemrut	Historical	Stratovolcano	1692 Apr 13	Eruption is UNCERTAIN	Explosive eruption (?)
Mt. Tendürek	Historical	Shield volcano	1855	Historical Records	Explosive eruption
Mt. Ağrı (Ararat)	Historical	Stratovolcano	1840 Jul 2	Historical Records	Explosive eruption, Mudflow(s) (lahars)...
Kars Plateau	Holocene?	Volcanic field	Unknown		

Table 1.1. Young volcanism in Turkey. Data from Global Volcanism Program (GVP: Simkin and Siebert, 2002-). Locations of these volcanoes can be found on Figure 1.2.

1.1. Tectonics and Volcanism in Anatolia

Complete demise of the Paleotethyan Ocean initiated the continental rifting in the present-day Mediterranean region in the Late Triassic and resulted in the opening of a Mesozoic Neotethyan Ocean (Şengör and Yılmaz, 1981). This rifting ceased during the Middle Jurassic with the development of a passive margin through the south of Cyprus (Garfunkel, 1988) while complex processes of terrain accretion and new continental crustal build-up started to the north (Şengör and Yılmaz, 1981; Şengör and Natal'in, 1996). Convergence between African and Eurasian plates, which began in the Late Cretaceous (Şengör and Yılmaz, 1981) resulted in the progressive closure of these ocean basins and amalgamation of the surrounding continental fragments (Bozkurt, 2001).

These relative plate motions resulted in the closure of the northern branch of Neotethyan Ocean and suturing in Anatolia during Paleogene and Early Miocene (Şengör and Yılmaz, 1981). Northward subduction of the African plate along Cyprean arc begun during the Early Miocene and during the middle Miocene, Arabia was separated from Africa along the left-lateral Dead Sea fault zone (e.g. Le Pichon and Gaulier, 1988; Fig. 1.1). Accompanying relative motion between Arabian and Eurasian plates formed Bitlis suture zone (Yürür and Chorowicz, 1998).

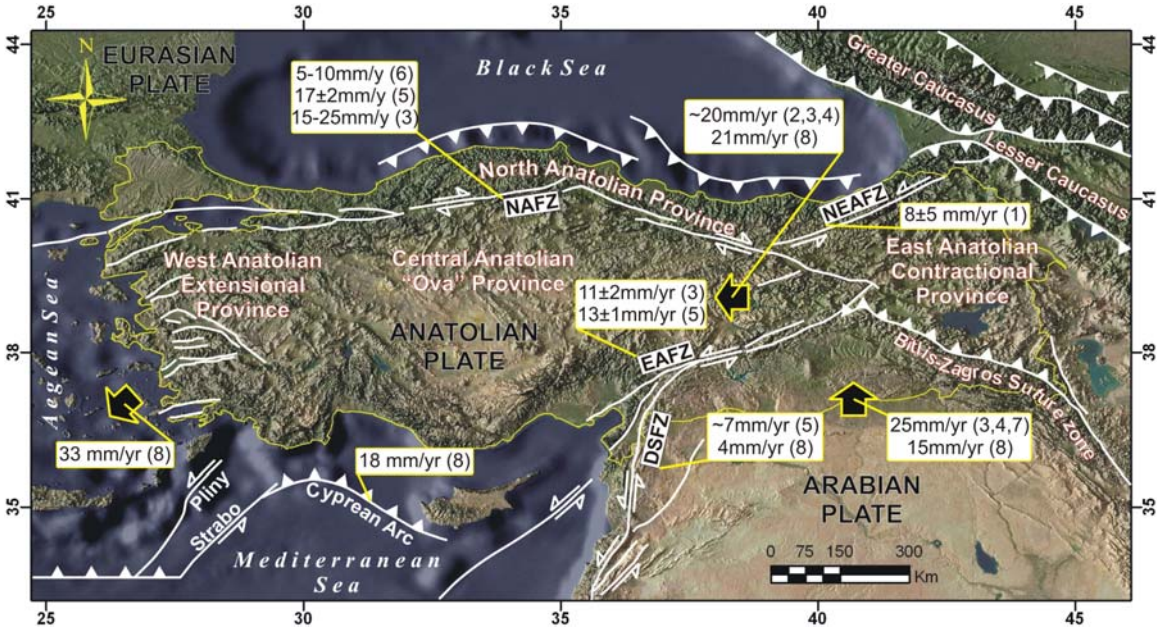

Figure 1.1. Simplified tectonic map of Turkey showing major neotectonic structures and neotectonic provinces (after Şengör et al., 1985; Barka, 1992; Bozkurt, 2001). NAFZ – North Anatolian Fault Zone, EAFZ – East Anatolian Fault Zone, DSFZ – Dead Sea Fault Zone, NEAFZ – Northeast Anatolian Fault Zone. Data for fault and plate slip rates indicated in boxes are from (1) Şengör and Yılmaz, 1981; (2) Straub and Kahle, 1995; (3) Reilinger et al., 1997; (4) Barka and Reilinger, 1997; (5) Westaway, 1994; (6) Barka, 1992; (7) Oral et al., 1995; (8) Reilinger et al., 2006. Datum: WGS84.

Later tectonic regime totally differs from the previous history of Anatolia. African-Arabian-Eurasian collision resulted in the formation of four neotectonic structural features in Anatolia: North Anatolian Fault Zone (NAFZ), East Anatolian Fault Zone (EAFZ), Northeast Anatolian fault (NEAFZ) zone and Bitlis suture zone (Fig. 1.1; McKenzie, 1970, 1972; Dewey and Şengör, 1979; McKenzie and Yılmaz, 1991; Bozkurt, 2001) dividing Anatolia into four main neotectonic provinces namely Western Anatolian extensional province, Central Anatolian “Ova” (plain)

province, North Anatolian province and East Anatolian contractional province (Şengör et al., 1985; Bozkurt, 2001).

The Anatolian plate is clearly “escaping” westward (Fig. 1.1) into the western Mediterranean oceanic tract, where its motion relative to Africa, is taken up by subduction at the Aegean Trench (Dewey and Şengör, 1979). Neotectonic movement of Anatolian plate has been observed by many researchers (e.g. Straub and Kahle, 1995; Reilinger et al., 1997; Barka and Reilinger, 1997; McClusky et al., 2000; Reilinger et al., 2006) and simply shown in Figure 1.1. The GPS-derived velocities for the interaction zone of the Arabian, African (Nubian, Somalian), and Eurasian plates indicates counterclockwise rotation of a broad area of the Earth’s surface including the Arabian plate, adjacent parts of the Zagros and central Iran, Turkey, and the Aegean/Peloponnesus relative to Eurasia at rates in the range of 20-30 mm/yr (Reilinger et al., 2006). This relatively rapid motion occurs within the framework of the slow-moving (~5 mm/yr relative motions) Eurasian, Nubian, and Somalian plates (Reilinger et al., 2006).

Within the frame of neotectonics of Anatolia, volcanism played an important role. Volcanics cover an area more than 250,000 km^2 which constitutes approximately ¼ of the total area of Turkey (Fig. 1.2). Volcanism in Northern Turkey is represented by older series. Quaternary and Neogene volcanism appears widely in the western, central and eastern Turkey. In western Anatolia, volcanic activity began during the Late Oligocene – Early Miocene compressional regime, represented by a widespread suite of andesitic and dacitic calc-alkaline rocks. Then the change from N-S compression to N-S stretching in the Middle Miocene was accompanied by a gradual transition to alkali basaltic volcanism (Yılmaz, 1990). In the Eastern Anatolia, volcanic activity began in the Late Miocene to Pliocene and continued into historical times. There is still a lack of knowledge about the Eastern Anatolian volcanism.

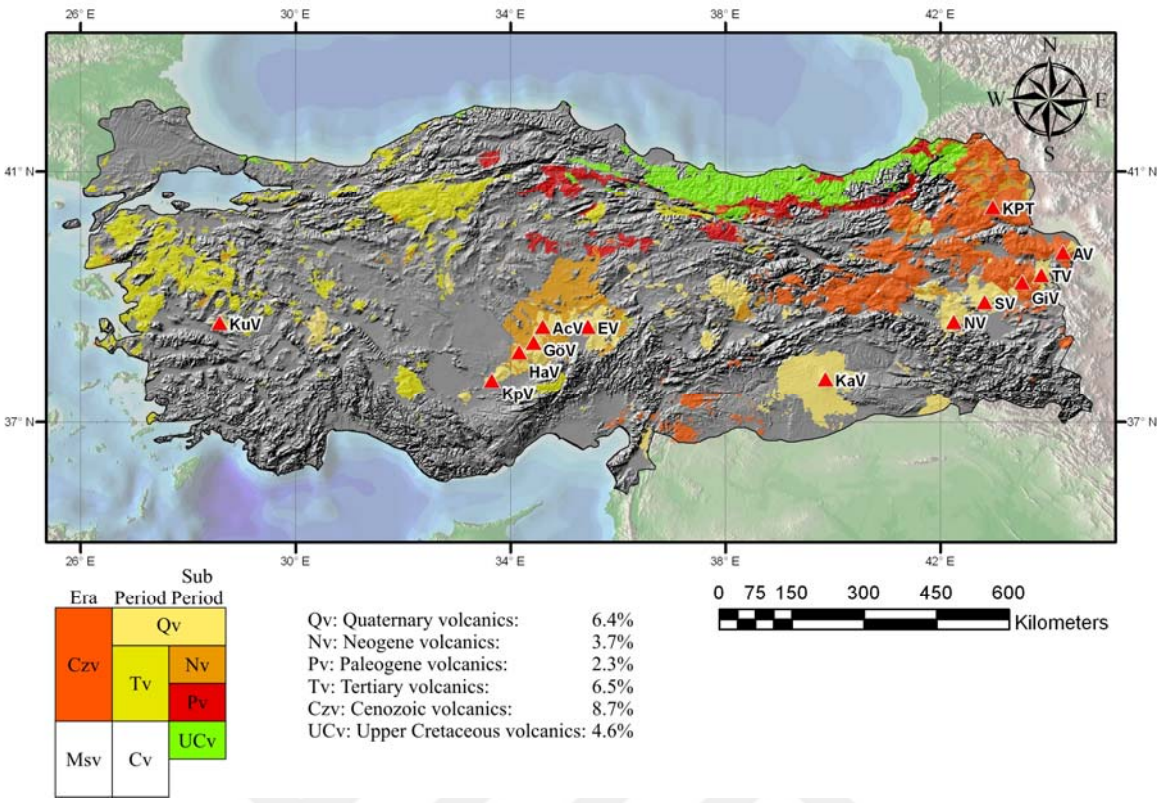

Figure 1.2. Layout of volcanic rocks in Turkey. Data from: MTA, 1964; Aydar, 1992; Pawlewicz et al., 1997. Percentages refer the area covered by the related color in the map relative to the area of Turkey. AV: Ağrı volcano, AcV: Acıgöl caldera complex, EV: Erciyes volcano, GiV: Girekol volcano, GöV: Göllüdağ complex, HaV: Hasan volcano, KaV: Karacadağ volcano, KPT: Kars plateau tuffs, KpV: Karapınar field, KuV: Kula volcanics, NV: Nemrut volcano, SV: Süphan volcano, TV: Tendürek volcano. Datum: WGS84.

Widely-known volcanoes of Eastern Anatolia are Ağrı, Süphan, Tendürek and Nemrut volcanoes. As well, they are not the only ones; Eastern Anatolia hosts a lot of volcanoes which are almost unknown (Fig. 1.3). Although there is some research on the eastern Anatolian volcanism, they represent a general approach in the context of petrology, geology and regional tectonics. Yet, there is limited research on the most well-known volcanoes in the region.

Eastern Anatolia is an area of special interest from the point of view of global tectonics (Innocenti et al., 1976) and the tectonic regime is certainly in close relation with the volcanism. Movement of Arabian plate (15 – 25 mm/yr: Reilinger et al., 1997; Barka and Reilinger, 1997; Oral et al., 1995; McClusky et al., 2000; Reilinger et al., 2006) relative to the Eurasian plate (Fig. 1.1) is fronted in the Caucasian belt forming the thrust zone. Relaxation of the Anatolian plate is accompanied by counter-clockwise rotation of the Anatolia in its western part with the help of NAFZ. On the contrary, although there is a general agreement for the

initiation and evaluation of the compressional regime in the eastern Anatolia, there are different approaches on the consequences of the compression and on the nature of dynamics of the Eastern Anatolian crust (Şengör and Kidd, 1979; Yılmaz, 1990; McClusky et al., 2000; Bozkurt, 2001; Koçyiğit et al., 2001; Şengör et al., 2003; Dhont and Chorowicz, 2005; Angus et al., 2006; Facenna et al., 2006; Reilinger et al., 2006).

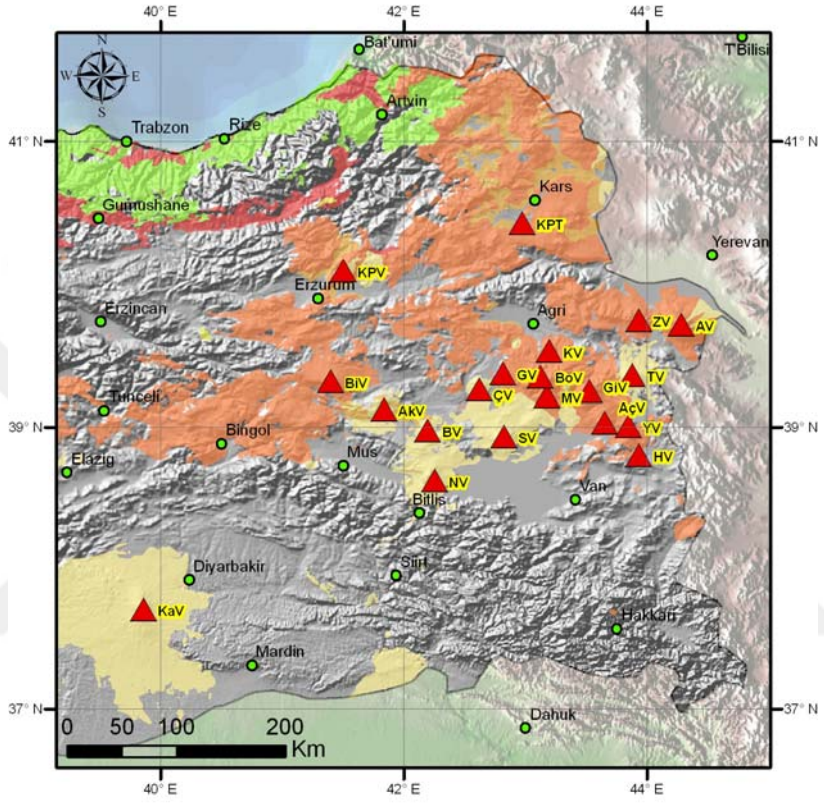

Figure 1.3. Main volcanic centers in the eastern Anatolia. AV: Ağrı volcano, AçV: Akça volcano, AkV: Akdoğan caldera, BV: Bilican volcano, BiV: Bingöl caldera, BoV: Bozdağ caldera, ÇV: Çıplak (Topdağı) volcano, GV: Gel volcano, GiV: Girekol volcano, HV: Hayal volcano, KV: Kandil volcano, KaV: Karacadağ volcano, KPV: Kargıpazarı volcanoes, KPT: Kars Plateau tuffs, MV: Meydan caldera, NV: Nemrut caldera, SV: Süphan volcano, TV: Tendürek volcano, YV: Yıllık volcano, ZV: Zor volcano. Colors of the volcanic rocks are as in Figure 1.2.

Eastern Anatolian tectonics may be discussed in terms of three main structural elements (Figs. 1.3 and 1.4; Koçyiğit et al., 2001; Bozkurt, 2001; Dhont and Chorowicz, 2005), these are; (1) NW-SE and NE-SW trending dextral and sinistral active strike-slip faults, (2) N-S, NNW-SSE and NNE-SSW trending/elongated fissures and/or Plio-Quaternary volcanoes (Fig. 1.4), and (3) undeformed basins related to strike-slip and/or trust faults which are filled with Plio-Quaternary volcano-sedimentary sequences (Fig. 1.3).

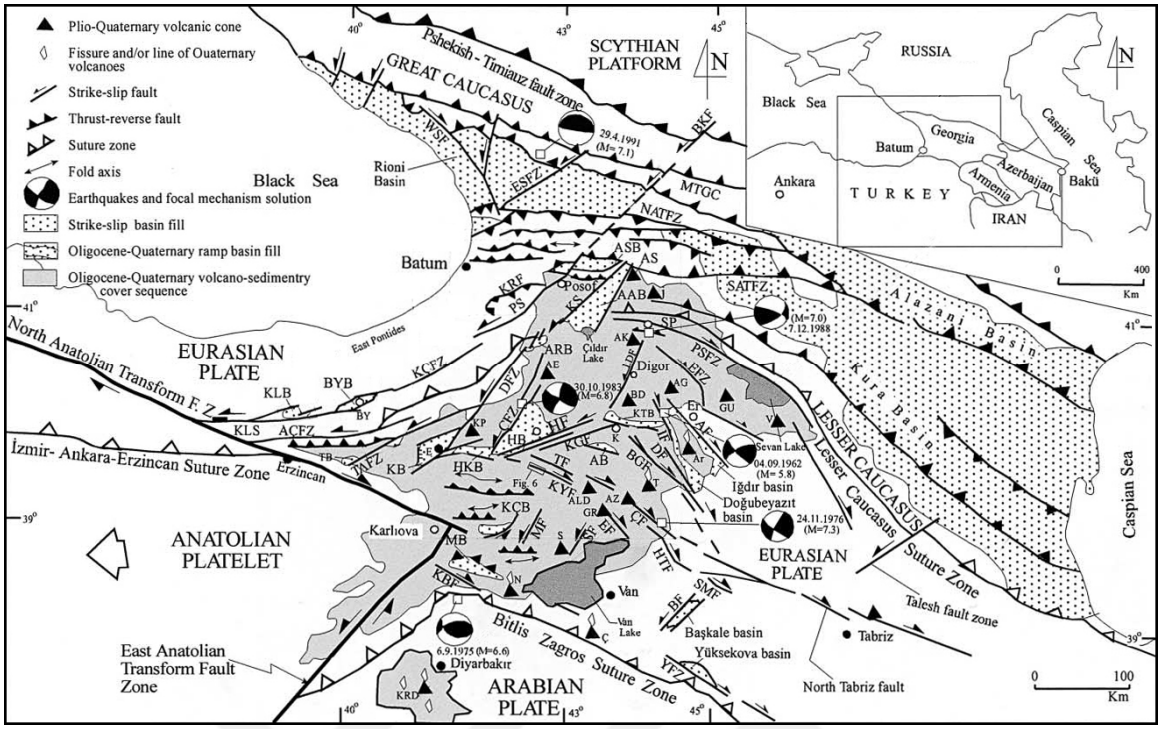

Figure 1.4. Simplified geological map showing major compressional and extensional structures (from Koçyiğit et al., 2001). Locations: BY. Bayburt, E. Erzurum, Er. Erevan, K. Kağızman, and Sp. Spitak; Volcanoes: AE. Allahuekber volcano, AG. Alagöz volcano, AK. Akbabadağ volcano, ALD. Aladağlar volcano, Ar. Ağrı volcano, AS. line of Aboul–Samsar volcanoes, AZ. Azizan volcano, BD. Böğütlüdağ volcano, Ç. Çatak volcano and fissure, GR. Girekol volcano, GU. line of Guegam volcanoes, J. line of Javakheti volcanoes, KP. line of Kargapazarı volcanoes, KRD. Karacadağ volcano, N. Nemrut volcano and fissure, S. Süphan volcano, and V. line of Vardinis volcanoes; AAB. Basins: Aktaş-Akhalkalaki basin, AB. Ağrı basin, ARB. Ardahan basin, ASB. Ahaltsikhe basin, BYB. Bayburt basin, HB. Horasan basin, HKB. Hasankale basin, KB. Karasu basin, KÇB. Karaçoban basin, KLB. Kelkit basin, KTB. Kağızman–Tuzluca basin, MB. Muş basin, and TB. Tercan basin; Fault zones: AÇFZ. Akdağ–Çayırlı fault zone, BF. Başkale fault, BGF. Balıkgölü fault, BKF. Borjomi–Kasbeg fault, ÇF. Çaldıran fault, ÇDS. Çobandede fault segment, ÇFZ. Çobandede fault zone, DF. Doğubeyazıt fault, DFZ. Dumlu fault zone, EF. Ercis¸ fault, EFZ. Erevan fault zone, ESFZ. East Samegrelo fault zone, HF. Horasan fault, HTF. Hasantimur Lake fault, IF. Iğdır fault, KBF. Kavakbaşı fault, KÇFZ. Kelkit–Çoruh fault zone, KGF. Kağızman fault, KLS. Kelkit fault segment, KRF. Karçal reverse fault, KS. Kura fault segment, LDF. Leninakan–Digor fault, MF. Malazgirt fault, MTGC. Master thrust of Great Caucasus, NATF. North Adjara–Trialetian thrust fault zone, PS. Posof fault segment, PSFZ. Pambak–Seven fault zone, SATFZ. South Adjara–Trialetian fault zone, SF. Süphan fault, SMF. Salmas fault, TAFZ. Tercan–Aşkale fault zone, TF. Tutak fault, WSF. West Samegrelo fault, and YFZ. Yüksekova fault zone.

Two systems of strike-slip faults occur in the east Anatolian Plateau: (a) NW-SE-trending dextral strike-slip faults paralleling the North Anatolian Fault Zone (NAFZ, Figs. 1.1 and 1.4) with the same sense of motion; (b) NE-SW trending sinistral strike-slip faults paralleling the East Anatolian Fault Zone (EAFZ) with the same sense of motion (Koçyiğit et al., 2001; Bozkurt, 2001). These two fault systems are same in age (Late Pliocene) and they are connected with stress field linked to the

N-S directed intra-continental convergence between the Eurasian and Arabian plates (Koçyiğit et al., 2001). Numerous strike-slip basins occur in the east Anatolian plateau (Fig. 1.4). They can be categorized, based on their age and type, into two groups: (1) Oligo-Miocene inverted basins or superimposed basins, and (2) newly formed pure strike-slip basins resulted from the geometric discontinuities including step-overs, bends and bifurcations along through going fault segments (Koçyiğit et al., 2001).

The third group of structures characterizing the east Anatolian plateau is the fissures, alignment of volcanic cones (Koçyiğit et al., 2001). Elongated volcanic edifices or craters and clusters of aligned vents are rooted on tension fractures and extensional features that are related to the step-over and horsetail geometries of the strike-slip faults (Adıyaman, 1998). Fissures or local extensional normal faults are well exposed at the summits of large isolated-to-composite strato-volcanoes of Plio-Quaternary age (Koçyiğit et al., 2001).

Koçyiğit et al. (2001), notes these fissures as isolated and NNW-SSW-trending single crack, or a zone of cracks ranging from 30 m to 2 km in width and 400 m to 50 km in length. Dhont and Chorowicz (2005), defines a mean value of N05ºE-trending fissures and extensions on the eastern Anatolian volcanoes (Fig. 1.5). On the other hand, different trends of the extensional features on the large edifices such as Mount Ağrı, Mount Aragat, Mt. Süphan are evident. Structure of eastern Anatolian volcanoes must be studied in detail for a more comprehensive approach in the context of plate dynamics.

The N-S-directed compressional-contractional tectonic regime and related structures (folds, thrust-to-reverse faults and ramp basins) are prominent in the north (Great Caucasus and the Transcaucasus), while the compressional-extensional tectonic regime related structures (both the sinistral and dextral strike-slip faults, various strike-slip basins and N-S trending fissures) become prominent in the south (the Lesser Caucasus and east Anatolian plateau, Figure 1.4; Koçyiğit et al., 2001). Tectonic evolution of east Anatolian plateau is schematically synthesized in Figure 1.5.

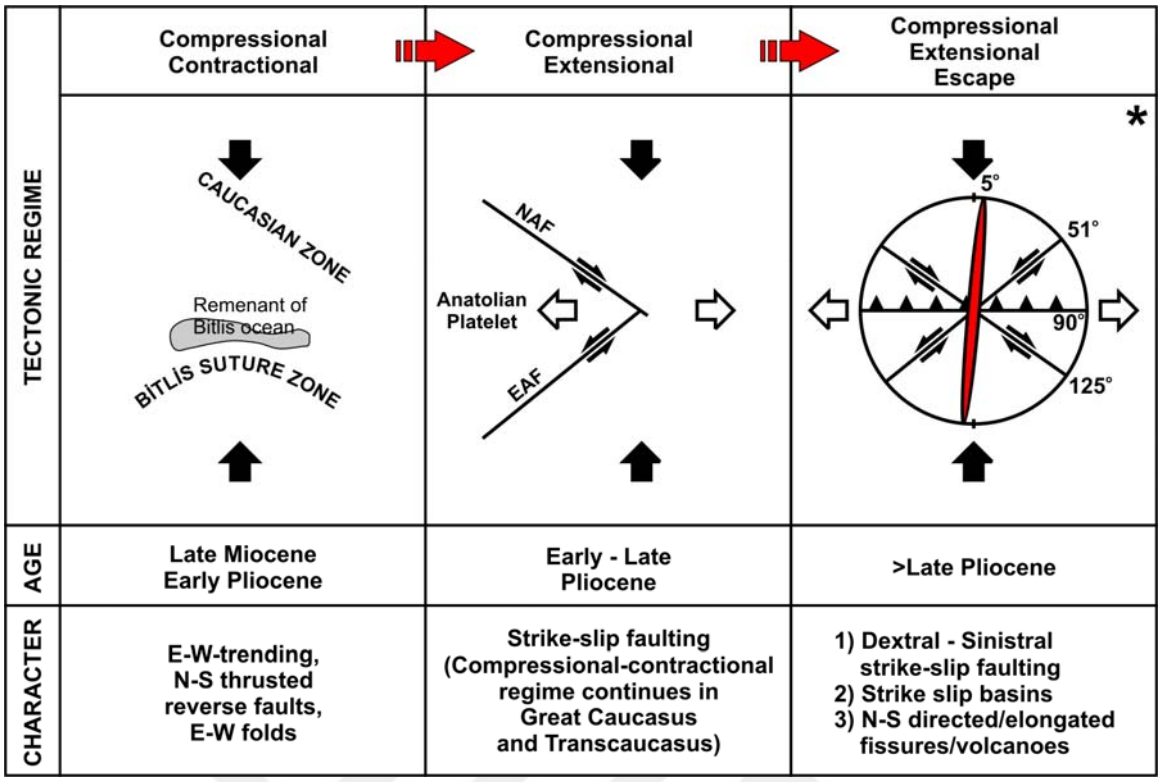

Figure 1.5. Schematic illustration of tectonic evolution of eastern Anatolia (Data from: Şengör and Kidd, 1979; Koçyiğit, 2001; Bozkurt, 2001, *Dhont and Chrowicz, 2006). Lines in figures: strike-slip faults, line with triangles: thrusting, red ellipse: elongation of volcanoes and volcanic fissures, black arrows: compression, white arrows: extension.

1.2. Nemrut Caldera

Plio-Quaternary volcanism played an important role in the present morphology of Eastern Anatolia. Mount Nemrut, situated to the western tip of Lake Van is one of the main volcanic centers in the region (Fig. 1.6), with a spectacular summit caldera 8.5 x 7 km in diameter (Fig. 1.7, Aydar et al., 2003; Ulusoy et al., 2008). Within 100 km radius, there are seven other volcanoes; these are, Süphan, Bilican, Akdoğan, Bingöl, Çıplak, Bozdağ and Meydan volcanoes (Fig. 1.6).

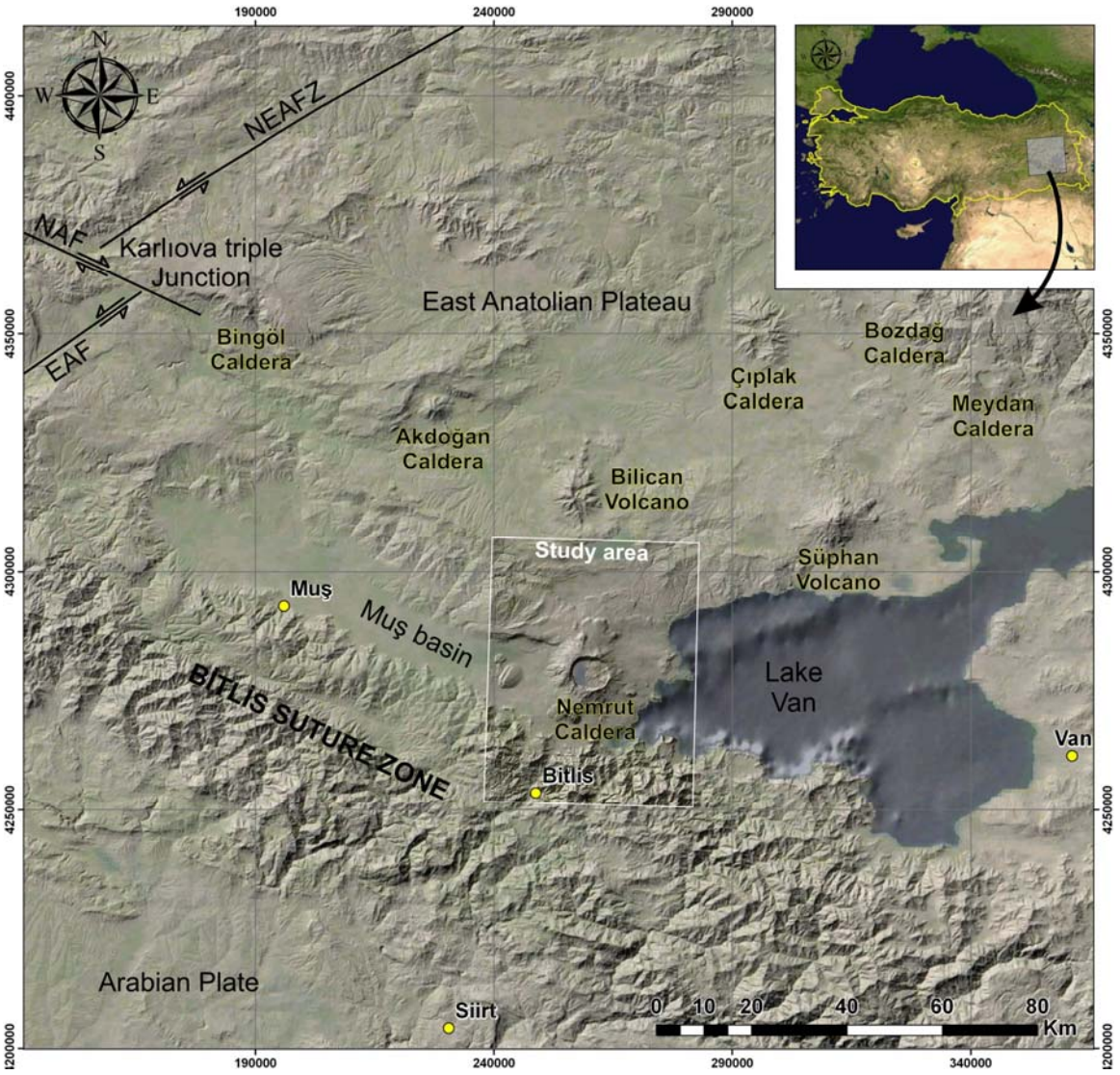

Figure 1.6. Map showing the study area and the volcanoes around the study area. Datum: European 1950 (UTM).

Nemrut caldera is situated just north of Bitlis-Zagros suture zone, close to the Bitlis edge (Figs. 1.1, 1.4 and 1.6). The Bitlis Suture is a complex continent-continent and continent-ocean collisional boundary that lies north of fold-and-thrust belt of the Arabian platform and extends from southeastern Turkey to the Zagros Mountains in Iran (Şengör and Yılmaz, 1981; Bozkurt, 2001 and references therein). Bitlis suture closed in the Eocene. This closure was then followed by prolonged convergence that involved distributed shortening all over the place, and then the strike-slip fault zones (NAFZ and MOFZ) came into being at <5 Ma, then the geometry changed at <3 Ma when the EAFZ developed (Bozkurt, 2001).

Muş basin with 10-18 km width and ~92 km length is the most important structural feature at the western side of the volcano. It corresponds to the deformed and dissected remnant of the WNW-ESE-trending Oligo-Miocene Muş-Van basin

located at the northern foot of the Bitlis suture zone (Koçyiğit et al., 2001). Although the Muş basin seems to still retain its earlier nature of ramp basin, its northern margin-bounding reverse fault has a considerable dextral strike-slip component, implying an inversion in the nature of tectonic regime in the Pliocene (Koçyiğit et al., 2001). On the other hand, Dhont and Chorowics (2006) define this basin as a half-ramp basin and indicate the northern boundary fault as a transtensional dextral oblique-slip fault.

Lake Van, by its volume of 576 km^3 is the fourth largest terminal lake and the largest soda lake on Earth (Landmann et al., 1996). The surface area amounts to 3522 km^2; its maximum depth reaches 460 m (Landmann et al., 1996). The water of the Lake is highly alkaline, with a pH of 9.8, and brackish with a salinity of 22 ‰ (Landmann and Kempe, 2005). Although the faults forming the Muş basin are WNW-ESE-trending, structural features in the Lake Van seem to be mainly directed in ENE-WSW and NNW-SSE (Fig. 1.6). Both this slight reversal in the structural alignments and location of Nemrut volcano at the center of this reversal is important in the context of regional tectonics.

Close to the Nemrut Caldera, İncekaya tuff cone, and Mazik and Girekol domes (Fig. 1.7) may be regarded as in the system of Nemrut volcanism. Nemrut volcano is in the vicinity of Bitlis city and closest populated towns are Tatvan, Ahlat and Güroymak towns (Fig. 1.7 and Table 1.2). Kirkor domes to the south and Nemrutbaşı cone to the north of the caldera are important parasitic volcanic features around the volcano (Fig. 1.7). There are five intra-caldera lakes. Three small lakes are seasonal, while western half of the caldera is filled by a fresh water. Near the northern rim, another lake with hot springs (~60º) is present where fumarolic activity can also be observed.

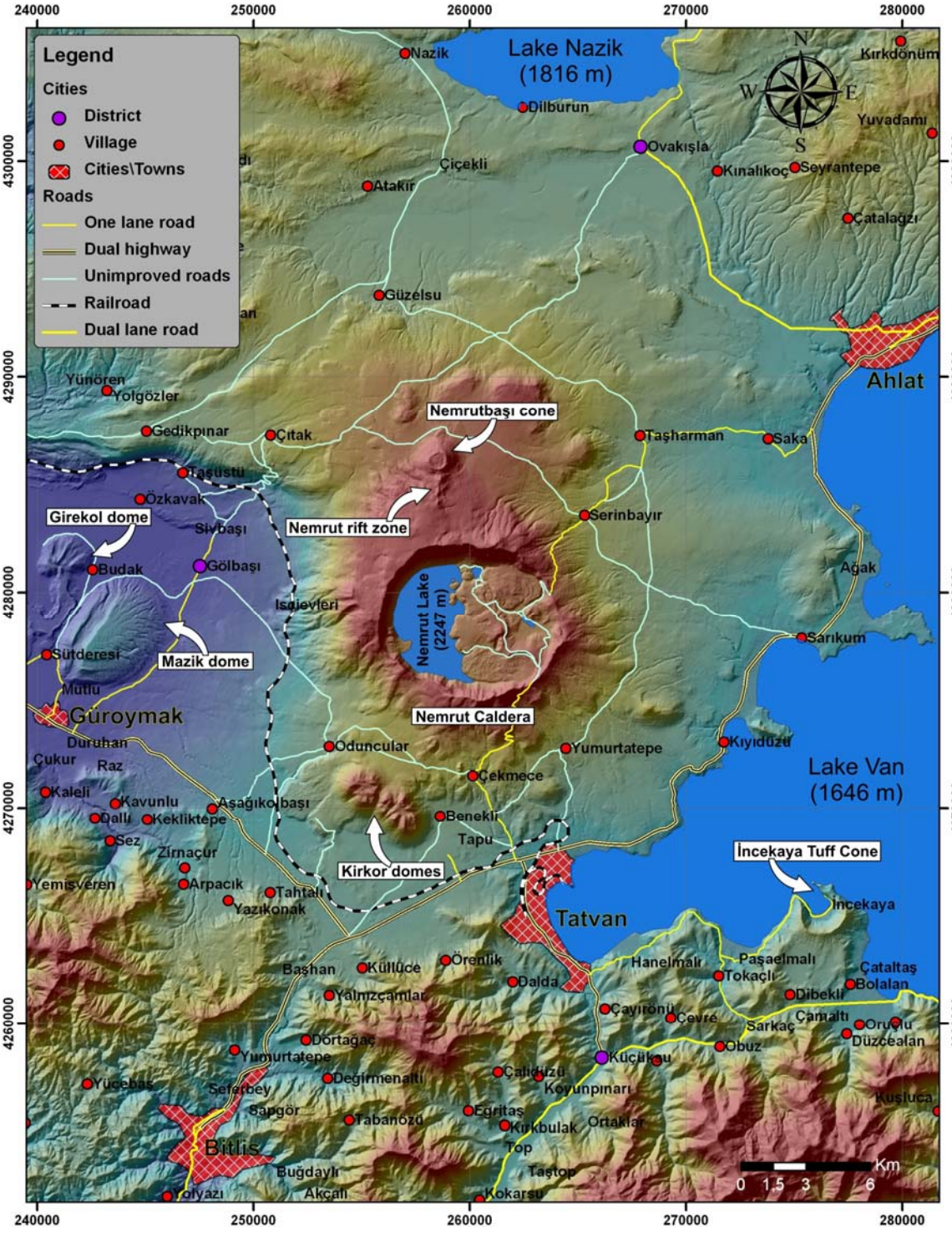

Figure 1.7. Study area, main roads, populated places, and important hydrogeologic, topographic and volcanic features in the study area. Datum: European 1950 (UTM).

1.3. Previous studies

Previous research on Nemrut volcano can not be disregarded amongst other poorly studied east Anatolian volcanoes. Latest research on east Anatolian volcanoes mainly focused on this volcano. Özpeker (1973a) studied petrogenesis of the volcano and presented a large scale geologic map. Güner (1984) presents a study for a general geological/volcanological approach on the Nemrut caldera. Research of Atasoy et al. (1988) is one of the extensive works carried out on the volcano focusing mainly geothermal energy potential of the volcano, also deals with volcanology and petrology of the volcano. Ünlü and Can (1983) also discussed the geothermal energy potential of the volcano. Bal (1986) presented the results of a magnetic etude aiming to investigate the geothermal potential of the volcano. Yılmaz et al. (1998) presents a general geological and petrologic state of the volcano together with other well-known volcanoes of eastern Turkey. More recently, research was focused on the petrology of Nemrut volcano (Özdemir et al., 2006, Çubukçu et al., 2007); lately Çubukçu (2008) presented a detailed and extensive research on the context of petrography and petrology. Karaoğlu et al. (2005), deals with the caldera forming eruptions and their stratigraphy. On the other hand, there is no research on the structure, structural evolution, and potential activity of the volcano. Natural risk of this potentially active volcano was also never studied before. Ersoy et al. (2006), proposed a qualitative method for qualitative textural discrimination of volcanic ashes, and applied the method to phreato-magmatic ash samples from Nemrut caldera. Although they are limited, there are also historical and mythological bibliography and researches (Şerefhan, 1597; Karakhanian et al., 2002, 2006; Gadjimuradov and Schmoeckel, 2005) that should be mentioned. Historical inscriptions and myths are complied and shortly summarized in Appendix A.

Results of this study were previously presented in (and submitted to) international peer reviewed journals and international conference proceedings (articles: Aydar et al., 2003 (Appendix B); Ulusoy et al., 2008; Ulusoy et al., submitted; proceedings: Ulusoy et al., 2006a, 2006b, 2007).

1.4. Structural Approach and Natural Risk of the Nemrut Caldera

Nemrut volcano is located on a highly active tectonic zone: high magnitude seismic events have been reported (29.03.1907, M: 5; 27.01.1913, M: 5; 14.02.1915, M: 6; 03.11.1997, M: 5; 30.05.1881 (data from Boğaziçi University, Kandilli Observatory and Earthquake Research Institute, National center of earthquake monitoring.); 18.05.1881, M: 6.7 (Karakhanian et al., 2002) within a 30 km radius of the volcano during the last century (Ulusoy et al., 2008). One of the most active tectonic zones in the world; Karlıova triple junction (Fig. 1.6) is located 125 km NW of the volcano, and Bitlis suture zone (Fig. 1.7) is 16 km south of the volcano. Structural evolution of the volcano in this active tectonic regime, its relation with the volcanic evolution and its role in the past and potential future activity forms one of the main aims of this study.

Latest works documented that Nemrut volcano witnessed volcanic activity in the last millennium (Aydar et al., 2003; Ulusoy et al., 2008; Karakhanian et al., 2002; 2006). Wisps of smoke and hot springs can be found inside the caldera, hot springs also appear around the Mazik and Girekol domes at the eastern flank of the volcano. The present active tectonic regime, historical eruptions, occurrence of mantle-derived magmatic gases (Nagao et al., 1989; Güleç et al., 2002), the fumarole and hydrothermal activities on the volcano make Nemrut Volcano a real danger for its vicinity (Aydar et al., 2002; Ulusoy, et al., 2006b). The population in the vicinity of the volcano (~135,000), especially in the nearby towns is significantly important (Table 1.2 and Fig. 1.7). Besides, Bitlis city grows to the north, towards the volcano. Nagao et al. (1998), and Feraud and Özkocak (1993), previously pointed out that Nemrut volcano may be potentially active. As well as other Anatolian volcanoes, there is a big gap on the research on the activity of Nemrut volcano. Second aim of this work is to identify the previous and the current activity of the volcano and their structural relationships.

	1990			2000			2007		
	Total	**City**	**Village**	**Total**	**City**	**Village**	**Total**	**City**	**Village**
BİTLİS									
City center	68 132	38 130	30 002	65 169	44 923	20 246			
Tatvan	81 992	54 071	27 921	84 276	66 748	17 528			
Güroymak	37 030	16 613	20 417	48 118	22 521	25 597			
Ahlat	34 217	16 742	17 475	52 814	34 787	18 027			
Total	**330 115**	**144 029**	**186 086**	**388 678**	**219 511**	**169 167**	**327 886**	**179 260**	**148 626**

Table 1.2. Demographical data from 1990, 2000 and 2007 consensus for the vicinity of the Nemrut volcano (Data from Turkish Statistical Institute).

1.4.1. Methodology

Wide variety of methodological approaches was used to introduce the structural evolution of the volcano and the associated natural risk. A comprehensive literature study was carried out before and during the study. Needful data found in the literature studies were complied and necessary data were digitized to reinforce the study.

Available useful digital data (such as SRTM elevation data, Landsat ETM+ imagery, GIS data, Seismic data, and others) provided for free use in the World Wide Web were collected, adopted and integrated to the database of this study. Earth Science Data Interface of Global Land Cover Facility, USGS open file reports and Boğaziçi University, Kandilli Observatory and Earthquake Research Institute, National center of earthquake monitoring are some of these databases.

Geological, volcanological and geophysical field studies constitute an integral part of this study. To reveal the volcanological and volcano-structural evolution, geological field surveys were focused on the structural context. General stratigraphy of the volcanic rocks and particularly caldera forming eruptions and their products were studied in detail.

Geophysical surveys constitute one of the fundamental parts of this study. Self-potential surveys were applied, not only to reveal the current hydrothermal activity of the volcano, but also to reveal the hydrothermal fluid circulation and its relation with the internal structure of the caldera. Research on hydrothermal condition of the caldera was supported by remote sensing approaches. Both diurnal imagery and night-time TIR imagery were used to analyze the hydrothermal background and status of the volcano.

Monitoring of the volcano was essential to constitute a general idea about the current activity state of the volcano and to make a quantitative approach on the natural risk potential of the volcano. For the first time, a seismological study was carried out on a volcano in Turkey. A small seismological network was installed around the caldera to monitor the volcano-seismic activity. Various problems were faced during the data transfer, maintenance, and analysis processes; these problems also gathered knowledge and experience in construction and maintenance of such systems. Additionally, for the monitoring purpose, four thermo-data-loggers have been recently installed on the volcano.

When necessary, computer codes were written to support, fasten, automate and facilitate the data processing and handling. Three codes were written to for analyzing and handling the seismic network. Another code (Ulusoy et al., submitted) using a new method was written for the image based retrieval of altitude and aspect effects on night time TIR imagery.

All the produced data were processed in computer environment and appended in the GIS environment. Extensive GIS database constructed for Nemrut volcano significantly aided and fastened the study and will facilitate future research on the volcano.

Chapter 02

Geology

and

Caldera forming eruptions

Virtual view of Nemrut volcano, before caldera collapse

2. Geology, Caldera forming eruptions

Beyond the geophysical, morphological and structural studies, in order to comprehend the evolution of the Nemrut volcano, a detailed geological study was carried out. This section discusses the Quaternary Nemrut volcanism under two subheadings as pre-caldera and post-caldera volcanism. With a special emphasis, pyroclastic stratigraphy and characteristics of pyroclastic deposits are discussed in detail for a better understanding of the formation stage of the caldera. Other then the Quaternary Nemrut volcanism, pre-volcanic basement is summarized shortly. Recent activity will be summarized at the end of the chapter.

Geological Map

During the study, a detailed geological map of the volcano has been elaborated (Fig. 2.1). Geological rock names were defined according to the extensive petrological work of Çubukçu (2008). We benefited from geological maps of Güner (1984) and Atasoy et al. (1988), especially at the northernmost section of our map area, but our map offers major additions and changes to previous maps. It should be appropriate to discuss these changes here, because important errors have been pointed out on previous maps.

Former geological maps of the volcano were presented by Özpeker (1973a), Güner (1984) and Atasoy et al. (1988). These maps were followed by maps of Yılmaz et al. (1998) and Karaoğlu et al. (2005) with no major changes. Contrarily, they followed the same mistakes. Aydar et al. (2003) presented a modified version of Yılmaz et al. (1998)'s map. Özdemir et al (2006) used the same map with Karaoğlu et al. (2005).

In all of these maps, there is a major discrepancy on the layout and the type of the pyroclastic units. Özpeker (1973a) mapped a pyroclastic unit encircling the topographic rim of the volcano, and combines this unit with the products of intra-caldera maar eruptions cresting the eastern caldera wall. He defined one ignimbrite unit on the flanks of the caldera. Yılmaz et al. (1998) presented the same map with Güner (1984). Güner (1984) was the first who mapped two different caldera forming ignimbrite series. Atasoy et al. (1988) also mapped these two ignimbrite series; they updated the boundary between the two ignimbrites mostly at northern and northwestern flanks of the volcano. But in their map, they did not completely separate these two series; they named the former as

“Crystalline welded tuff + pumice” and the latter as “Crystalline welded tuff”. However, in their report, Atasoy et al. (1988) clearly indicated that they identified two different ignimbrite flows. Karaoğlu et al. (2005) surprisingly removed the second ignimbrite series, disregarded previous definitions and related the collapse of the caldera with only one ignimbrite series. Additionally, they used approximately the same boundaries for the upper ignimbrite series defined by Güner (1984) and Atasoy et al. (1988), but changed the unit to “plinian fall deposits”. In our fieldwork, we defined two ignimbrite series leaded to the collapse of the caldera and mapped them carefully (Fig. 2.1, Nemrut ignimbrites and Kantaşı ignimbrites). For the first time, we defined and mapped two other ignimbrite units older than the products of caldera forming eruptions (Fig. 2.1, Tuğ ignimbrite and Yasintepe ignimbrite).

The second discrepancy initiated with the map of Güner (1984) and followed by Karaoğlu et al. (2005) without acknowledging his work. At the northern flank of the caldera and around the rift zone, Güner (1984) defined many lava flows and named them as “scoria flows”. According to us, this was a considerably fundamental error. In the maps of Güner (1984), Yılmaz et al. (1998) and Karaoğlu et al. (2005), these “scoria flows” are originated from the ridge forming the Nemrut rift zone between Kantaşı hill (Fig. 2.1) and northern rim of caldera and flowed along eastern and western side of this ridge up to ~4 km distance. We particularly want to indicate that there are no “scoria flows” in this area. Whole area is covered with the Kantaşı ignimbrites. Latest activity of Nemrut volcano generated along the rift zone, and few comenditic and basalt flows originated from the rift flowed to east and western side of the rift. Boundaries of these few lava flows are very clear and the flows extended to a maximum distance of about 1.5 km. They are lying upon the Kantaşı ignimbrites. In the close vicinity of the rift zone there are ballistic ejecta and there are dispersed basalts of aa-like lava flows, but these vesicular basalts are limited and the dispersion is not dense. These materials and highly welded Kantaşı ignimbrite were most probably confused with “scoria flows” and caused the error in the maps of Güner (1984), Yılmaz et al. (1998) and Karaoğlu et al. (2005). This error was corrected totally in Atasoy et al. (1988) and partially in Aydar et al. (2003).

The third major error was introduced to the literature with the maps of Karaoğlu et al. (2005) and Özdemir et al. (2006). They define monzonitic intrusions exposed in

topographic lows within the caldera. Çubukçu et al. (2006) discussed this error in detail. They have neither given any petrographical/mineralogical description nor geochemical analysis of this unit (Çubukçu et al., 2006). In addition, the area mapped (~0.4 km^2) as monzonite is within intra-caldera maars whose post-caldera products contain abundant holocrystalline fragments (Çubukçu et al., 2006). These intra-caldera maars are among the centers of post-caldera phreatic/phreatomagmatic activities (Çubukçu et al., 2006). Their basements are filled with post-eruption deposits while their walls are subjected to intense hydrothermal alteration (Çubukçu et al., 2006). This error was checked again in our later fieldworks and no monzonitic bodies and rocks defined in Karaoğlu et al. (2005) and Özdemir et al (2006) were observed.

We introduced a map purified from these errors and removing the discrepancy on the definition of pyroclastic units.

2.1. Pre-volcanic basement

Pre-volcanic basement rocks can be divided into three main groups as Bitlis metamorphics, Çatak ophiolites, and Tertiary sediments (Ahlat formation). The stratigraphy of the basement rocks in the Nemrut area is fairly well known (Gunderson, 1988). However, the basement rocks have been structurally disrupted several times since the Mesozoic (Gunderson, 1988). In the vicinity of Nemrut, all of the pre-volcanic basement rocks are cut by the faults which separate Muş basin from Bitlis metamorphics on the south and from Tertiary sedimentary rocks on the north (Gunderson, 1988).

Figure 2.1. Geological map of Nemrut Volcano

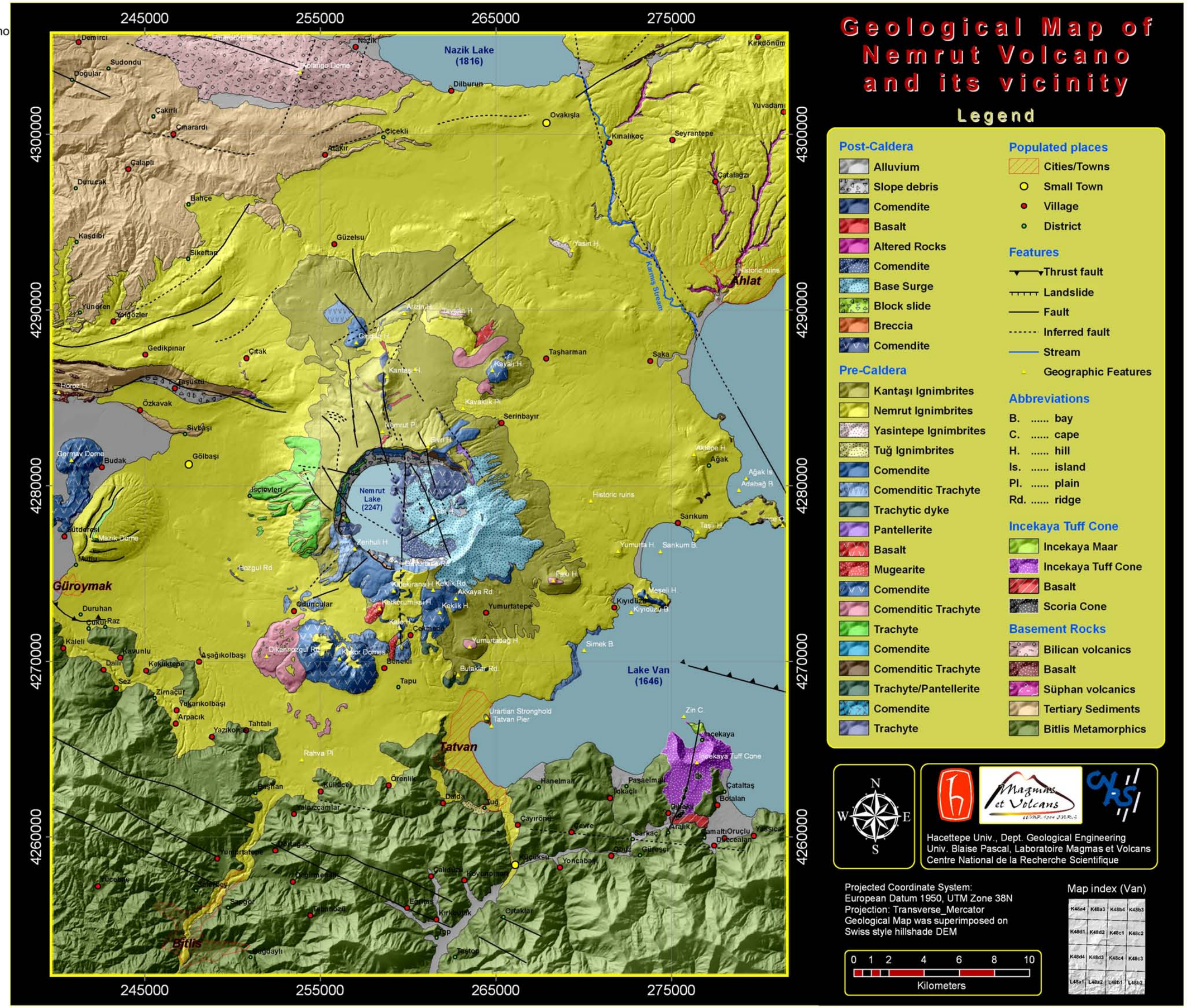

2.1.1. Bitlis Metamorphics

The oldest crustal rocks underlying Nemrut are the Precambrian to Mesozoic Bitlis Metamorphics (Güner, 1984; Gunderson, 1988). They cropped out along the steep mountains at the southern margin of Muş basin (Atasoy et al., 1988), ~15 km south of the Nemrut (Fig. 2.1). The Bitlis Massif forms a part of the Tethyan suture zone that was assembled during Late Mesozoic – Early Cenozoic time (Yılmaz et al., 1993; Robertson, 1998). It is a regional-scale allochthonous unit with a high-grade metamorphic basement and a lower-grade cover sequence (Göncüoğlu and Turhan, 1984; Ustaömer et al., in press). These metamorphics consist of metapelites, metabasites, amphibolite-biotite gneisses, chlorite-schists, calc-schists, meta-quartzites and recrystalized marbles (Gunderson, 1988; Atasoy et al., 1988). Small granitic plutons and associated granitic dykes intrude the pre-Devonian basement of the Bitlis Massif (Ustaömer et al., in press). The thickness of the units is unknown but presumed to be more than a few kilometers. Historic Urartian stronghold near Tatvan pier was built on recrystalized limestones of Bitlis Metamorphics (Fig. 2.1).

2.1.2. Çatak Ophiolites

Commonly thrust on top of the Bitlis Metamorphics are Cretaceous ophiolitic rocks (Gunderson, 1988; Atasoy et al., 1988), these rocks are usually thrust from north to south, and were emplaced during Eocene and Miocene compressional events (Gunderson, 1988). Çatak ophiolites typically include serpentines, greenstones, cherts, micrites, limestones, and greywackes (Gunderson, 1988). These rocks are cropped out east of Ahlat town, out of our study area. Tertiary sediments are overlain by volcanic products of Nemrut along Yolgözler, Yünören, Sikeftan, Bahçe and Atakır villages, though it is not possible to observe ophiolites. North to the Nemrut volcano, they are probably overlain by volcanic products (Atasoy et al., 1988).

2.1.3. Tertiary Sediments (Ahlat formation)

Tertiary sedimentary rocks overlie Cretaceous ophiolitic rocks unconformably (Gunderson, 1988). The sedimentary rocks were deposited in small, usually E-W-trending elongated basins that were opened between the Eocene and Miocene (Gunderson, 1988). The sedimentary sequences typically include sandstones,

mudstones, carbonates, lacustrine and coarse-grained fluvial deposits (Gunderson, 1988). Tertiary sedimentary rocks outcrop to the west and northwest of Nemrut volcano and at the east of the Ahlat Town. Ahlat formation is represented by Eocene and Oligocene conglomerates and sandstones, Miocene limestones, and Pliocene lacustrine deposits (Güner, 1984; Gunderson, 1988; Atasoy et al., 1988).

2.2. Volcanism in the vicinity of Mt. Nemrut

In the near vicinity of the Nemrut volcano, there are four main volcanic centers: Süphan volcano, Bilican volcano, Kolango dome, and İncekaya Tuff Cone. A short note on these volcanoes is essential to define the structural state of the region and the relationship between the products of these volcanoes and Nemrut volcano. İncekaya Tuff cone is thought to be activated during the pre-caldera activity of Nemrut volcano. Our remarks on the İncekaya volcanism will be discussed below (see section 2.2.3).

2.2.1. Süphan Volcano

Süphan volcano is situated 60 km northeast of Mt. Nemrut and 15 km north of Lake Van (Fig. 1.6). It is the second highest mountain of Turkey with an elevation of 4158 m. It culminates on the well known (e.g. Dhont and Chorowicz, 2006) NE-SW directed sinistral Süphan fault. Quaternary volcanism (Notsu et al., 1995) of Mt. Süphan is compositionally defined as mildly sub-alkaline (Yılmaz et al. 1998).

In the study area, ignimbrite units of Süphan volcano outcrops around Ahlat town commonly in the valleys (Fig. 2.1). In the Ahlat town, the historic caves (Fig. 2.1) were built into these ignimbrites (Fig. 2.2a). The ignimbrite unit is consolidated, beige in color, bears white pumices and the thickness of the unit reaches 13 m. Another unit of Süphan ignimbrites appears closer to the Lake Van; it is reddish burgundy in color and it bears coarse prismatic quartz crystals in pumices. This unit is overlain by lacustrine sediments. Pyroclastics of Süphan volcano outcrops at the northeastern side of the Karnıç stream which is bounding Lake Nazik to Lake Van. Both ignimbrite units of Süphan volcano are covered by the fall-back units of Nemrut ignimbrite series. Near the historic ruins (Fig. 2.1) in the Ahlat town, the thickness of these fall-back units reaches up to ~17 m (Fig. 2.2b).

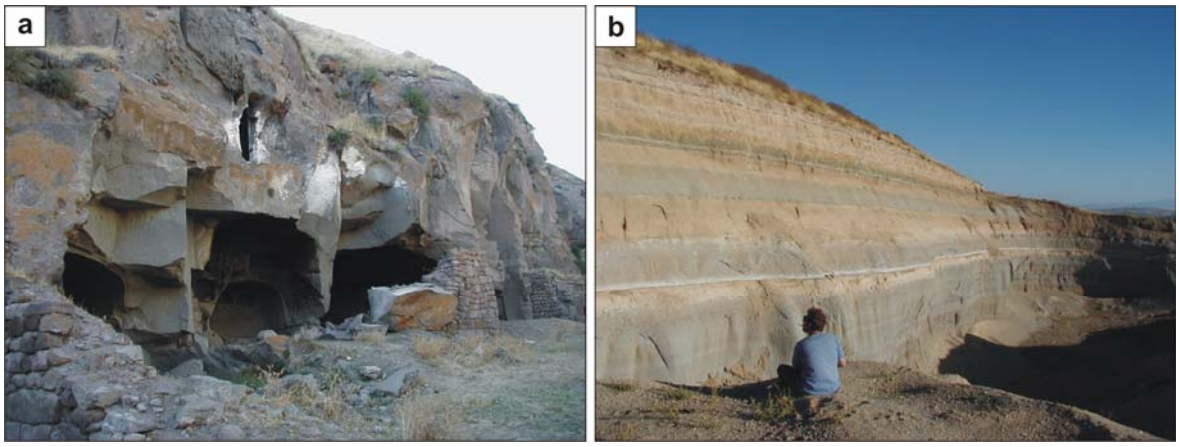

Figure 2.2. Pyroclastic outcrops in the Ahlat town. **a)** Historic caves in the upper ignimbrite unit of Süphan volcano. **b)** Fall-back units of Nemrut ignimbrites overlying Süphan ignimbrites.

2.2.2. Bilican volcano and Kolango dome

Bilican volcano lies 38 km north of Mt. Nemrut (Fig. 1.6); highest peak of the edifice is 2754 m. Other than the morpho-structural definition made by Adıyaman et al. (1998), the information about Bilican is limited. Calc-alkaline Bilican volcano is a volcanic edifice rooted on a tension fracture (Adıyaman et al., 1998). The tension fracture has about 12 km length and at the largest point, its width is about 3 km (Fig. 1.6). At north of the edifice, there are five adjacent cones forming a linear cluster trending N12ºE (Adıyaman et al., 1998). Several small volcanic cones are found near the Bilican volcano (Adıyaman et al., 1998). To the east, they form two linear clusters parallel to the main one. To the west, cones are not adjacent to each other but they are still aligned in the same direction. To the south, no linear cluster can be identified but some of the edifices are elongated approximately in the N–S direction (Adıyaman et al., 1998).

Kolango dome is situated 26 km north of Nemrut volcano and 10 km SSW of Bilican volcano at the western shore of Nazik Lake (Fig. 2.1). There is a lack of data about this volcano; the Kolango dome could be included to the Bilican system. Its summit culminates at 2321 m. A NW-SE-trending lineament passing through the summit of the dome is evident on the satellite images. Moreover, there is also a WNW-ESE-trending rift zone along the ridge westbound of Kolango dome. Pınardüzü hills (Fig. 2.1) form the northern ridge of the rift zone which is about 6 km long and reaches to ~800 m width. The WNW-ESE-trending rift zone is noteworthy. The volcanism in the eastern Turkey is often said to be rooted on N-S-

trending fracture/fault systems, but there are many exceptions to this assumption (including Mt. Ağrı, Mt. Süphan, Mt. Girekol, and Mt. Aragat in Armenia).

2.2.3. İncekaya Tuff Cone

İncekaya Tuff Cone is located on the southwestern shore of Lake Van, 25 km SE of Nemrut volcano; it rises 387 m from the Lake level (Figs. 2.1 and 2.3). Bitlis Metamorfics constitute its basement (Fig. 2.1). Özpeker (1973a), and Güner (1984) defined the İncekaya system as a caldera but, both its morphology and products clearly depict that İncekaya is a tuff cone. There is a relatively small maar (İncekaya maar) forming the NE end of the tuff cone at Zin cape (Figs. 2.1 and 2.3). South to the Cone there are six scoria cones and four of them are aligned along an inferred fault (Fig. 2.1). Largest of these cones is situated near Dibekli village and named Dibekli cone. Originating from southern side of the Dibekli dome, a basaltic lava flow is lying (Fig. 2.1).

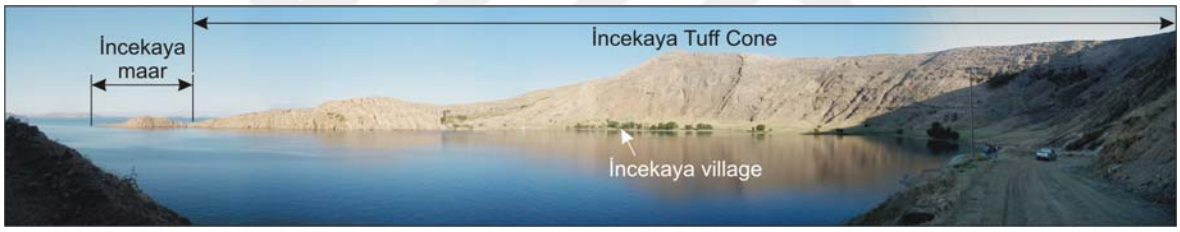

Figure 2.3. Panoramic photograph of inner view of İncekaya Tuff Cone and İncekaya maar at the left side.

Surge units of the cone are mainly basaltic in composition (Güner, 1984) and have black, gray and greenish colors. Consolidated accretionary lapilli rich levels, coarse quartz and schist xenoliths belonging to the metamorphic basement are evident in the surge units (Figs. 2.4a, b). Products of the tuff cone, that flown over Lake Van are observed 14 km NNE of the cone, on the İnce cape (Figs. 2.1 and 2.4c). On the hills across the Lake Van that are facing the eastern flanks of İncekaya Tuff Cone, plaques of surge units flown away up to 10 km across the lake, were also observed.

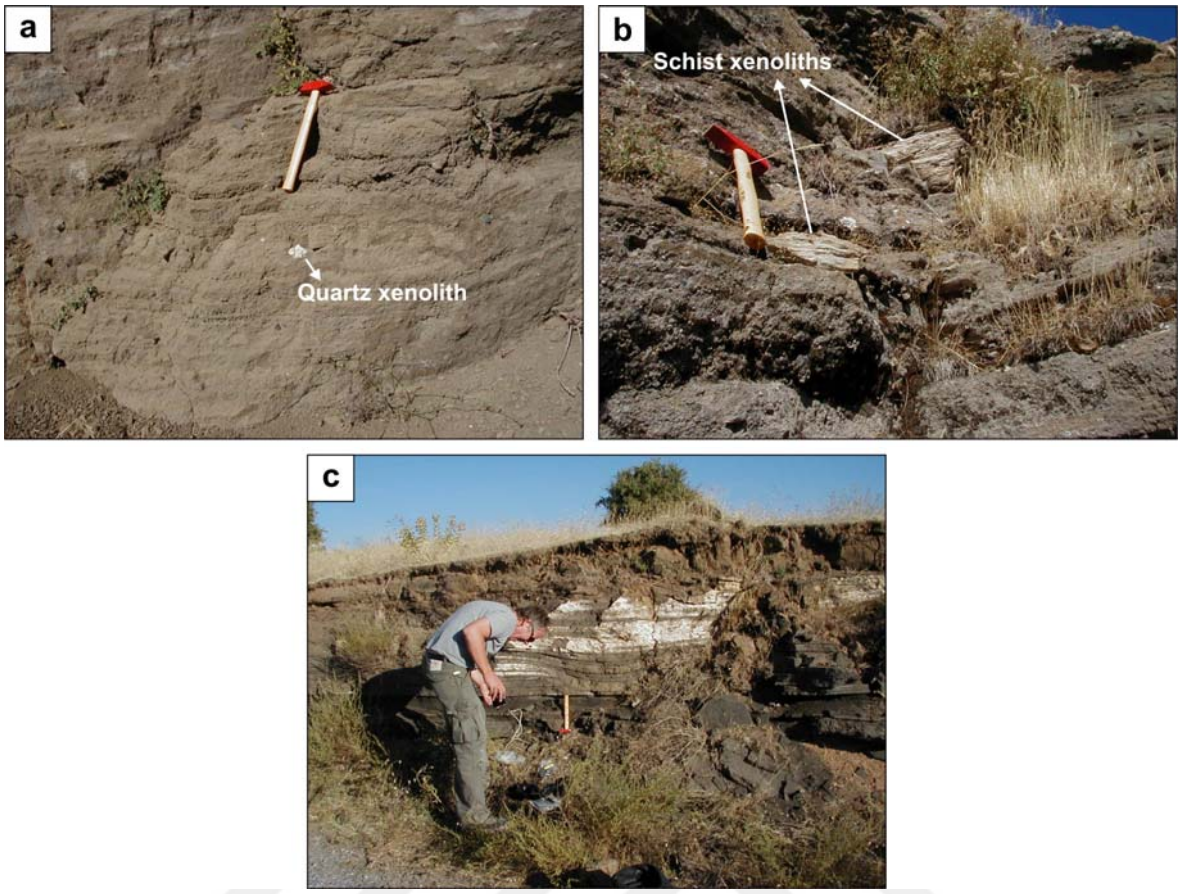

Figure 2.4. Products of İncekaya Tuff Cone. **a)** Quartz and **b)** schist xenoliths in the surge units. **c)** Fine-grained units of İncekaya Tuff Cone observed on İnce cape, north of Lake Van.

2.3. Geological evolution of Nemrut volcano

Nemrut volcano started its activity ~1 Ma ago and continued until historical times (Ulusoy et al., 2008; Çubukçu, 2008). Mt. Nemrut exhibits a spectacular summit caldera with dimensions of 8.5 × 7 km. The summit of the caldera rim, Sivri hill, is on the north side and is 2935 m high; the highest point within the caldera is Göl hill (2486 m) located in the eastern part (Figs. 2.1 and 2.28). The western half is filled by a freshwater lake (Nemrut Lake, Fig. 2.1) with a surface area of 12.36 km^2, and a smaller lake with hot springs. The altitude of the lake surface is 2247 m. The eastern half of the caldera is filled by pyroclastic deposits of maars, lava domes and flows (Ulusoy et al., 2008).

Since the introductory study of Özpeker (1973a), detailed studies of volcanological evolution of Nemrut caldera were a matter of debate (Çubukçu, 2008). Most of the previous researchers described various evolutionary stages for the volcano without evident structural phase changes or petrological differences. Atasoy et al.

(1988) divided volcanic evolution of the Nemrut volcano into four stages namely, pre-cone, cone-building, caldera-forming and post-caldera stages. Yılmaz et al. (1989) proposed pre-cone, cone-building, climactic, post-caldera and late phases. However, Yılmaz et al. (1989) also propose the same evolutionary template for other volcanoes of eastern Anatolia (Süphan, Ağrı and Tendürek) which are located on a complex tectonic system and present different petrological characters. Karaoğlu et al. (2005) and Özdemir et al (2006) proposed three evolutionary stages: pre-caldera, post-caldera and late stages. Furthermore, the criteria for such discrimination (i.e. separating the late stage from the post-caldera stage) were unclear, ambiguous and volcanological point of view is lacking (c.f. Çubukçu et al., 2007; Çubukçu, 2008). Aydar et al. (2003) and Çubukçu (2008) suggested two main evolutionary stages intervened by the paroxysmal eruptions leading to the caldera collapse: pre-caldera and post-caldera stages. Moreover, Çubukçu (2008) detailed this volcano-structural discrimination according to the petrological evolution of the volcano. Evolutionary stages of the volcano will be proposed as pre-caldera and post-caldera here (Table 2.1, Fig. 2.5), and the volcano-stratigraphy will be built upon the detailed petrological description of Çubukçu (2008). Evolution of the volcano is also presented as video, produced by modifications of DEM and evolutionary representation of the Geological map of the volcano (e-Appendix-1).

Stage	Sub-stage	ID	Eruption dates	Product	Event	Method (source)
POST CALDERA	**VIII.** Rift activity (bimodal)	a1	13.April.1692	?	Eruption of gas and ash	Historical (1)
		a2	1597 AD	Comendite, Basalt	Lava fountains and flows	Historical (2,3)
		a3	1441 AD	Comendite, Basalt	Lava fountains and flows	Historical (1)
	VII. Intra-caldera Phreatic/ Phreatomag. eruptions, Lava flows and domes	a4	657 ± 24 BC	Ash	Ash eruption	varve (4)
		a5	787 ± 25 BC	Ash	Ash eruption	varve (4)
		a6	4055 ± 60 BC	Ash	Ash eruption	varve (4)
		a7	4938 ± 69 BC	Ash	Ash eruption	varve (4)
		a8	5242 ± 72 BC	Ash	Ash eruption	varve (4)
		a9	7 ± 4 ka **(*)**	Mugearite	Lava flow	K/Ar (11)
		a10	8 ± 3 ka	Ash (Comenditic)	Phreatic Eruption	K/Ar (11)
		a11	<10 ka	Rhyolite	Lava flow	K/Ar (7)
		a12	9950 ± 141 BC	Ash	Ash eruption	varve (5)
		a13	10042 ± 142 BC	Ash	Ash eruption	varve (5)
		a14	10111 ± 143 BC	Ash	Ash eruption	varve (5)
		a15	10305 ± 145 BC	Ash	Ash eruption	varve (5)
		a16	10330 ± 145 BC	Ash	Ash eruption	varve (5)
		a17	10356 ± 146 BC	Ash	Ash eruption	varve (5)
		a18	11010 ± 166 BC	Ash	Ash eruption	varve (5)
	VI. Intra-caldera Lava flows	a19	15 ± 1 ka	Comendite	Lava flow	K/Ar (11)
		a20	15 - 19 ka	Comendite	Lava flow	K/Ar (6)
		a21	<20 ka	Comendite	Lava flow	K/Ar (7)
		a22	24 ± 1 ka	Comendite	Lava flow	K/Ar (7)
		a23	<30 ka	Comendite	Lava flow	K/Ar (9)
	V. Caldera forming eruptions: Nemrut and Kantaşı ignimbrite series					
PRE CALDERA	**IV.** Lava flows	a24	80 ± 20 ka	Olivine basalt	Lava flow	K/Ar (7)
		a25	89 ± 2 ka	Comenditic Trachyte	Lava flow	K/Ar (11)
		a26	93 ± 3 ka	Comenditic Trachyte	Lava flow	K/Ar (11)
		a27	99 ± 3 ka	Pantellerite	Lava flow	K/Ar (11)
		a28	100 ± 50 ka	Mugearite	Lava flow	K/Ar (7)
		a29	158 ± 4 ka	Comendite	Lava flow	K/Ar (11)
	III. Peripheral Doming and Lava flows	a30	242 ± 15 ka	Comendite	Lava flow	K/Ar (6)
		a31	263 ± 6 ka	Comenditic Trachyte	Lava flow	K/Ar (11)
		a32	272 ka	Ignimbrites (?)	Ash flow	K/Ar (6)
	II. Lava flows	a33	310 ± 100 ka	Comendite	Lava flow	isotope (10)
		a34	333 ± 41 ka	Comenditic Trachyte	Lava flow	K/Ar (6)
		a35	384 ± 23 ka	Pantelleritic Trachyte	Lava flow	K/Ar (6)
	I. Lava flows	a36	567 ± 23 ka	Comendite	Lava flow	K/Ar (6)
		a37	<700 ka	Comenditic Trachyte	Lava flow	K/Ar (8)
		a38	1.01 ± 0.04Ma	Trachyte	Lava flow	K/Ar (6)

Table 2.1. Historical and older eruptions of the Nemrut volcano. Data source: 1: Karakhanian et al. (2002); 2: Şerefhan (1597); 3: Aydar et al. (2003); 4: Landmann (1996); 5: Landmann et al. (1996) corrected according to Landmann and Kempe (2005); 6: Atasoy et al. (1988); 7: Notsu et al. (1995); 8: Pearce et al. (1990); 9: Ercan et al. (1990); 10: Yılmaz et al. (1998); 11: Çubukçu (2008); (*) indicates the suspicious (Çubukçu, 2008) analysis of Mugearite. Geochemical descriptions of lava flows are taken from Çubukçu (2008). Known locations of dated samples are indicated in Figure 2.5 with reference IDs given in this table (a1-a38).

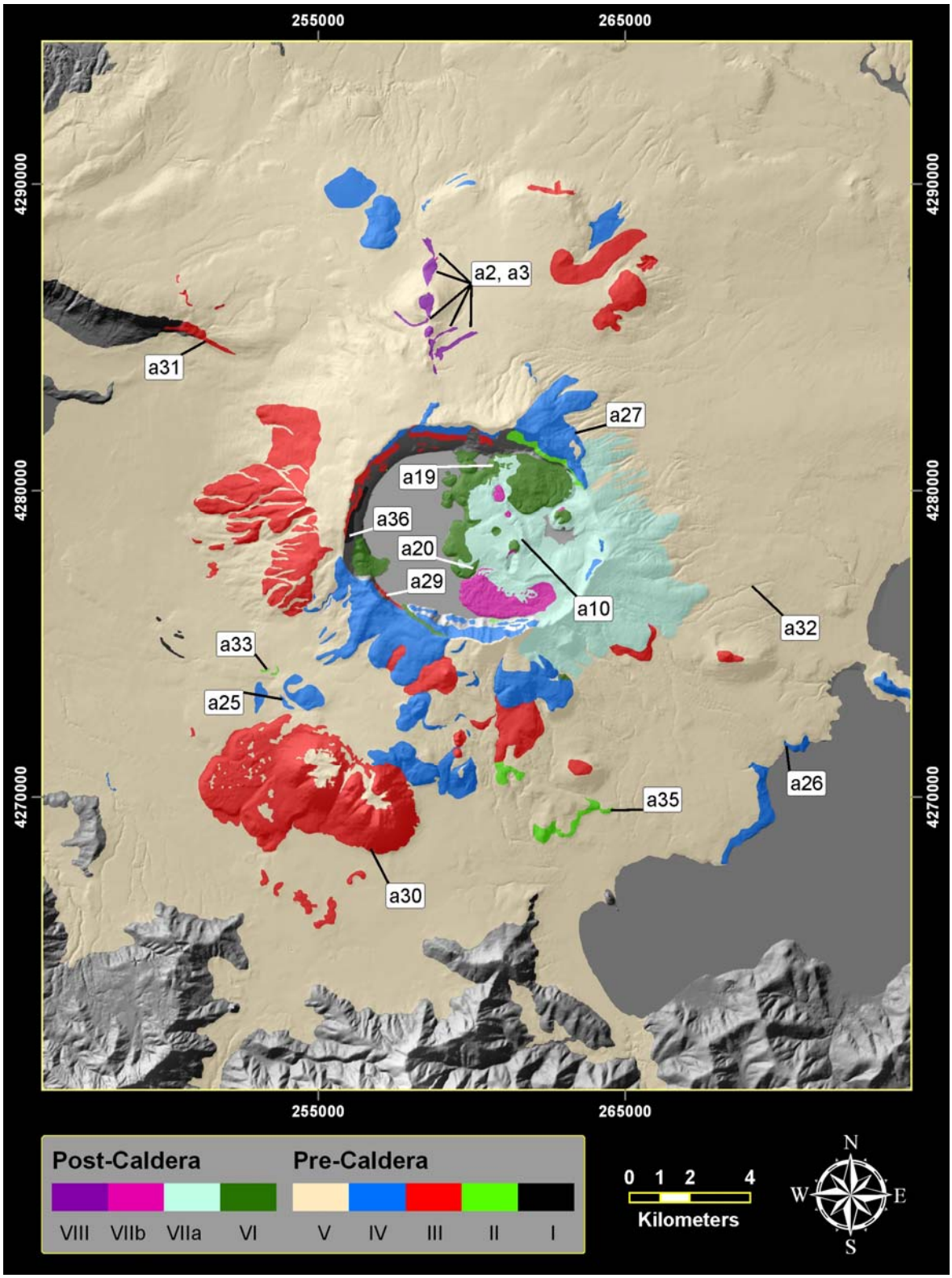

Figure 2.5. Stratigraphical evolution of Nemrut Volcano. Roman numerals in the legend reference the sub-stages given in Table 2.1. Quotations made in white boxes are the known locations of dated samples given in Table 2.1. Geological representation was superimposed on Swiss style hillshade of DEM. Projection: UTM, European Datum 1950.

2.3.1. Pre-caldera activity

Pre-caldera stage of Nemrut volcanism extends from 1.0 Ma to 80 ka. This construction period can be divided into five sub-stages (Table 2.1, Fig. 2.5: I, II, III, IV, V); two initial sub-stages (I, II) are represented by lava flows and in the third one (III) peripheral doming is associated with lava flows. Lava flows dominated the forth sub-stage (IV), and the final stage (V) corresponds to the pyroclastic activity which lead to the formation of caldera.

Pre-caldera products of Nemrut volcanism, prior to the caldera forming eruptions, are dominantly composed of silica oversaturated trachytes and rhyolites (Çubukçu, 2008). Nevertheless, there are scarce outcrops of basaltic trachyandesites (mugearites) and metaluminous trachytes (Çubukçu, 2008).

It has been suggested that the oldest volcanic products of Nemrut volcanism were fissure basalts (e.g. Özpeker, 1973a; Güner, 1984; Atasoy et al., 1988; Karaoğlu et al., 2005; Özdemir et al., 2006) located in Bitlis Valley, ~45 kilometers south of the Nemrut volcano (Çubukçu, 2008). On the contrary Ercan et al. (1990) proposed a fissural basaltic origin different than Nemrut for these lava flows. Two different ages were obtained from these basalts: <2.5 Ma (Ercan et al. (1990) and 0.79 Ma (Atasoy et al., 1988). Both Çubukçu (2008) and Ercan et al. (1990) suggested that these relatively older Bitlis valley basalts should not be included into the Nemrut volcanic system. These flows most probably belong to an earlier different system.

Sub-stage I (~1.0 Ma – 500 ka)

Nemrut volcanism has been initiated with lava flows represented by metaluminous felsic rocks exposed on the southeastern flanks of the volcano, and continued with, the oldest known peralkaline silicic (Çubukçu, 2008) lavas represented by the samples of Atasoy et al. (1998) and Pearce et al. (1990) taken from the western caldera wall. Lower contacts of these lava flows were not observed in our field studies; consequently this age signifies the lowest limit of temporal space of Nemrut volcanic history (Çubukçu, 2008). These lava flows are about 300 m above the western base of the main cone, it would be viable to state that the volcanism has initiated prior to this activity.

Sub-stage II (500 – 300 ka)

During sub-stages II and III, volcanic activity seems to be intensified and the central cone was formed (Çubukçu, 2008). The lava flows of the second sub-stage exhibit stratigraphical, thus temporal evolution from trachytic to rhyolitic compositions (Çubukçu, 2008).

Sub-stage III (300 – 200 ka)

The third sub-stage continued to produce rhyolitic and trachytic lava flows. However, peripheral doming marked the third sub-stage, forming Kirkor domes, Yumurtadağ, Fakı, Kalekirana hills and Kale Hills (Figs. 2.1 and 2.6a, b) at the southern flank and Mazik and Girekol domes at the lower western flank of the volcano (Fig. 2.1 and 2.7). The geochemical data and dating are lacking, but stratigraphically domes forming Kayalı, Tavşan and Arizin hills at the northern side of the volcano belong to the same sub-stage. All of these domes are partially covered by the later pyroclastic units.

Kirkor domes (Fig. 2.6a) culminates at 2478 m (western peak) and 2442 m (eastern peak). Domes are comenditic in composition (Çubukçu, 2008) and dated at 242 ± 15 ka (Atasoy et al. 1988) Lavas originating from Kirkor complex have flowed 3 km to the southwest (Figs. 2.1, 2.5 and 2.6a) and formed steep plateaus of ~ 30 m height.

Kale Hills west of the Çekmece village and Kalekirana hill (Figs. 2.1 and 2.6b) are comenditic in composition. These domes are aligned on a fault and as it will be discussed later, the same fault probably separates the caldera into two blocks.

Mazik and Girekol domes are at the western flank of the volcano and southeastern end of Muş basin (Figs. 1.6, 1.7, 2.1 and 2.7). Mazik dome is a trachytic lava dome, covered with ignimbrites, that culminates at 1680 m, rising 370 m from Muş basin.

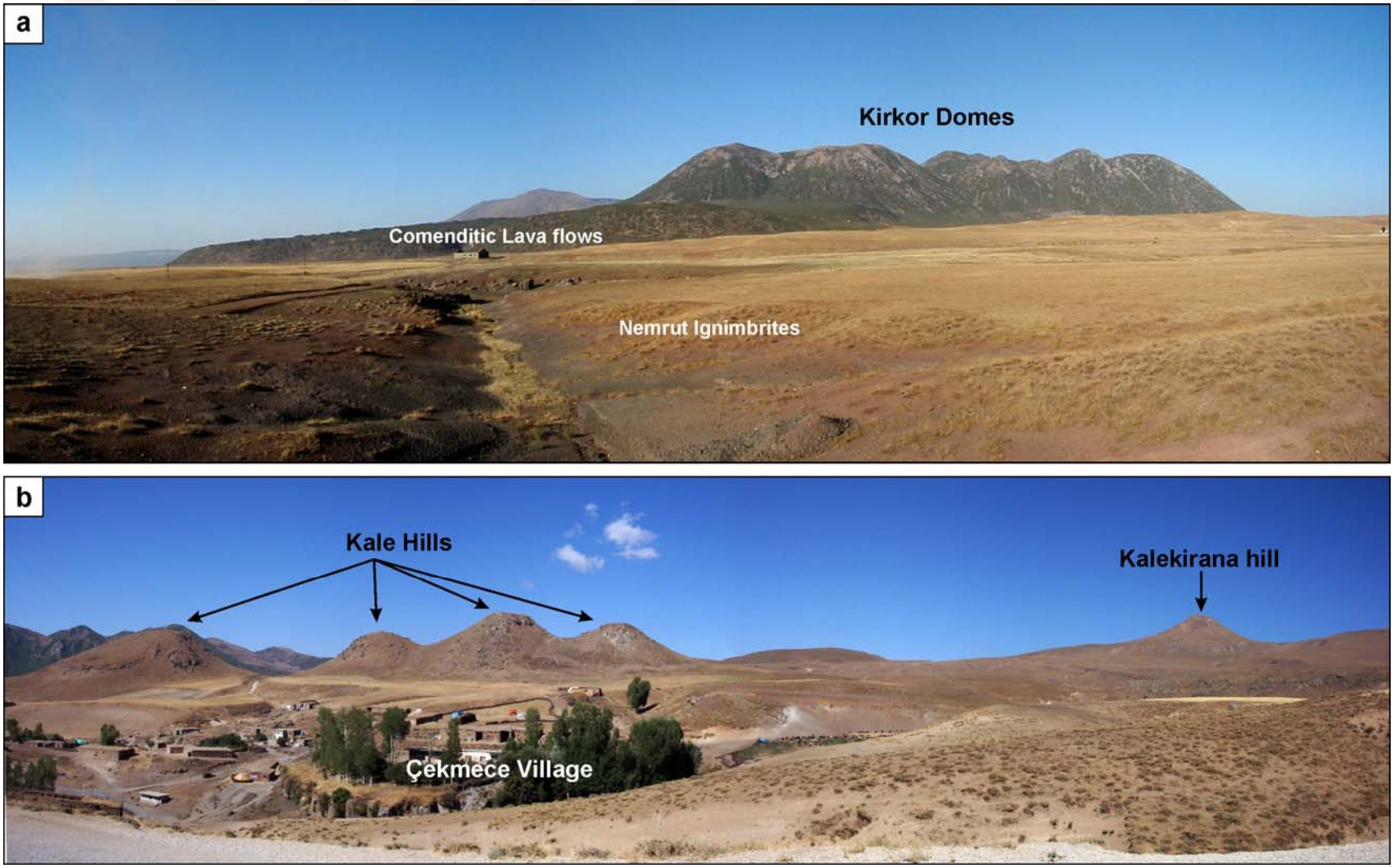

Figure 2.6. Peripheral domes at the southern flank of Nemrut volcano. **a)** Kirkor domes and associated lava flows (Comenditic Trachytes) as viewed from south, **b)** Aligned Kale Hills and Kalekirana hill (from east).

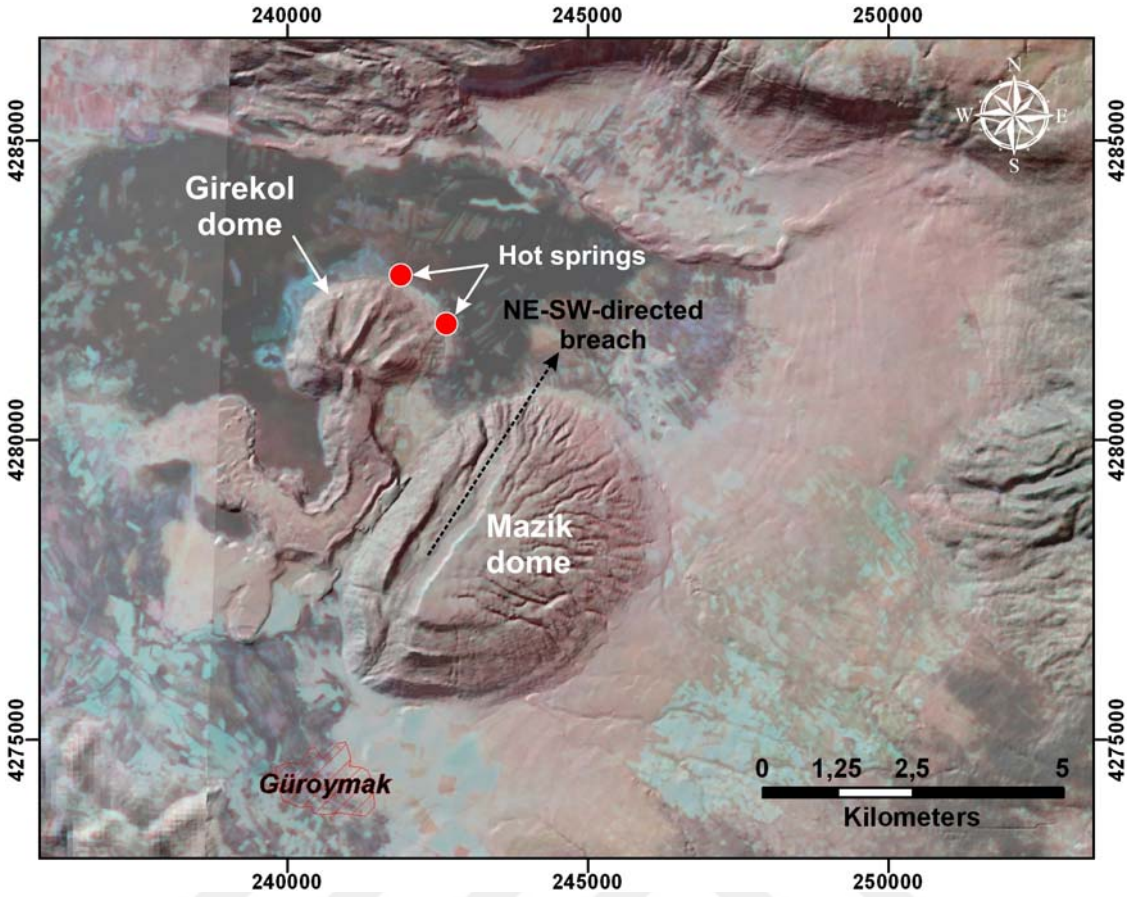

Figure 2.7. Mazik and Girekol domes at east of Nemrut volcano. Landsat image (6:3:1) superimposed on DEM. Projection: UTM, European Datum 1950.

The most striking feature of the Mazik dome is the NE-SW-trending breach related to the two faults on the top of the dome. Together with the concentric faults at southern flank of the dome (Figs. 2.1 and 2.7), it resembles an interrupted tumescence of a rigid body. Girekol dome is smaller, its total height is 200 m, and it culminates at 1480 m. A lava flow originates from comenditic Girekol dome (Figs. 2.1 and 2.7), and at the northern side, there are (at least) two hot springs (Fig. 2.7).

Atasoy et al. (1988) stratigraphically places the İncekaya volcanism concurrent with the post-caldera volcanism of Mt. Nemrut. On the contrary by petrological means, Çubukçu (2008) suggest that İncekaya volcanism is generated in the third evolutionary sub-stage, during the pre-caldera period. Although there are no dated samples representing İncekaya volcanism, fine-grained base-surge deposits observed at İnce cape north of Lake Van are overlain by caldera forming Nemrut Ignimbrites. Consequently, İncekaya volcanism was most probably generated prior to the collapse of the caldera.

Sub-stage IV (200 – circa 80 ka)

Initial period of this stage is represented by lava flows of basaltic and mugearitic composition. One of these flows can be observed on Kerkorumıksi hill (Figs. 2.1 and 2.28). The other one crops out through Kale hills to Benekli village at south (Fig. 2.1 and 2.28). This flow observed as small outcrops covered with ignimbrites (Fig. 2.8a). Later period generated pantellerite, comenditic trachyte and comendite type lava flows. First group of these flows occur at elevations higher than ~2100 m (Figs. 2.1 and 2.5) and gave the final shape to the pre-caldera volcanic edifice. A comendite flow, which is observed to change direction after bumping onto Kelakirana and Kerkorumıksi domes, is older than 158 ± 4 ka (i.e. Çubukçu, 2008). Çubukçu (2008) concluded that the timing of peripheral doming, in at least the well-exposed southern area, could be confined to ages older than 160 ka. The second group of the fourth sub-stage lava flows is distributed on the lower flanks at the periphery of the edifice, they are observed near the peripheral lava domes at north of the caldera and on the shoreline of Lake Van (Figs. 2.1 and 2.5).

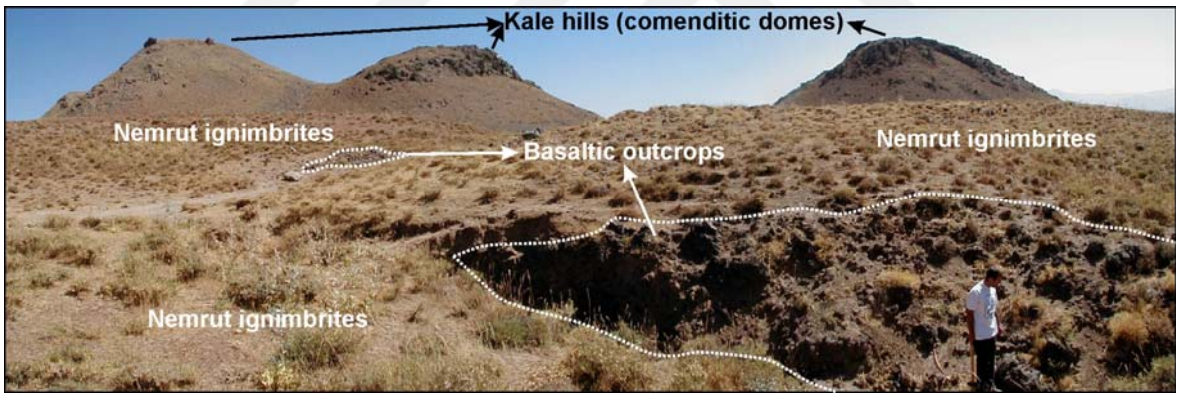

Figure 2.8. Mugearite outcrops covered with ignimbrites at southeast of Kale hills.

Tuğ and Yasintepe ignimbrites

There are at least two pyroclastic activities within the third and probably fourth sub-stages. Although these pyroclastic units are covered by the products of later activities, they were observed in the drill holes of UNOCAL and TPAO (Atasoy et al., 1988 and references therein) and alternate with lava flows of third and fourth sub-stages.

In our field studies, we evidenced two ignimbrite units that are differing from caldera forming ignimbrite series; they were not mentioned in previous studies. The first ignimbrite unit was observed south of Tatvan town (Fig. 2.1) at about 17

km distance from the caldera. Ignimbrite unit outcrops along the E-W directed valley between Dalda village and Tuğ district, close to Tuğ district and named after it. Tuğ ignimbrite unit is white-yellow in color and bears white pumice fragments up to 3-4 cm. The ignimbrite is often overlain by resedimented layers and lacustrine sediments, or at some locations, by plinian units. These ignimbrite deposits are subjected to intense weathering. On the northern flank of the valley, Nemrut ignimbrites uncomformably overlie the Tuğ ignimbrites.

The second ignimbrite unit is observed at Yasin hill west of Ahlat town. Yasin hill is at 6.5 km north of Taşharman village, and 17 km NE of Nemrut caldera (Figs. 2.1 and 2.9a). This unit is named after this location as Yasintepe ignimbrite. Large pumices (Fig. 2.9a; mean of 5 max. pumice sizes: 14.9 cm) and white color of the unit (Fig. 2.9b) are the most distinctive characteristics of the Yasintepe ignimbrite. The ignimbrite outcrops along Yasin hill, southwestern and northeastern side of the exposure is covered with later Nemrut ignimbrites. Other ignimbrite units do not bear coarse pumices as Yasintepe ignimbrite at a distance of 17 km from the caldera. For the origin of Yasintepe ignimbrite, possibility of a source different than Nemrut volcano should not be disregarded.

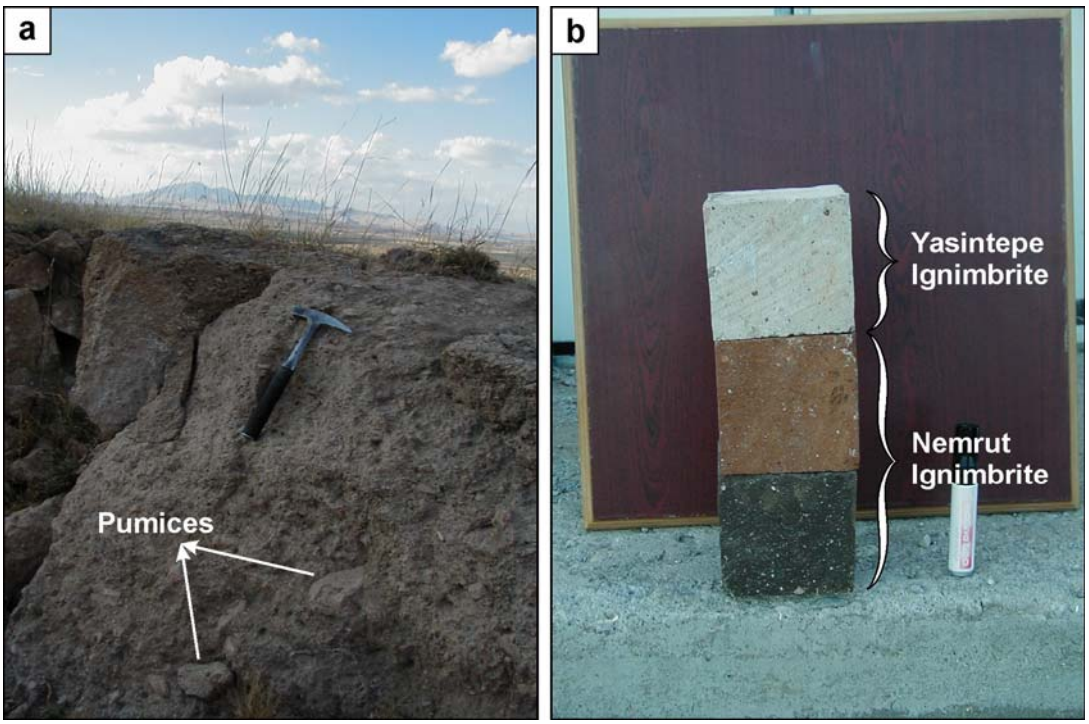

Figure 2.9. a) Outcrop of Yasintepe ignimbrite at Yasin hill, **b)** Sample ignimbrite blocks mined for commercial purposes. Color changes in Nemrut ignimbrite from black to reddish brown. Yasintepe ignimbrite displays white color, differently from all other ignimbrite units in the vicinity of Nemrut volcano.

2.3.2. Caldera forming eruptions (Sub-stage V)

Products of eruptive activity that caused the collapse of the caldera were studied in detail. At 63 locations, stratigraphic sections of the pyroclastic units were measured. Location map of these sections is given in Figure 2.10. At all these locations, physical features of pyroclastics were investigated, thickness of the units, maximum size of lithics and pumices were measured. To create a color distribution map, ignimbrite units were photographed at all locations. Because of the large size of the data, detailed stratigraphic sections with descriptions and photographs were provided in electronic appendix-2. All the stratigraphic sections were correlated; these correlations are presented in Figure 2.11 (a stratigraphical accordance was chosen to present the correlations).

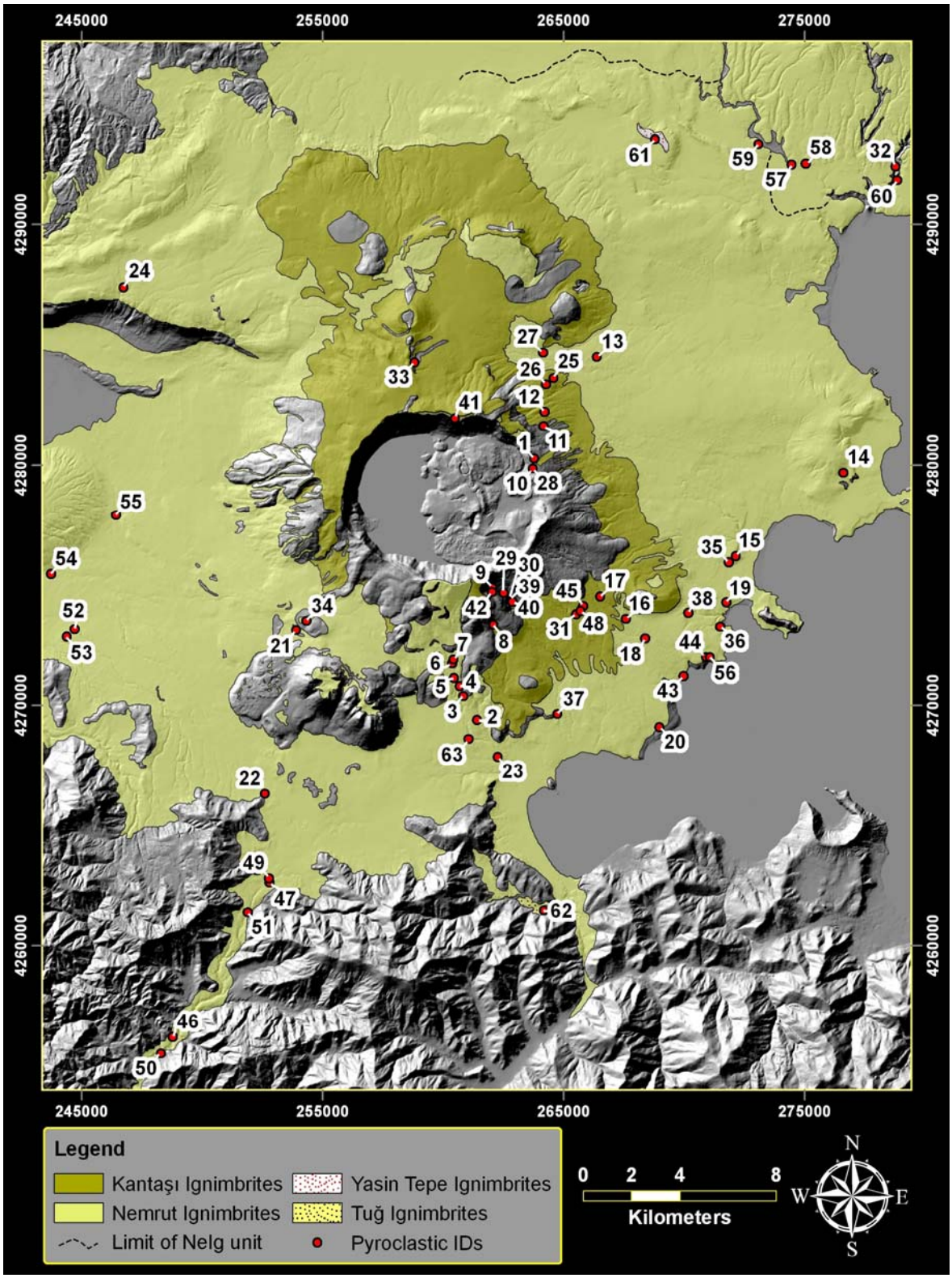

Figure 2.10. Location map of stratigraphic sections. Pyroclastic IDs (PID) point the stratigraphic section locations. Detailed stratigraphic sections are presented in e-appendix-2 with same PIDs. Projection: UTM, European Datum 1950.

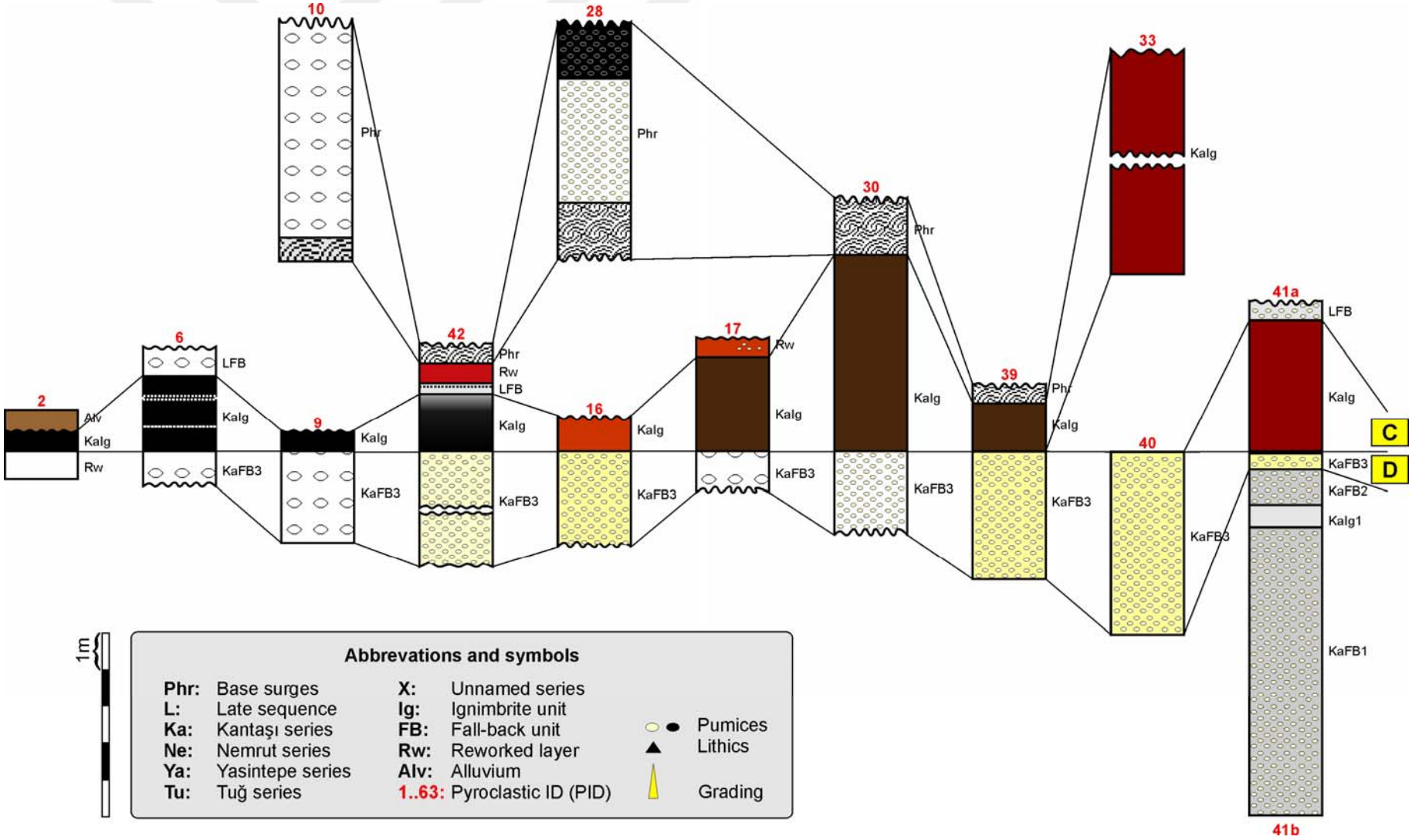

Figure 2.11. a) Correlation of stratigraphic sections. Locations of the sections are provided in Figure 2.10 with Pyroclastic IDs (PID). Letters in yellow boxes indicate the correlation in the next figures.

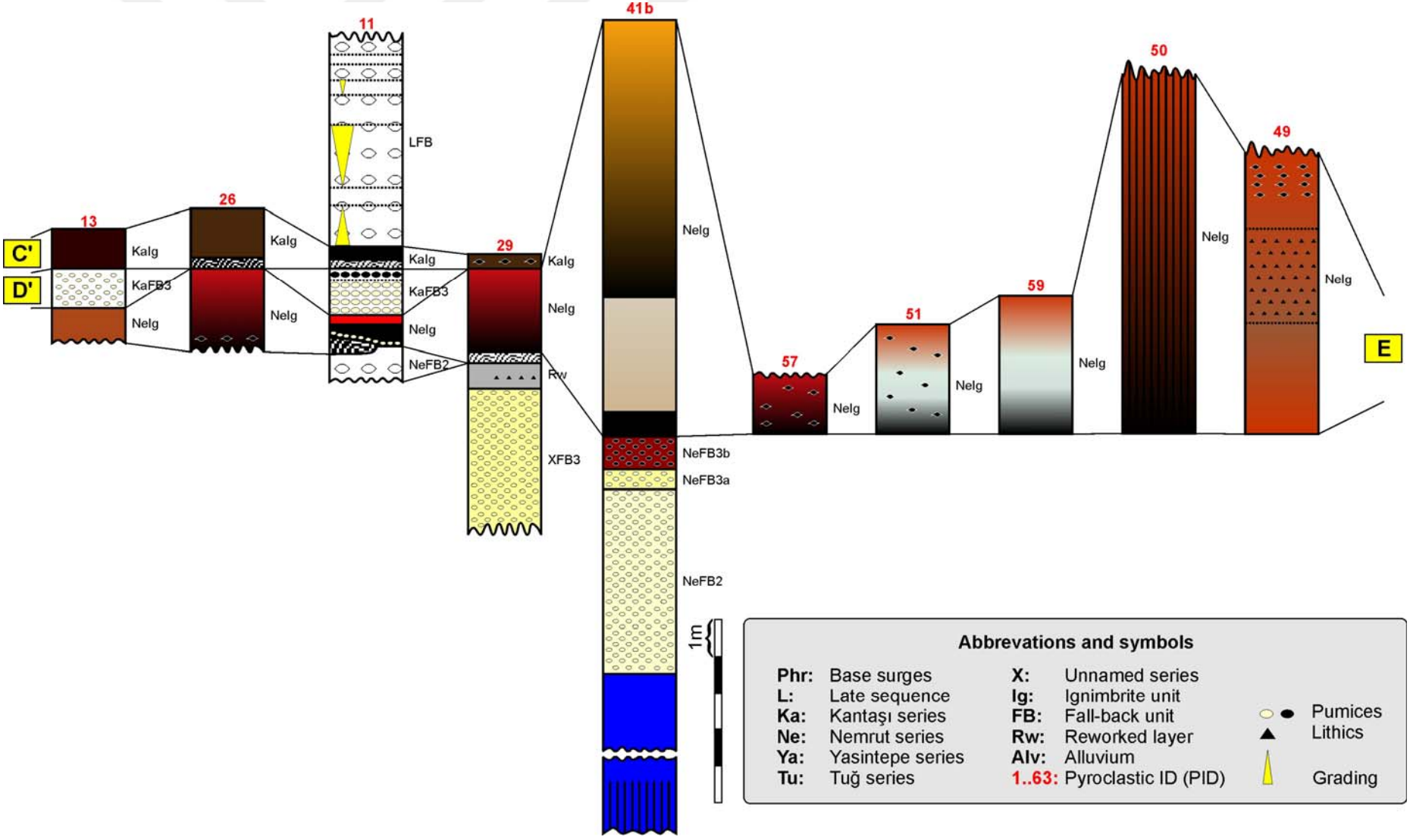

Figure 2.11. b) Correlation of stratigraphic sections (continued). Locations of the sections are provided in Figure 2.10 with Pyroclastic IDs (PID).

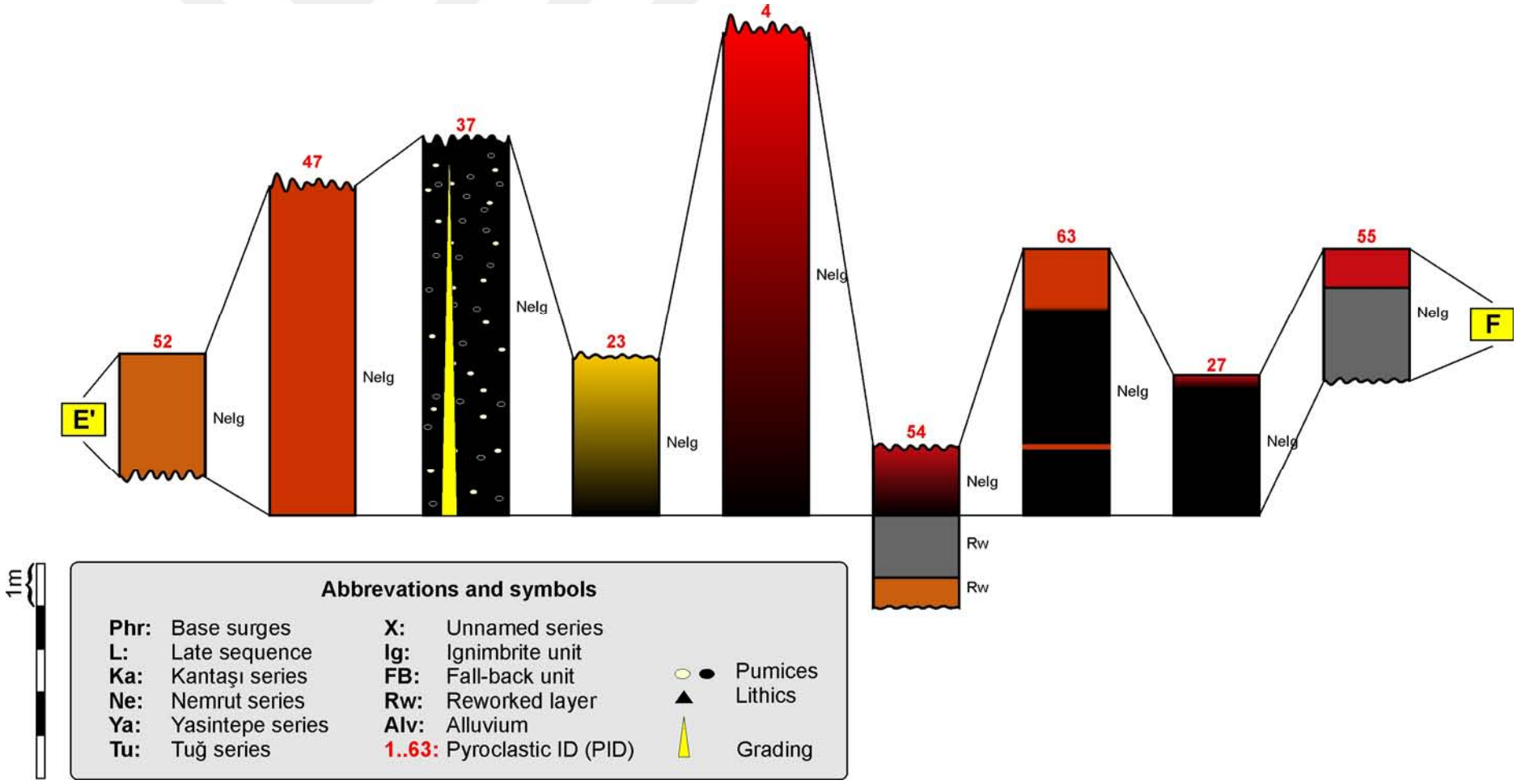

Figure 2.11. c) Correlation of stratigraphic sections (continued). Locations of the sections are provided in Figure 2.10 with Pyroclastic IDs (PID).

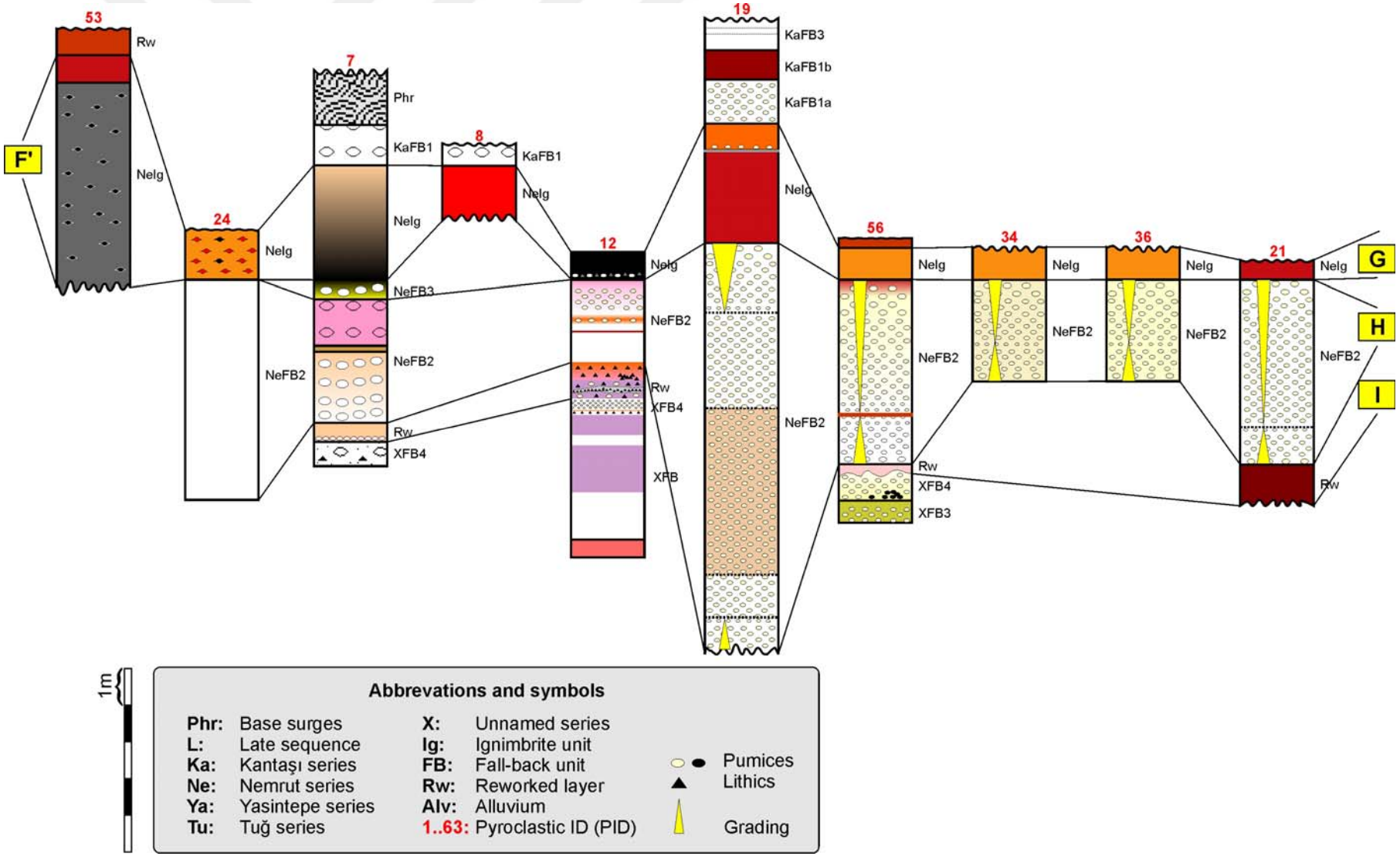

Figure 2.11. d) Correlation of stratigraphic sections (continued). Locations of the sections are provided in Figure 2.10 with Pyroclastic IDs (PID).

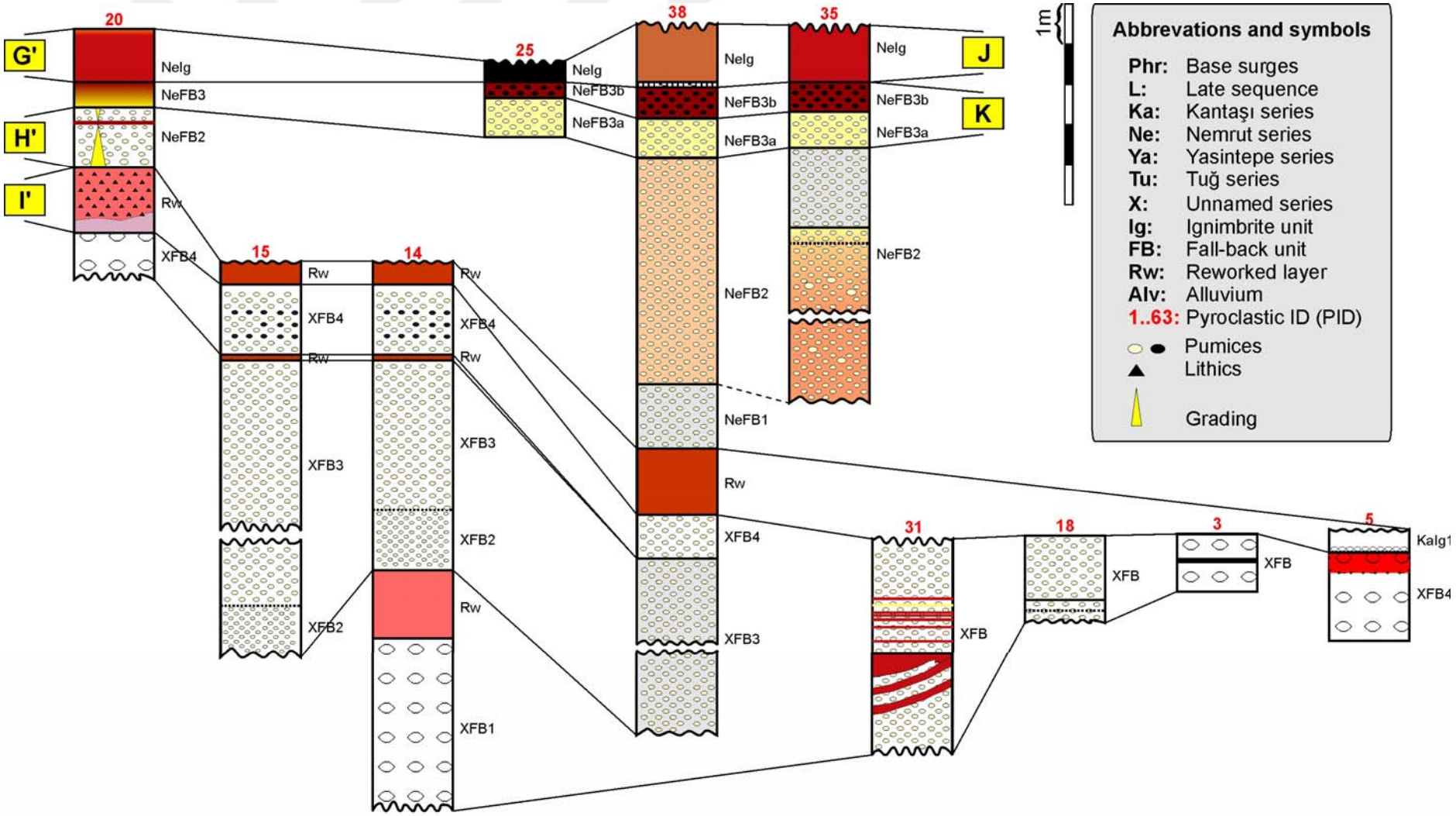

Figure 2.11. e) Correlation of stratigraphic sections (continued). Locations of the sections are provided in Figure 2.10 with Pyroclastic IDs (PID).

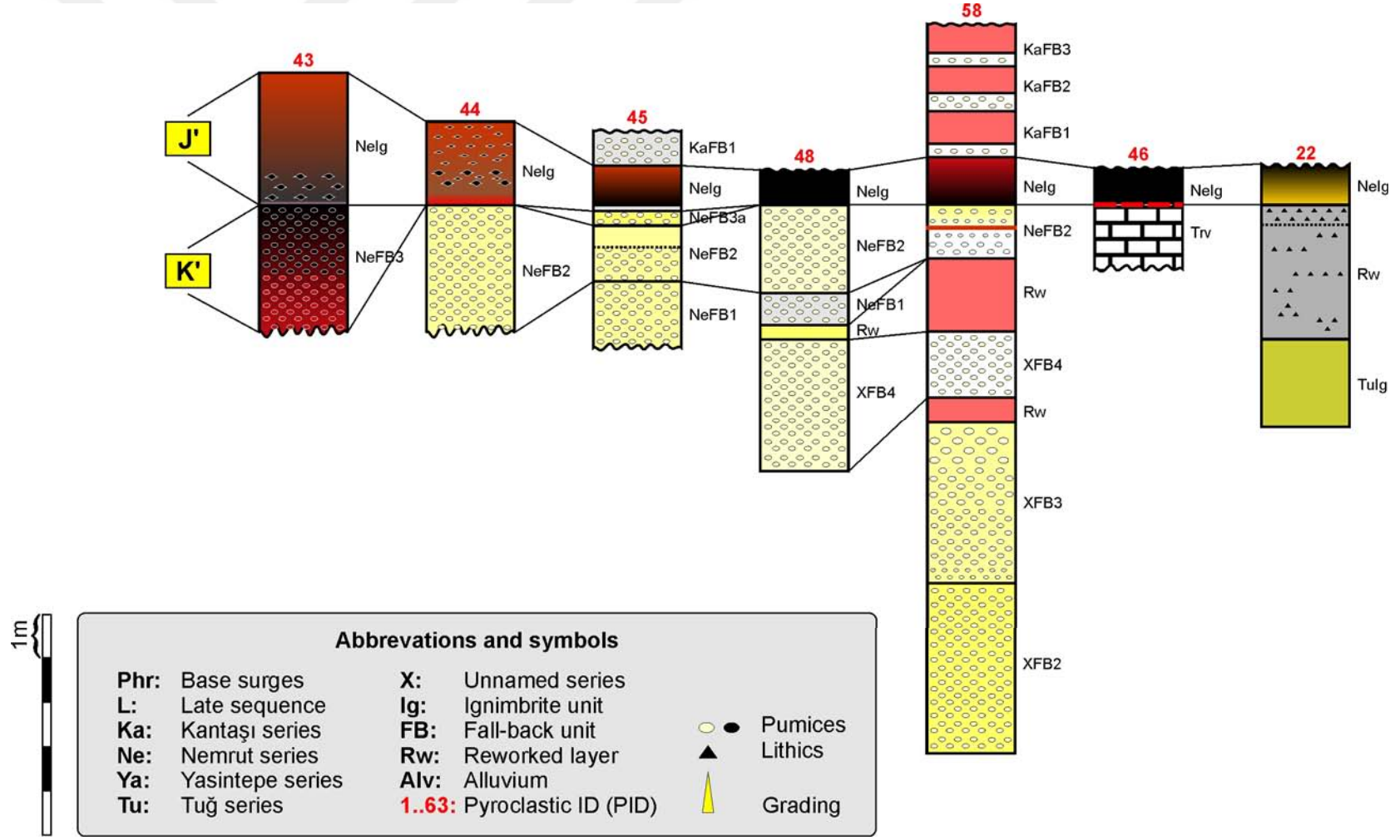

Figure 2.11. f) Correlation of stratigraphic sections (continued). Locations of the sections are provided in Figure 2.10 with Pyroclastic IDs (PID).

Generalized pyroclastic section of pyroclastic products is presented in Figure 2.12. Two different ignimbrite series related to the formation of the caldera were identified: Nemrut ignimbrites and Kantaşı ignimbrites.

Older eruptions

Emplacements of plinian units older than Nemrut and Kantaşı ignimbrites were observed (Figs. 2.11 and 2.12). These units are separated from Nemrut ignimbrites by reworked layers. Four older fall-back units were discriminated (Figs. 2.11 and 2.12: XFB1-4). These units are composed of pumice-rich material and there are many quarries working on these units. XFB1 is observed on Aktepe hill, at north of Sarıkum village (Fig. 2.12: PID: 14). Outcrops of XFB2, XFB3 and XFB4 (Fig. 2.12) are distributed over an area between Tatvan town and Saka village southeast of Ahlat town. Between XFB1 and XFB2, we observed a reworked layer (Fig. 2.12); XFB2 and XFB3 were emplaced with no time gap, and XFB4 overlies these units again over a resedimented layer (Figs. 2.12 and 2.13). This second reworked layer is thinner (few tens of centimeters) when compared to the first one. Pumice sizes in XFB2 are homogeneous, whereas they are heterogeneous and larger in XFB3 (Fig. 2.13, Table 2.2). The contact between these levels is gradational and these two levels must be regarded as one unit that represent a change in the eruption intensity rather than two different units. XFB4 is rich in lithics when compared to XFB2 and XFB4. Rapid change in pumice size in XFB2 and XFB3, reworked layers and lithics in XFB4 are key features to differentiate these fall-back units.

Pumice and ash sample from a valley north of Fakı hill (Fig. 2.5: a32) was dated at 272 ka (Table 2.1), and is considered to be related to Nemrut ignimbrites (Atasoy et al., 1988). However, we observed that Nemrut ignimbrites overlie lava flows that were dated between 89 ka to 263 ka (Table 2.1), and could not be older than 89 ka (e.g. Çubukçu, 2008). Sample dated by Atasoy et al. (1988) probably represents XFB units. In hence, XFB units are not related to caldera forming eruptions, they were emplaced in sub-stage IV and sub-stage V.

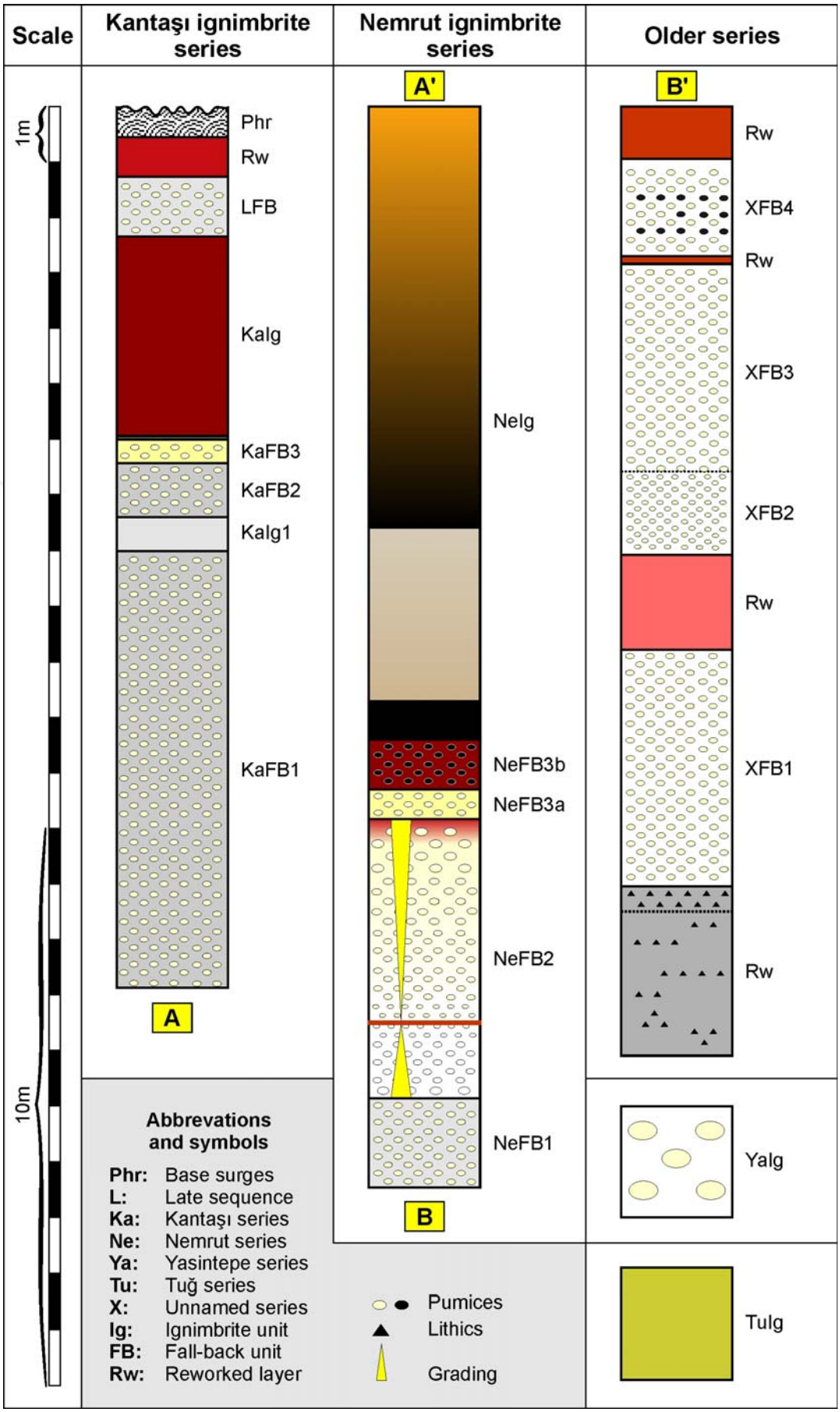

Figure 2.12. Generalized stratigraphic sections of pyroclastic units.

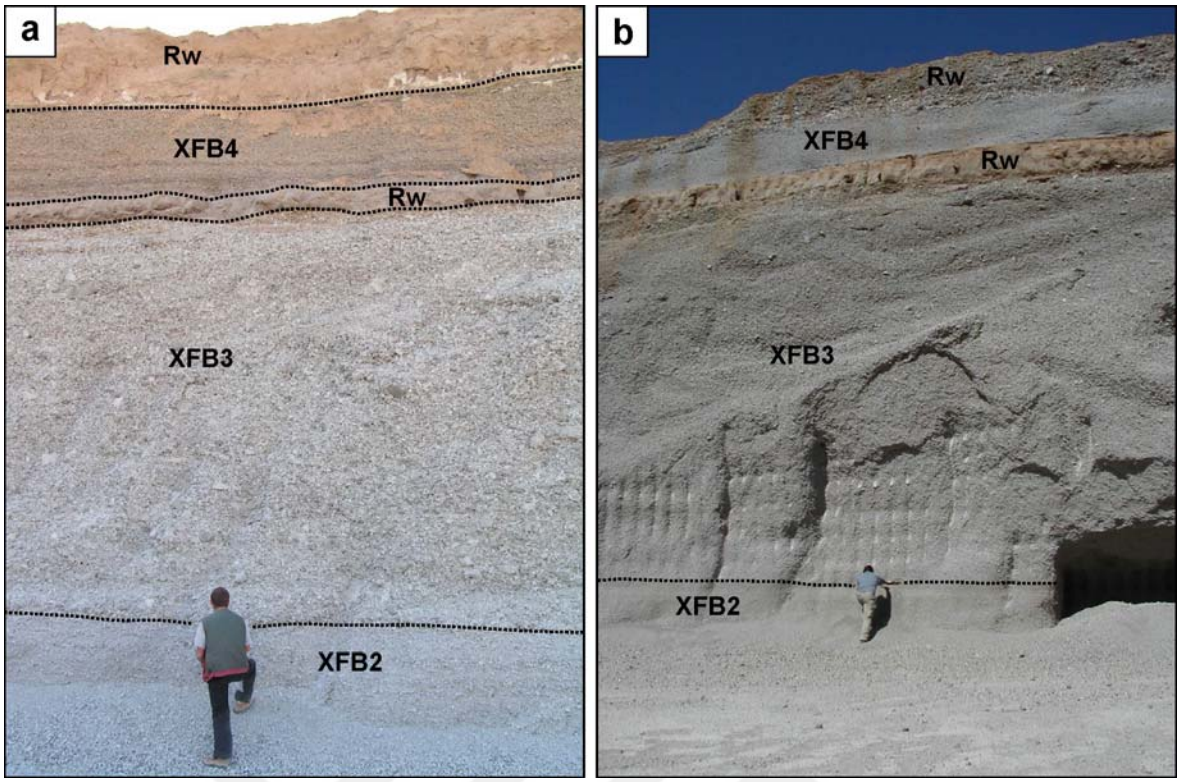

Figure 2.13. Photographs of fall-back units older than caldera forming eruptions (XFB2, XFB3 and XFB4) and reworked levels (Rw) **a)** at a quarry north of Sarıkum village (PID: 14) and **b)** at a quarry on Yumurta hill located east Sarıkum bay (PID: 15).

	Average of 5 max. Pumice size (cm)				Thickness (cm)			
PID	**XFB1**	**XFB2**	**XFB3**	**XFB4**	**XFB1**	**XFB2**	**XFB3**	**XFB4**
3		5.9				74	63	
5				5.6				270
7								66
12								385
14	8.9	12.2	24.4	10	800	150	374	176
15			24.8			129	960	
18		4.5	5.1			57	160	
20				3.7				
29			11.8				400	
38							898	109
48								300
56			4.8	7.7			60	64
58		5.5	11.1	6.4		386	366	150
				Total	800	796	3281	1520
				Mean	800	159.2	410.1	190
				~Volume (km^3)	5	3.5		1.2

Table 2.2. Average of maximum 5 largest pumice sizes, thicknesses and volume estimations of XFB units. For locations, refer to PID values in Figure 2.10.

No ignimbrites related to those fall-back units were observed, but Yasintepe ignimbrite or Tuğ ignimbrite may be related to these eruptive phases. Mean thicknesses of XFB units are given in Table 2.2. Using these thicknesses, we made a rough calculation of the volume of these pyroclastics (Table 2.2). An approximate area (620 km^2) considering the distribution of the XFB units was used in the calculation.

Nemrut Ignimbrite Series

Nemrut ignimbrites have the largest outspread amongst the other products of the Nemrut volcano. Karaoğlu et al. (2005) also used the nomenclature "Nemrut ignimbrite", but the stratigraphic and physical description they introduced is totally different from the one that will be presented here. Moreover, they did not identified Kantaşı ignimbrites.

In the study area (Fig. 2.1), Nemrut ignimbrites cover an area of 1089 km^2. Moreover, fall-back units extend through NE and the pyroclastics in Lake Van must not be disregarded.

Nemrut ignimbrite series are composed of three plinian units (Fig. 2.12: NeFB1, NeFB2 and NeFB3) and an ignimbrite unit (Fig. 2.12: NeIg). It is possible to observe these plinian units occur almost all around the volcano.

Products of caldera forming eruptions begin with felsic fallout tephra that has formed during the initial plinian phase (Çubukçu, 2008). NeFB1 is the lowermost plinian unit of the series and overlies older fall-back units with a hiatus that is represented by a reworked layer (Fig. 2.14a). NeFB1 is a grey, yellowish colored pumice fall-back unit (Fig. 2.14a). When compared to other units of the Nemrut series NeFB1 is the least observed unit. Outcrops of this unit occur between Kıyıdüzü village and southeastern flank of the volcano (Fig. 2.10); extension of the unit is limited within this area.

Figure 2.14. Photographs of pyroclastics of Nemrut ignimbrite series (Rw: reworked levels): **a)** at a quarry east of Fakı hill (PID: 38), **b)** reverse to normal graded NeFB2 (Nemrut fall-back) unit and overlying Nemrut ignimbrite (NeIg) near Kıyıdüzü village (PID: 56), **c)** NeFB2 unit at southwest of Nemrut volcano, near Kirkor domes and **d)** thick NeFB2 unit and overlying Nemrut ignimbrite at north of Kıyıdüzü village.

NeFB2 and NeFB3 are the key units in the series. NeFB2 is a pumice fall-back unit, generally white, grayish and yellowish in color. Typically from the bottom of the unit to the top, NeFB2 has well-developed reverse to normal grading (Figs. 12 and 2.14b). At some outcrops, top few decimeters are dominated by a reddish, brownish color. Sometimes it is possible to observe a thin brownish ash level between reverse graded and normal graded horizons (Figs. 2.11, 2.12 and 2.14b,c).

Maximum pumice diameters (average of 5 largest pumices) and tephra thickness at 13 outcrops were measured for NeFB2 unit (Table 2.3). The maximum pumices at each outcrop occur generally in the upper horizons, presumably when maximum eruption intensity occurred. We were able to produce an isopleth map (Fig. 2.15) for NeFB2 deposit. Isopleths show that the eruption cloud was evolved towards Lake Van under the effect of prevailing wind which was directed E05ºS. On the other hand, at the present day, prevailing wind is directed SSW with a max velocity of 29.0 m/s (Fig. 2.15, black arrow; Table 2.4) towards Bitlis city.

	Average of 5 max. Pumice size (cm)						Thickness (cm)		
PID	**NeFB1**	**NeFB2 bottom**	**NeFB2 middle**	**NeFB2 upper**	**NeFB3a**	**NeFB3b**	**NeFB1_t**	**NeFB2_t**	**NeFB3_t**
7			5.4		3	3		336	53
12			4.2	11				225	
19		4.2	6.3	20.3				1120	
20		7.4	1.7	2.6		8.3		104	
21		7		7.5				504	
24		0.063	0.063	0.063				600	
25					4.6				137
34		6	1.8	7.2					
35				23.7				1150	163
36		4.5		19.4					
38							161	566	140
41								506	144
43					19.2	19.2			300
44				17.4					
45	0.3		6.2	8.7	3.5			175	33
48							73	200	
56		6.9		17.2	12	12		503	
58		4.2	4.2	4.2	0.063	0.063		122	

Table 2.3. Average of maximum 5 largest pumice sizes and thicknesses of NeFB units. For locations, refer to PID values in Figure 2.10.

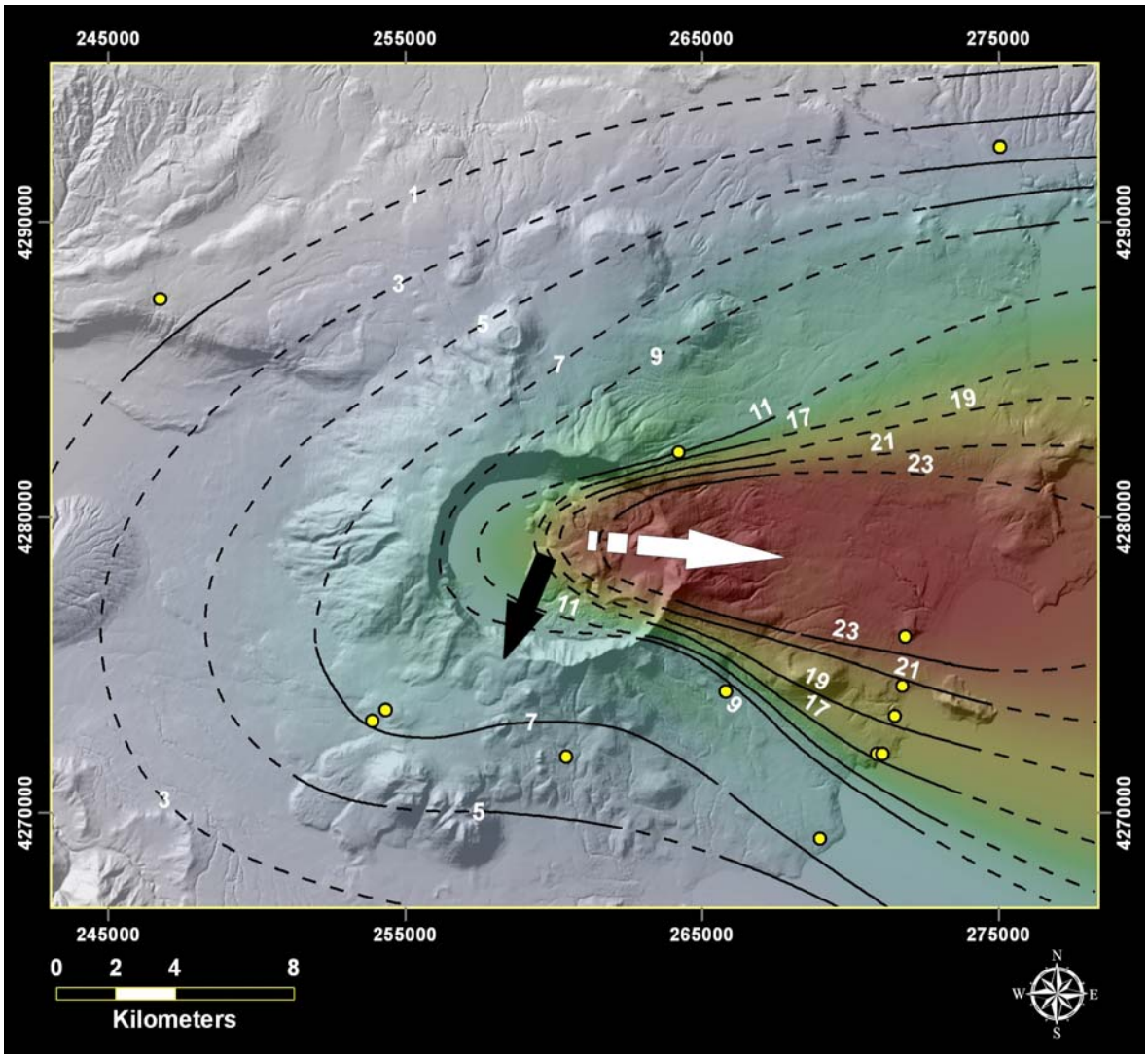

Figure 2.15. Isopleths for NeFB2 unit, drawn using average 5 maximum pumice sizes measured at 13 locations (yellow points). White numbers referencing the isopleths are in centimeters. White arrow points the probable prevailing wind direction in the time of eruption. Black arrow points the annual average of prevailing wind direction for the last 30 years. Projection: UTM, European Datum 1950.

	Months												Annual Average
	I	II	III	IV	V	VI	VII	VIII	IX	X	XI	XII	
Direction	SSW	SSW	ESE	SSW	SSW	S	W	WNW	SW	ENE	WNW	SW	SSW
Velocity (m/s)	29.0	25.4	25.3	26.5	28.3	23.0	18.0	25.3	20.0	22.8	23.6	20.9	29.0

Table 2.4. Direction and velocity of prevailing wind at maximum velocity (Average of 30 years). Data from Turkish State Meteorological Service.

NeFB2 is overlain by another plinian unit: NeFB3 (Fig. 2.12). Although, outspread of NeFB3 is not as large as NeFB2, this unit is well observed especially at the eastern and southern flanks of the volcano and around the southeastern flatlands. The unit is generally thinner than NeFB2 and reaches up to 3 m (Table 2.3). NeFB3 is typical with a color change; lower horizon (NeFB3a) of the unit is yellow,

whereas, the upper horizon is (NeFB3b) brown/black/reddish (Fig. 2.16). In addition to the intense color change in the unit, petrographical differences were also noted by Çubukçu (2008): White pumices of NeFB3a bear euhedral to subhedral alkali feldspar phenocrysts in a highly vesicular glass, microphenocrysts of clinopyroxene and olivine are very scarce. Opaque minerals are observed only as microlites. Moreover, NeFB3b is comprised of ternary feldspar, clinopyroxene and minute olivine. Clinopyroxenes are subhedral, whereas olivines are anhedral and display slight resorption. Groundmass is highly vesicular aphyric.

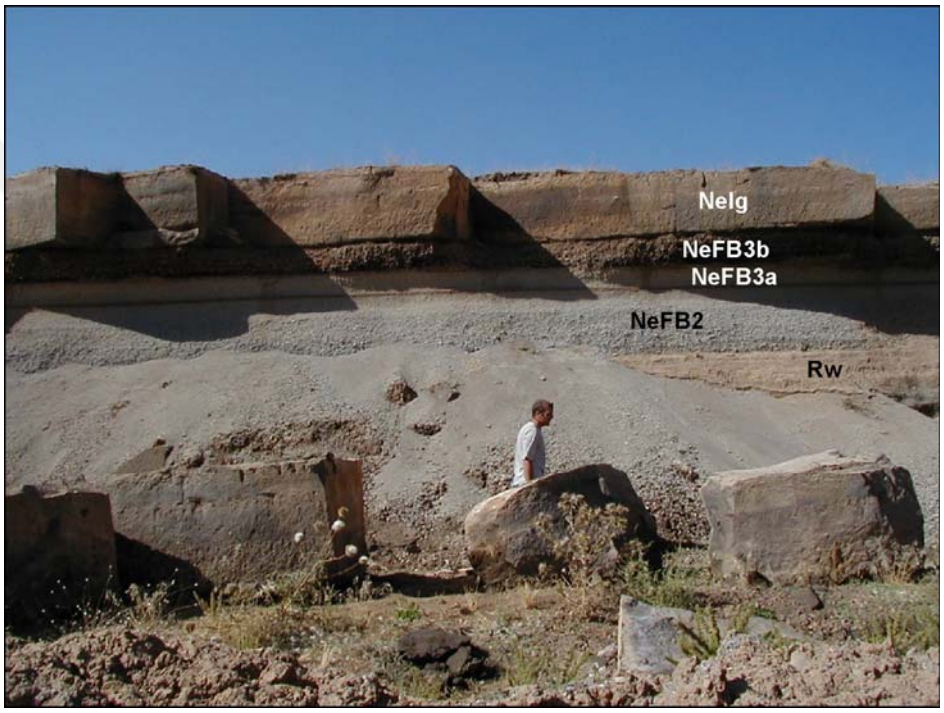

Figure 2.16. Plinian and flow unit of Nemrut ignimbrite series near Simek bay northeast of Tatvan (PID: 20), and yellowish to black/brown color change in NeFB3 fall-back unit (NeIg: Nemrut ignimbrite, NeFB: Nemrut fall-back units).

These two plinian phases are overlain by the main ignimbrite flow: Nemrut ignimbrite (Figs 2.12, 2.14 a,b,d and 16: NeIg), observed extensively in the region. At the eastern and northeastern flanks of the volcano, a ground surge level constitutes the lowermost section of the ignimbrite unit. With its largest outspreading (Figs. 2.1 and 2.10), Nemrut ignimbrite is the most voluminous product of the volcano. With some exceptions the flow unit is generally welded, well-welded and consolidated. Blocks of ignimbrite are used as raw material for construction purposes for thousands of years. Regionally, Nemrut ignimbrite constitutes the main construction material of Urartian, Seljukian, Armenian and

Ottoman architecture. This tradition continues today; especially Ahlat town and old Bitlis city are constructed totally by using Nemrut ignimbrite. Locally, the welded ignimbrite blocks mined from Nemrut ignimbrite are called “Ahlat stone”. In addition to the modern production processes, it is still possible to see the traditional production methods (Fig. 2.17).

Figure 2.17. Traditional mining of ignimbrite blocks, near Yasin hill at west of Ahlat town. Photograph by Adem SÖNMEZ (*Those who wrest a living from the stone*), used with permission of photographer.

Karaoğlu et al. (2005) defined two ignimbrite series and named them as “initial” and “main (*Nemrut*)” ignimbrites. They divided the initial ignimbrite into five different layers according to their degree of welding and physical features. They located these layers in the Bitlis valley, and somehow located a pumice flow deposit underlying this initial phase. They also defined a second ignimbrite series with an ignimbrite flow sequence composed of four different units/layers. On the contrary, it is essential to state that the ignimbrite unit in the Bitlis valley (“initial ignimbrite” in Karaoğlu et al., 2005) and the ignimbrite that outspread the plains around the volcano (“main ignimbrite” in Karaoğlu et al., 2005) are the same ignimbrite unit (Fig. 2.12: Nemrut ignimbrite, Neıg) and composed of only one flow unit. Güner (1984), Atasoy et al. (1988) and Yılmaz et al. (1998) also defined these units as one ignimbrite unit. There is no pumice or scoria flow units in the

vicinity of the volcano as described by Karaoğlu et al., (2005), there are no different layers/units indicating an interruption in the ignimbrite flow.

Nemrut ignimbrite is single flow unit, and represents rheological changes. Change in the degree of welding, consolidation and in the form of the components is common in the unit because of local variations in emplacement properties (i.e. channeling in Bitlis valley). Progressive change in color is the most evident characteristic of the unit; the color of the unit changes from black / dark grey / dark brown to light brown / reddish / pale yellow from bottom towards the top of the unit (Fig. 2.18). In the basal black level, a grayish/greenish horizon is marked at the northern caldera wall and in the Bitlis valley (Fig. 2.18d).

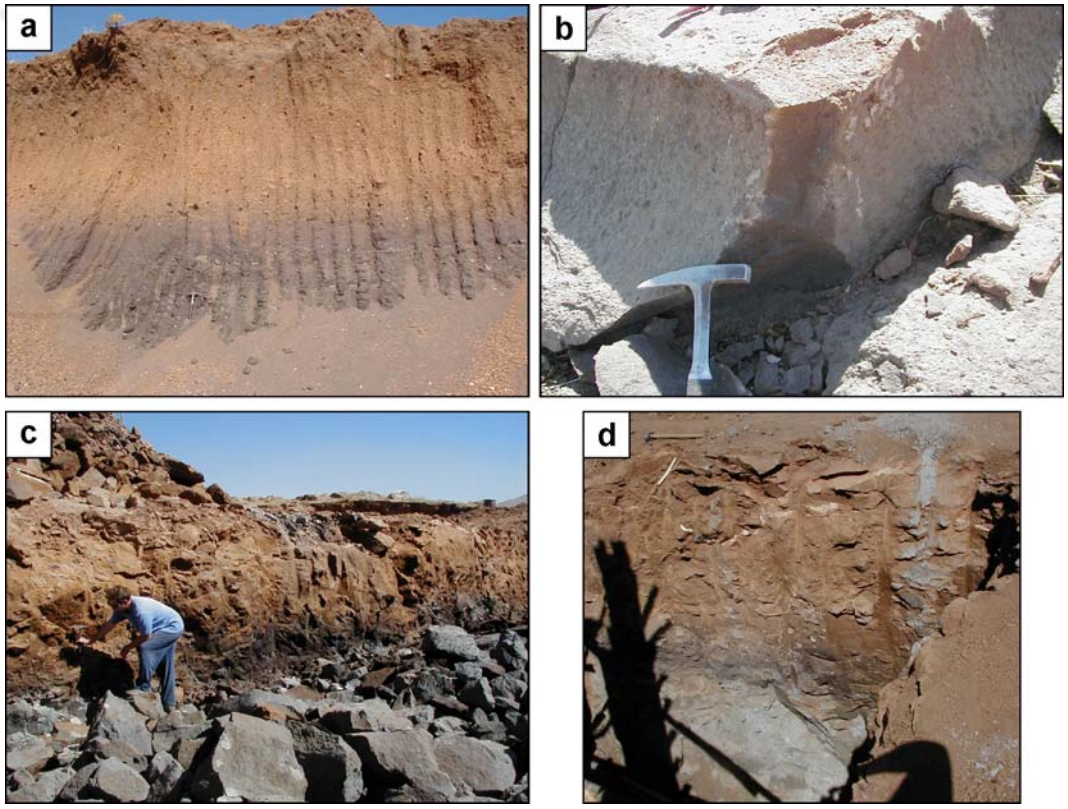

Figure 2.18. Progressive color change in Nemrut ignimbrite unit at outcrops **a)** near Tatvan town (PID: 23), **b)** near Serinbayır village (PID: 27), **c and d)** at a construction site north of Bitlis valley (PID: 51).

This color change is gradual in all locations except for two places (Fig. 2.19a,d). Near Tapu district (Fig. 2.1) which is located at northeast of Tatvan town, a thin light brown/orange colored level in the basal black horizon is clear (Fig. 2.19a,b,c). Around this outcrop near Tapu district, the change in color between basal black and upper light brown horizons is sharp (Fig. 2.19a), but when perused in detail,

no interruption could be observed between the two horizons. On the other hand, in the area between Aşağıkolbaşı village southwest of Kirkor domes and Raz district southeast of Güroymak town (Fig. 2.1), the upper light brown level is well welded and consolidated while the lower black level is not consolidated. In this area, locally, these two levels appear as if they are two different units (Fig. 2.19d).

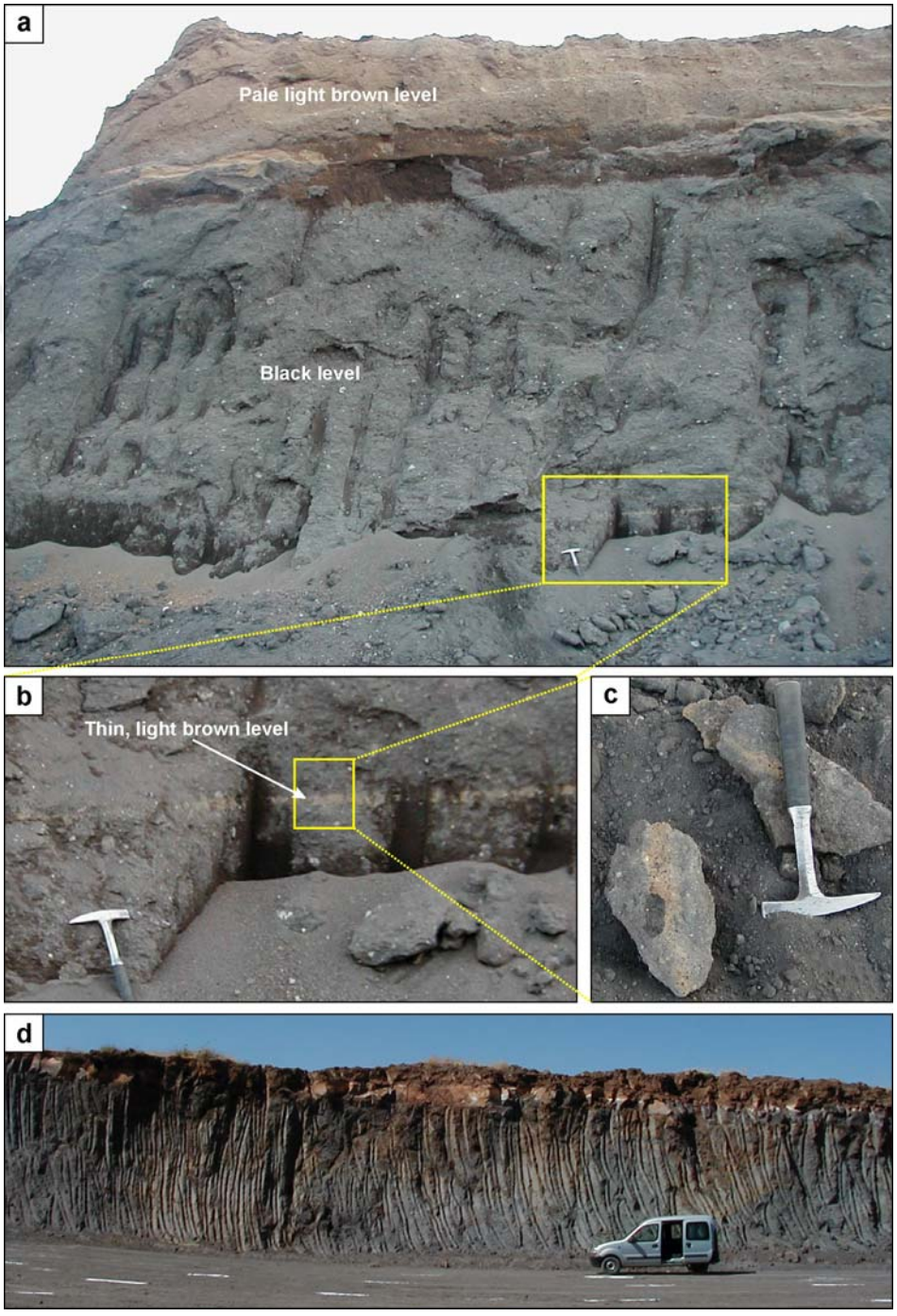

Figure 2.19. Nemrut ignimbrite with black basal and light brown upper horizons: **a)** Outcrop near Tapu district (PID: 63), **b,c)** thin light brown level in this outcrop, and **d)** outcrop where upper level emplaced like a different unit on the black lower horizon (PID: 53).

In addition to the change from bottom through the top of the unit, color of the Nemrut ignimbrite also changes spatially. For a better visualization of the spatial color change, we used the photographs of the unit. Red (R), Green (G) and Blue (B) color values for upper and lower horizons were sampled with an average of 5x5 pixels from the photographs of the unit at various locations. A table of R, G and B values was constituted for different locations; then these values were interpolated separately (i.e. R values to constitute a red band) using spatial locations of the samples. The final R, G and B bands were combined to compose two color change maps, one for the basal (Fig. 2.20) and the other for the upper (Fig. 2.21) levels of the Nemrut ignimbrite.

Basal black colored level of the ignimbrite is absent on the northwestern flanks and on the eastern flatlands (Fig. 2.20). This absence can be explained either by the limited flow of basal black level through the N, NE, S, SW and W flanks of the volcano (Fig. 2.20: white arrows), or by the change of the color of basal level during the cooling of the unit on the eastern and northwestern parts.

On the other hand, light brown color of the upper level is the dominant color of the ignimbrite with a large outspread (Fig. 2.21). At the northern section of the volcano, and in the Bitlis valley, color of the upper level slightly becomes dark brown and reddish (Fig. 2.21: 5, 6), where the ignimbrite is very well welded and consolidated (Fig. 2.22a). Fiammes are abundant in these well welded zones (Fig. 2.22c). In Bitlis valley, NeIg typically exhibit columnar jointing (Fig. 2.22a). It is strongly welded with significant fiammes exhibiting eutaxitic texture (Çubukçu, 2008). These collapsed and deformed juvenile pumice fragments are dark brown in color set in brown to black matrix composed of (fine) ash (Çubukçu, 2008). It comprises free juvenile crystals and lithic fragments. Lithic fragments belong to former volcanics and metamorphic basement. These metamorphic fragments (Fig. 2.22b) reach up to 2-3 cm in size and interestingly look like euhedral alkali feldspar crystals at the first glance in hand specimens (Çubukçu, 2008).

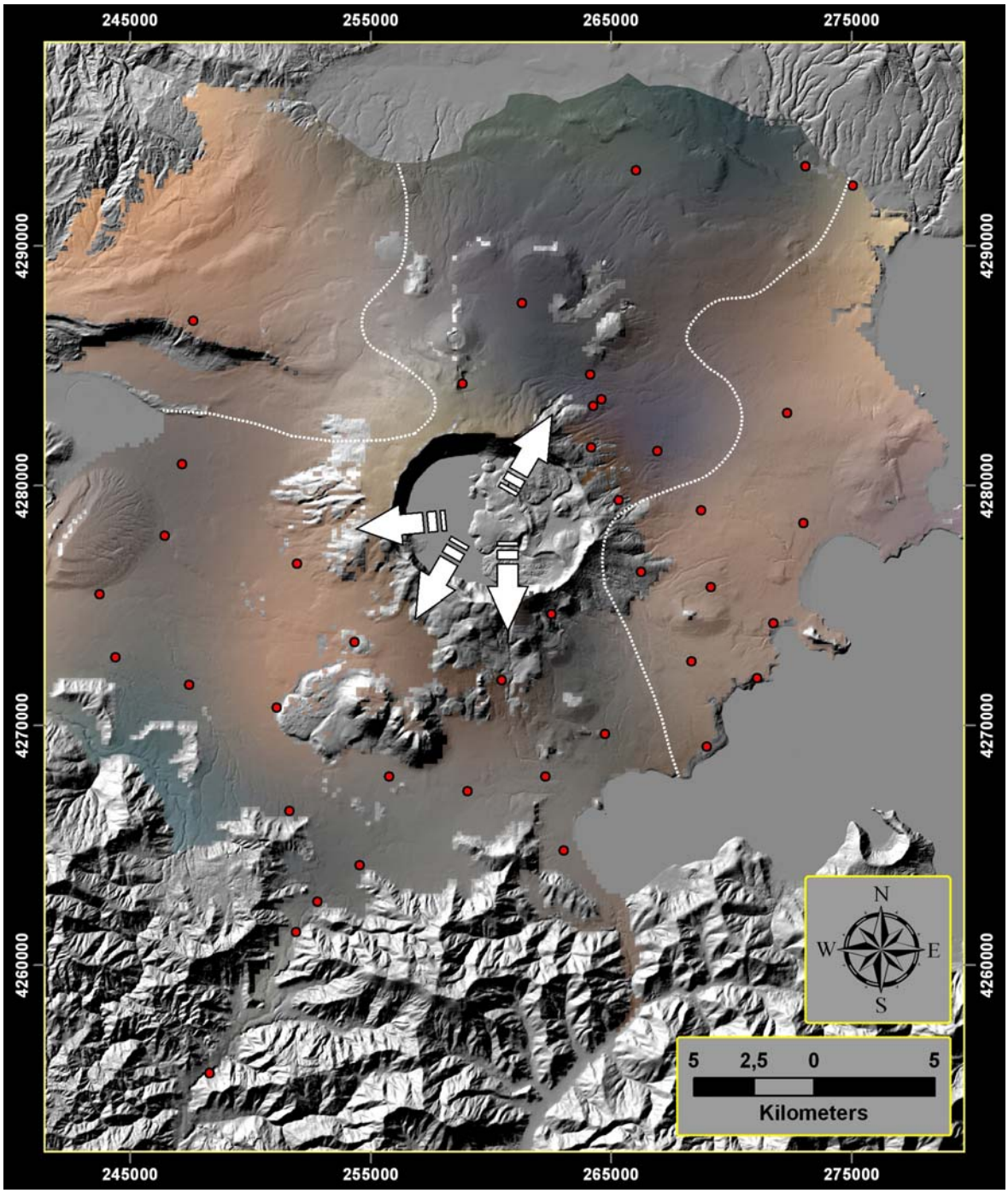

Figure 2.20. Map of spatial color change of the lower level of Nemrut ignimbrite around the volcano. Red dots are the R, G, B sample locations. White dotted line draws the approximate limits of basal black colored level of the NeIg. Projection: UTM, European Datum 1950.

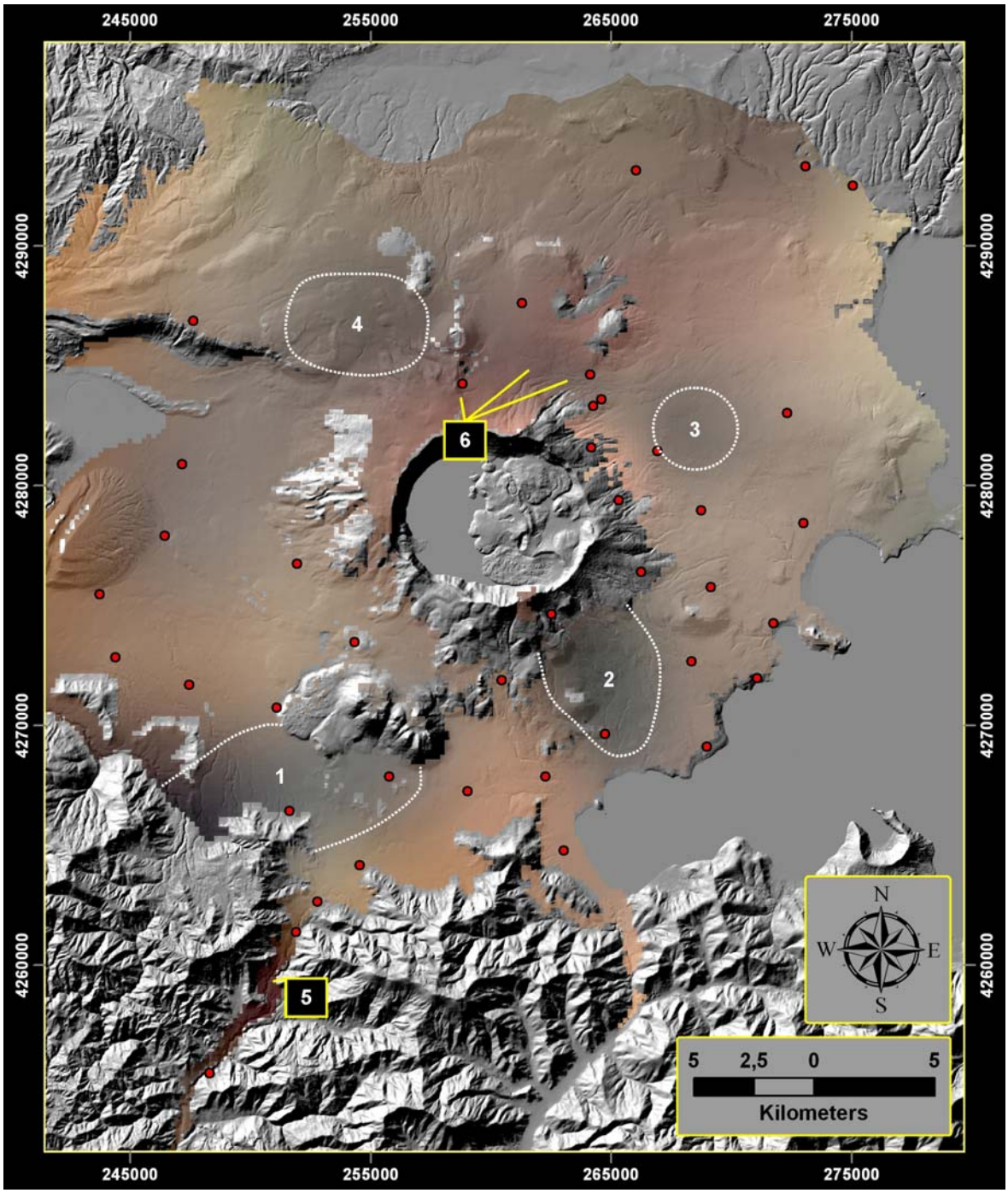

Figure 2.21. Map of spatial color change of the upper level of Nemrut ignimbrite around the volcano. Red dots are the R, G, B sample locations. Areas limited with white dotted line draw the approximate limits where upper light brown level is absent. Projection: UTM, European Datum 1950.

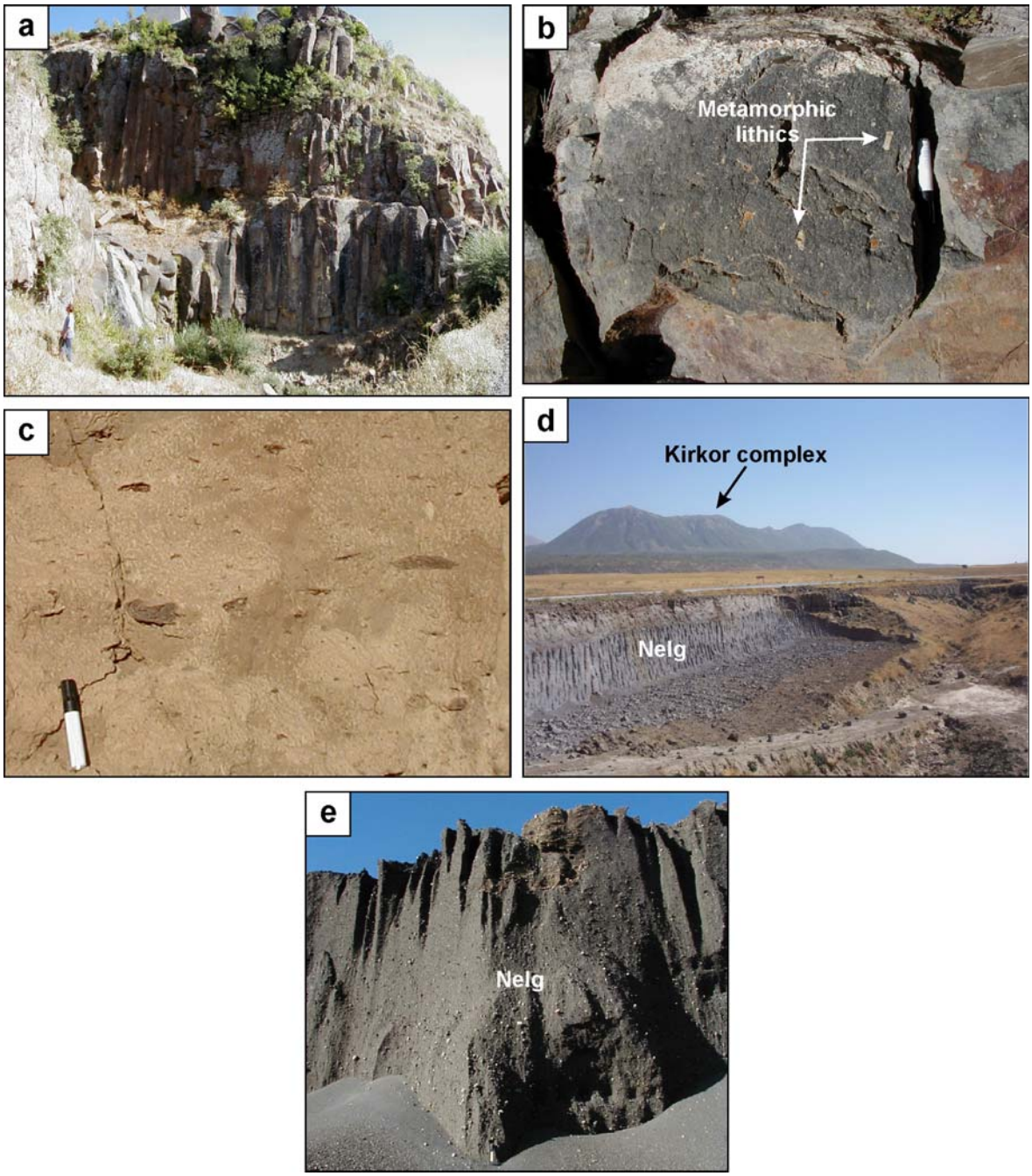

Figure 2.22. Different outcrops of Nemrut ignimbrite (NeIg): **a)** Columnary jointed NeIg in the Bitlis valley (PID: 50), **b)** Metamorphic lithics in the basal level of columnary jointed ignimbrites in the Bitlis valley (PID: 50), **c)** Fiammes in the well welded NeIg unit (PID: 49), **d)** Poorly welded, grey colored basal level of NeIg at southwest of Kirkor domes, **e)** Basal black colored level of NeIg where upper light brown level is absent (PID: 37).

Upper light brown level is absent at southwest of Kirkor dome (Fig. 2.21: 1 and Fig. 2.22d), at the southeastern flank of the volcano (Fig. 2.21: 2 and Fig. 2.22e) and partially absent at southeast of Serinbayır village (Fig. 2.21: 3). At northwest of the volcano, another darker colored area appeared (Fig. 2.21: 4), but we have no data for the color interpolation here. Locations at the SE and ENE of the volcano (Fig. 2.21: 2, 3) are the same locations where small scaled laharic flows occurred on 19.07.2007 due to sudden, heavy rain. The upper level of the NeIg unit was never emplaced to these areas, or the repeated laharic flows / floods have swept the upper part of the ignimbrites.

NeIg is observed to cover nearly all former lava flows and domes. Particularly, during its flow, Kirkor Dome complex in the southwest; Mazik dome in the west, Yumurtatepe and Fakı domes in the southeast acted as obstacles, onto which Nemrut ignimbrite has bumped and changed its direction (Fig. 2.1; Çubukçu, 2008). Flow unit bumping at the northern flanks of Kirkor domes has partially surmounted the domes, leaving material on the summit of the domes and on the lava flows originating from Kirkor domes. At the southeastern flatlands of Kirkor domes, the ignimbrite is extremely poorly welded (Fig. 2.22d). Only the basal black colored part of the NeIg (Fig. 2.22d) was deposited on the southeastern side of the Kirkor complex, upper light brown level is absent here (Fig. 2.21: 1). The bump probably caused the jump of the turbulent flow producing an enlarged turbulent cloud of ash rich material (Fig. 2.23b, c), which leads to relative cooling of the cresting material. Following light brown-reddish colored material were channeled on the eastern and western sides of the Kirkor domes (Fig. 2.23c, d), sweeping some of the remnant black basal part from the north of the domes. This latter light brown-reddish colored flow was deposited like a second, unrelated flow unit on top of the unconsolidated black colored deposits in the southwestern vicinity of Kirkor complex (Fig. 2.19d). This hypothesis may explain the poorly welded black colored deposits on the northeastern side of the Rahva plain (Figs. 2.22d and 2.23d) and separation of basal black colored and upper light brown-reddish colored levels of the NeIg (Fig. 2.19d) on the southwestern side of Kirkor domes.

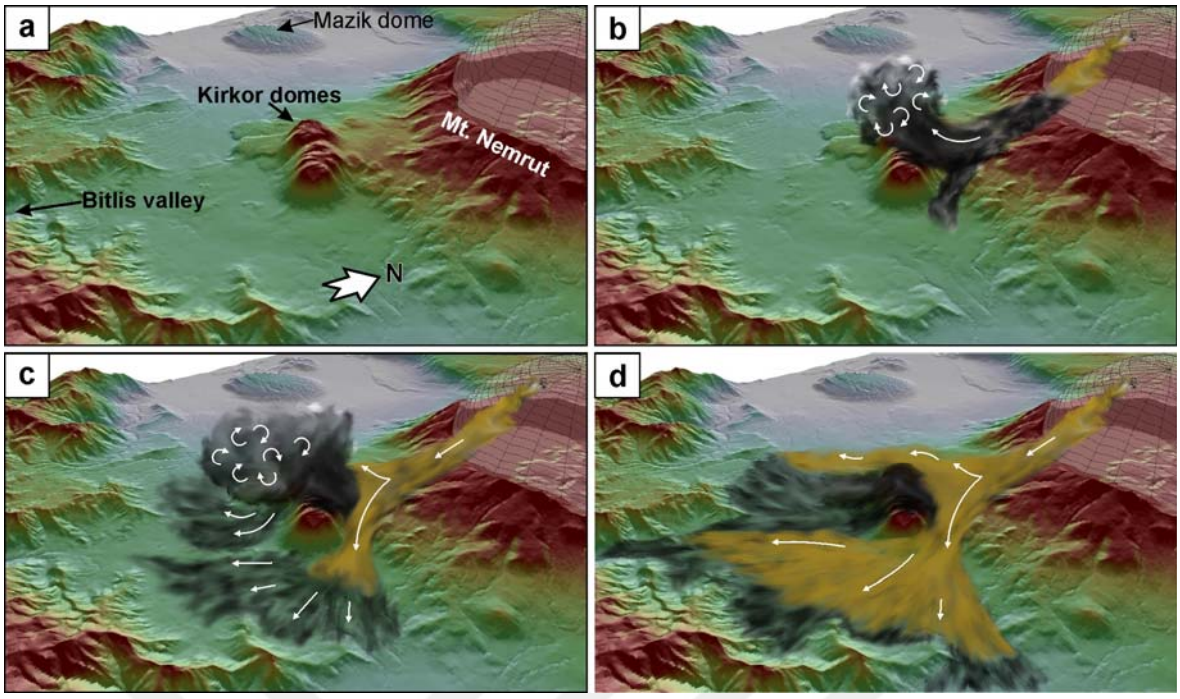

Figure 2.23. Synthesized emplacement model of Nemrut ignimbrite at the southwestern sector (Note that pyroclastic flow at the eastern flank is not limited to one channel; figure was simplified for an improved visualization). **a)** 3D view of the area, **b)** black colored basal part bumps to the Kirkor barrier and forms a small turbulent cloud, **c)** light brown colored upper flow channels around Kirkor domes, **d)** Emplacement of upper, light brown horizon around flatlands except SW sector of the Kirkor complex.

Thickness of the NeIg unit varies around the volcano (Table 2.5); ignimbrite unit is observed to reach its maximum thickness in the Bitlis valley where it channeled into. Run out distance of the ignimbrite was measured 17.5 km from the southern end of Rahva plain (Fig. 2.1) and ~35.5 km from the center of the caldera. The columnary jointing at the basal layer, high consolidation and welding is thought to be highly related with the emplacement thickness and consequently with the cooling rate of the unit in the valley.

Pumice fragments in NeIg are various in colors between dark brown to whitish. Their sizes and distribution within the flow unit vary (Table 2.5; Çubukçu, 2008). Besides, the degree of welding depends on the location with respect to paleo-topography and distance from the volcano (Çubukçu, 2008). Free crystals are omnipresent throughout the flow unit. However, the nature of lithic fragments depends on the relative levels in the unit (Çubukçu, 2008). As we have mentioned above, basal sections bear readily metamorphic fragments whereas their abundance diminishes upward and these metamorphic fragments become absent towards the top, replaced by trachytic and rhyolitic fragments (Çubukçu, 2008). Furthermore, abundant obsidian fragments are also observed in the upper

sections of the unit (Çubukçu, 2008). NeIg is trachytic in composition, mineral compositions and forms slightly differ from bottom to the top of the unit. Lower sections of the unit bear euhedral to subhedral alkali feldspar phenocrysts in a densely welded crystal and lithic rich fine ash matrix and abundant lithic fragments are composed of presumably pre-volcanic basement, namely micaschists and former volcanics (Çubukçu, 2008). Middle section is dominantly crystal rich with anhedral spongy cellular phenocrysts of ternary feldspar, subhedral clinopyroxenes and anhedral moderately resorbed olivines. Besides, lithic fragments of former volcanics are observed. Groundmass is composed of fine ash matrix (Çubukçu, 2008). Upper section is pumice rich with again anhedral spongy cellular ternary feldspars, subhedral clinopyroxene and slightly resorbed anhedral olivine with opaque reaction rims which represent the crystal assemblage. Groundmass is glassy with minor axiolitic devitrification (Çubukçu, 2008).

	PID	4	7	11	12	19	22	23	24	25	27
Av. Max. Pumice sizes (cm)	Lower black horizon				2.5		7	2.5			
	Upper yellow horizon					4		8.8			
Thickness (cm)		1170*	624	86	74	325	93	383*	140*	55	310

	PID	29	34	37	38	41	43	44	45	47	49
Av. Max. Pumice sizes (cm)	Lower black horizon	2.6		11.3			7	16.6			
	Upper yellow horizon	2.6						1.6			
Thickness (cm)		260	92*	820*	163*	1130	320	189	103	800*	800*

	PID	50	51	52	53	54	55	56	58	59	61
Av. Max. Pumice sizes (cm)	Lower black horizon						5.7				9.2
	Upper yellow horizon										
Thickness (cm)		1020*	6500**	2620*	652*	170*	318	86	108	379	578*

Table 2.5. Average of maximum 5 largest pumice sizes and thicknesses of NeIg unit. For locations, refer to PID values in Figure 2.10. (*) refers apparent thickness where upper and/or basal contact is not observed, (**) refers the thickness in a private drilling at the northern end of Bitlis valley.

Kantaşı Ignimbrite Series

Kantaşı ignimbrite series represent the second eruptive phase of the caldera forming eruptions (Fig. 2.10). Outspreading of this second ignimbritic sequence is not large when compared to Nemrut ignimbrites and the area covered (~150 km^2) is limited to the northern, northeastern, southeastern and partially western and eastern flanks of the volcano. These pyroclastic series are termed as Kantaşı ignimbrite series due to their best exposure at the northern sector of the volcano and on the Kantaşı hill (Fig. 2.1). No reworked unit representing a hiatus was observed between Nemrut and Kantaşı ignimbrite series. The contact between the two series can be observed especially on the northern caldera wall (Fig. 2.24a) and around Serinbayır village (Figs. 2.1 and 2.24b).

Kantaşı ignimbrites are composed of three plinian units (KaFB1, KaFB2 and KaFB3, Figs. 2.12 and 2.24a) and Kantaşı ignimbrite unit (KaIg, Figs. 2.12 and 2.24a). Only at the northern rim of the caldera (PID: 41), a relatively thin grayish/yellowish ignimbrite flow unit related to KaFB1 crops out in a limited area (Fig. 2.24a, red box). Plinian pumice deposits of Kantaşı series are best observed at the outcrops on the northern and northeastern flanks and rim of the caldera (Fig. 2.11). KaFB1 and KaFB2 are grayish, whitish colored pumice fall-back deposits. Average pumice sizes and thicknesses related to Kantaşı ignimbrite series are given in Table 2.6.

Most widely observed plinian unit of Kantaşı series is KaFB3; the unit reaches to its maximum thickness at the southeastern flank of the volcano over an altitude of 2200 m (Table 2.6, PID: 40, 42). On the northern caldera wall, proximal outcrop of KaFB3 overlain by Kantaşı ignimbrite unit (KaIg) is well exposed (Fig. 2.25). In the upper horizon of this yellowish pumice fall-back unit (KaFB3), a greenish colored vitrified zone (Fig. 2.25b,c) which is formed due to the emplacement of KaIg unit is evidenced.

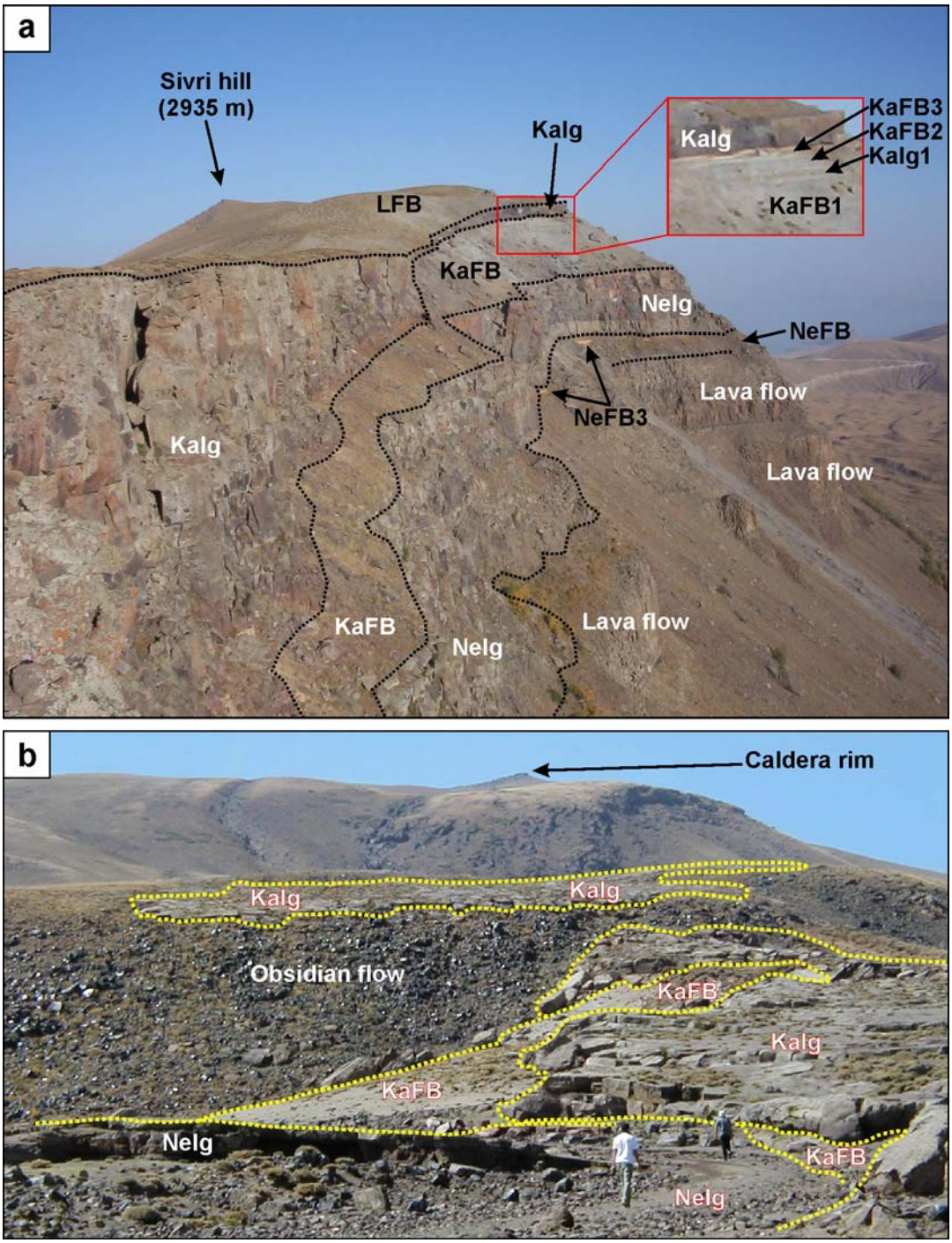

Figure 2.24. Kantaşı and Nemrut ignimbrite series (Ne: Nemrut, Ka: Kantaşı, Ig: ignimbrite, FB: fall-back, L: last). **a)** Photograph from northern caldera wall, where all the deposits of caldera forming are well observed. Sivri hill is the highest point of the caldera rim (PID: 41). **b)** Photograph from west of Serinbayır village where Nemrut ignimbrites and kantaşı ignimbrites are observed together (PID: 26). Blocky outlook of the KaIg unit is because of columnary jointing. For the abbreviations, refer to Figure 2.12.

	Average of 5 max. Pumice size (cm)						Thickness (cm)					
PID	**KaFB1**	**KaFB2**	**KaIg1**	**KaFB3**	**KaIg**	**LFB**	**KaFB1**	**KaFB2**	**KaIg1**	**KaFB3**	**KaIg**	**LFB**
2											58	
5			17.8						74			
6											416	80
7	8.9						110					
8	6.5						61					
9				9.4						250		
11						7.6				130	58	583
13				2.5								
16				3.2	0.9						98	
17											260	
19	1.4						200					
26											164	
29											40	
30											540	
33					12.0						1959	
39										350		
40										500		
41		5.1					786	97	61	49.6	361	
42				4.6						600	159	30
58	0.063	0.063		0.063			105	101				
61	14.9											

Table 2.6. Average of maximum 5 largest pumice sizes and thicknesses of Kantaşı ignimbrite series and LFB unit. For locations, refer to PID values in Figure 2.10.

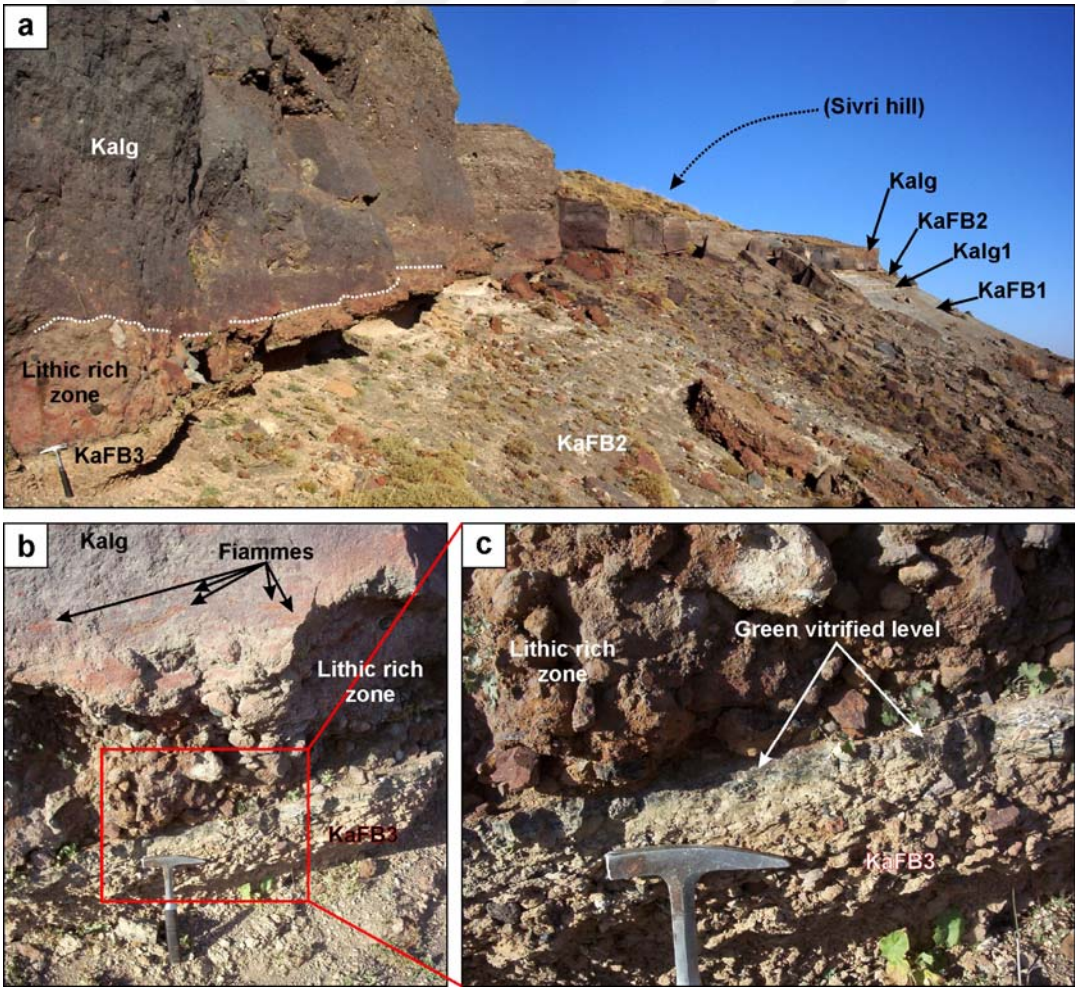

Figure 2.25. Plinian units and flow unit of Kantaşı ignimbrite series (Ka: Kantaşı, Ig: ignimbrite, FB: fall-back). **a)** Proximal deposits of Kantaşı ignimbrites (PID: 41). **b)** Closer view of the basal level of the ignimbrite and KaFB3. **c)** More closer view of the contact between KaIg and KaFB3 units. Note the vitrified upper level of plinian deposit.

Kantaşı ignimbrite unit (KaIg, Fig. 2.12) constitutes the final pyroclastic flow of the Kantaşı series. Ignimbrite unit is best exposed on the northern flank of the volcano; moreover outcrops of both NeIg and KaIg, and their stratigraphic relationships are also exposed on the northern and northeastern sectors (Fig. 2.24). KaIg is burgundy, black and dark brown in color, and well welded (Fig. 2.25a). On the proximal outcrops (i.e. on the caldera rim), basal level of the unit is marked with a lithic rich brecciated zone (Fig. 2.25).

This zone is dominated with a pale reddish color, and average of 5 maximum lithics is 13.2 cm in this zone (PID: 41). At the basal level of KaIg, brown colored fiammes (flattening ratio: 3.6) are typical (Fig. 2.25b). It is also possible to observe greenish colored fiammes in the black / burgundy colored middle horizon of the unit (Fig. 2.26c).

Thickest outcrop of the KaIg is measured (19.6 m) in the crack of Nemrut rift zone (PID: 33, Fig. 2.26b; Table 2.6). At the other locations, KaIg unit is generally thinner (Table 2.6). Thinner outcrops of KaIg unit are marked with a columnar jointing (i.e. Feraud and Özocak, 1993) with column diameters between 0.5 – 1.5 m. These columnary formations are best exposed around the rift zone, on the Kantaşı hill (Fig. 2.26a) and at the northeastern flanks of the volcano (Fig. 2.24b).

Çubukçu (2008) summarizes the petrographical properties of KaIg as follows: *In poorly welded or partially welded counterparts, subordinate feldspar mineralization with fan shape or axiolitic texture is observed in the vesicles of nondeformed pumice. Hence, vapor phase crystallization, which involves the growth of fine-grained minerals in pore space within non-welded pyroclastic flow deposits* (McPhie et al., 1993)*, is thought to occur after emplacement. Subhedral to anhedral cellular alkali feldspar with plagioclase, euhedral clinopyroxene and scarce olivine represent the phenocryst assemblage set in a glass rich fine grained matrix. Lithic fragments consist of either cognate or former volcanic activities.*

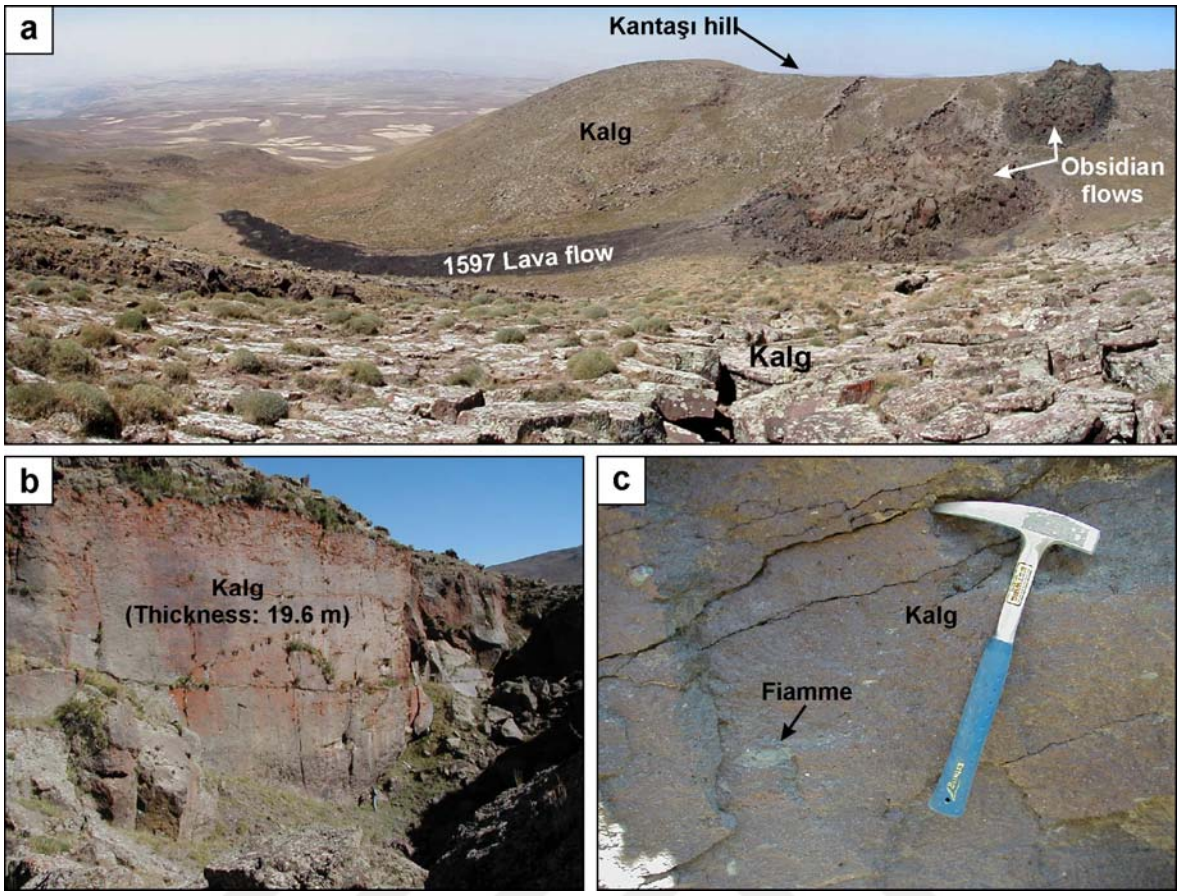

Figure 2.26. Kantaşı ignimbrite unit (Kalg) at north of Nemrut caldera. **a)** Kalg unit and young lava flows around Kantaşı hill at northern margin of Nemrut rift zone. Blocky outlook of the ignimbrite unit is because of columnary jointing. **b)** Thickest Kalg unit which is exposed in the crack of Nemrut rift zone. **c)** Fiamme in the Kalg near Kantaşı hill.

A whitish colored plinian unit (LFB) is observed to overlie Kalg unit. Small outcrops of this unit were observed on the Sivri hill (Figs. 2.1 and 2.24a), on the northeastern flank and north of Çekmece village (Fig. 2.1). This unit constitutes the latest episode of the caldera forming eruptions.

Volume of the caldera related pyroclastics and collapse of the caldera

Using the thicknesses measured (Tables 2.3, 2.5 and 2.6) for Nemrut and Kantaşı ignimbrite series; we calculated the volume of the caldera forming pyroclastic deposits. Measured thicknesses of the pyroclastic deposits were interpolated to constitute thickness maps for ignimbrites and for tephra deposits, and the volume of the pyroclastics was then calculated. Volumes of Nemrut ignimbrite and Kantaşı ignimbrite are 32.6 km^3 and 3.8 km^3, respectively. When the ignimbrites emplaced under Lake Van are considered, a total volume over 36.4 km^3 could be estimated for the caldera related ignimbrites. Volume of the fall-back tephra of Nemrut and Kantaşı ignimbrites are 32.8 km^3 and 6.1 km^3 respectively. With an assumption of

50% loss, dense rock equivalent total volume of plinian tephra is roughly 19.5 km^3. Though, rough estimation for the total caldera related pyroclastic volume is 56 km^3 (36.4 km^3 + 19.5 km^3).

During its construction, the volcano is thought to be reaching to an altitude of 4500 m (Aydar et al., 2003). This elevation leads to a collapsed volume of 64.3 km^3 (including volume of Nemrut lake: 1.264 km^3).

Due to the large volume pyroclastic activity, excess lithostatic pressure on the emptied reservoir led to the collapse of the roof (Fig. 2.27). The exact timing of caldera collapse is unknown, but as we mentioned earlier, previous timing (272 ka) suggested by Atasoy et al., (1988) is questionable, while the caldera forming Nemrut ignimbrites overlie the lava flows dated 89 ka. The collapse of the caldera has possibly occurred between 80 to 30 ka ago (e.g. Çubukçu, 2008).

Figure 2.27. Nemrut caldera from the northern rim. Photograph by Adem SÖNMEZ; used with permission of photographer.

2.3.3. Post-caldera activity

Post caldera volcanic activity was generated in the caldera and on the northern rift zone. We present a small-scaled geological map focusing the caldera for better visualization (Fig. 2.28). Post caldera volcanism is divided into three sub-stages (Table 2.1: Sub-stage VI, VII, and VIII). Western half of the caldera is covered with a fresh water lake (Fig. 2.28: Nemrut lake), limiting observation of the post-caldera activity in only the eastern part of the caldera. There is also a hot lake at the foot of the northern caldera wall which is fed by hot sources (Fig. 2.28: Ilığ lake).

Sub-stage VI (30 -12 ka)

This period is represented by comenditic intra-caldera lava flows and domes (Table 2.1; Fig. 2.28). Planar flow banding is evident in these lava flows (Fig. 2.29a); holohyaline, obsidian facies units, occurrence of vesicular pumiceous zones are common (Çubukçu, 2008). In addition, intra-caldera lavas bear benmoreitic enclaves (Fig. 2.29b; Çubukçu, 2008). Clues of local hydrothermal alteration is evident especially in the lava dome forming Göl hill (Figs. 2.28 and 2.29c) and in the lavas encircling the elongated maar at south of Göl hill (Fig. 2.28). Hydrothermal alteration is marked with a strong devitrification. Former obsidian flow is marked with relict, angular glasses, surrounded with a devitrified casing around Göl hill (Fig. 2.29c, d). In larger scale, alteration is typical with reddish, brownish oxidation colors in the caldera (Fig. 2.29c).

Sub-stage VII (12 ka - AD)

Intra-caldera phreatomagmatic - phreatic activity is dominant in this sub-stage (Table 2.1). Moreover, there are multitudinous maars in the caldera; their products are stratigraphically interbedded, consequently the distinction of their products is not easy. They cover most of the former intra-caldera comenditic lava flows (Fig. 2.28). Products of the Big maar (Fig. 2.28) are widespread in the caldera, plaqued on the western shore of Nemrut Lake. They also surmount the caldera rim and are deposited on the NE, E and SE flanks of the volcano.

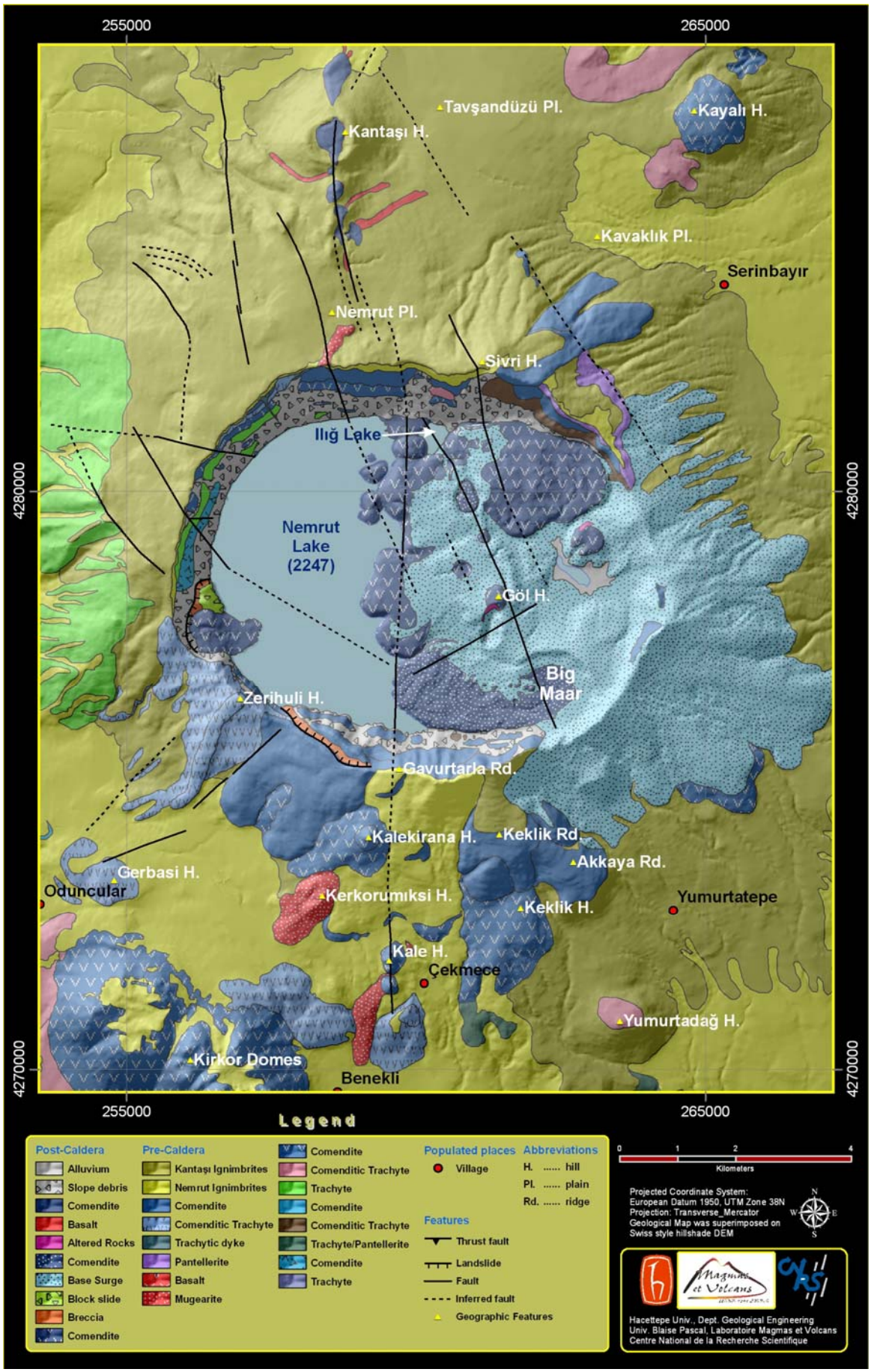

Figure 2.28. Geological map of Nemrut caldera.

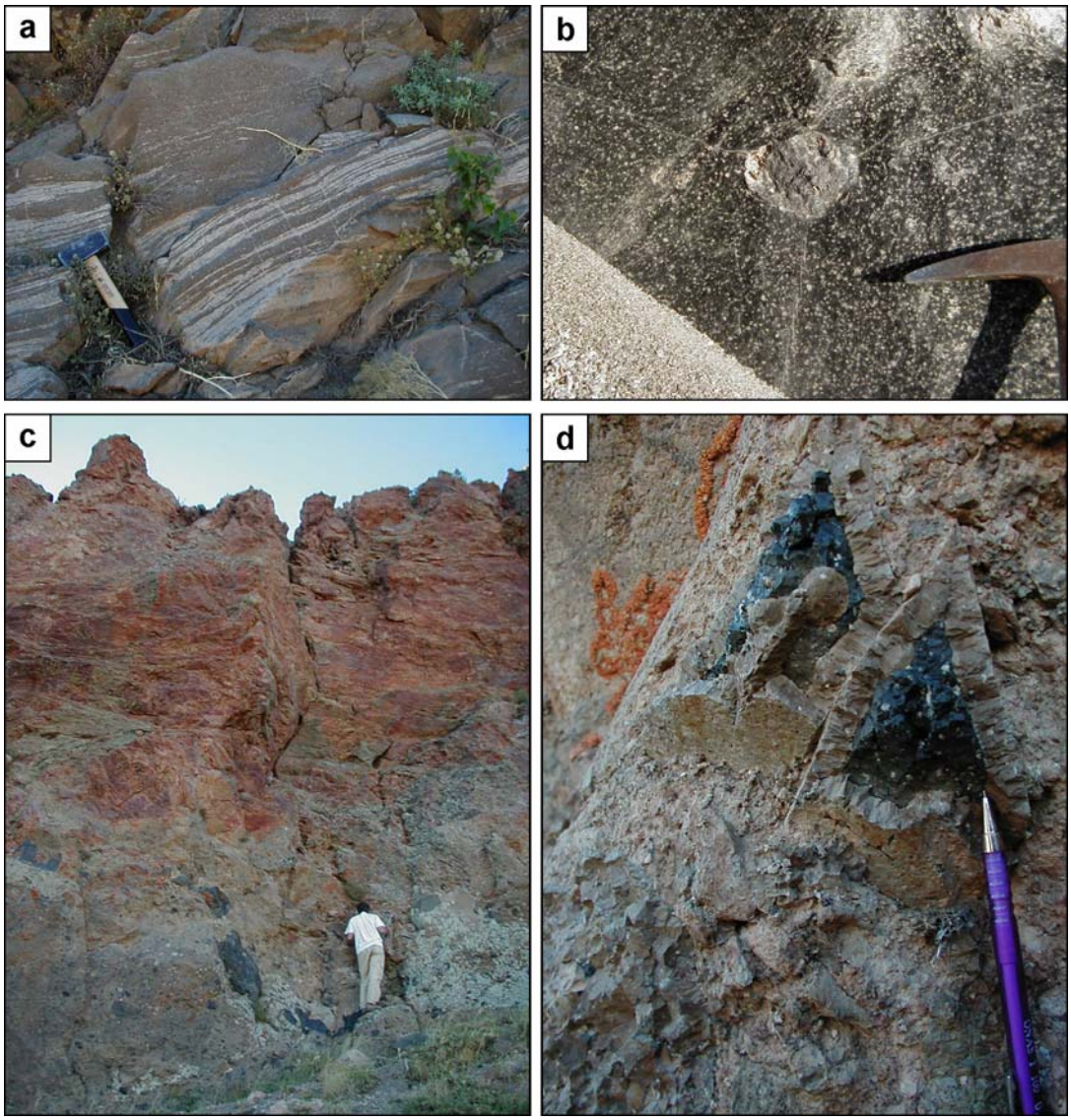

Figure 2.29. Post-caldera lava flows and hydrothermal alteration. **a)** Flow bending in lava flow, **b)** Benmoreitic enclave in obsidian, **c)** Hydrothermal alteration on Göl hill, **d)** Devitrified obsidian flow on Göl hill.

Big maar continued its activity with a comenditic lava flow through west. Deposits of a latter maar (south of Göl hill) partially cover the comenditic flow of Big maar. Base surge deposits are typical with dune and anti-dune structures, bomb sags (Fig.2.30a, b), breadcrust bombs (Fig.2.30c) and cross bedding (Fig.2.30d). At the northeastern caldera rim, products of Big maar presents a very local, whitish – yellowish – dark brown colored sequence (Fig. 2.30e). Especially, yellowish and dark brown colored horizons of this sequence bear large (up to 25 – 30 cm) pumices and lithics. At first glance, these horizons may be confused with a plinian fall (i.e. NeFB3); however, there are large obsidian, basalt and most importantly, ignimbrite clasts in the brown horizon.

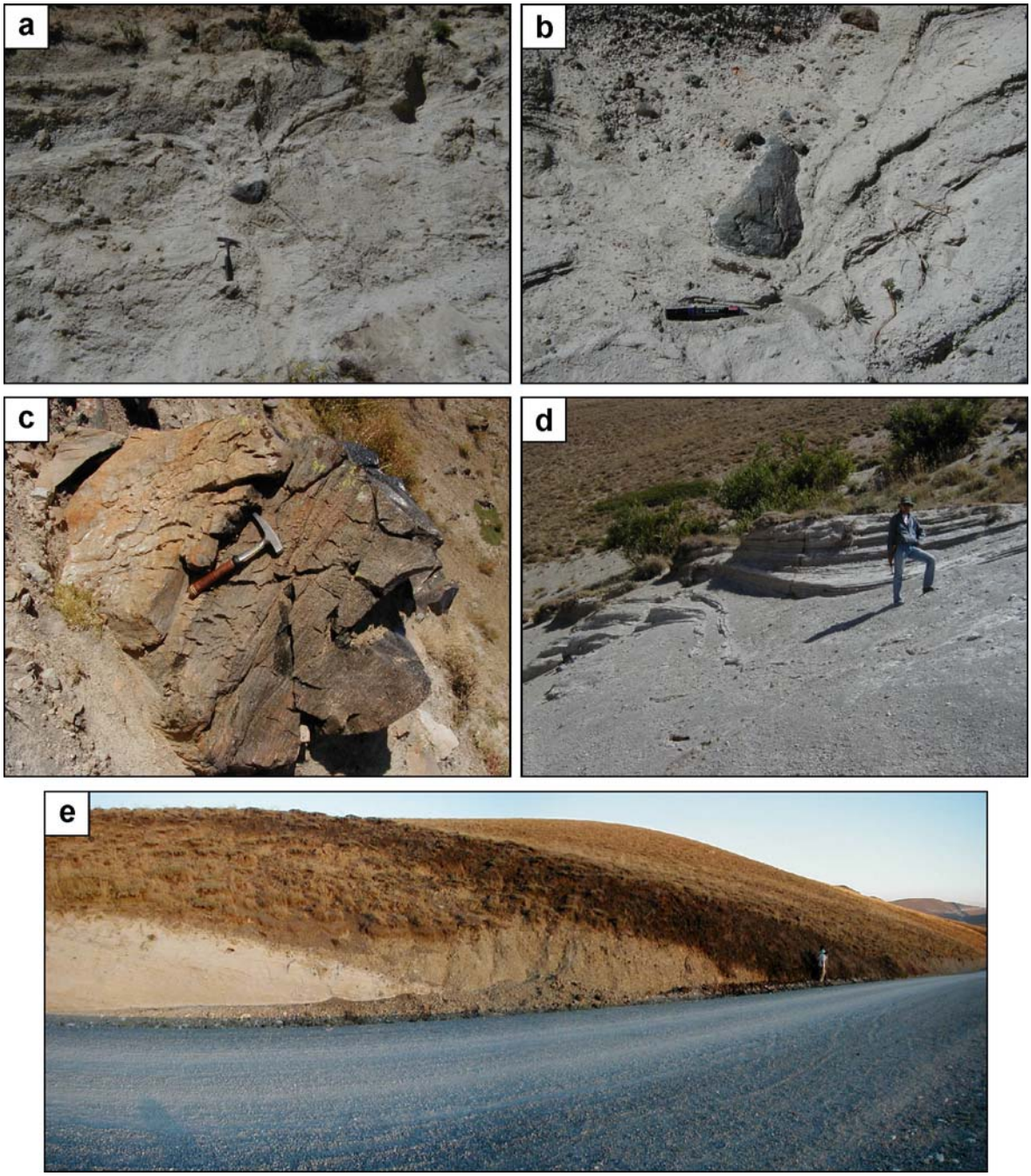

Figure 2.30. Base surge deposits and their components in the caldera. **a, b)** Bomb-sag structures, **c)** Large breadcrust bomb on the tuff ring, **d)** Cross-bedding in the base surge deposits, **e)** Proximal phreatomagmatic deposits with large clasts.

Nemrut Rift zone (Sub-stage VIII; AD - Today)

Latest activities took place in the historical times. This sub-stage is represented by rift zone activity (1441 – <1597 AD) on the northern flank of Nemrut volcano. Karakhanian et al. (2002) reported an historical event, which occurred around Tatvan town (Appendix-A); however, precise location of this event is still a matter of debate. Recent activity will be discussed in the subsequent chapters.

The rift activity occurred between Nemrut plain and Kantaşı hill (Fig. 2.28); the ridge along the rift and its surrounding is covered with Kantaşı ignimbrite. Throughout the ridge, rifting cracked the welded Kantaşı ignimbrites; lava poured and flown over them. The rift zone is slightly bended from NNW to N and continues throughout ~5 km. We observed paralleling fault cracks at the southern section of the zone; the cracks are relatively narrow (Fig. 2.31a) when compared to middle (Fig. 2.26b) and northern sections (Fig. 2.31b) of the rift zone.

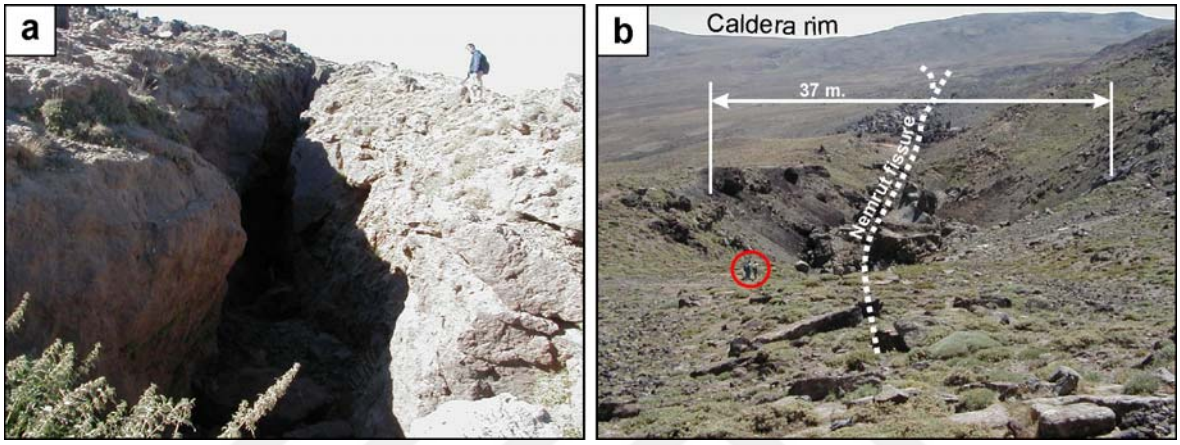

Figure 2.31. Nemrut rift zone at the northern section of the volcano. **a)** Narrower rifting cracks closer to the caldera and **b)** northern section of the rift zone with a larger crack and domal obsidian knob in the middle. For the scale please note the presence of three members of our team in red circle.

Except the southernmost part of the rift zone, lava activity is obvious in the rift. The activity in the rift is observed as knobs of obsidians (Fig. 2.31b); furthermore, there are locations where the crack is totally filled with obsidians and basalts (Fig. 2.32a, c). Breadcrust bombs are found along the rim of the rift (Fig. 2.32b).

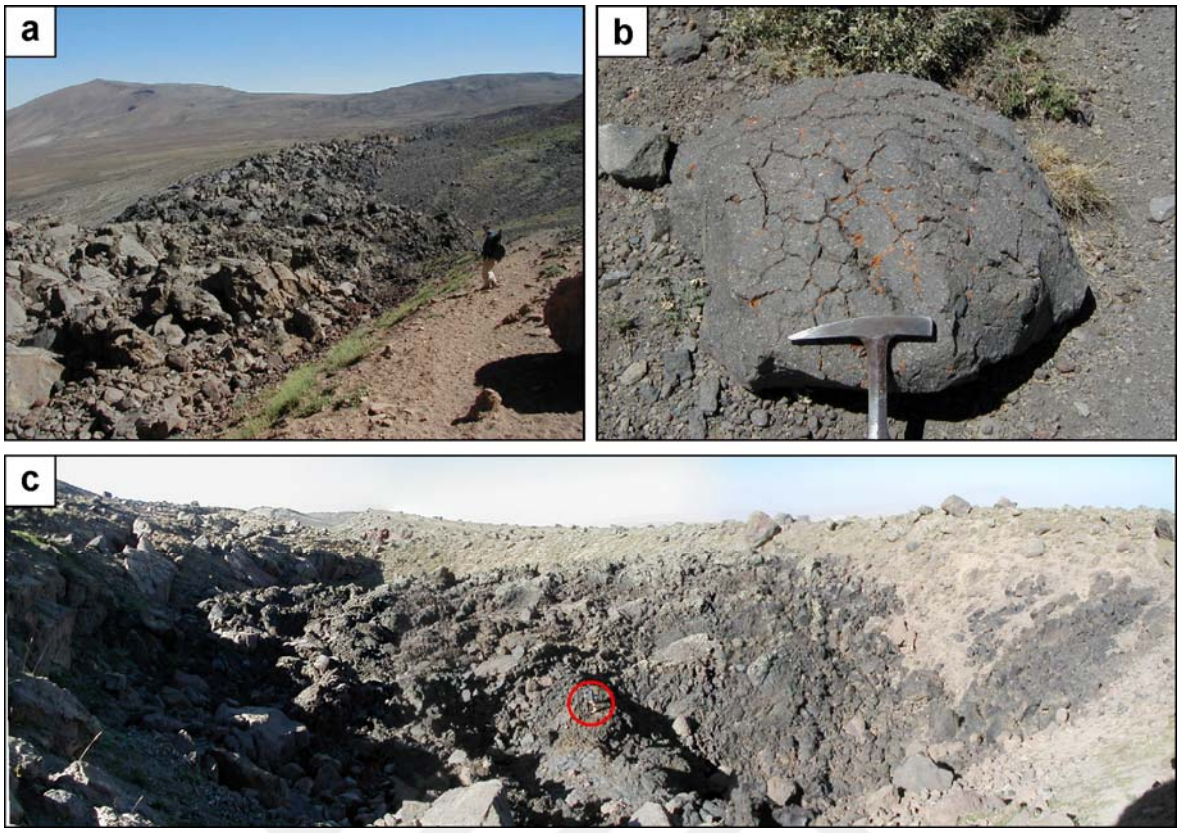

Figure 2.32. Nemrut rift zone and comenditic products. **a)** Rift crack filled with comenditic obsidians, **b)** Breadcrust bomb found at the rim of the rift, **c)** Basaltic lava pooled at the draining spot. For the scale please note the presence of the member of our team in red circle.

In the crater of the cone forming Kantaşı hill, there is a comenditic lava lake (Fig. 2.28) from which lava poured and flown through north (extent: 1 km) and south (extent: 230 m) (Figs. 2.26a and 2.33a).

The most spectacular feature of the rift zone is the bimodal activity. Synchronously with the comenditic flows, basalt flows were effective at the rift zone (Fig. 2.33b). Şerefhan (1597) witnessed and well delineated the basaltic activity. He invigilated lava fountains for repeating years and described the lava flows (Aydar et al., 2003; Appendix-A). Originating from the rift, two (aa-like) basaltic flows are obvious throughout the eastern flank and their length reaches up to 890 m and 1.3 km respectively (Figs. 2.28 and 2.33c). Another basaltic flow originates from the southern side of the Kantaşı hill and extends 1.2 km to the east (Figs. 2.28 and 2.26a). Two branches of basaltic lavas are overlain by obsidian flow at the northern side of Kantaşı hill (Figs. 2.28, 2.1 and 2.33b). Their lengths are 130 and 780 m, respectively. Thicknesses of the obsidian flows may reach up to ~10 m, while basaltic flows are thinner than ~2 m.

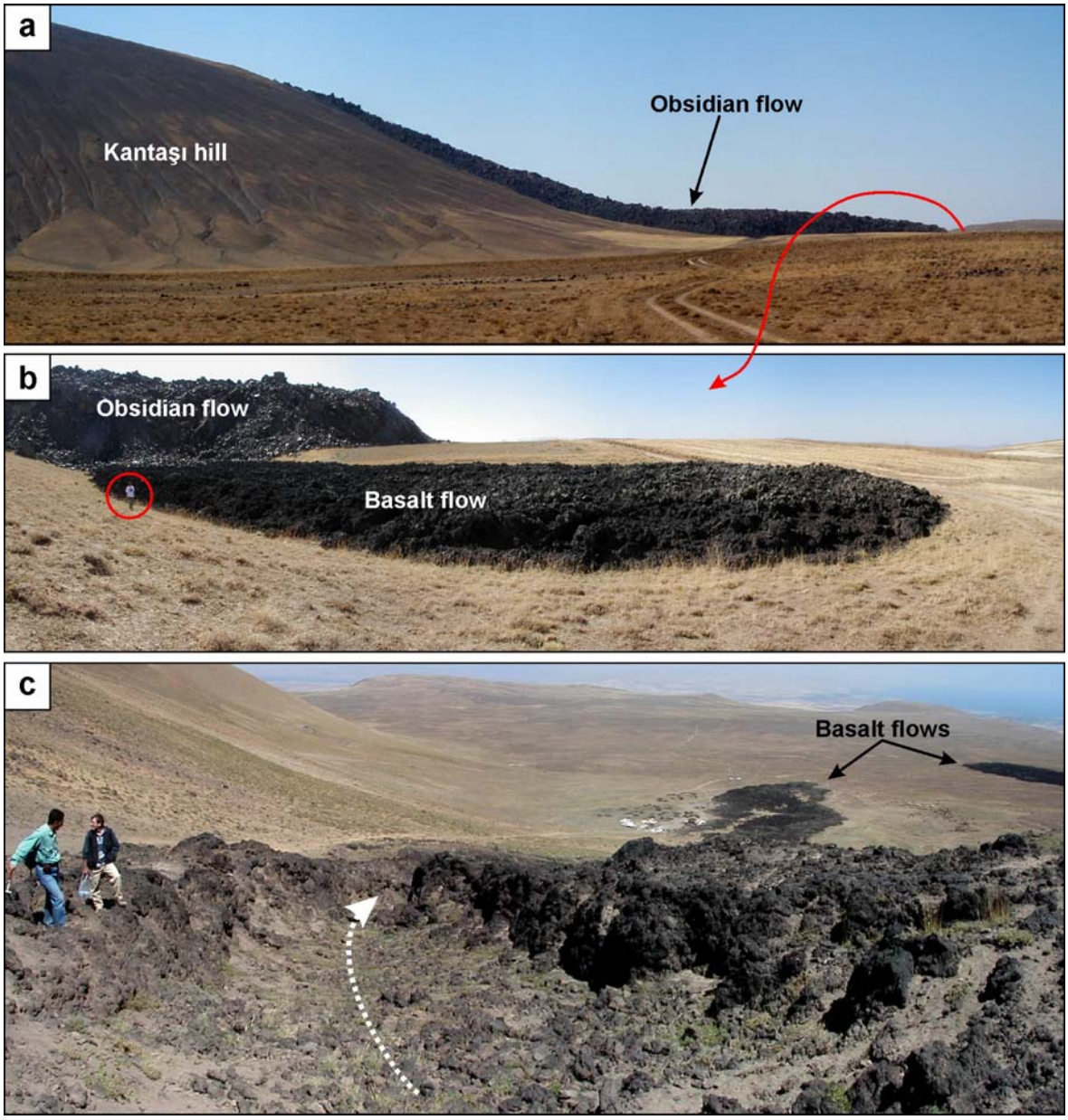

Figure 2.33. Products of bimodal rift zone activity. **a)** Obsidian flown throughout north flank of Kantaşı hill and **b)** underlying basalt flow at the northern front of this obsidian flow. For the scale please note the presence of the member of our team in red circle. **c)** Basaltic flows originated from the rift, flown through the eastern flank of the ridge. Please note the flow channel indicated with white pointed line.

2.4. Synthesis

Nemrut volcano rises upon the pre-volcanic basement composed of Bitlis metamorphics, Çatak ophiolites, and Tertiary sediments (Ahlat formation). With nearby volcanic centers such as Süphan, Bilican, Kolango dome and İncekaya tuff cone, Nemrut is one of the important eruption centers around Bitlis city. Nemrut

volcano has a semi-elliptical summit caldera, western half of the caldera is filled with a fresh water lake.

The new, detailed geological map of the volcano offers rectifications to previous maps. Relying upon our observations, we made changes on the layout and the type of the pyroclastic units; “unknown” scoria flows at the northern sector and “unknown” monzonitic intrusions were removed from the map.

Nemrut started its volcanic activity ~1 Ma ago and continued until historical times. Evolution of the volcano is investigated in two main stages (pre-caldera and post-caldera) separated by catastrophic caldera collapse. Pre-caldera stage is divided into five sub-stages, our observations on effusive and eruptive activity is presented in detail with a special emphasis on caldera forming eruption products. Pre-caldera lava flows are composed of trachytes, comendites, comenditic trachytes, pantellerites, basalts and mugearites. Peripheral doming generated in the pre-caldera stage is comenditic and trachytic in composition. Nemrut ignimbrite series and Kantaşı ignimbrite series represent the caldera forming activity; sequences are composed of plinian units and ignimbrite flows. Post-caldera activity of the volcano is presented in three sub-stages. Intra-caldera activity and rift zone activity are discussed. Intra-caldera activity is represented by comenditic lava flows, domes and phreatomagmatic/phreatic eruptions. Locally, hydrothermal activity is effected intra-caldera lavas and domes. Nemrut rift zone was activated during the historical times, and is characterized by bimodal activity with comenditic obsidians and basaltic lava flows.

Chapter 03

Hydrothermal activity and fluid circulation

3. Introduction

Recently, the most outstanding activity of the volcano is the hydrothermal activity and the fumaroles. Both in the caldera and around the Mazik and Girekol domes, there are hot springs. The hot sources in the caldera seem to be gathered around a small hot lake; namely Ilığ lake (Ilığ: warm; Fig. 2.28). Moreover, there are at least two hot sources at the shoreline of Nemrut Lake (Fig. 2.28). Thermal activity along the shoreline was also documented by Şerefhan (1597). In addition to the hot sources, there are also fumarole activities in the caldera floor (Aydar et al. 2003). Fumarole activity is best observed around the Ilığ Lake; as well, bubbling in the sources of the hot water is obvious.

The quantification of hydrothermal activity in the caldera and its relationship with the structure of the caldera was investigated with geophysical surveys and remote sensing methods. Attained facts and results of our studies were presented to be published in a peer reviewed international journals. Here, in this chapter these papers will be presented and our further investigations will be handled.

The first paper presented here (Chapter 3.1) deals with the correction of slope aspect and altitude gradient effects on nighttime thermal infrared images and proposes a simple method for this correction. This method is applied to Nemrut case, application and results are then discussed. Method proposed is image based and applicable to other cases facing with the same problem, accordingly, an IDL (Interactive Data Language) code is written to automate the procedure with a GUI (Graphical User Interface). Written code and the procedure has been prepared to be published as an article and submitted to a journal, Computers and Geosciences. The article is under review since January 2008. Additional electronic content related to this code and procedure is provided in e-Appendix-3. Electronic content provided consists of source code, input data (for testing), output data (for testing), a short user-guide and a read-me text file.

The second paper presented (Chapter 3.2) deals with the geophysical and remote sensing approach to the hydrothermal dynamics of the Nemrut caldera. We used Self-Potential (SP) method to characterize the hydrothermal fluid circulation, and to reveal the relationship between the structural features of the caldera system and the hydrothermal system. In addition to SP surveys, our field observations and morphological approaches were discussed. Remotely sensed data (ASTER

nighttime TIR, Landsat ETM+) were processed and the results were interpreted in the hydrothermal – structural context. Self-Potential maps and Thermal anomaly image derived from ASTER TIR data were correlated. Finally, our findings were used to gather a structural model for the collapsed caldera. This paper has been published (Ulusoy et al., 2008) in Journal of Volcanology and Geothermal Research.

3.1. Image based retrieval and correction of altitude and aspect effects on nighttime TIR imagery

STcorr: An IDL code for image based retrieval and correction of altitude and aspect effects on nighttime TIR imagery

İnan Ulusoy*[1, 2], Philippe Labazuy[2], Erkan Aydar[1]

[1]Hacettepe Univ. Dept. of Geological Engineering, 06532, Beytepe-Ankara, Turkey

[2]Univ. Blaise Pascal, OPGC, Lab. Magmas et Volcans - UMR-6524 CNRS, 5 rue Kessler, 63038 Clermont Ferrand Cedex, France

**e-mail: inan@hacettepe.edu.tr*

Abstract

Thermal infrared imagery (TIR) is a useful tool to detect and monitor the surface temperature anomalies associated with geothermal fields. Monitoring temporal changes in surface temperature is an important aspect of volcano monitoring. Although day-time TIR images have long been used for temperature anomaly mapping after appropriate corrections, the increase of spatial resolution of commercially available nighttime thermal imagery provided a new scope to the remote geothermal monitoring and exploration. Still, the nighttime thermal imagery involves some major effects that needs appropriate corrections. The first of them is the masking of small-scale thermal anomalies by the thermal gradient of the region and the second one is the relict diurnal heat due to the radiation of sun. Correction of nighttime TIR imagery according to altitude and slope aspect of the region may reveal out more reliable data.

STcorr is an IDL code to perform an image based polynomial regression analysis approach for the correction of altitude and aspect effects in nighttime thermal imagery. Surface Kinetic Temperature (ST) image and Digital Elevation Model (DEM) are used to calculate a thermal gradient model. After the retrieval of thermal gradient, depending on the relationship between corrected image and the aspect image, an illumination correction is performed. Interactive step by step structure of the code allows user to visually improve the quality of the raw thermal data. Advanced Spaceborne Thermal Emission and Reflection Radiometer (ASTER) nighttime ST image of the Mt. Nemrut volcano was corrected using STcorr and the quality of the final image is further discussed.

Keywords: Nemrut, volcano, ASTER, topographic, illumination, correction

1. Introduction

The thermal infrared (TIR) imagery becomes a widely used tool in earth sciences during the last decade and finds the application domaines for; the detection of geothermal fields/spots (e.g. Coolbaugh et al.,2007; Lombardo and Buongiorno, 2006), environmental studies (e.g. Wentz and Schabel, 2000), soil moisture assessment (e.g. Hejmanowska, 1998), mineral mapping (e.g. Vaughan et al., 2005; Rowan et al., 2006) and volcano monitoring (e.g. Pieri and Abrams, 2005; Pugnaghi et al., 2006). The images from satellites bring different features using various filters in our knowledge. The remote sensing methods may be applied on two kind of principal images: daylight and nighttime images. While remote sensing increases its role in a large variety of research, success of the efforts in some cases has been limited by the difficulty in modeling the diurnal heating effects due to the sun (Coolbaugh et al., 2007). In daytime images, the topographic effect causes a phenomenon as the sun facing slopes appear brighter than the opposite slopes. Removal of this disturbing phenomenon is necessary before digital image classification or mathematical modeling of physical processes on the Earth (Hejmanowska, 1998). Depending on the acquisition time, this effect can also be evident in the nighttime thermal images. Different surface materials with specific physical properties such as thermal inertia, albedo, emissivity, and moisture content differently respond to solar radiation, resulting in different surface temperatures along 24-hours of a day (Elachi, 1987; Watson, 1973; Coolbaugh et al., 2007). Even during predawn hours, significant differences in temperature persist due to the differential heating effects of the sun of the previous day (Coolbaugh et al., 2007). Where topographic slopes are relatively steep and variable, such as mountainous terrain, it can be difficult and tedious to distinguish thermal anomalies from strong false anomalies caused by warmer sun-facing slopes in uncorrected nighttime images (Coolbaugh et al., 2007).

Depending of the topographic characteristics of the region, a thermal gradient effect may also be coeval with the illumination effect. On volcanoes and around the active fault zones, geothermal activity may be masked due to the dominant signature of thermal gradient. Besides, it is relatively easy to detect high thermal anomalies around the summit zone of an active volcano where temperature decrease with height creates an obvious contrast with the thermal anomalies; however around the foot of the volcano, lack of this contrast may hide possible

anomalies. Clearly, the most difficult-to-detect thermal precursor anomalies on volcanoes are those that are only slightly warmer than the ambient background temperature (Pieri & Abrams, 2005).

Following these observations, we implemented a surface temperature correction program (STcorr). STcorr is an IDL code designed to perform an image based approach for the correction of these two topographic effects in nighttime TIR imagery. Using nighttime surface kinetic temperature (ST) image, Digital Elevation Model (DEM) and the slope aspect image, it interactively removes the thermal gradient and the illumination effects from the ST image. Product is a thermal anomaly image. It was designed for Advanced Spaceborne Thermal Emission and Reflection Radiometer (ASTER) nighttime ST images but it can also be used for any nighttime ST image (concerning with the same problem). The ASTER instrument provides some important capabilities in the area of detection of volcanogenic energy anomalies as thermal precursors (Pieri & Abrams, 2004). The availability of five thermal bands on ASTER makes it possible to identify wavelength-dependent variations in emissivity so that true kinetic temperatures can be estimated (Hook et al., 1999). In addition, ASTER sensor has a high TIR spatial resolution of 90m/pixel (Abrams and Hook, 2002).

2. Topographic correction of satellite images, methodology used in STcorr

Quantitative theoretical modeling of the physical variables to predict surface temperatures involves differential equations and LaPlacian transformations that require iterative numerical solutions (Elachi, 1987; Kahle, 1977; Watson, 1973; Coolbaugh et al., 2007). Main methods to correct topographic effects depending on bidirectional reflectance distribution are cosine method (Smith et al., 1980; Teillet et al., 1982), Minneart correction (Minneart, 1941; Smith et al., 1980; Holben and Justice, 1980; Teillet et al., 1982), backscattering method (Hapke, 1963; Hugli and Frei, 1983) and their advanced versions. Some known bugs of these methods such as over-correction of cosine method were previously discussed (Hejmanowska, 1998; Nichol et al., 2006; Law and Nichol, 2004). Empirical methods such as two-stage normalization (Civco, 1989; Nichol et al., 2006) and minimization of temperature variations due to surface physical properties (Coolbaugh et al., 2007) give reliable results with less effort. However,

these methods are aiming the topographical correction of daytime images and in different spectral ranges; on the other hand, nighttime TIR images may reflect a strong topographic effect.

Methodology used in STcorr is a semi-empirical, image based, two-stage regression method to correct the thermal gradient and aspect effects in nighttime TIR images. In the first stage, a thermal gradient image is produced using the ST image and DEM. Thermal gradient correction of the image is made according to this calculated thermal gradient image. This procedure can be described simply as:

$$f(G_1) = \left(\frac{dT}{dz}\right) \times f(z) \qquad (1)$$

$$f(C_1) = f(T) - f(G_1) \qquad (2)$$

Where "G_1" is the thermal gradient according to elevation, "T" is surface kinetic temperature, "z" is elevation, "$f(C_1)$" is the altitude corrected image. The second stage uses the thermal gradient corrected image and aspect image to generate an aspect corrected image:

$$f(G_2) = \left(\frac{dC_1}{da}\right) \times f(a) \qquad (3)$$

$$f(C_2) = f(C_1) - f(G_2) \qquad (4)$$

Here, "G_2" is the aspect gradient according to slope aspect, "a" is slope aspect and "$f(C_2)$" is the final (aspect) corrected image.

3. Program design

STcorr is an IDL (version 6.2 for Microsoft Windows© OS) code that can alternatively run standalone with runtime application, with IDL virtual machine or in the IDL environment. Seven images and two graphic windows open during the operations; to simplify the usage, code uses independent windows to visualize images. Each image is displayed with an appropriate color table (i.e. DEM with classic black-white linear color-scale representation), and stretched to visualize anomalous data. STcorr can deal with georeferenced images and uses GeoTIFF file format to interact with other image processing tools and GIS platforms before

and after the corrections. In the graphical user interface (GUI), systematic, step by step operations are provided to guide the user during calculations, each command button is activated if only necessary input is given or necessary calculations are made.

3.1. Data preparation and input

Prior to calculations, input data must to be processed to a certain level. From raw data to input, these processes are given in Figure 1. Reducing the spatial size of the input image according to the studied region, increases the speed of the program, working with a jumble of large display windows is avoided and possibility to detect false thermal anomalies due to unknown surface conditions is eliminated.

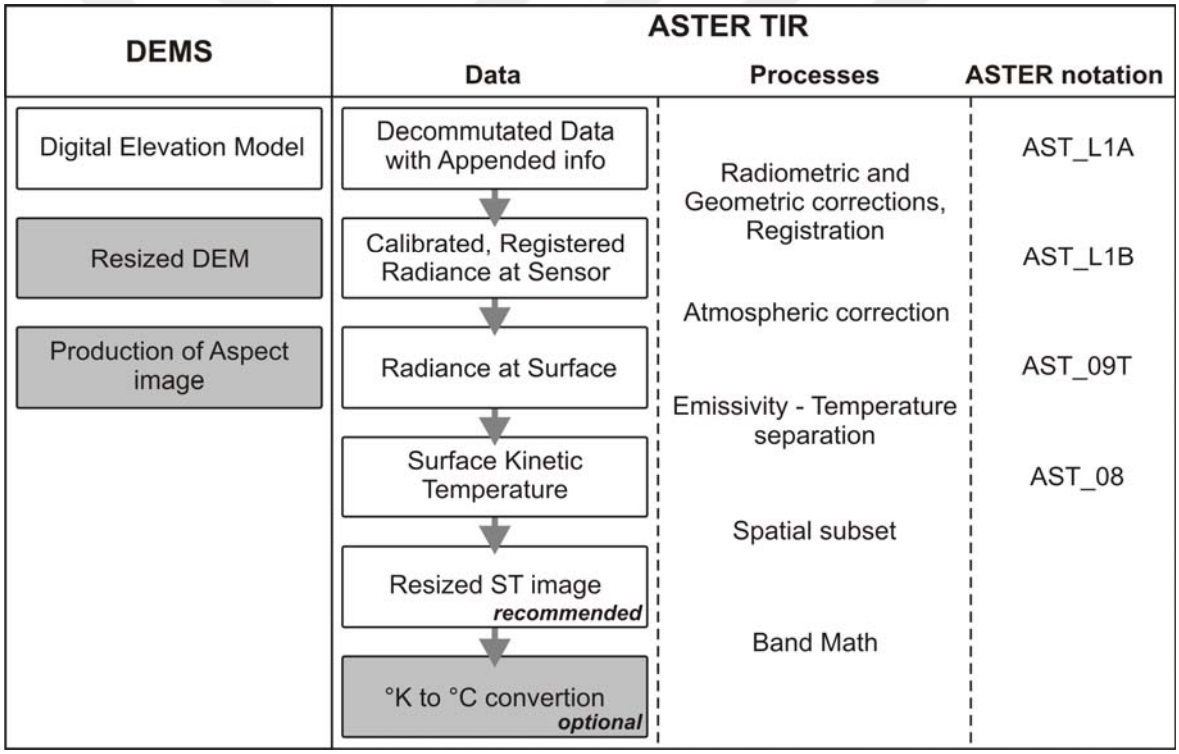

Figure 1. Preparation process of input data for STcorr. Digital Elevation Model, Aspect image and ST image must be in the same spatial size. Prior to aspect and altitude correction, Thermal infrared raw data must be processed to achieve Surface Kinetic Temperature image.

DEM must be spatially resized to the same spatial size and resolution with ST image; that is 90m/pixel in the case of ASTER data. Slope aspect image (in terms of 1 - 360 degree) should be derived from the DEM, with the same spatial size and resolution. Surface Kinetic Temperature image should be derived from the raw data; processing from raw ASTER TIR to Surface Kinetic Temperature image can

be found in Abrams and Hook (2002). Originally the unit of ST image is °K. STcorr could process data in both °K and °C. Optionally, if time series night TIR imagery for the same date are present, a correction for the differential cooling rate of various lithologic units can be applied. If the georeference information is embedded in the input Surface Kinetic Temperature image, STcorr utilizes this information, and registers the output according to this information. Grey boxes in Figure 1 depict the input images.

3.2. Computation

Simplified flow chart of STcorr is given in Figure 2. After the selection of the three input images (ST image, DEM and Aspect image), a masking option is given to the user. This option allows masking of input images interactively by defining a region of interest (ROI) polygon instead of using the full-scene images for corrections (default option). In some cases, blanking out the known (especially large) thermal anomalies may be useful to minimize their effect for altitude and aspect effect calculations. If masking option is selected, ROI is used as a blanking mask applied to the three input images. The corrections could be initiated with previously activated “Altitude vs. Temperature” button, which plots an altitude versus temperature scatter plot using DEM and ST image. It is then possible to apply a polynomial fit to the image with the appropriate (1 to 4^{th}) degree. Polynomial fit will also be displayed on the Altitude vs. Temperature graph. Using the selected polynomial fit, STcorr will compute the thermal gradient image using equation 1 and display it. Following this step, user could generate an altitude corrected image (equation 2), that represent surface temperature anomaly, where thermal gradient effect is removed. This image will be used for aspect correction.

Similarly, a second polynomial fit regression is used to correct relict illumination effects of diurnal heat. Briefly, an Aspect versus Temperature anomaly graph is plotted and a polynomial fit (with an interactive choice of 1 to 6^{th} degree) is applied to the plot. Using equation 3, an aspect gradient image which includes the illumination defects of the ST image will be produced. Lastly, “Generate aspect corrected image” button uses equation 4 to produce the final corrected image.

Input ST image, altitude corrected ST anomaly image and the final corrected ST anomaly image are displayed with the same color table, allowing visual comparison between them. A text window on the user interface displays chi-

square goodness-of-fit values during polynomial fit calculations. It is also possible to use full-scene images for altitude correction and masked images for aspect correction and vice-versa (masking could be applied after the first correction or full-scene ST image could be reloaded after the first correction).

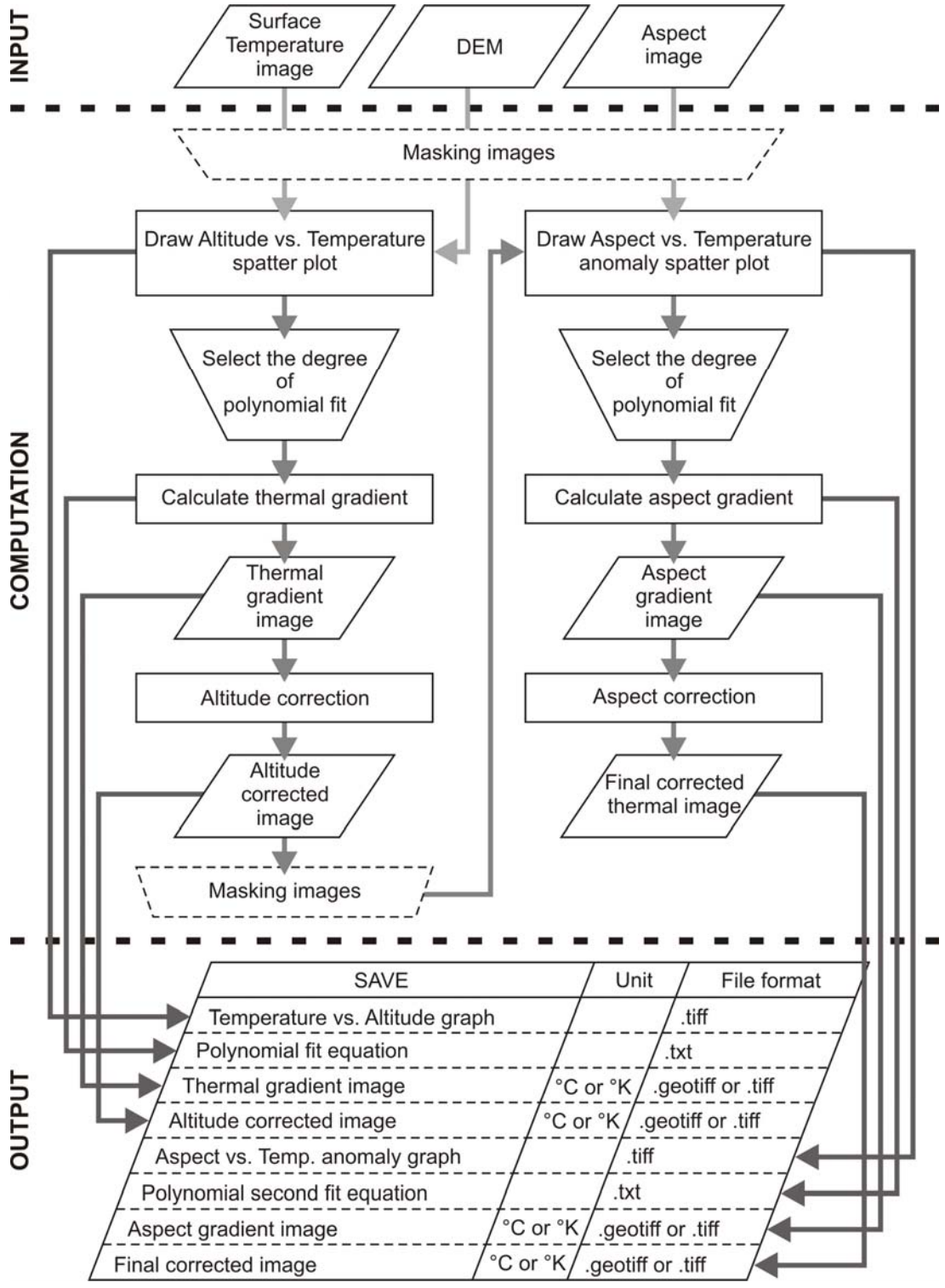

Figure 2. Simplified flow-chart of STcorr inferring the calculation process for altitude and aspect correction.

3.3. Output

STcorr generates four output images that are respectively called “Thermal gradient”, “Altitude corrected thermal anomaly”, “Aspect gradient” and “Corrected thermal anomaly” images. Even if the masking option was selected, the code applies fit equations on the full-scene images to produce full-scene outputs. Depending on the unit of input ST image, the units of the output images are °C or °K. If map coordinate information was provided with the input ST image, user could save these images with georeference information in GeoTIFF file format; otherwise they will be saved as TIFF. Two plotted graphs and polynomial fit equations used to generate images can also be saved (as .TIFF and .TXT respectively).

4. Correction of nighttime TIR image of Mt. Nemrut volcano

Correction of nighttime TIR image using STcorr algorithm has been applied to Mt. Nemrut, an active dormant volcano situated in the eastern Turkey. It has a summit caldera with dimensions of 8.5 × 7 km (Fig. 3). The western half of the caldera is filled by a freshwater lake (Nemrut Lake) and a small lake with hot springs locates at the northern part (Fig. 3). Bathymetrical surveys exhibit that the maximum depth of the larger lake reaches to 176 m, while the deepest point of the small-hot lake is close to 11 m (Ulusoy et al., 2008). The eastern half of the caldera is filled by pyroclastic deposits related to maars, lava domes and flows. Fumerolic activity and hot springs can be observed within the caldera; hot springs also appear around the Mazik dome at the western flank of the volcano (Fig. 3). The temperatures of the springs around the Mazik dome were reported as 34°C and 35°C (Atasoy et al., 1988). Temperature of one of the source springs of the hot lake was daily measured during one month period during 2005 field campaign; an average of 58°C was obtained (Ulusoy et al., 2008). Spring situated at the shore of the Nemrut Lake was measured 34°C. The temperature measured in the fumerolic vent east of the hot lake is 41.3°C and in the two other vents situated west of the hot lake temperatures are 41.2°C and 31.8°C (Ulusoy et al., 2008).

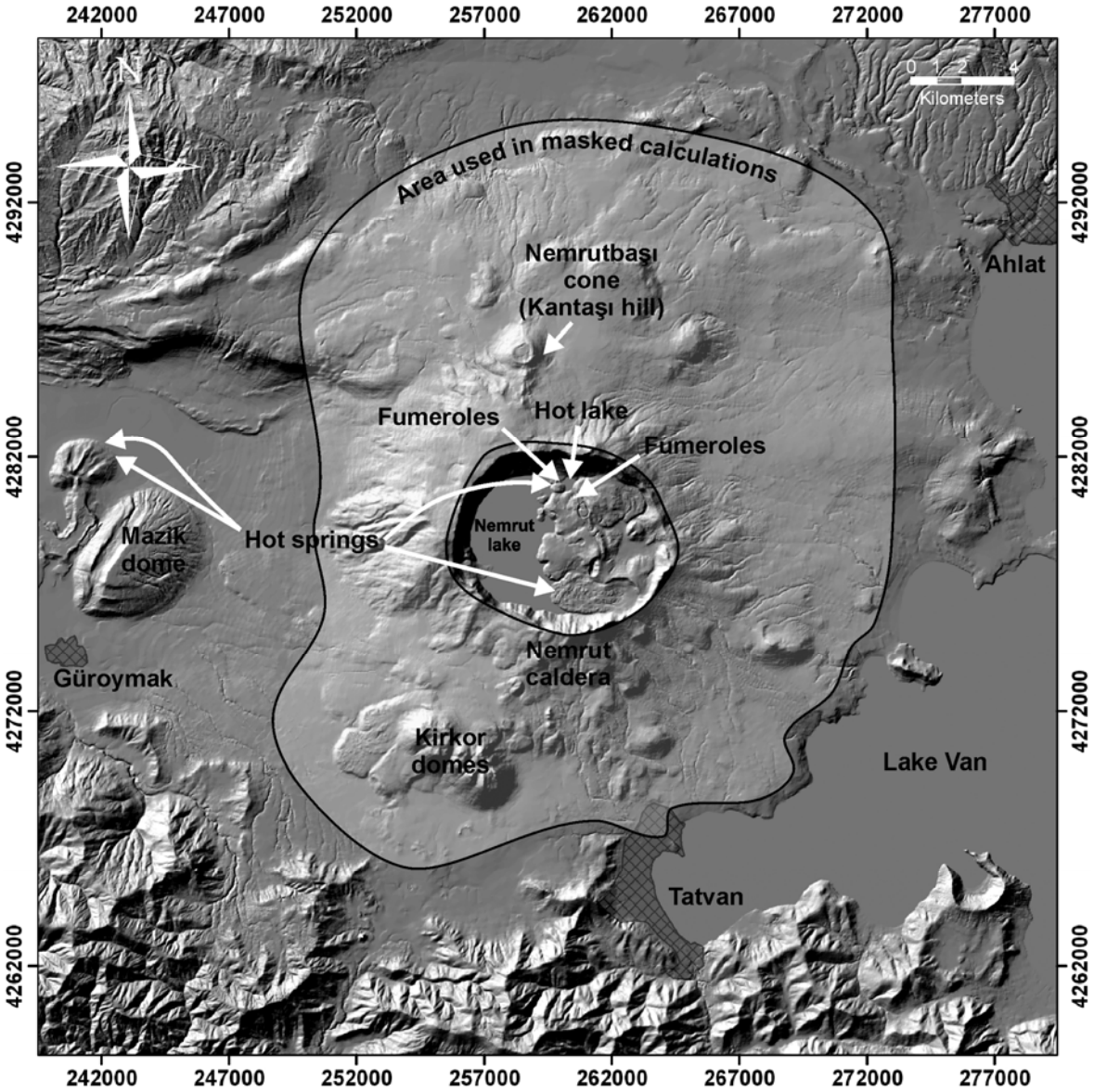

Figure 3. Hillshade image of Nemrut volcano showing the major geothermal hotspots and important volcanic features cited in the text. Area used in the masked copmutations of STcorr is framed. Cross hatched areas are the main populated areas around the volcano. Coordinate system: UTM(m), European datum (1950).

Nighttime ASTER L1B TIR image of the volcano was acquired in 08.07.2005 at 19:17:45 UTC (21:17:45 at local time), 1 hour and 38 minutes after the sunset. The “Radiance at sensor” data was atmospherically corrected and using the 5 TIR bands of the image, temperature and emissivity were separated applying emissivity normalization method (Hook et al., 1992; Kealy and Hook, 1993). Produced Surface Kinetic Temperature data in Kelvin was converted into Celsius degrees. A 400x400 pixel subset of the image was cropped from the original image preserving the original spatial resolution of 90 m/pixel. DEM of the same area was resized to 90 m/pixel and an aspect image was derived. ST image was

blanked out to remove the well known hydrothermal area (Fig. 3). Stcorr was both ran using the masked images and the original full-scene images.

5. Results

Scatter plots derived from the different steps of the method applied to Nemrut volcano are shown in Figure 4. Linear relationship between altitudes and surface temperatures is evident (Fig. 4a). For the altitude correction, regression equation generated by Stcorr can be defined as follows:

$$f(z) = a \times f(T) + b \qquad (5)$$

Where slope (a) defines the thermal gradient coefficient and the y-intercept (b) defines the theoretic sea level temperature. In theory, this equation (which is defining the thermal gradient) could be applied to the aspect corrected image to produce the aspect corrected real temperature image.

When a masked dataset is used to correct the aspect effect (Fig. 4b), the relationship between the aspect and the temperature anomaly is more rigorous compared to the usage of the full-scene images (Fig. 4c). Applying the altitude correction before the aspect correction gives more reliable relationship than the aspect correction applied before the altitude correction (Fig. 4b, d), because the first case uses “temperature anomaly” instead of raw “temperature” data to build the relationship.

Figure 5 shows the input ST image and output images of STcorr for the masked computation case. To avoid the lost of relative information between neighboring pixels, note that none of the images are enhanced using operations such as Look up table. Later application of such enhancement may reinforce the anomalies visually. Removal of altitude effect clearly reinforce the thermal signature especially around and on the Mazik dome (Fig. 5b) when compared to the uncorrected ST image (Fig. 5a). Still, the aspect effect due to relict diurnal heat is evident in altitude corrected image (Fig. 5b). Second regression step remove this aspect effect, and produce final corrected image (Fig. 5c).

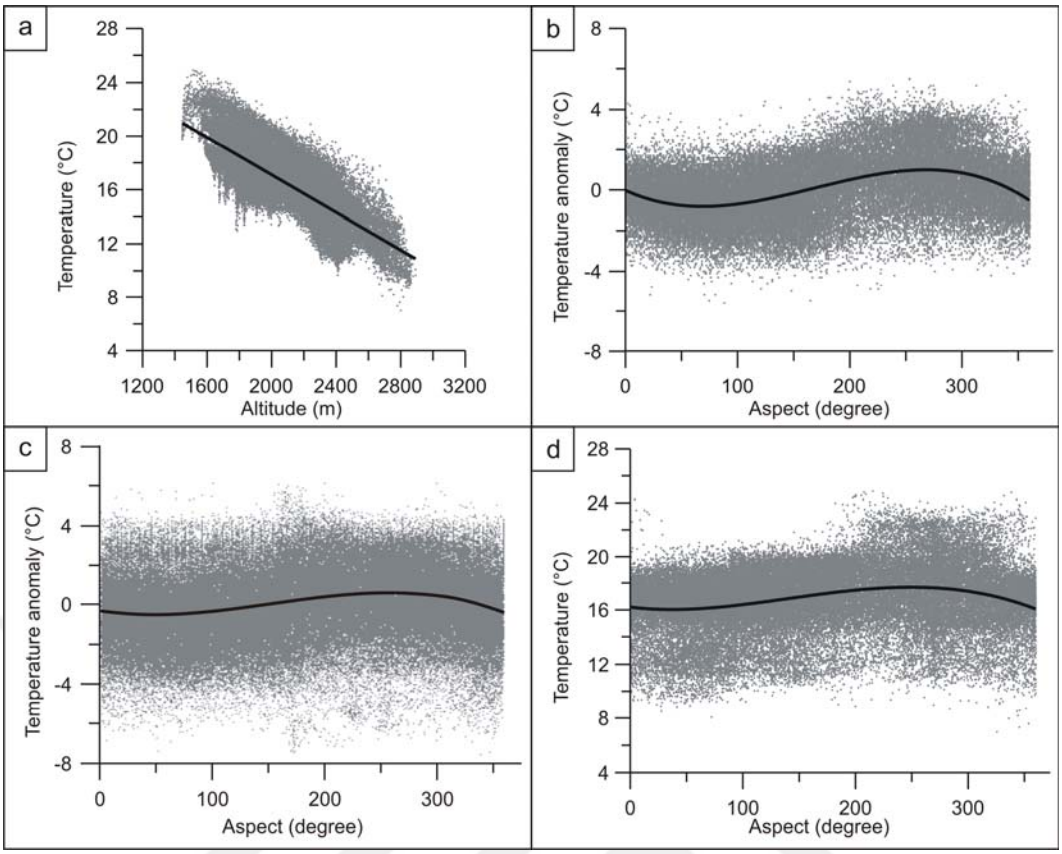

Figure 4. Scatter graphs of various applications of STcorr code for Mt. Nemrut. **(a)** Surface Kinetic Temperature – Altitude relationship in full-scene image, **(b)** Temperature anomaly – Aspect relationship after altitude correction using masked image, **(c)** Temperature anomaly – Aspect relationship after altitude correction using full-scene image, **(d)** Surface Kinetic Temperature – Aspect relationship when the altitude correction is discarded.

The relict heat causing a warmer false anomaly on the western and southwestern facing slopes of the domes, cones and the volcano itself is thus removed. Anomalies in the corrected image are consistent with the hydrothermal activity and the hot spots detected by self-potential measurements (Ulusoy et al., 2008). Ambiguous thermal anomalies appearing on the cone (Nemrutbaşı cone, Fig. 3) at the northern part of the volcano (Fig. 5c: arrows) are thought to be caused by the albedo effect. They correspond to basalt and obsidian lava flows and the lava lake of the 1441 and 1597 activities (Aydar et al., 2003). Temperature variations on lake surfaces appear noisy. As they normally must have no slope aspects, during the aspect calculations they were also classified according to DEMs. The temperature values on altitude corrected image are more reliable for water bodies.

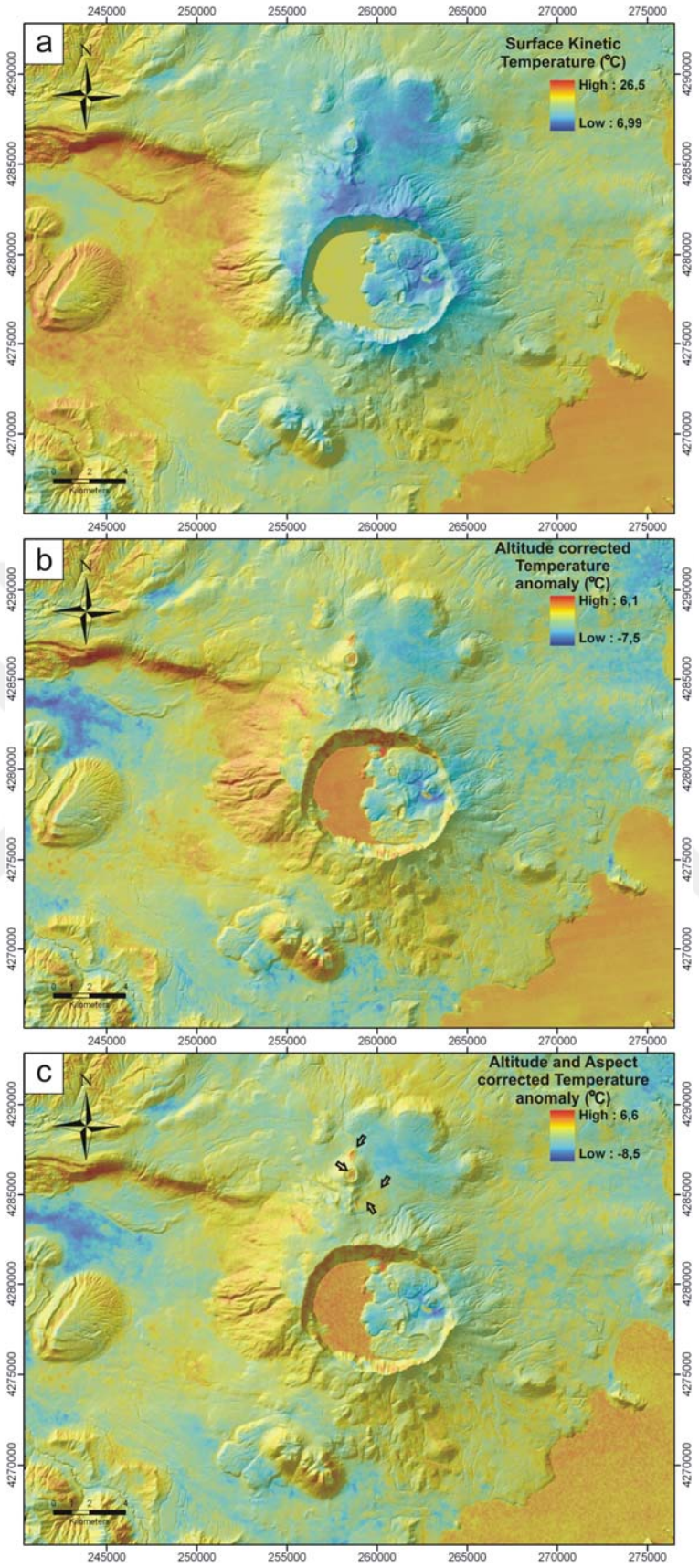

Figure 5. Unprocessed and corrected thermal images of Mt. Nemrut. **(a)** Original Surface Kinetic Temperature image, **(b)** Temperature anomaly image after altitude correction, **(c)** Final corrected image after altitude and aspect corrections. Coordinate system: UTM(m), European datum (1950).

6. Discussion

We have used basic statistical analyses to show the quality of the produced images when compared to the initial image. Calculations can be grouped according to (1) selected areas of investigation depending on geological feature (Table 1: analysis - 1), (2) areas defined by pixel values greater than mean temperature (Table 1: analysis - 2), and (3) directional response. For geological approach, two known hydrothermal areas (Mazik dome and intra-caldera land area) and a hydrogeological area (where we observed pure hydrogeological signals in self-potential surveys, Ulusoy et al., 2008) were selected (Fig. 6). In the first group of statistical analyses, the standard deviation of temperature values were compared using the same selected areas in the original image and in the corrected images. The standard deviations of produced images are clearly reduced when compared to the uncorrected image in all the corrected images (Table 1: analysis - 1). This is an expected result, exhibiting the improvement after corrections.

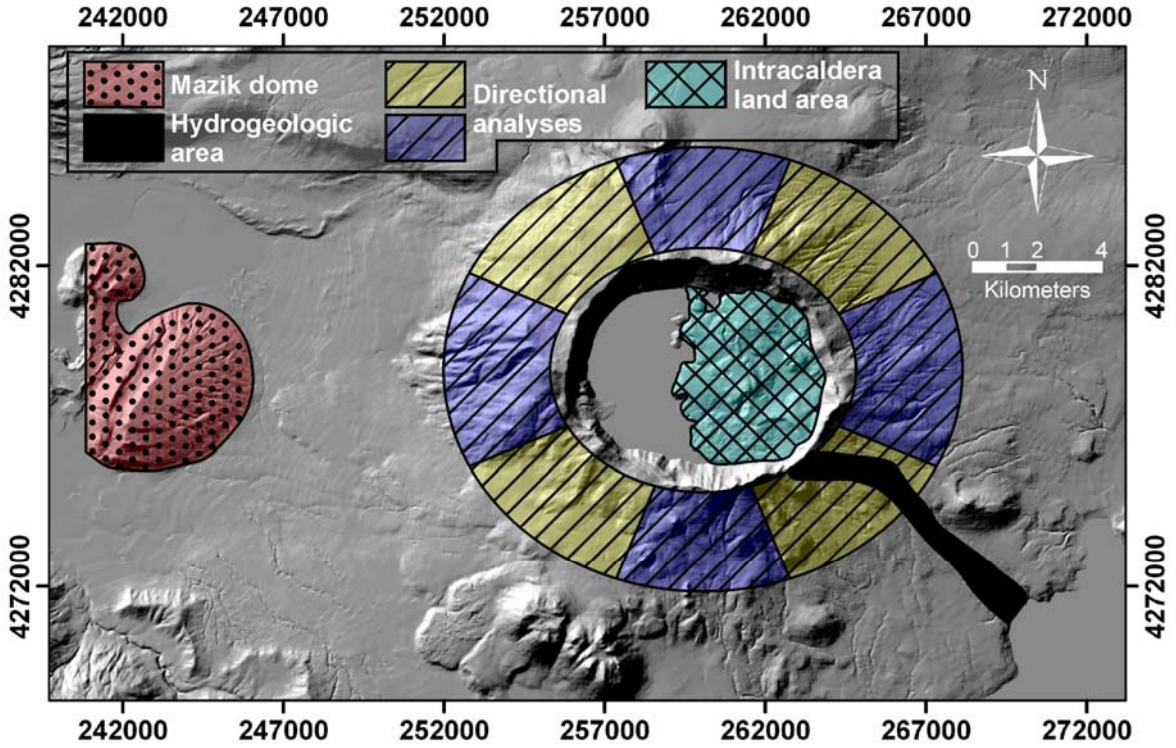

Figure 6. Map showing the area subsets used in statistical calculations. Coordinate system: UTM(m), European datum (1950).

Statistics	Dataset	Subset	Min (°C)	Max (°C)	Mean (°C)	Stdev	# of pixels
Analyses 1: According to selected area	A	Whole image	7,00	26,46	18,03	2,72	160000
	B		-7,62	6,36	0,00	1,78	
	C		-8,20	6,75	0,03	1,81	
	A	Intra caldera land area	8,44	18,46	13,28	1,68	2245
	B		-6,60	2,55	-1,66	1,62	
	C		-6,69	3,01	-1,51	1,62	
	A	Mazik dome	17,37	25,88	21,55	1,20	3615
	B		-3,25	4,38	0,59	1,08	
	C		-1,74	3,44	0,38	0,84	
	A	Hydrogeologic zone	12,51	21,41	16,96	2,08	925
	B		-1,71	3,12	0,15	0,82	
	C		-1,74	3,44	0,38	0,84	
Analyses 2: Acording to area defined by pixels greater than mean temperature	A	Whole image	18,04	26,46	20,33	1,59	75325
	B		0,00	6,36	1,41	1,07	79725
	C		0,00	6,75	1,41	1,08	81505
	A	Intra caldera land area	18,46	18,46	18,46	-	1
	B		0,01	2,55	0,75	0,61	366
	C		0,00	3,01	0,81	0,67	425
	A	Mazik dome	18,07	25,88	21,56	1,18	3607
	B		0,00	4,38	1,11	0,74	2582
	C		0,00	4,21	1,06	0,71	2271

Table 1. Simple statistical parameters of unprocessed and processed image datasets for selected specific areas and areas defined by pixels which have density number values greater than mean temperature. Image datasets are defined as **A:** unprocessed Surface Kinetic Temperature image, **B:** images after full-scene STcorr process and **C:** images after masked STcorr processes.

Standard deviation calculations based on the selection of areas may strongly depend on the selected areas; a second test based on pixel values has been performed (Table 1: analysis - 2). For the pixel value approach, mean temperature of the images were used as a base threshold value. Consequently, areas having values greater than mean temperatures and their intersection with previously selected areas (Fig. 6) were used to create regions of interest. Based on the standard deviation values, increase in the quality of the produced images is evident (Table 1: analysis - 2). In the second analyses, minimum values of the processed image sets are close to zero which indicates the success of the regression process. In both analyses, it is obvious that standard deviations of the masked STcorr process results are generally lower when compared to the full-scene process.

Finally, to investigate the changes in the sense of opposite facing slopes, directional statistical analyses were applied using 45° partitioned area surrounding the outer flank of the volcano (Fig. 6). An evident directional change in both ΔT_{mean} and ΔT_{max} between the altitude corrected and aspect corrected images is observed (Fig. 7). Furthermore, this change is more evident when masked images (excluding hydrothermal areas) are used (Fig. 7). As the Nemrut volcano is situated on the northern hemisphere at 38°37' latitude, sunset occurs at WSW to the volcano. After the correction using masked dataset, while the relict diurnal heat abundant on the W, SW, S and NE facing slopes were decreased, temperatures on the opposite facing slopes were considerably increased in the order of 0.62°C (maximum) and 0.59°C (mean). Higher intensity of the decrease of T_{mean} (-0.67°C) when compared to the decrease of T_{max} (-0.35°C) on the lately sun facing slopes, reflects the preservation of anomalies on while retrieval of the relict diurnal heat effect.

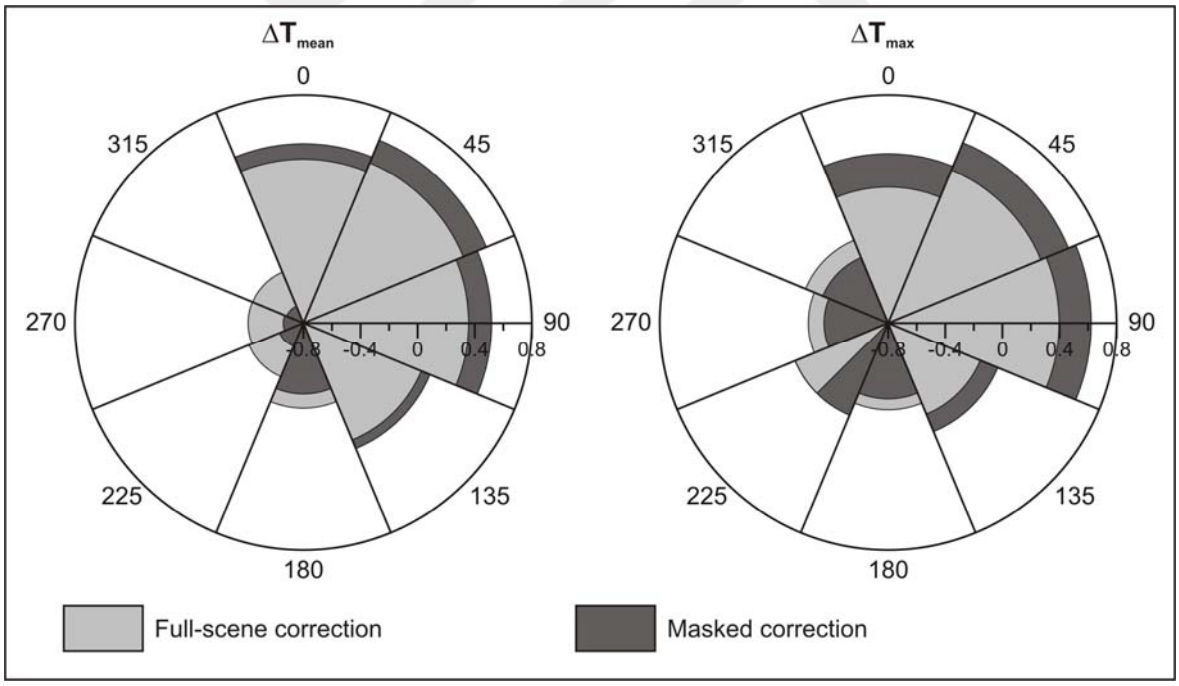

Figure 7. Polar graphs of change in T_{mean} and T_{max} between altitude corrected image and aspect corrected image for full-scene process and masked process.

7. Conclusion

For cases where topographic variations affect the geothermal anomalies and for volcano monitoring, retrieval of altitude and aspect effects may be essential in nighttime TIR imagery applications.

Most of the illumination correction methods are dealing with daytime TIR images, even some are using uncorrected nighttime images to correct the daytime images.

Most of the illumination correction methods, used in correction of the daytime TIR images, are using hill shade images (produced with a fixed sun azimuth angle and direction) instead of aspect correction. After the appropriate preprocessing aiming to reduce other daytime effects which were not described in this paper, this technique could be used in daytime images too. Aspect correction offers a whole scale correction while hillshade calculation may partially lose aspect related information depending on the resolution.

Analysis based on the masked images, excluding the known hydrothermal areas give better and more rigorous results than using the whole image datasets, where hydrothermal anomalies are affecting the calculations.

Regression is an efficient method to correct the nighttime TIR images. STcorr is using regression approach to correct the altitude and the aspect effects, and its computations are based on the image, which could give the appropriate response to variable conditions. Array oriented structure of the STcorr code allows rapid calculations when considered that it interacts with large image datasets.

Acknowledgements

This work benefited from a research grant of Hacettepe University Scientific Research Foundation (Project No: 01 01 602 021). It was also financially supported by Blaise Pascal University, CROUS, UMR-CNRS 6524 and benefited 3 integrated PhD grants from French Ministry of Foreign Affairs. French embassy in Turkey and Hacettepe University were supported several scientific expert missions.

3.2. Structure of the Nemrut caldera (Eastern Anatolia, Turkey) and associated hydrothermal fluid circulation

Journal of Volcanology and Geothermal Research 174 (2008) 269–283

Contents lists available at ScienceDirect

Journal of Volcanology and Geothermal Research

journal homepage: www.elsevier.com/locate/jvolgeores

Structure of the Nemrut caldera (Eastern Anatolia, Turkey) and associated hydrothermal fluid circulation

İnan Ulusoy [a,b,*], Philippe Labazuy [b], Erkan Aydar [a], Orkun Ersoy [a,b], Evren Çubukçu [a,b]

[a] Hacettepe University Department of Geological Engineering, 06532, Beytepe-Ankara, Turkey
[b] University Blaise Pascal, OPGC, Lab. Magmas et Volcans, UMR-6524 CNRS, 5 rue Kessler, 63038 Clermont Ferrand Cedex, France

ARTICLE INFO

Article history:
Received 25 August 2007
Accepted 27 February 2008
Available online 15 March 2008

Keywords:
self-potential
hydrothermal
caldera
Landsat
ASTER

ABSTRACT

Plio-Quaternary volcanism played an important role in the present physical state of Eastern Anatolia. Mount Nemrut, situated to the west of Lake Van is one of the main volcanic centers in the region, with a spectacular summit caldera 8.5×7 km in diameter. The most recent eruptions of the volcano were in 1441, 1597 and 1692. Nemrut Lake covers the western half of the caldera; it is a deep, half-bowl-shaped lake with a maximum depth of 176 m. Numerous eruption centers are exposed within the caldera as a consequence of magma–water interaction. Current activity of Nemrut caldera is revealed as hot springs, fumaroles and a small, hot lake.

Self-potential and bathymetric surveys carried out in the caldera were used to characterize the structure of the caldera and the associated hydrothermal fluid circulation. In addition, analyses based on digital elevation models and satellite imagery were used to improve our knowledge about the structure of the caldera. According to SP results, the flanks of the volcano represent "the hydrogeologic zone", whereas the intra-caldera region is an "active hydrothermal area" where the fluid circulation is controlled by structural discontinuities. There is also a northern fissure zone which exhibits hydrothermal signatures. Nemrut caldera collapsed piecemeal, with three main blocks. Stress controlling the collapse mechanism seems to be highly affected by the regional neotectonic regime. In addition to the historical activity, current hydrothermal and hydrogeologic conditions in the caldera, in which there is a large lake and shallow water table, increase the risk of the quiescent volcano.

© 2008 Elsevier B.V. All rights reserved.

1. Introduction

Mount Nemrut is a stratovolcano located in Eastern Turkey (Fig. 1), which exhibits a spectacular summit caldera with dimensions of 8.5×7 km. The summit of the caldera rim, Sivri hill, is on the north side and is 2935 m high; the highest point within the caldera is Göl hill (2486 m) located in the eastern part (Fig. 2a, b). The western half is filled by a freshwater lake (Nemrut Lake) with a surface area of 12.36 km^2, and a smaller lake with hot springs. The altitude of the lake surface is 2247 m. Bathymetric surveys show that the maximum depth of the larger lake is 176 m, while the deepest point of the small, hot lake is approximately 11 m. The eastern half of the caldera is filled by pyroclastic deposits of maars, lava domes and flows. Our field studies have revealed the existence of 10 maars (8 phreatomagmatic, 2 phreatic), 12 lava domes and 3 lava flows in the caldera (Fig. 2b). Five of the maars, including the Big Maar, four of the lava domes and the hot lake are aligned within the caldera (Fig. 2).

Nemrut volcano has been well studied petrologically (Yılmaz et al., 1998; Özdemir et al., 2006; Çubukçu et al., 2007), and only rarely physically (Atasoy et al., 1988). For the first time the structure of the caldera, its collapse mechanism, the active hydrothermal zones and their relationships with structural features within the caldera are demonstrated in this paper. Geophysical methods and remote sensing studies, in addition to the field survey, were incorporated into this study.

In order to reveal structural relationships and the hydrothermal fluid circulation we used the self-potential (SP) method that has already been applied to other volcanic regions (i.e. Jackson and Kauahikaua, 1987; Lénat et al., 1998; Zlotnicki et al., 1998; Finizola et al., 2002, 2004). Self-potential surveys carried out on stratovolcanoes (Aubert and Dana, 1994; Zlotnicki et al., 1998; Finizola et al., 2004) show positive anomalies from a few hundreds to thousands of millivolts in amplitude. These positive anomalies often overlap with hydrothermal or active zones whereas hydrogeologic zones show negative trends (i.e. Finizola et al., 2004; Lénat, 2007). In most volcanoes the downward flow of meteoric water gives rise to negative anomalies, whereas the upward flow of the hot fluids in the active areas produces positive anomalies (Zlotnicki et al., 1998; Lénat, 2007) with some exceptions (Finizola et al., 2006). Therefore, negative trends of SP anomalies are often observed on the flanks of volcanoes, while summit zones are represented by hydrothermal areas with

* Corresponding author. Hacettepe University Department of Geological Engineering, 06532, Beytepe-Ankara, Turkey. Tel.: +90 312 2977700; fax: +90 312 2992034.
E-mail address: inan@hacettepe.edu.tr (İ. Ulusoy).

0377-0273/$ – see front matter © 2008 Elsevier B.V. All rights reserved.
doi:10.1016/j.jvolgeores.2008.02.012

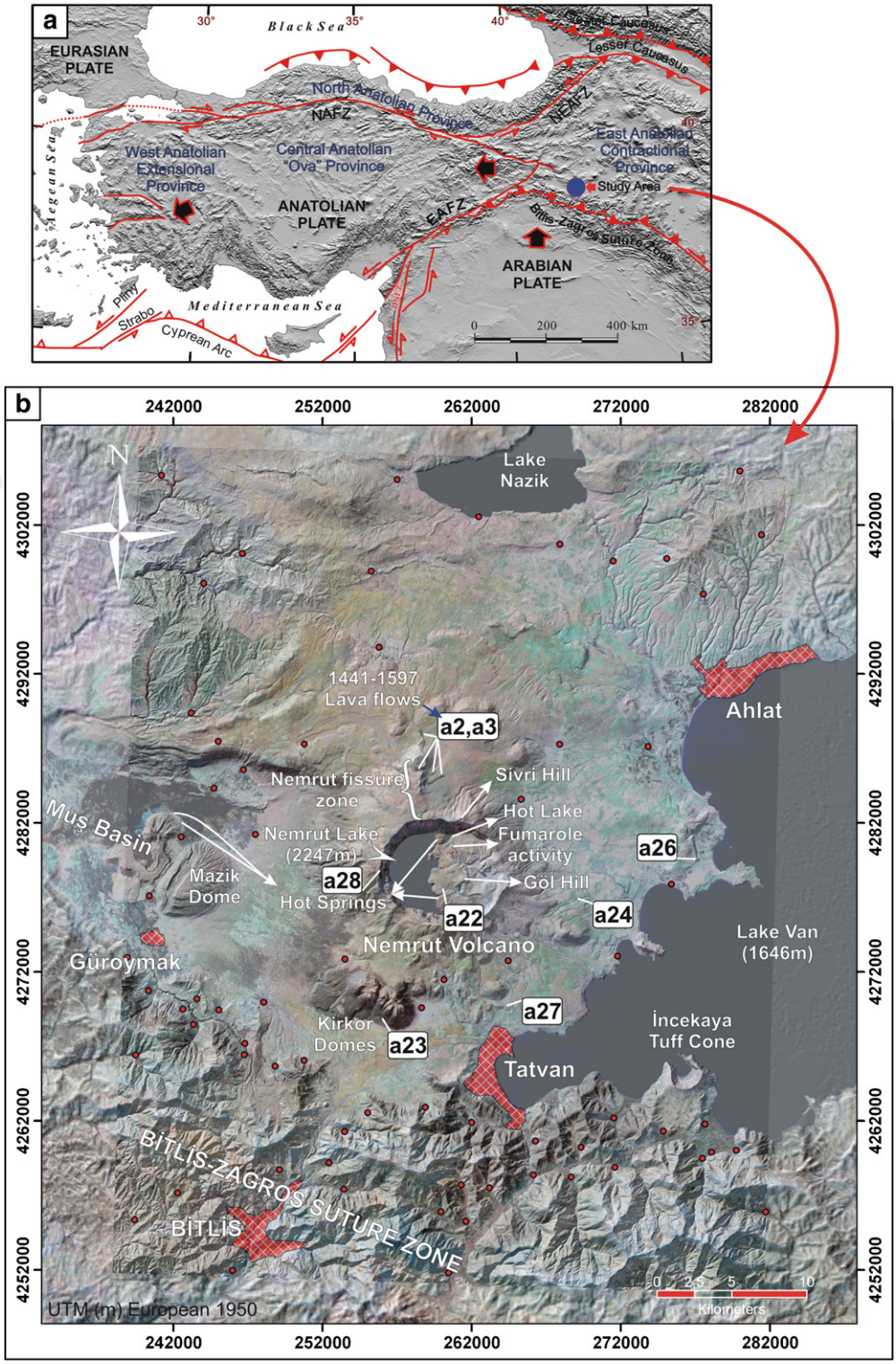

Fig. 1. Study area. (a) Simplified tectonic map of Turkey showing major neotectonic structures and neotectonic provinces (after Şengör et al., 1985; Barka, 1992; Bozkurt, 2001). (b) Landsat image of the study area showing major volcanic centers, Muş basin, Bitlis suture zone, locations of hot springs, fumeroles, and latest effusive eruptions. Bitlis City, Tatvan, Ahlat and Güroymak towns were indicated. Small red circles are the locations of the villages. Numbers given in boxes refer to known locations of dated samples given in Table 1. (For interpretation of the references to color in this figure legend, the reader is referred to the web version of this article.)

relatively positive SP signals (Fig. 3a). Potential sources of SP signals have been previously explained by electro-chemical, thermal, and electro-kinetic processes (Corwin and Hoover, 1979; Revil et al., 1999a, b; Zlotnicki and Nishida, 2003; Revil et al., 2004).

We also used digital elevation model (DEM) and satellite imagery analyses. In regions where bedrock is exposed multi-spectral remote sensing can be used to recognize altered rocks by their reflectance spectra, which differ from those of the unaltered country rock (Sabins, 1999). Considering the fact that the hydrothermally altered rocks may overlap with the fluid circulation zones we used Landsat imagery to detect these zones. In order to highlight the active hydrothermal zones we have also used a method (Ulusoy et al., submitted for

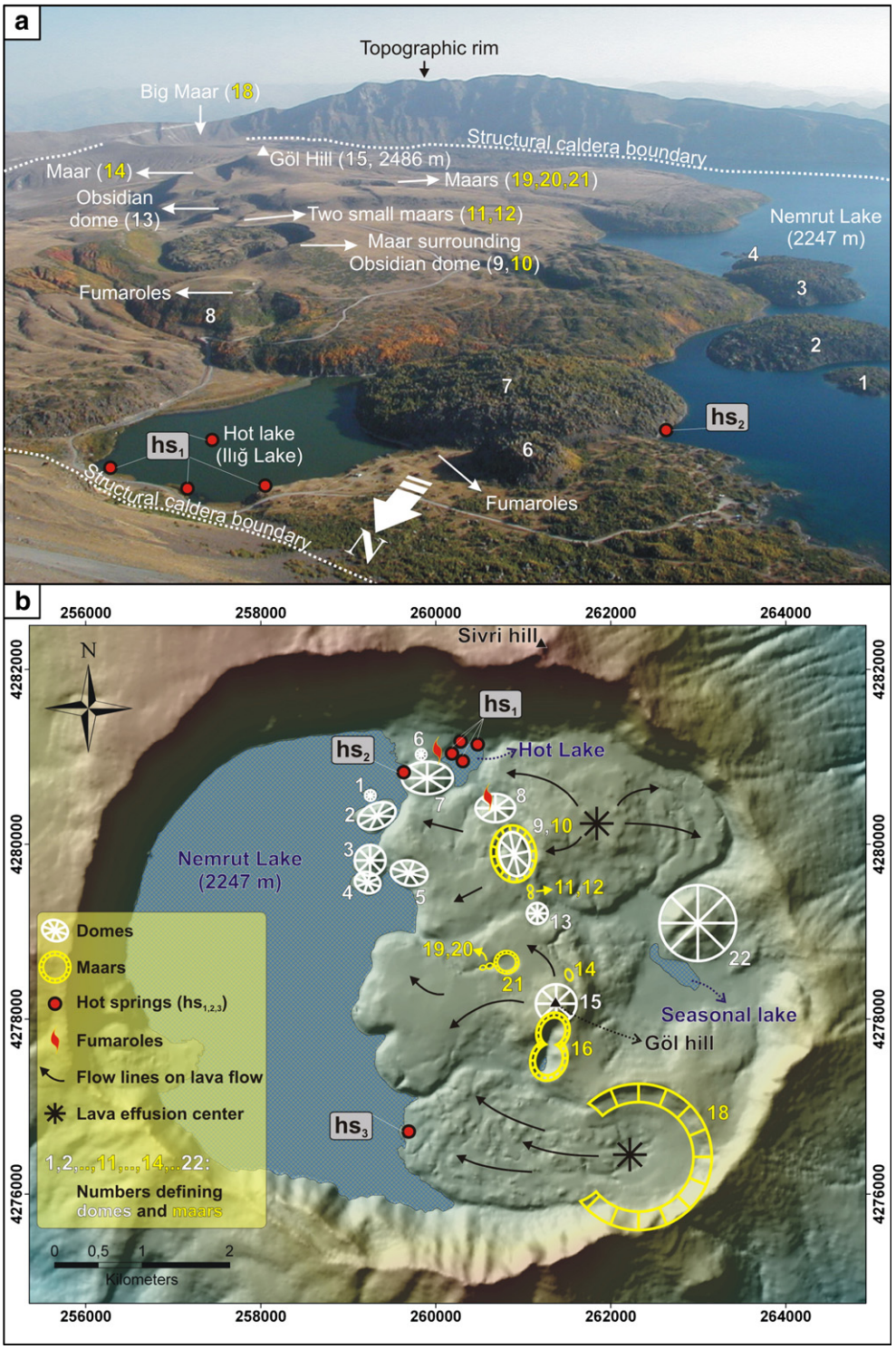

Fig. 2. Nemrut caldera. (a) View of the Nemrut caldera from northern caldera wall. Lineation of the main volcanic centers in the caldera is indicated. (b) Geomorphologic indication of the main volcanic centers in the caldera.

publication) which utilizes Aster night-thermal imagery, permitting the identification of the surface kinetic temperature.

2. Previous and historical activity of the volcano

Nemrut volcano started its activity 1 Ma ago and continued until historical times (Table 1). Effusive lava flows and fountains in 1441 (Karakhanian et al., 2002) and 1597 (Şerefhan, 1597; Aydar et al., 2003) were reported. Historical data presented by Karakhanian et al. (2002) showed that the latest volcanic activity (gas and ash eruptions) occurred on April 13, 1692. Moreover, new data revealing other ash eruptions were presented in comprehensive varve aging studies from Lake Van (Landmann, 1996; Landmann et al., 1996; Landmann and Kempe, 2005). Ten drill points of this study lie between the three main volcanic centers: Mt. Nemrut, Mt. Süphan and the Incekaya tuff cone (Fig. 1). Any of these systems may be responsible for the ash varves found in Lake Van. Formation of the Incekaya tuff cone was placed stratigraphically after the collapse of Nemrut caldera by Atasoy et al.

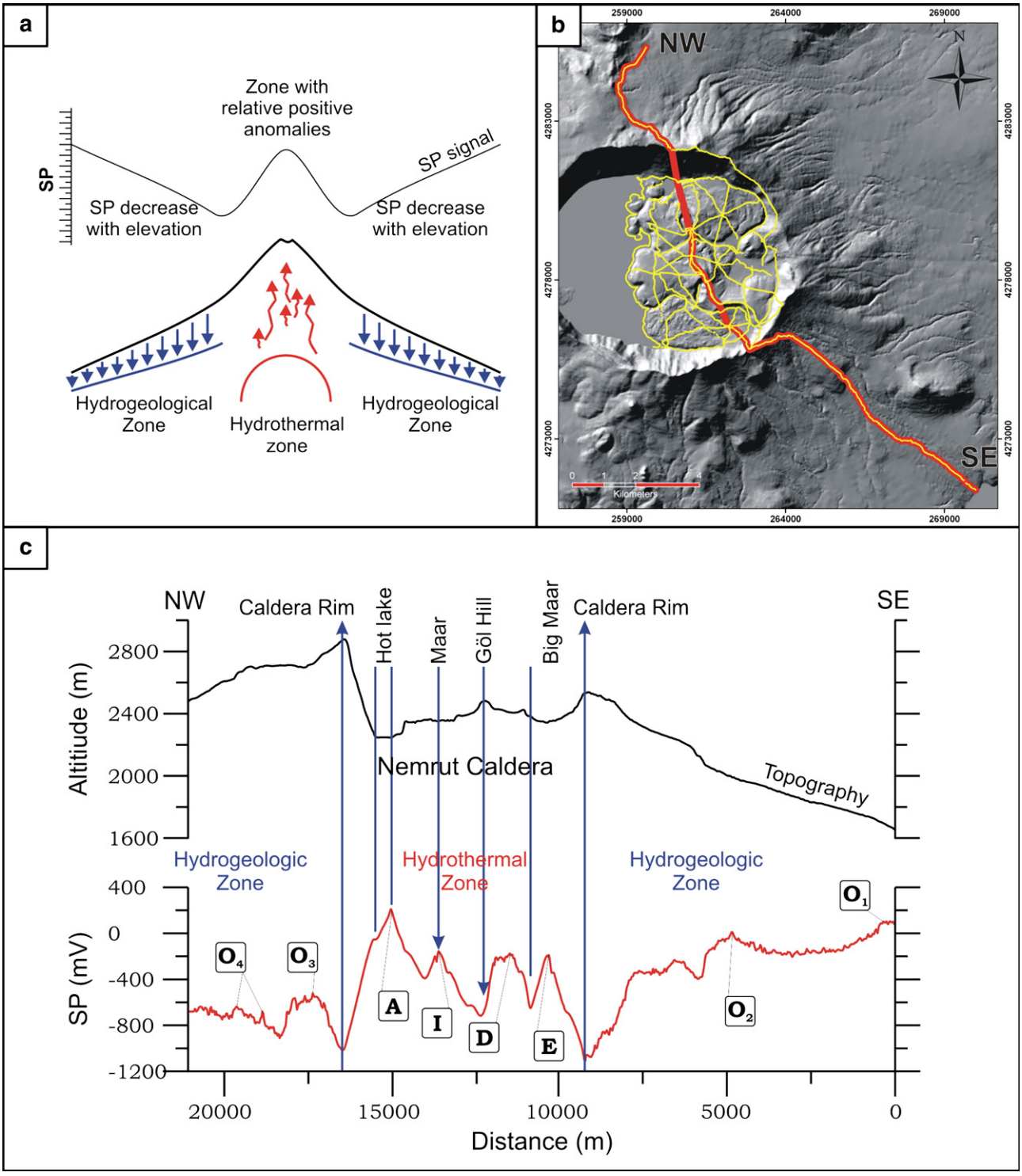

Fig. 3. Self-potential patterns. (a) Conceptual model of SP patterns on a volcano (from Lénat, 2007). The typical pattern of SP anomalies is shown on the upper part. Hydrogeological zone created by the mostly downward flow of water and hydrothermal zone where hot fluids move upward and their relationship with SP anomalies are shown. (b) SP profiles and topographic section profile. (c) SP pattern observed at Nemrut volcano. Hydrogeological zone on the flanks of the volcano and the hydrothermal zone overlapping the caldera can be seen in the figure. Main volcanic centers along the profile in the caldera are indicated. Anomalies discussed in the text are indicated with letters. "O_2" refers to the small, positive anomaly located near the shoreline of Lake Van indicating the intrusion of lake water.

(1988). However, the last known activity of the Süphan system was 0.10±0.02 Ma (Notsu et al., 1995). Since the Nemrut volcano has the most recent known eruptions of this region, we believe that the Nemrut system would be the source for most of these ash levels. Eruptions giving rise to ash layers dated at 657 BC and 787 BC (Table 1) by Landmann (1996) might have been witnessed by the Urartian civilization, which reigned in the area. Çilingiroğlu (1997) indicates that the Urartian "Ayanis Castle" (situated ~30 km east of Mount Süphan) was burned, demolished, and abandoned after 650 BC. He noted that the reason for this demolition was unclear, but probably

Table 1
Historical and older eruptions of the Nemrut stratovolcano. For the varve dates see the explanation in the text. Data source: 1: Karakhanian et al. (2002); 2: Şerefhan (1597); 3: Aydar et al. (2003); 4: Landmann (1996); 5: Landmann et al. (1996) corrected according to Landmann and Kempe (2005); 6: Atasoy et al. (1988); 7: Notsu et al. (1995); 8: Pearce et al. (1990); 9: Ercan et al. (1990); 10: Yılmaz et al. (1998). Known locations of dated samples are indicated in Fig. 1 with reference numbers given in this table (a1–a31)

No.	Eruption dates	Product	Event	Method (source)
a1	13.April.1692	?	Eruption of gas and ash	Historical (1)
a2	1597 AD	Obsidian, basalt	Lava fountains and flows	Historical (2,3)
a3	1441 AD	Obsidian, basalt	Lava fountains and flows	Historical (1)
a4	657±24 BC	Ash	Ash eruption	Varve (4)
a5	787±25 BC	Ash	Ash eruption	Varve (4)
a6	4055±60 BC	Ash	Ash eruption	Varve (4)
a7	4938±69 BC	Ash	Ash eruption	Varve (4)
a8	5242±72 BC	Ash	Ash eruption	Varve (4)
a9	<0.01 Ma	Rhyolite	Lava flow	K/Ar (7)
a10	9950±141 BC	Ash	Ash eruption	Varve (5)
a11	10,042±142 BC	Ash	Ash eruption	Varve (5)
a12	10,111±143 BC	Ash	Ash eruption	Varve (5)
a13	10,305±145 BC	Ash	Ash eruption	Varve (5)
a14	10,330±145 BC	Ash	Ash eruption	Varve (5)
a15	10,356±146 BC	Ash	Ash eruption	Varve (5)
a16	11,010±166 BC	Ash	Ash eruption	Varve (5)
a17	<0.02 Ma	?	?	K/Ar (7)
a18	0.02±0.01 Ma	Rhyolite	Lava flow	K/Ar (7)
a19	<0.03 Ma	Rhyolite	Lava flow	K/Ar (9)
a20	0.08±0.02 Ma	Olivine basalt	Lava flow	K/Ar (7)
a21	[illegible].05 Ma	Trachybasalt	Lava flow	K/Ar (7)
a22	0.13 Ma	Comendite	Lava flow	K/Ar (6)
a23	0.242 Ma	Quartz trachyte	Lava flow	K/Ar (6)
a24	0.272 Ma	Ignimbrites	Ash flow/caldera formation (?)	K/Ar (6)
a25	0.31 Ma	Trachyte	Lava flow	Isotope (10)
a26	0.333 Ma	Quartz trachyte	Lava flow	K/Ar (6)
a27	0.384 Ma	Quartz trachyte	Lava flow	K/Ar (6)
a28	0.567 Ma	Quartz trachyte	Lava flow	K/Ar (6)
a29	<0.7 Ma	Trachyte	Lava flow	K/Ar (8)
a30	<0.79 Ma	Hawaiite	Lava flow	K/Ar (6)
a31	1.01 Ma	Trachyte	Lava flow	K/Ar (6)

caused by a natural disaster like earthquake or fire. Following this disaster, the castle was plundered after the collapse of central authority (Çilingiroğlu and Salvini, 2001).

2.1. Seismicity and current activity of the volcano

Fumarolic activity and hot springs are found in the caldera (Fig. 2b); hot springs also exist around the Mazik dome at the western flank of the volcano (Fig. 1). In our field observations the temperature of one of the springs in the hot lake (Fig. 2b, hs_1) was daily measured over a one-month period; an average of 58 °C was obtained. A new hot spring has appeared in the summer of 2007 at the shore of Nemrut Lake (Fig. 2b, hs_2), and the temperature of this source was measured at 34.4 °C. The temperature of the springs around the Mazik dome was reported as being 34 °C and 35 °C (Atasoy et al., 1988). The temperature measured in the fumarolic vent, east of the hot lake, is 41.3 °C and in the two other vents, situated west of the hot lake, are 41.2 °C and 31.8 °C, respectively. Helium isotope ratio ($^3He/^4He$) analyses indicate the magmatic contribution to the samples of the hot lake and fumaroles (Nagao et al., 1989; Kipfer et al., 1994; Ercan et al., 1995), with the highest values in Anatolia (between 7.954±0.052 and 10.671±0.050; Güleç et al., 2002). The ratios reveal a significant mantle contribution in most parts, with almost pure mantle-He being emitted in the crater lake of Nemrut volcano and in Lake Van (Güleç et al., 2002). Nagao et al. (1989) note that this magmatic contribution implies that the volcano still has potential activity.

The first volcano-seismic network in Turkey has been installed at Nemrut volcano for real-time volcano monitoring. The seismic activity around the volcano has been observed since October 2003 with 3 stations equipped with one broadband and two short-period seismometers. Data collected in the stations are sent to Hacettepe University with a real-time Frame-Relay data communication link. Raw data are processed by an automated numerical code in near real-time. Following the hypocenter solutions of the seismic events, event types are determined by frequency and depth spectrum analyses.

Within a two year period, between October 2003 and October 2005, 219 events were recorded; 98 of them were long-period (LP) tectonic events and 89 were low magnitude local and regional earthquakes. 32 events of volcanic origin (VT and Hybrid) have been observed with a frequency of 1.3 events per month. A total of 133 events were observed in the vicinity of the volcano, with magnitudes (Md) ranging from 1.3 to 4.0 (Ulusoy et al., 2006).

3. Data acquisition and treatment

3.1. Bathymetry and digital elevation model of the Nemrut caldera

During the 2004 field expedition, the bathymetry of the Nemrut caldera lake was explored by a group of our expedition team. A Sonar/GPS equipped boat was used to measure the depth of the lake. Continuous data were recorded along the trip profiles. 19,976 data points were collected to produce the bathymetry map.

The 10 m spatial resolution DEM of the area was obtained by digitizing the elevation contour lines of sixteen 1:25,000 scaled topographic maps. The DEM was generated using the Krigging (with linear interpolation) method.

3.2. SP surveys

The self-potential surveys were performed during the 2004, 2005 and 2006 field campaigns. A total of 99.7 km of SP profiles were carried out with 25 m spacing (3988 measurements). Equipment used for the survey was a high input impedance voltmeter, a pair of Cu/$CuSO_4$ non-polarizing electrodes and an insulated Cu cable. All the measurements were marked by a GPS receiver.

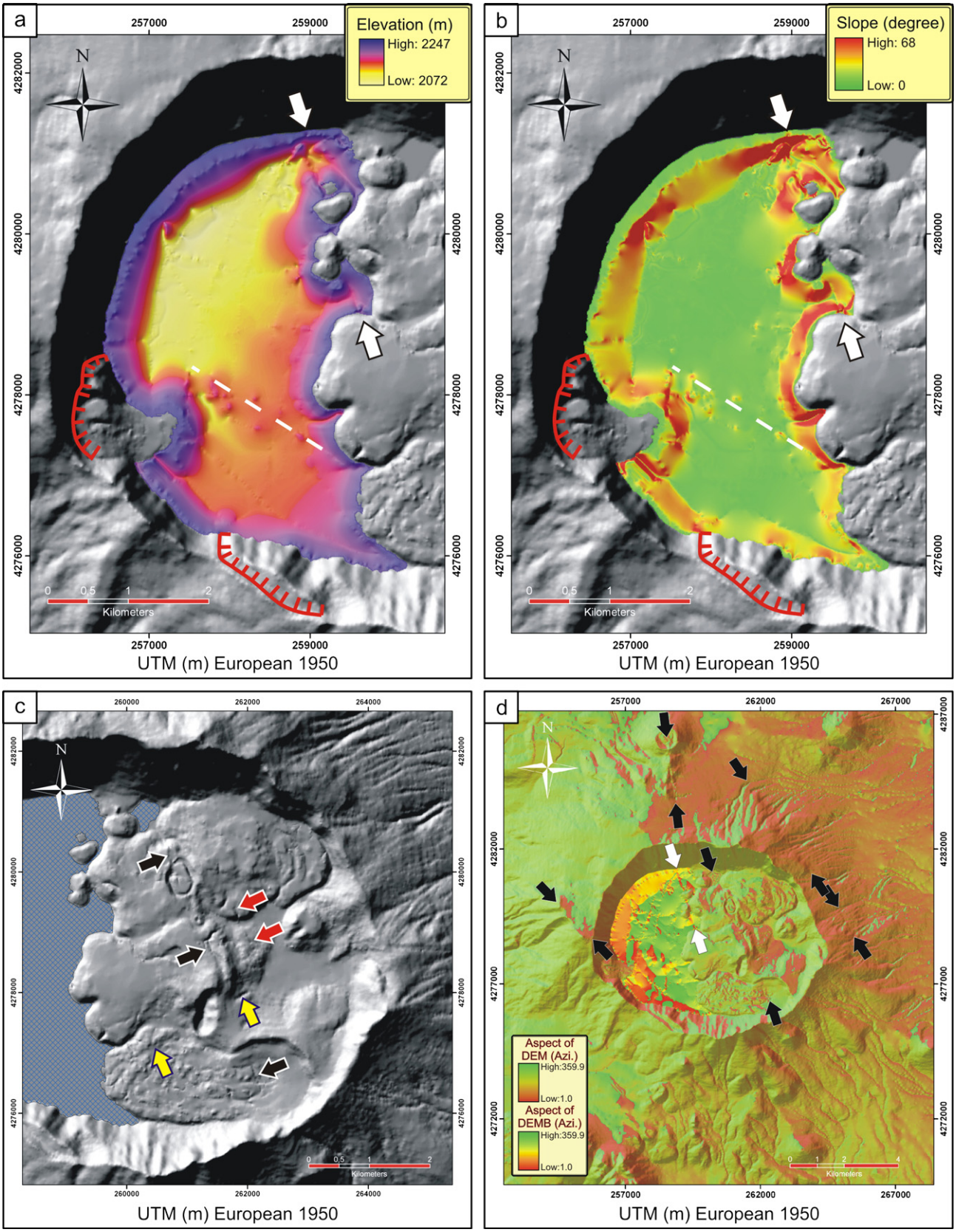

Fig. 4. Bathymetry and topography. (a) Bathymetry of Nemrut Lake. Dashed line in the lake shows the lineation interpreted as a structural discontinuity. White arrows point to the clear linear topographic change. (b) Slope image of bathymetry of Nemrut Lake. (c) Hillshade image showing the topographic traces of the faults. (d) Aspect map of DEM and DEMB. Sharp, linear, reverse changes in the topography are indicated between arrows. (For interpretation of the references to color in this figure legend, the reader is referred to the web version of this article.)

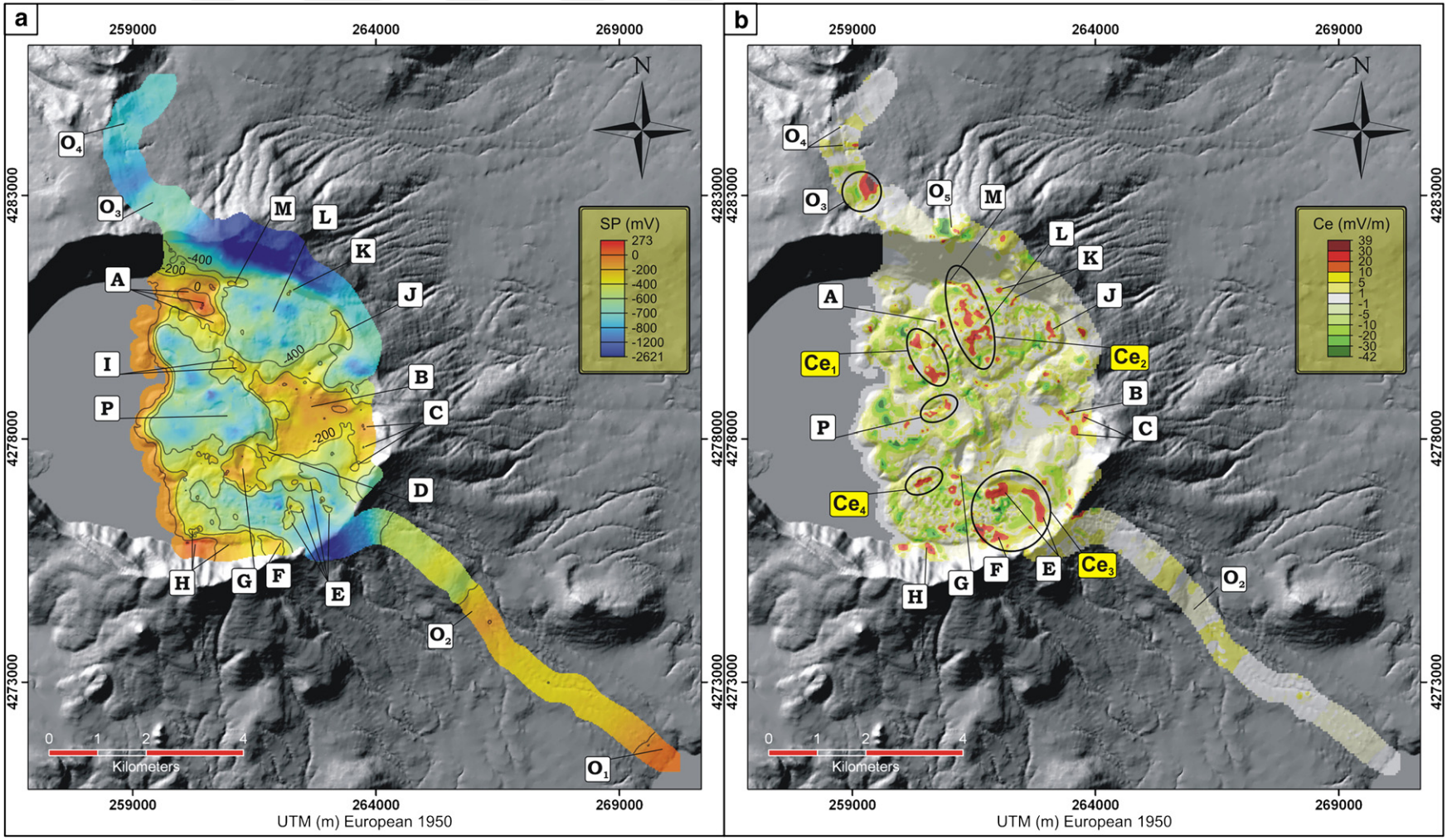

Fig. 5. Self-potential survey results. (a) SP map of Nemrut caldera. Positive SP anomalies discussed in the text are indicated with letters. (b) Ce gradient map of Nemrut caldera. Positive Ce anomalies discussed in the text are indicated with letters.

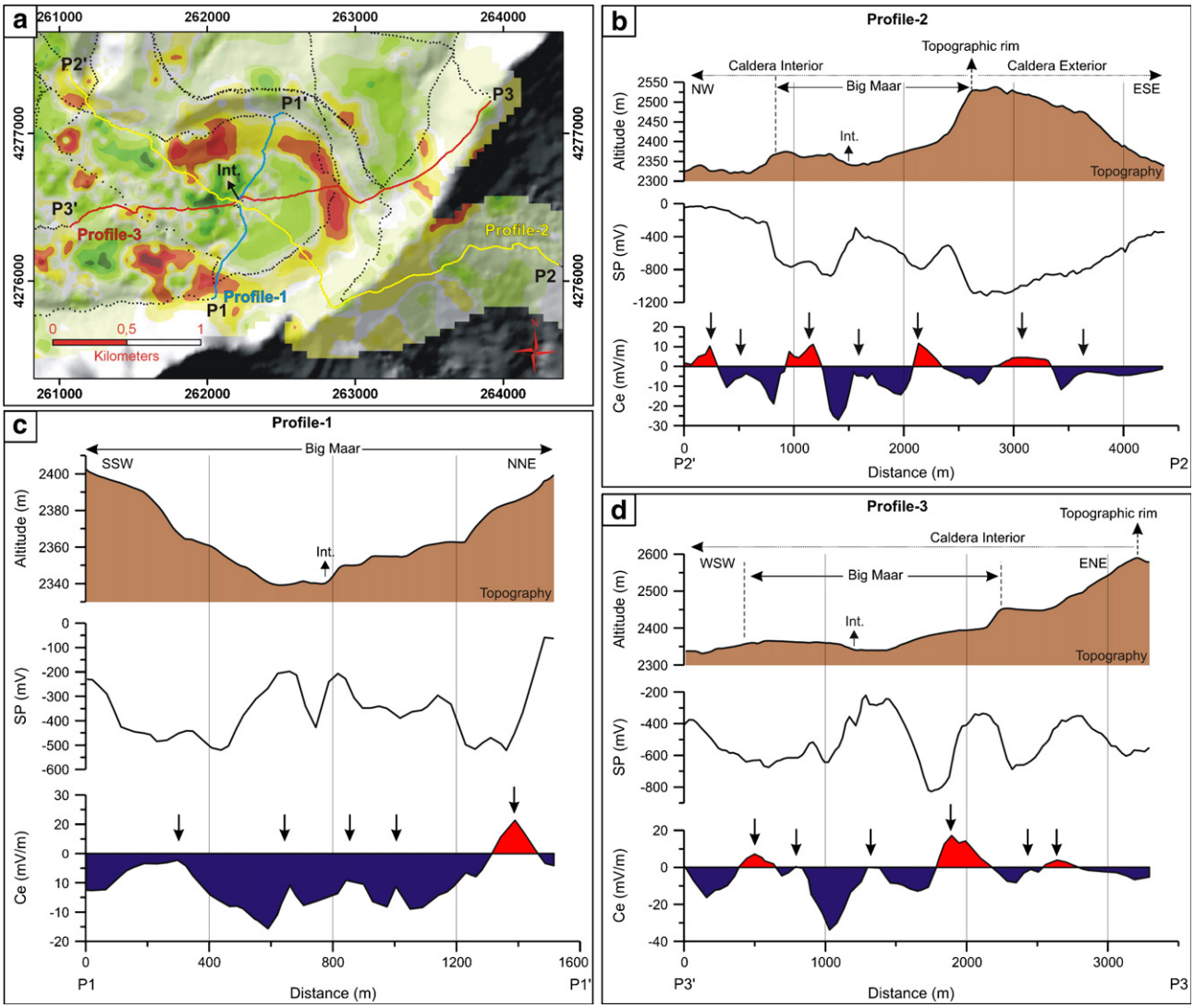

Fig. 6. Ce values on planar areas. (a) Closer view of Ce map showing southeastern part of the caldera near Big Maar. (b, c and d) Self-potential and Ce profiles along the Big Maar. Relative positive rises of Ce are shown with black arrows.

Two long SP profiles, one to the southeast, the other to the northwest were carried out on the outer flanks of the caldera (Fig. 3b). Nemrut Lake was selected as 0 mV reference for the interpolation of the data. An additional isopotential profile of 25 m data spacing was created on Nemrut Lake, along the shoreline with 0 mV potential. Two profiles are out of the caldera, the southern profile reaches to Lake Van. The northern profile was carried out to examine the hydrothermal activities along the northern fault zone where the latest effusive activities occurred. A further 23 profiles were measured in the caldera, where hot springs and fumaroles are situated. The two same profiles were repeated in 2004–2005 to identify if there had been annual changes; no annual differences were observed.

All of the data were combined with reasonable closure corrections (<50 mV) permitting a high-resolution SP map of the caldera to be generated. The interpolation of the data was carried out in three steps. SP data were interpolated using a 100 m resolution. Next, the original data, together with the regional 100 m grid, were interpolated to obtain a 40 m resolution grid. Finally, handling the original data again and the 40 m grid, an SP grid of 25 m resolution was constituted. This gradational interpolating technique was implemented in order to preserve the original resolution of measurements.

4. Data analysis

4.1. Bathymetry and DEM

The digital elevation model of bathymetry (DEMB) of Lake Nemrut and the digital elevation model (DEM) of the volcano were also analyzed for topographic footprints of the caldera structure. Bathymetric studies depict that Lake Nemrut is a half-bowl-shaped deep lake, where the average depth is around 140 m over the majority of the lake (Fig. 4a). The maximum depth of the lake is 176 m and the calculated volume is 12.4 km^3. The northern and southern parts of the lake bottom are separated by an approximately WNW-directed lineament (Fig. 4a, b). This discontinuity seems to be comprised of dome-shaped topographic features. When compared with the northern domain, the southern domain is topographically higher.

Topographic traces of some structural features are visible on the DEM (Fig. 4c). Two major collar collapses have been observed on the west and SSW flanks of the caldera wall (Fig. 4c). Evidence of both collapses are topographically expressed and the extent of the western collapse is significant on the bathymetry map. Tectonic breccia limiting the western slide was also noted during the field expeditions.

An aspect map of DEM and DEMB was produced to investigate the main topographical features related to structural discontinuities (Fig. 4d). Aspect identifies the steepest downhill direction from each cell to its neighbors, i.e. is the direction that is perpendicular to the contour lines on the surface, and an aspect map can be thought of as a slope direction map (Moore et al., 1993). A NNW directed lineation of the volcanic centers in the caldera is evident in the aspect map. This lineation clearly separates the eastern part (land area) of the caldera floor into two parts. Topography and flanks in the eastern part of this structure are facing to the ENE, while in the western part they face towards the WSW. The dominant and abrupt change in topographical features is illustrated on aspect maps (black arrows, Fig. 4d). Except for the one in the lake (Fig. 4d, white arrows), these structural features are also visible in the field, as reported by previous researchers (Güner, 1984; Atasoy et al., 1988).

4.2. SP pattern of Nemrut volcano

We observed a signal of amplitude ~2900 mV on the SP survey of the Nemrut volcano. This value is at the higher range of values previously observed in active volcanoes (~450 mV on Stromboli (Finizola et al., 2002), ~4500 mV on Misti (Finizola et al., 2004), ~3800 mV on Piton de la Fournaise (Lénat, 2007)). The SP pattern exhibits both hydrogeologic and hydrothermal zones similar to known examples worldwide (Fig. 3a, i.e. Zlotnicki et al., 1998; Finizola et al., 2002, 2004). The two profiles extending from the caldera rim to the foot of the volcano give an accurate estimation of the geometry of the hydrogeologic zone with characteristic negative trending SP–altitude gradient (Fig. 3c). Negative peaks are associated with the caldera rim. Relatively positive peaks are observed within the caldera. Some positive anomalies are overlapped by the hot springs and fumarolic vents (Fig. 3c). A hydrothermal zone, like the examples observed on the summit zones of other active volcanoes, is identified in the caldera of Mount Nemrut.

The SP map of the survey (Fig. 5a) illustrates the observed negative and relative positive anomalies. Some positive anomalies ($O_{1,2,3,4}$) are noticeable on the measurements out of the caldera (Fig. 5a). "O_1" is a small SP positive that was measured within the first 350 m from the shoreline of Lake Van, with a maximum of 118 mV (Figs. 3c and 5a). From Lake Van to the land, intrusion of brackish (22‰) and high pH (9.8) water (Landmann and Kempe, 2005) may be responsible for this small positive increase. "O_2" is a geological signal measured due to the lithological change at an obsidian flow–pyroclastic flow contact. The anomalies "O_3" and "O_4" are situated north of the topographic caldera rim and they may have a hydrothermal up-flow signature. They are above the fissure zone located on the northern flank of Mount Nemrut.

In the caldera, the suspected hydrothermal areas are described as higher order (A, B, C, D, E, F, G, H, I, J, M) and lower order (K, L, P) relative positive anomalies (Fig. 5a). Highest positive potential in the caldera was measured as +273 mV around the hot lake (Fig. 5a, "A"). "A" also identifies the anomaly observed on the Dome 8 (Fig. 2), where the fumaroles exist. Relative positive anomaly "B" rises in the planar area surrounding a seasonal lake in the eastern end of the caldera. "H" anomaly is in the southern part, near the shore of Nemrut Lake. The fourth anomaly "I" was observed along a lineation which comprised 4 monogenetic vents (maars 11, 12; dome 13, and maar 10 occupied by lava dome 9). "D" defines the anomaly which appears 400 m southeast of Göl Hill (Fig. 2). "E" anomaly can be divided into two geophysical structures: the first was measured in the fault (Fig. 4c, black arrow) which passes through the Big Maar; the second can be defined as a circular shaped anomaly observed at the bottom of the Big Maar, close to the tuff ring. "G" was observed around, and in, maars 16 and 17. "M", "J", "C" and "F" anomalies appear respectively along the northern, north-eastern, eastern and southern part of the structural boundary of the caldera. The lower order "K" is pointing out the relative positive anomalies on the structural caldera boundary, too. "L" is situated in the middle of the northern trachytic obsidian lava flow and "P" is beside the maar-like deep (90 m) explosion crater (referred as "maar 21" in Fig. 2).

As well as these positive SP values, which may be related to up-flow hydrothermal fluid circulations, the relatively planar topography of the caldera may give rise to misinterpretations due to the different possible electric potential source mechanisms. Superimposition of hydrothermal and hydrogeologic anomalies must be discriminated. Such a problem can be overcome by considering the altitude with respect to SP.

4.2.1. SP–elevation relationship on Nemrut volcano

Negative SP and elevation relationships are observed on Nemrut volcano as documented in earlier studies on volcanoes (Corwin and Hoover, 1979; Jackson and Kauahikaua, 1987; Lénat, 1987; Aubert and Yene Atangana, 1996; Finizola et al., 2004). Jackson and Kauahikaua (1987) defined a correlation coefficient "Ce", which is the ratio between the horizontal SP gradient and elevation. It is calculated on portions of a profile where a linear relationship between SP and altitude is observed (Lénat, 2007). Finizola et al. (2004) have used a Ce gradient map on Misti volcano for a structural approach. There are two significant advantages of calculating Ce values: firstly, it was noted that a negative SP–elevation relationship is correlated with the piezometric head, or with the thickness of the unsaturated zone (Jackson and Kauahikaua, 1987; Aubert et al., 1990), thus it can be used to estimate the depth of the water table; secondly, they can amplify the SP anomalies while masking any hydrogeologic gradient. The Ce gradient approach appears to be promising for the qualitative interpretation of SP surveys in volcanic areas as well as in other environments (Lénat, 2007).

4.2.1.1. Ce map. A Ce map, produced with an automated code written by Lénat (2007), clearly shows bipolar, positive and negative anomalies (Fig. 5b). This code computes the SP/elevation gradient in four directions (SN, WE, SW–NE and SE–NW) and utilizes the highest SP gradient to form a Ce map. Considering the topography inside the caldera is not steep in comparison to the flanks of a volcano, within the calculation process $\Delta z < 1$ m were masked to avoid anomalous Ce values. A DEM and SP map of 50 m resolution were used for gradient calculation. Using 3, 5, 7, 9 sample points respectively, gradients were calculated from the SP map of Nemrut caldera. Accuracy of the Ce map and the short wavelength anomalies increases from 9 points of calculation to 3 points. Here, a 5-sample point gradient map is shown for the visual quality (Fig. 5b). A 3×3 median filter was used to remove the relict short wavelength signals from the gradient.

In addition to the detection of hydrothermal fluid activity spots, the Ce gradient also helps to visualize the related structural discontinuities (Fig. 5b). Four main SP–altitude gradient anomalies, namely "Ce_1", "Ce_2", "Ce_3" and "Ce_4" are noteworthy (Fig. 5b). "Ce_1" appears on the western side of domes 9 and 13 and maars 10, 11 and 12. The group of anomalies defined as "Ce_2" is elongated in a NNW direction. "O_5", which is situated on the northern caldera wall, is observed on a fault reported by Güner (1984). This fault probably continues through the anomalies constituting the "Ce_2" group (Fig. 5b) and the red arrows in Fig. 4c indicate its topographic signature on its southern edge. The "Ce_3" anomaly covers the designated area of the Big Maar (maar 18) in the SE of the caldera, with a circular positive anomaly along the diatreme area (Fig. 5b). This positive Ce anomaly is supposed to be an evidence of the hydrothermal signature of the "Big Maar". The "Ce_4" anomaly is situated along the fault exposed topographically (Fig. 4c yellow arrows) which is considered to be continuing through the elongated maar (maar 16). Another hot spring (Fig. 2b hs_3) was noted on the SW end of this fault (Güner, 1984). Anomalies marked with "H", "C", "J" and "K" correspond to the positive Ce values along the structural caldera boundary. "A" anomaly

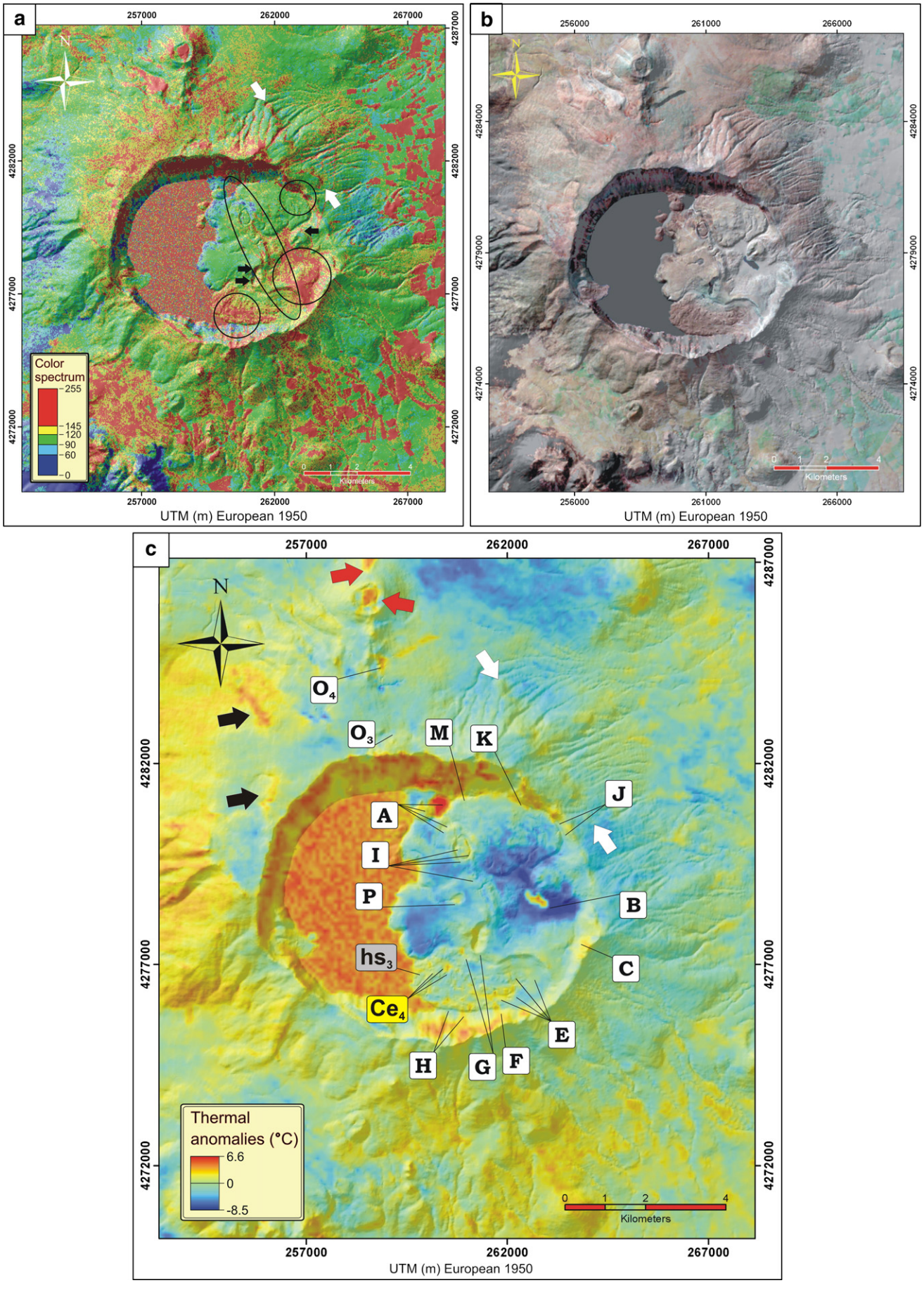
a
257000
262000
267000
4287000
4282000
4277000
4272000
N
Color spectrum
255
145
120
90
60
0
0 1 2 4
Kilometers
UTM (m) European 1950
b
256000
261000
266000
4284000
4279000
4274000
N
0 1 2 4
Kilometers
UTM (m) European 1950
c
257000
262000
267000
4287000
4282000
4277000
4272000
N
O4
O3
M
K
J
A
I
P
B
hs3
C
Ce4
E
H
G
F
Thermal anomalies (°C)
6.6
0
-8.5
0 1 2 4
Kilometers
UTM (m) European 1950

lies on the fumaroles of dome 8. "O_3" and "O_4" appear on the rift zone at the northern flank of Mount Nemrut. Lénat (2007) theoretically showed that bipolar Ce anomalies are generated above heat sources. "O_4" is a bipolar anomaly where the rifting fissure is situated along the positive and negative inversion.

The Ce map shows that some anomalies disappear by the minimization of the topographic effect. It is noteworthy that Ce anomalies on "H" and "B" are not as strong and large as appeared in the SP map. Low water table is responsible for these anomalies in the SP map. The seasonal lake (Fig. 2b) where "B" anomaly strongly appears in the SP map denotes the low water table. Furthermore, no hydrothermal signature was noted in these areas during the fieldwork.

It is important to note that Ce maps on planar topography where the topographic effects are relatively less than the outer flanks of a volcano must be investigated with care and in detail. This phenomenon produces higher values of Ce due to calculation procedure. As discussed above, we used a filter in the computation process to minimize these effects. This effect was investigated using profiles along SP measurement points on one of the planar areas in the caldera where we observed "Ce_3" anomaly (Fig. 6a). Big Maar has relatively low topographic contrast; on the other hand, Ce values observed are dominant here. When analysed in detail, it is evident that even in the caldera (i.e. Fig. 6a, profile-1); there is considerable altitude difference (~60 m) along the profiles. The intra-caldera is not totally flat; there are noticeable differences of altitude in the caldera. Ce anomalies on the profiles in Fig. 6 are not simply overexposed values; they reflect the positive and negative gradient of the self-potential.

4.3. Image analysis

4.3.1. Landsat TM image

The spectral bands of Landsat TM are well suited for recognizing assemblages of alteration minerals (iron oxides, clay and alunite) that occur in hydrothermally altered rocks (Sabins, 1999). Correlating SP maps with image recognition of hydrothermally altered rocks may be useful for fracture mapping and the future progress of SP techniques as well. The 5/7 band ratio of a Landsat+ETM image was used for the image derivative approach (Fig. 7a). This method helps to visualize the hydroxyl clay minerals (alunite, illite, kaolinite and montmorillonite) and was previously used for the investigation of the ore bodies (Sabins, 1999 and references therein). This method utilizes the reflectance spectra characteristics of clay minerals mentioned above (Fig. 8a). The reflectance values of these minerals within band 5 are higher than in band 7. Ratio images can emphasize and quantify these spectral differences (Sabins, 1999). Proper use of color density distribution (Fig. 8b) may highlight the areas where these clay minerals are abundant.

It is noteworthy that the hydrothermal alteration map derived from the Landsat ETM+image (Fig. 7a) yields compatible results with SP anomalies (Fig. 5a). In Fig. 7a, red values (high values) theoretically indicate the zones where hydroxyl clay minerals are abundant. SP positive anomalies signed in Fig. 5a as "A", "B", "H", "I", "D", "E", "J" and "P" are evident in the derived image (Fig. 7a). However, fresh soil and rock surfaces are marked by the higher values in the Landsat image while the areas covered with vegetation tend to give relatively lower values. High alteration zones on the Landsat image, which are similar to SP positives "B" and "H", correspond to the fresh rock surfaces. It should not be confused with hydrothermal alteration. Landsat image

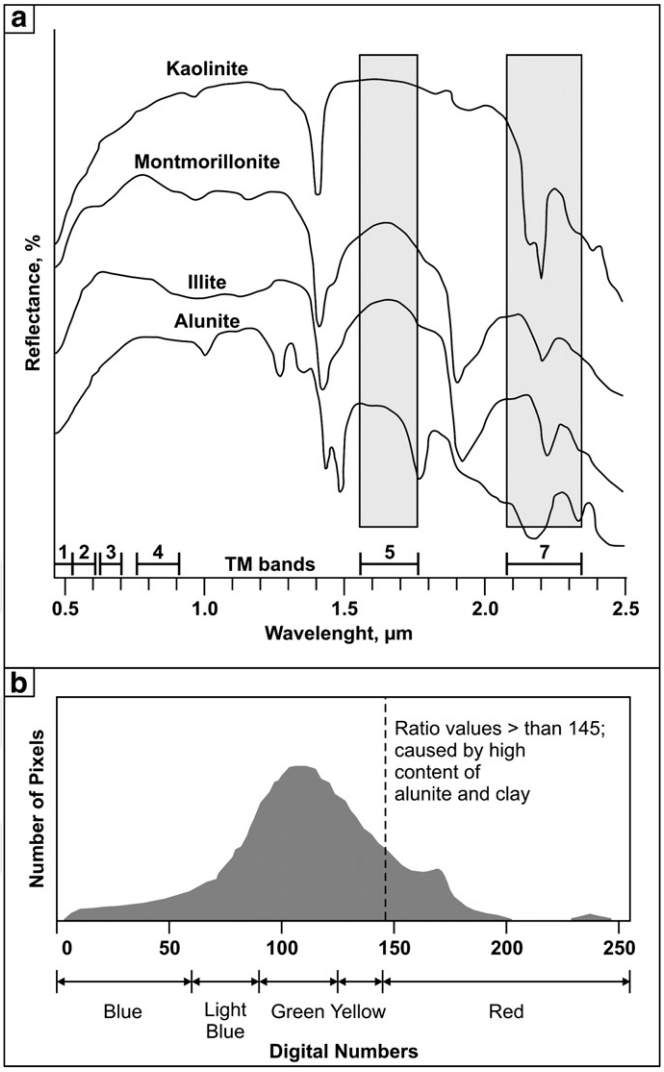

Fig. 8. Spectral characters and remote sensing processing of clay minerals. (a) Laboratory reflectance spectra of alunite, kaolinite, montmorillonite and illite and the ranges of Landsat bands (from Sabins, 1999). The 5/7 band ratio image amplifies the hydrothermal alteration because of the different spectral reflectance percentage of these minerals in fifth and seventh bands. (b) Histogram of the derivated Landsat image (F[illegible] and the color spectrum used to visualize the high accumulations of the minerals mentioned. For the theoretical base of this color ramp, see Sabins (1999).

superimposed on DEM is shown in Fig. 7b for comparison. Plant cover around the small hot lake masks the hydrothermal alteration around the area. Hydrothermal alteration spots observed in the caldera (Fig. 7a: black arrows) are evident features on the image. Lineation of high values along the ellipse in Fig. 7a infers hydrothermal alteration.

4.3.2. ASTER night-thermal image

An ASTER L1B night-thermal image acquired on 08.07.2005 at 19:17:45 (GMT) was used to produce a surface temperature image of the volcano. The "Radiance at sensor" data were atmospherically corrected and using the 5 TIR bands of the image, temperature and

Fig. 7. Remote sensing data processes for Nemrut volcano. (a) Hydrothermal alteration map derived from Landsat image. Red zones are theoretically indicating alunite, kaolinite, montmorillonite and illite rich areas. Small red areas pointed out by the black arrows are indicating the highly altered rocks observed in the field. The linear red zone between white arrows is also topographically visible on the aspect map. Black circles and ellipse show the areas which correlate well with the SP map (Fig. 5a). (b) Landsat image of Nemrut volcano superimposed on DEM. Image is stretched linearly, color composition is: R: Band 7, G: Band 3, B: Band 2. (c) Thermal anomaly image derived from ASTER surface kinetic temperature image with altitude and aspect corrections. Letters and arrows are pointing out the thermal anomalies. Red arrows point out the false anomalies.

Table 2
Thermal anomalies in the unprocessed ASTER surface kinetic temperature image and in the thermal anomaly image after altitude and aspect corrections. Notation in the first column refers to the notations in Figs. 4a and 8c. ΔT refers to the thermal anomaly difference between the hot spot and the cold region surrounding these spots

Notation	Name	# of DNs	Min (°C)	Max (°C)	Mean (°C)	SD	ΔT (°C)
Unprocessed ASTER surface kinetic temperature scene							
A	Hot lake	29	18.93	21.32	20.46	0.82	9.31
	Nemrut Lake	1136	18.39	20.48	19.40	0.28	8.25
hs_3	Hot source	9	17.72	19.49	18.79	0.60	7.64
B	Seasonal lake	15	14.18	20.05	17.09	1.73	5.94
E	Big maar	19	15.52	17.07	16.49	0.45	5.34
G	Long maar	17	14.36	17.07	15.90	0.67	4.75
P	Crater	4	15.00	16.10	15.57	0.46	4.41
I	Obsidian maar	19	13.82	15.79	15.13	0.57	3.97
	Cold regions	331	8.44	13.69	11.15	0.96	
Thermal anomalies after altitude and aspect corrections							
A	Hot lake	29	3.68	6.59	5.05	0.90	9.12
	Nemrut Lake	1136	2.07	5.50	3.89	0.69	7.96
hs_3	Hot source	9	1.82	4.21	2.83	0.80	6.90
B	Big maar	19	1.21	2.69	1.96	0.40	6.03
E	Seasonal lake	15	−1.04	4.50	1.73	1.54	5.80
G	Long maar	17	0.77	2.84	1.57	0.60	5.64
P	Crater	4	0.63	1.46	0.93	0.38	5.00
I	Obsidian maar	19	−0.18	1.87	0.89	0.63	4.96
	Cold regions	331	−7.69	−2.40	−4.07	0.96	

emissivity were discriminated by emissivity normalization method (Hook et al., 1992; Kealy and Hook, 1993; Johnson and Young, 1998; Hernandez-Baquero, 2000). Produced surface temperature data in Kelvin were converted into degrees Celsius. The altitude–temperature gradient was corrected using DEM with a second-degree polynomial equation. Finally, aspect difference due to the travel path of the sun was corrected using the Aspect of DEM image and a fourth-degree polynomial equation (Ulusoy et al., submitted for publication).

The corrected night-thermal surface temperature anomaly image of Nemrut volcano is given in Fig. 7c. High compatibility between the SP map (Fig. 5a) and the surface temperature image is evident. Anomalies observed on the SP map, such as "A", "E", "G", "I", "O_3", "O_4", and "P", were also observed on the surface temperature image (Fig. 7c). The data of these anomalies in terms of temperature are summarized in Table 2. SP anomalies along the structural caldera boundary "H", "F", "C", "J", "K" and "M" are also detectable on the surface temperature image. The shallow seasonal lake appeared as an anomaly on both the SP map and the temperature image (Figs. 5a and 7c: "B"). This false anomaly is due to the existence of a seasonal lake and a low water table around it in the SP map. Daytime warming up of this shallow lake (<1 m) is easy compared to the other lakes of Nemrut, resulting in a positive anomaly on surface temperature image. Nemrut Lake also gives higher temperature values than adjacent areas. This is because of the thermal inertia difference between water and other materials. It is known that diurnal radiant temperature variation of standing water gives lower response than rocks and soils (Sabins, 1997). Hence, water bodies give higher radiant temperature values than rocks and soils during nighttime and lower values at noon.

The fresh, glassy surface of obsidian outcrops at the northern fissure zone and the seasonal lake surface resulted in false temperature anomalies (Fig. 7c: depicted by red arrows). Several anomalies out of the caldera are visible on the image (Fig. 7c: black and white arrows). The linear anomaly observed on the NE flank of the caldera, which appears on both aspect and Landsat images, is noteworthy (Fig. 7c: depicted by white arrows); future SP surveys should be focused on this area.

5. Structural and hydrothermal model for Nemrut caldera

Calderas are important features in all volcanic environments and are commonly the sites of geothermal activity and mineralization (Cole et al., 2005). Yet, it is only in the last 25 years that a detailed three-dimensional study of calderas has been carried out, utilizing studies of eroded calderas, geophysical analysis of their structures and analogue modeling of caldera formation (Cole et al., 2005).

Within the scope of our surveys and analyses, we present here an innovative structural model of the Nemrut caldera (Fig. 9), stating that it collapsed by a piecemeal mechanism. It consists of three main blocks; namely P_1, P_2 and P_3 (Fig. 9). Actual hydrothermal fluid circulation quantified by SP analyses and the intra-caldera eruption centers are mostly located on the structural discontinuities limiting these blocks and on the caldera boundary faults. Blocks "P_1" and "P_2" form the eastern part of the caldera. The structural boundary between these blocks controls the main hydrothermal fluid flow in the caldera and is supposed to be responsible for the major explosive intra-caldera activity. Some other faults parallel to this one are evident in and out of the caldera.

The other block, "P_3" constitutes the western part of the caldera, the bowl shaped topographic low, housing the Nemrut Lake. There is an elevation difference of about 140 m between blocks "P_2" and "P_3" (Fig. 9), separating the eastern and western parts of the caldera. This zone is evident in both the DEMB (Fig. 4a) and the slope image of DEMB (Fig. 4b) with high altitude difference and steep slopes. At the shoreline of Nemrut Lake, this discontinuity is visible at some locations (Figs. 9a and 4c). The lowest part of the caldera floor is the deepest point of Nemrut Lake, at 176 m depth, and is situated at the western edge of the caldera. Dome shaped bodies constituting a WNW-directed lineation at the bottom of the lake are probably lineated along a fault. This fault continues to the west and appears on the western caldera wall as a reverse fault with approximately 50 m displacement (Figs. 9 and 10) which is coupled with an ENE reverse fault with a small displacement (Figs. 9 and 10). Near to the WNW fault, four dikes with a similar orientation are observed on the caldera wall (Figs. 9a and 10). Karaoğlu et al. (2005) and Özdemir et al. (2006) reported that these dikes are post-caldera formations; we find, on the contrary, that these dikes were formed in the pre-caldera phase.

Intra-caldera hydrothermal activity seems to be mainly controlled by the internal structure of the caldera. Faults and the structural boundaries of the caldera floor seem to be the main pathways for the circulation of hydrothermal fluids. Positive SP and Ce anomalies mainly appear on these structures (Fig. 9b: SP: red and Ce: blue points). Thermal anomalies detected on the night-thermal image reinforce that these zones are hydrothermally active and have been active as visualized by the hydrothermal alteration image defining clay mineralizations. The highest positive SP anomaly appears around the Hot Lake, at the northern edge of the fault limiting the blocks "P_1" and "P_2". The structural boundary separating blocks P_1 and P_2 meets the caldera boundary at its northern end and this intersection is situated at the topographic low within the caldera. This is why the hot springs occur in this location. Other positive SP anomalies along this boundary appear on the post-caldera maars as well. Most of the post-caldera activity is hosted by this boundary. Although there is no topographic difference between blocks P_1 and P_2, on the surface, these blocks are facing the opposite directions (Figs. 4d and 9b). If there were, topographic differences between these two blocks are further reduced since they are both now covered with post-caldera units. Possible scenario for this boundary is that it may simply be a post-caldera fault detaching one block.

Within the spectrum of new data, the structural elements of the Nemrut caldera were calculated as: topographic diameter: 8.5×7 km; structural diameter: 6.7×5.3 km; topographic area: 46.7 km^2; structural area: 27.9 km^2; maximum collapse on the eastern part: 600 m; maximum collapse from the bottom of the lake: 650 m; structural

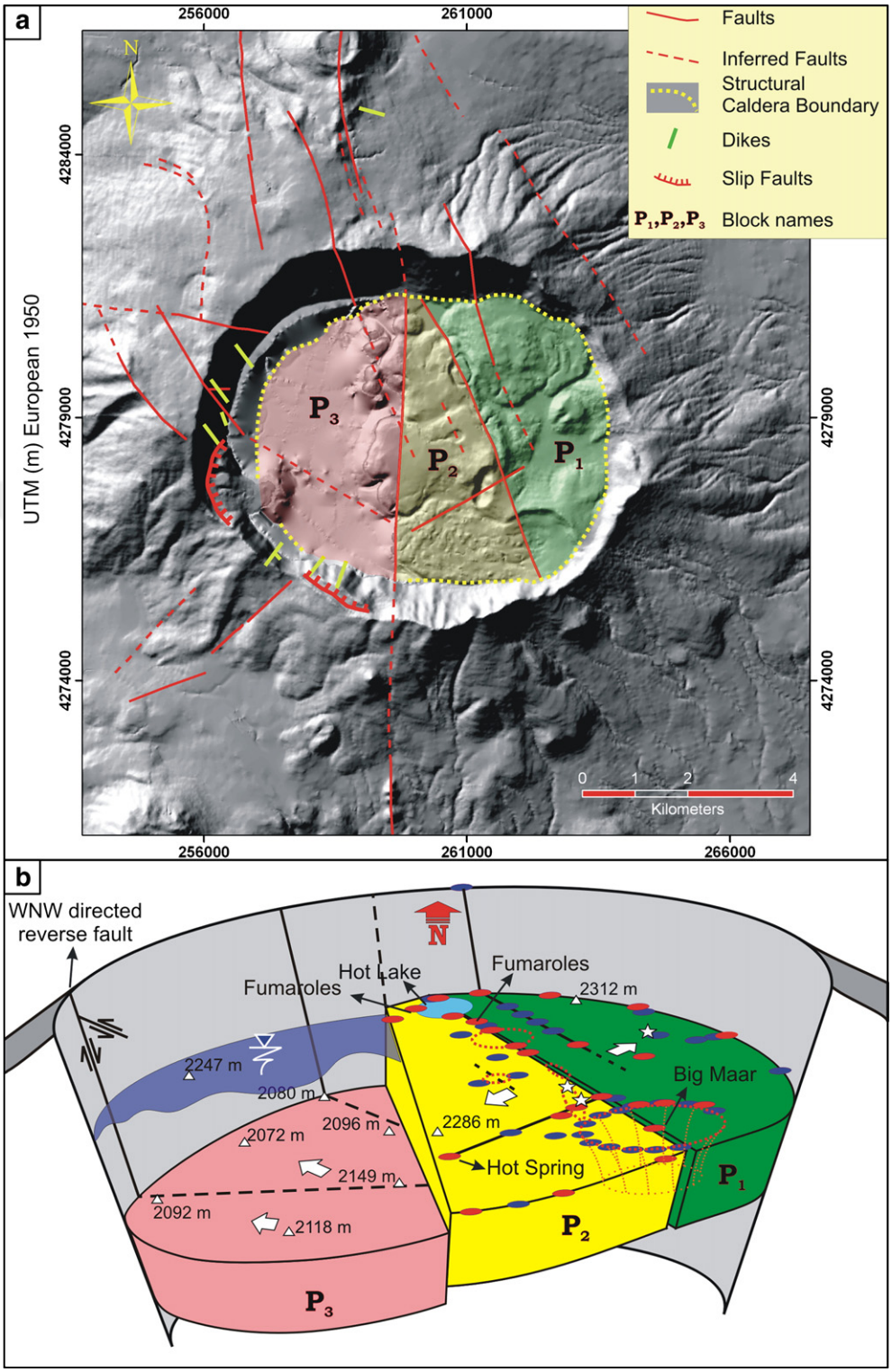

Fig. 9. Structure of Nemrut caldera. (a) Structural map of Nemrut caldera and the blocks responsible for the piecemeal collapse of the caldera. (b) Simplified structural model of the Nemrut caldera. The faults, hydrothermal spots and collapsed blocks are indicated. White stars: observed hydrothermal alterations; white arrows: general slope direction of the block; white triangles: altitude points; dashed red circles: maars; red points: positive PS anomalies; blue points: positive Ce anomalies; black lines: known and observed faults; dashed black lines: inferred faults; "P_1, P_2, P_3": caldera blocks. To simplify the visualization, caldera fill is discarded; note that there are approximately 280 m of caldera infilling products according to drill logs of Atasoy et al. (1988).

volume: 18.14 km^3; topographic volume: 32.9 km^3; northern collar angle (on land): 29.2°, western collar angle (from lake bottom): 27.9°. The lower collar angle value computed from the bottom of the lake reflects a higher collar slide mechanism due to the existence of Nemrut Lake.

6. Discussion

A Plio-Quaternary-aged compressional–extensional tectonic regime, caused by the N–S collision between the Eurasian and Arabian plates, generated N–S and NNW trending fissures on the Plio-

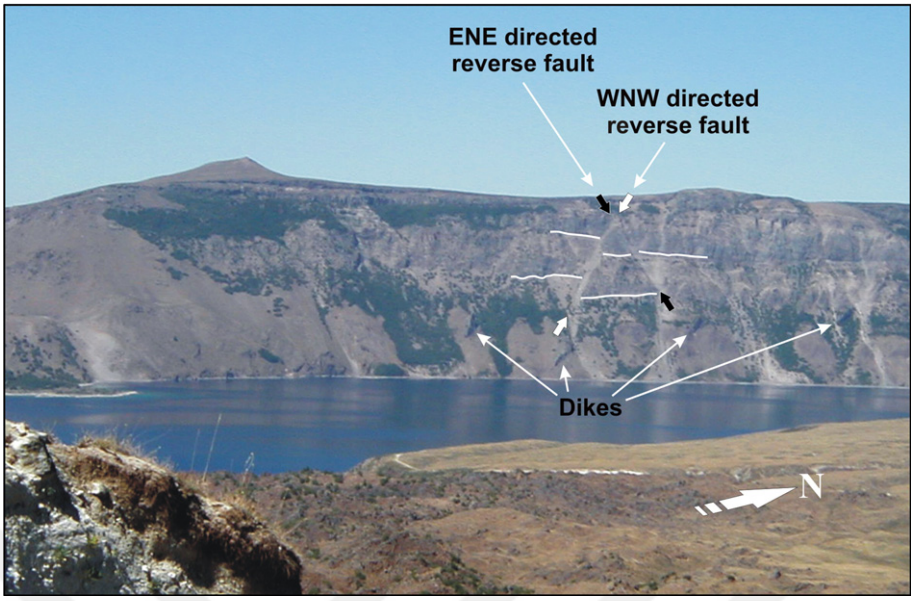

Fig. 10. Two visible structural features in the caldera: WNW trending reverse fault (white arrows) observed on the western caldera wall with ~50 m displacement and the ENE trending reverse fault (black arrows) coupling it. Pre-caldera dikes parallel and sub-parallel to the WNW trending fault are shown.

Quaternary-aged Eastern Anatolian volcanoes (Bozkurt, 2001; Koçyiğit et al., 2001). Around the summit zone of Tendürek, Ağrı, Nemrut, Bilican and Çatak volcanoes, clear examples of these fissures can be observed. On the Eastern Anatolian plateau, Koçyiğit et al. (2001) indicate that NW–SE trending dextral strike-slip faults parallel the North Anatolian Transform Fault Zone (NATFZ) with the same sense of motion. Together with the NE–SW trending sinistral faults, NW–SE trending strike-slip faults constitute the two important structural systems in the area.

Observed N–S and NNW dominant directions of the faults and structural boundaries indicate the effect of regional tectonic stress on the structural context of the Nemrut caldera. The continuation of these structural elements both in and out of the Nemrut caldera denotes that the regional tectonic stress played an important role on the structural evolution of the volcano. In addition, they are responsible for most of the post-caldera activity both in the caldera and at the northern fissure zone. These faults control the major hydrothermal activity. Regional and local structures have a profound effect on the morphology of calderas (Cole et al., 2005). Pre-existing structures can break up the caldera floor into a number of blocks that can collapse independently of one another, depending on the withdrawal dynamics and depth of the underlying magma chamber (Branney and Kokelaar, 1994; Cole et al., 2005).

In comparison with the eastern flanks, the altitude difference between the caldera rim and the basal plateau of the edifice on the western side is huge. The altitude difference is 1350 m on the western side, compared to only 800 m on the eastern side of the volcano (over a 10 km radius). Nemrut Lake, with a volume of 12[illegible] km^3, is located in the western half of the caldera. Nemrut volcano is situated on a highly active tectonic zone: high magnitude seismic events have been reported (29.03.1907, M: 5; 27.01.1913, M: 5; 14.02.1915, M: 6; 03.11.1997, M: 5; 30.05.1881 (data from Boğaziçi University, Kandilli Observatory and Earthquake Research Institute, National center of earthquake monitoring); 18.05.1881, M: 6.7 (Karakhanian et al., 2002)) within a 30 km radius of the volcano during the last century. There are previous examples of block slides on the caldera wall at the southwestern part: sudden release of water out of the caldera could be catastrophic, especially for the town of Güroymak to the west.

7. Conclusions

Hydrothermal fluid circulations on the Nemrut caldera and the structure of the caldera have been investigated using a self-potential survey, bathymetry data, derivatives of DEMs, Landsat and ASTER images. Nemrut caldera collapsed in a piecemeal manner and was composed of three main blocks. Boundaries delimiting these blocks and the main structural caldera boundary seem to control the hydrothermal activity in the caldera.

Negative SP–altitude relationships were observed on the profiles outside the caldera. A Ce gradient map was utilized for the interpretation of SP anomalies within the caldera. SP maps are useful tools for the analysis of hydrothermal fluid circulations on volcanoes. Moreover, Ce derivatives of SP maps have a potential to improve our knowledge about the structure of volcanoes.

This new structural model of the Nemrut caldera gives us some important clues about the nature of its structure and hydrothermal fluid circulations in the caldera. Active tectonic regimes, historical eruptions, occurrence of mantle-derived magmatic gases, fumarolic and hydrothermal activities on the volcano make Nemrut volcano a real danger for its vicinity (Aydar et al., 2003). “Merciless, cruel, and sulky”, from which the name Nemrut derives, outlines the danger of the volcano. It is obvious that the post-caldera activity of the volcano is mainly controlled by the minor and major structural context of the region; the caldera is still hydrothermally active. Knowing that the most recent intra-caldera events correspond to maar eruptions, the current hydrogeologic state of the caldera may give rise to violent phreatomagmatic eruptions in the future.

Acknowledgements

This work benefited from a research grant of Hacettepe University Scientific Research Foundation (Project No.: 01 01 602 021). It was also financially supported by UMR-CNRS 6524 and benefited from 3 integrated PhD grants from the French Ministry of Foreign Affairs. French embassy in Turkey supported several scientific expert missions. We would like to thank the Governor Generalship and General Command of Gendarmerie of Bitlis City, Tatvan, Güroymak and Ahlat villages. We also thank Jean-François Lénat for allowing us

to use his code to generate Ce map, and Türker Kurttaş and Levent Tezcan for providing the Bathymetry data of the Nemrut Lake.

References

Atasoy, E., Terzioğlu, N., Mumcuoğlu, H.Ç., 1988. Nemrut volkanı jeolojisi ve jeotermal olanakları. T.P.A.O. Research Group Report, p. 109.

Aubert, M., Dana, I., 1994. Interpretation of the self-potential radial profiles in volcanology: possibilities of the SP method for the monitoring of the active volcanoes. Bull. Soc. Geol. Fr 2, 113122.

Aubert, M., Yene Atangana, Q., 1996. Self-potential method in hydrogeological exploration of volcanic areas. Ground Water 34 (6), 1010–1016.

Aubert, M., Dana, I.N., Livet, M., 1990. Vérification de limites de nappes aquifères en terrain volcanique par la méthode de polarisation spontanée. C. R. Acad. Sci. 311 (II), 999–1004.

Aydar, E., Gourgaud, A., Ulusoy, I., Digonnet, F., Labazuy, P., Sen, E., Bayhan, H., Kurttas, T., Tolluoglu, A.U., 2003. Morphological analysis of active Mount Nemrut stratovolcano, eastern Turkey: evidences and possible impact areas of future eruptions. J. Volcanol. Geotherm. Res. 123, 301–312.

Barka, A.A., 1992. The North Anatolian Fault zone. Ann. Tecton. 6, 164–195.

Branney, M.J., Kokelaar, P., 1994. Volcanotectonic faulting, soft-state deformation, and rheomorphism of tuffs during development of a piecemeal caldera, English Lake District. Geol. Soc. Amer. Bull. 106, 507–530.

Bozkurt, E., 2001. Neotectonics of Turkey — a synthesis. Geodin. Acta 14 (1–3), 3–30.

Cole, J.W., Milner, D.M., Spinks, K.D., 2005. Calderas and caldera structures: a review. Earth Sci. Rev. 69, 1–26.

Corwin, R.F., Hoover, D.B., 1979. The self-potential method in geothermal exploration. Geophysics 44, 226–245.

Çilingiroğlu, A.E., 1997. Urartu Tarihi ve Sanatı. Ege Univ. Publications, İzmir, pp. 21–47.

Çilingiroğlu, A.E., Salvini, M. (Eds.), 2001. Ayanis I: Ten Years' Excavations at Rusahinili Eiduru-kai. CNR Istituto per gli Studi Micenei ed Egeo-Anatolici, Rome, pp. 1989–1998. ISBN 88-87345-04X.

Çubukçu, E., Aydar, E. and Gourgaud, A., 2007. Comment on "Volcanostratigraphy and petrogenesis of the Nemrut stratovolcano (East Anatolian High Plateau): The most recent post-collisional volcanism in Turkey" by Ozdemir et al., 226, 189–211, Chemical Geology.

Ercan, T., Fujitani, T., Matsuda, J.I., Notsu, K., Tokel, S., Ui, T., 1990. Dogu ve Guneydogu Anadolu Neojen-Kuvaterner volkaniklerine iliskin yeni jeokimyasal, radyometrik ve izotopik verilerin yorumu. MTA Dergisi 110, 143–164.

Ercan, T., Matsuda, J.I., Nagao, K., Kita, I., 1995. Noble gas isotopic compositions in gas and water samples from Anatolia. In: Erler, A., Ercan, T., Bingöl, E., Örçen, S. (Eds.), Geology of the Black Sea Region: Proc. Int. Symp. on the Geology of the Black Sea Region, Ankara, Turkey. General Directorate of Mineral Research and Exploration and the Chambers of Geological Engineers of Turkey, Ankara, pp. 197–206.

Finizola, A., Sortino, F., Lénat, J.-F., Valenza, M., 2002. Fluid circulation at Stromboli volcano, (Aeolian Islands, Italy) from self-potential and soil gas surveys. J. Volcanol. Geotherm. Res. 116 (1–2), 1–18.

Finizola, A., Lénat, J.F., Macedo, O., Ramos, D., Thouret, J.C., Sortino, F., 2004. Fluid circulation and structural discontinuities at Misti volcano (Peru) inferred from self-potential and CO2 measurements. J. Volcanol. Geotherm. Res. 135 (4), 343–360.

Finizola, A., Revil, A., Rizzo, E., Piscitelli, S., Ricci, T., Morin, J., Angeletti, B., Mocochain, L., Sortino, F., 2006. Hydrogeological insights at Stromboli volcano (Italy) from geoelectrical, temperature, and CO_2 soil degassing investigations. Geophys. Res. Lett. 33, L17304.

Güleç, N., Hilton, D.R., Mutlu, H., 2002. Helium isotope variations in Turkey: relationship to tectonics, volcanism and recent seismic activities. Chem. Geol. 187, 129–142.

Güner, Y., 1984. Doğu Anadolu Kuvaterner volkanizması (Nemrut Yanardağı), MTA Genel Müdürlüğü, Temel Araştırmalar Dairesi, Ankara, p. 77.

Hernandez-Baquero, E., 2000. Characterization of the earths surface and atmosphere from multispectral and hyperspectral thermal imagery. Ph.D. Dissertation. Rochester Institute of Technology, Chester F. Carlsom Center for Imaging Science, Rochester, NY, USA.

Hook, S.J., Gabell, A.R., Green, A.A., Kealy, P.S., 1992. A comparison of techniques for extracting emissivity information from thermal infrared data for geologic studies. Remote Sens. Environ. 42, 123–135.

Jackson, D.B., Kauahikaua, J., 1987. Regional self-potential anomalies at Kilauea volcano. Volcanism in Hawaii. USGS Professional paper, vol. 1350, pp. 947–959. Chap. 40.

Johnson, B.R., Young, S.J., 1998. In-scene atmospheric compensation: application to SEBASS data collected at the ARM site. Technical Report, Space and Environment Technology Center, The Aerospace Corporation.

Karakhanian, A., Djrbashian, R., Trifonov, V., Philip, H., Arakelian, S., Avagian, A., 2002. Holocene-historical volcanism and active faults as natural risk factors for Armenia and adjacent countries. J. Volcanol. Geotherm. Res. 113, 319–344.

Karaoğlu, Ö., Özdemir, Y., Tolluoğlu, A.Ü., Karabıyıkoğlu, M., Köse, O., Froger, J.L., 2005. Stratigraphy of the volcanic products around Nemrut Caldera: implications for reconstruction of the Caldera Formation. Turk. J. Earth Sci. 14, 123–143.

Kealy, P.S., Hook, S.J., 1993. Separating temperature and emissivity in thermal infrared multispectral scanner data: implications for recovering land surface temperatures. IEEE Trans. Geosci. Remote Sens. 31 (6), 1155–1164.

Kipfer, R., Aeschbach-Hertig, W., Baur, H., Hofer, M., Imboden, D.M., Signer, P., 1994. Injection of mantle-type helium into Lake Van (Turkey): the clue for quantifying deep water renewal. Earth Planet. Sci. Lett. 125, 357–370.

Koçyiğit, A., Yılmaz, A., Adamiac, S., Kuloshvili, S., 2001. Neotectonics of East Anatolian Plateau (Turkey) and Lesser Caucasus: implication for transition from thrusting to strike-slip faulting. Geodin. Acta 14, 177–195.

Landmann, G., 1996. Van See/Turkei: Sedimentologie, Warvenchronologie und regionale Klimageschichte seit dem Spätpleistozän. PhD-Thesis, Fac. Geosci. Univ. Hamburg, Germany, 123 pp.

Landmann, Kempe, 2005. Annual deposition signal versus lake dynamics: microprobe analysis of Lake Van (Turkey) sediments reveals missing varves in the period 11.2–10.2 ka BP. Facies 51, 135–145.

Landmann, G., Reimer, A., Lemcke, G., Kempe, S., 1996. Dating Late Glacial abrupt climate changes in the 14570 yr long continuous varve record of Lake Van, Turkey. Paleogeo. Paleoclimatol. Paleoecol. 122, 107–118.

Lénat, J.F., 1987. Structure and dynamique interne d'un volcan basaltique intraplaque océanique : Le Piton de la Fournaise (île de la Réunion). Thèse de doctorat, Univ. Blaise Pascal, Clermont-Ferrand (France).

Lénat, J.F., 2007. Retrieving self-potential anomalies in a complex volcanic environment: an SP/elevation gradient approach. Near Surf. Geophys. 5, 161–172.

Lénat, J.F., Robineau, B., Durand, S., Bachélery, P., 1998. Etude de la zone sommitale du volcan Karthala (Grande Comore) par polarisation spontanée. C. R. Acad. Sci. 327, 781–788.

Moore, I.D., Lewis, A., Gallant, J.C., 1993. In: Jakeman, A.J., et al. (Ed.), Terrain Properties: Estimation Methods and Scale Effects, Modeling Change in Environmental Systems. John Wiley and Sons, New York.

Nagao, K., Matsuda, J.I., Kita, I., Ercan, T., 1989. Noble gas and carbon isotopic composition in Quaternary volcanic area in Turkey. Jeomorfol. Derg. 17, 101–110.

Notsu, K., Fujitani, T., Ui, T., Matsuda, J., Ercan, T., 1995. Geochemichal features of collision-related volcanic rocks in central and Eastern Anatolia, Turkey. J. Volcanol. Geotherm. Res. 64, 171–192.

Özdemir, Y., Karaoğlu, Ö., Tolluoğlu, A.Ü., Güleç, N., 2006. Volcanostratigraphy and petrogenesis of the Nemrut stratovolcano (East Anatolian High Plateau): the most recent post-collisional volcanism in Turkey. Chem. Geol. 226 (3–4), 189–211.

Pearce, J.A., Bender, J.F., De Long, S.E., Kidd, W.S.F., Low, P.J., Güner, Y., Saroglu, F., Yilmaz, Y., Moorbath, S., Mitchell, J.G., 1990. Genesis of collision volcanism in Eastern Anatolia, Turkey. J. Volcanol. Geotherm. Res. 44 (1–2), 189–229.

Revil, A., Pezard, P.A., Glover, P.W.J., 1999a. Streaming potential in porous media: 1. Theory of the zeta potential. J. Geophys. Res. 104, 20021–20031.

Revil, A., Schwaeger, H., Cathles, L.M., Manhardt, P.D., 1999b. Streaming potential in porous media: 2. Theory and application to geothermal systems. J. Geophys. Res. 104, 20033–20048.

Revil, A., Finizola, A., Sortino, F., Ripepe, M., 2004. Geophysical investigations at Stromboli volcano, Italy: implications for the ground water flow and paroxysmal activity. Geophys. J. Int. 157 (1), 426–440.

Sabins, F.F., 1997. Remote Sensing: Principles and Interpretation, 3rd ed. 0-7167-2442-1. 494 pp.

Sabins, F.F., 1999. Remote sensing for mineral exploration. Ore Geol. Rev 14, 157–183.

Şengör, A.M.C., Görür, N., Şaroğlu, F., 1985. Strike-slip faulting and related basin formation in zones of tectonic escape: Turkey as a case study. In Strike-slip Faulting and Basin Formation. Soc. Econ. Paleontol. Mineral. Sp. Pub., 37, pp. 227–264.

Şerefhan, 1597. Şerefname: Kürt tarihi (translated from Arabic to Turkish by M. Emin Bozarslan), 4th ed. (1990). Hasat yayınları. 544 pp.

Ulusoy, I., Labazuy, P., Aydar, E., Ersoy, O., Cubukcu, E., Bayhan, H., Gourgaud, A., Tezcan, L., Kurttas, T., 2006. Pioneer Seismic Network installed on an Anatolian volcano: Mount Nemrut (Eastern Turkey). Fourth Conference of Cities on Volcanoes, Abstracts Volume, p. 113.

Ulusoy, İ., Labazuy, P., Aydar, E., submitted for publication. STcorr: An IDL code for the image based retrieval of altitude and aspect effects on night time TIR imagery. Computers and Geosciences.

Yılmaz, Y., Güner, Y., Şaroğlu, F., 1998. Geology of the quaternary volcanic centers of the east Anatolia. J. Volcanol. Geotherm. Res. 85, 173–210.

Zlotnicki, J., Nishida, Y., 2003. Review on morphological insights of self-potential anomalies on volcanoes. Surv. Geophys. 24, 291–338.

Zlotnicki, J., Boubon, G., Viodé, J.P., Delarue, J.F., Mille, A., Bruére, F., 1998. Hydrothermal circulation beneath Mount Pelée inferred by self potential surveying. Structural and tectonic implications. J. Volcanol. Geotherm. Res. 84, 73–91.

Chapter 04

Seismic monitoring of Nemrut Volcano

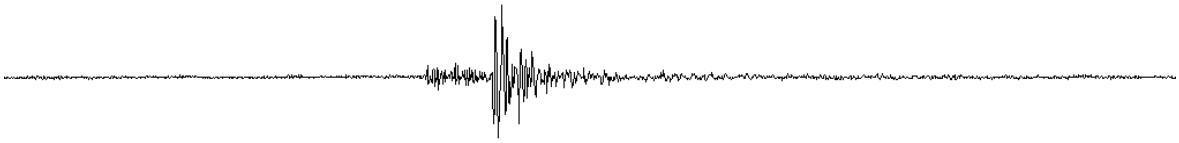

4. Introduction

Eastern Anatolia is an intensively seismic area due to the contractional-extensional tectonic events. Literature data show that the volcano witnessed dense volcanic activity since ~1 Ma; most of the volcanics are younger than 500 ka (Aydar et al, 2003). Recently, ongoing studies on the Eastern Anatolia lead us to expand our knowledge on the historical eruptions of Mt. Nemrut (Table 2.1). Latest volcanic activities of the volcano occurred in 1441 (Lava flows, Karakhanian et al., 2002), before 1597 (Lava fountains and flows, Şerefhan, 1597; Aydar et al., 2003) and 13 April 1692 (Eruption of gas and ash, Karakhanian et al., 2002). Beside the historical records, the volcano still have some hydrothermal and fumerol activities (Ulusoy et al., 2008).

Güleç et al. (2002) showed that the Helium isotope ratio ($^3He/^4He$) values of water and gas samples of Nemrut caldera have the highest mantle derived Helium contribution in Anatolia. Besides, water samples collected from different levels of the greater caldera lake indicate an increase in mantle derived Helium contribution from top to the bottom in the lake (Kipfer et al., 1994).

Reanalyzing the data of Kipfer at al. (1994), Songsheng and Ming (2008) mentioned a large amount of ^3He and ^4He release at the bottom of Lake Nemrut, associated with heat flow injection. $^3He_{ex}$ (excess tritium) and $^4He_{ex}$ are linearly related and indicate the injection of MORB-like mantle helium with an isotopic $^3He/^4He$ ratio of $1.032x10^{-5}$ (Songsheng and Ming, 2008). The excess ^3He at the bottom of Lake Nemrut is 100 times higher than at Lake Van (Songsheng and Ming, 2008). The ^3He flux into Lake Nemrut is estimated to be $1x10^{-16}$ $mol.m^{-2}.s^{-1}$, much higher than that into LakeVan $(3 – 5)x10^{-18}$ $mol.m^{-2}.s^{-1}$ (Kipfer et al., 1994). The global mantle ^3He flux deduced from ^3He flux in MOR fluids was estimated to be $7x10^{-20}$ $mol.m^{-2}.s^{-1}$ (c.f. Craig. et al., 1975). Thus, the ^3He flux in Lake Nemrut is 3 orders of magnitude higher than the global value.

These consequential clues lead us to strictly consider about the possibility of a future eruption of the Nemrut volcano which is situated in a very active tectonic frame. Inhabitants of Bitlis city, Tatvan, Güroymak and Ahlat towns (Table 1.2) could be affected by future eruptions of this volcano; and the potential risk is undefined. There are many examples that volcanoes have created great catastrophes (eg. Mt. Pelée,1902; Nevado del Ruiz, 1985; Mt. Pinatubo, 1991),

even after long periods of silence. Hence, as a beginning, to monitor the volcano three seismometers were installed around the Nemrut volcano. The monitoring network was established, and data are being collected since October 2003. This is the first volcano-seismic observation network built around a Turkish volcano. On the basis of the recorded seismic data, our scope is to share and discuss the preliminary results in this chapter.

4.1. Seismic Network

A small seismic network containing three seismometers installed around the volcano approximately on a circle of 20 km radius (Fig. 4.1). The stations are established in the Gendarmerie headquarters of the Tatvan, Güroymak and Ahlat towns. The network is equipped with a broadband (0.033Hz-50Hz, in Tatvan) and two short-period (1Hz-80Hz, in Güroymak and Ahlat), 3-component Güralp seismometers. Data are digitized with 24 bit, 3-channeled digitizers and transferred to the acquisition systems (PC computers). Collected data are transferred to our laboratory in real-time by a frame-relay data communication link of Turkish Telecom. Data are being recorded in our laboratory (in Ankara) since October 2003.

Seismic stations are configured with seismic monitoring equipment reinforced by power and data regulatory devices (Fig. 4.1). Seismometers are connected to a GPS device for real-time data acquisition. Collected data are transferred to local computers that manage each station. Computers are connected to a frame-relay modem via router devices (Fig. 4.1). Routers are assigning unique IP (internet protocol) addresses to each computer. For teleprocessing, a special data link called “frame-relay” is used. The capacity and the speed of the link are limited with the infrastructure of the local telecommunication network (8 kbps) of Bitlis city. In frame-relay teleprocessing system, data are flowing throughout two endpoints. Between those endpoints the data flow channel is variable and can not be predefined; the frame-relay network handles the transmission over a frequently-changing path transparent to all end-users. This data flow process is called as “frame-relay cloud” (Fig. 4.1).

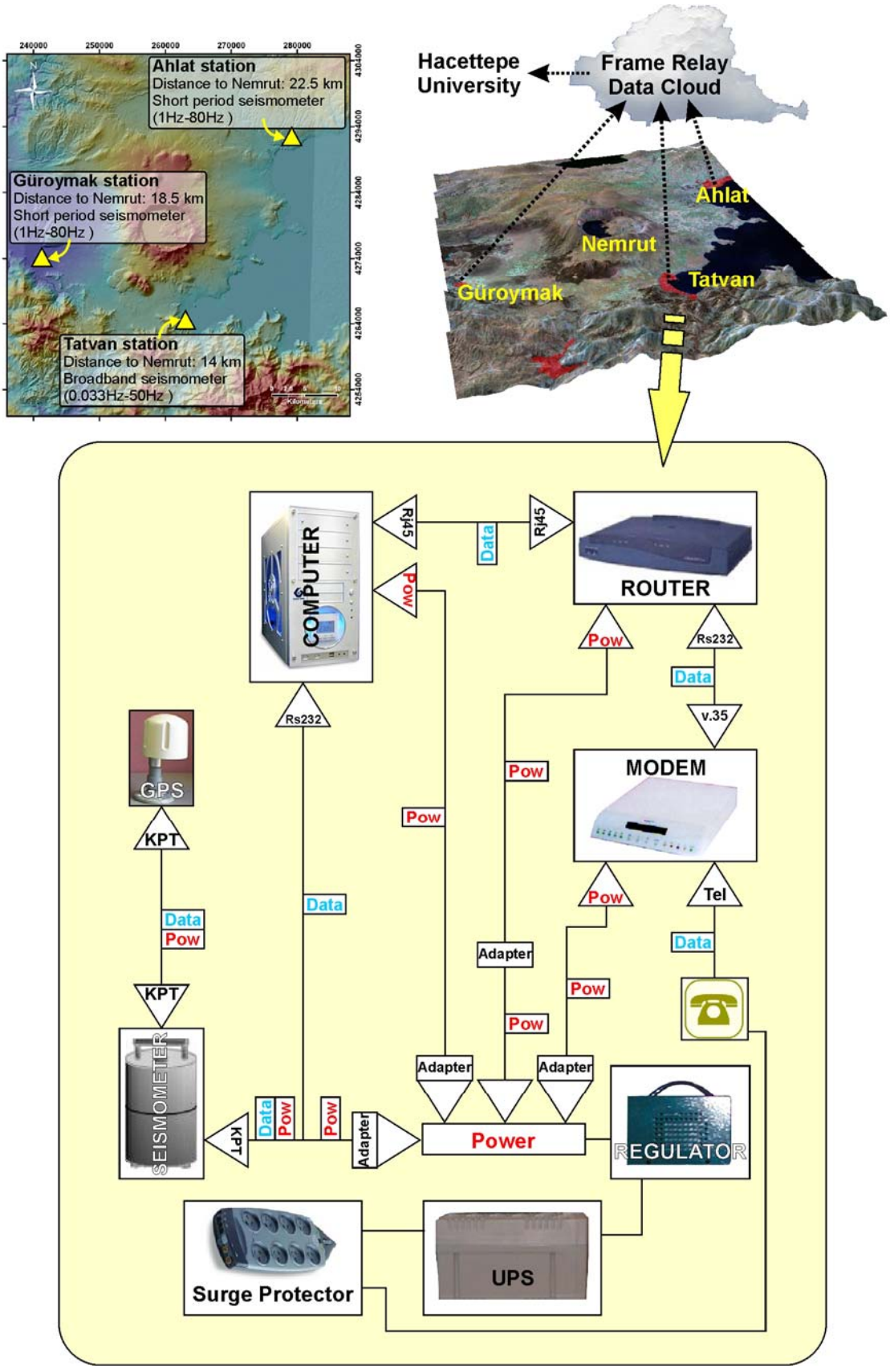

Figure 4.1. Teleprocessing, configuration and location of the seismic stations.

The frame-relay line is ended in a computer running in our laboratory at Hacettepe University (Ankara). Computers are designed for auto-run, the hardware and software are reinitializing in case of a power-cut. “SCREAM!” software of Güralp systems which is pushing (and pulling for the Hacettepe University side) data runs on all of the computers. Operating systems of the computers are configured for remote controlling, though in case of a problem, it is possible to manage the system from Hacettepe University. It is also possible to control and change the configuration of the digitizers remotely via “SCREAM!” software.

Power system of the stations is reinforced with a regulator, an UPS (Uninterruptible power supply) and a surge protector. Surge protector and an additional circuit are also protecting the telephone line (connected to the modem) for any overcharging event (Due to a lightning stroke on the telephone line, away from the seismic stations, one of our frame-relay modem was demaged).

4.1.1. Limitations, problems faced and efficiency of the network

Nemrut seismic monitoring network is active since October 2003. Although the stations are equipped with proper devices, we faced with various limitations that affected the quality of the data and problems that interrupted the data flow from three stations. Accordingly, it is essential to discuss these problems and the efficiency of the monitoring network.

Number of seismometers and their distance from the volcano

The small monitoring network consists of three seismic stations. Beyond debate, the number of the stations is the first limitation for the network. Any interruption of data flow from one of the seismometers because of any type of device malfunction, unsurprisingly disallowed the hypocenter solution. The nearest station of the National Earthquake Monitoring Center (Boğaziçi University, Kandilli Observatory and Earthquake Research Institute) is situated at Varto, 90 km away from the Nemrut volcano equipped with a vertical component short period seismometer. Moreover, Kandilli Observatory publishes event based waveform data for magnitudes >3.5.

Safety and security conditions in the region constrained us to install the stations in the Gendarmerie Headquarters, situated in the town centres; as a result, record of noise due to daily human activity was ineluctable. Additionally, stations were

installed relatively away from the volcano (14 km for Tatvan, 18.5 km for Güroymak and 22.5 km for Ahlat) resulting to lose some aftershocks in the noise.

Electricity

City mains are another constraining feature to stabilize the continuous data flow. Although stations are equipped with UPS devices, long-term electrical cuts or voltage drops passes beyond the capability of the stations. Time to time, especially in Güroymak town drop of voltage does not allow even efficient run of basic electronic devices, moreover, cause harm to the devices. Our configuration managed to overcome the damage caused by the electrical circuit however lost of data due to long-term cuts were unavoidable.

Teleprocessing

At the time of installation of the seismic stations (summer 2003) teleprocessing capability of telecommunication infrastructure of Bitlis city was limited. Cost of conventional networking tools were very high and were not efficient for data transfer. For example, ADSL (Asymmetric Digital Subscriber Line) system was not available in the Bitlis city, and to send data through an internet line was requiring a server system in the city. Only possible data communication system was Frame-relay networking and the speed of this system was limited to 8 kbps in Bitlis. Although digitizers were capable of both recording in higher sample rates, speed limitation of Frame-ralay infrastructure only allowed the transfer of 50 sample per second (sps) data. Additionally, we were not able to use STA/LTA (Short term average / Long term average) filtering capability of the digitizers because the bandwidth available for data transfer was not large enough to acquire both continuous and triggered data.

Efficiency of the seismic network

Consequently, local conditions have highly affected the efficiency of the data flow. To check and update the efficiency status monthly, we wrote an Excel VBA (Visual Basic for applications) script. Script allows us to check the existence of hourly data for monthly periods and creates a worksheet. Created monthly worksheets were used to analyse the efficiency of the network (Fig. 4.2).

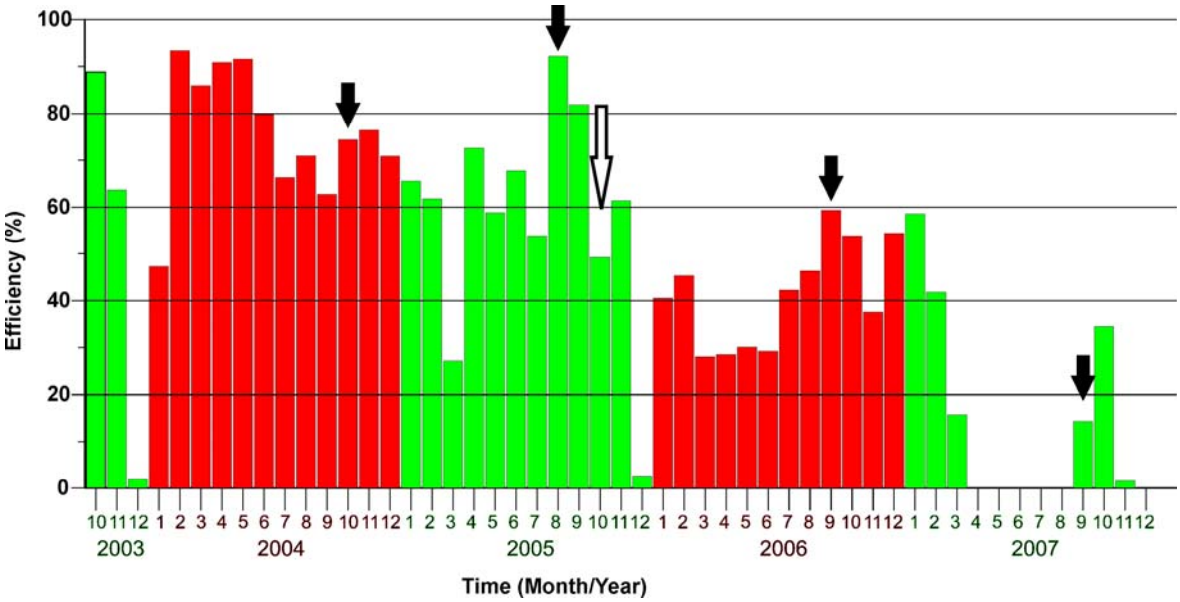

Figure 4.2. Monthly efficiency chart of the seismic network. Black arrows are pointing the yearly maintenance dates. White arrow is pointing the starting date of malfunction of Güroymak station initiated by a lightning strike.

Overall efficiency for the network for four years of data recording is 62%, 49% and 32% for Tatvan, Ahlat and Güroymak stations respectively. In September 2005, because of a lightning that stroke on the local telephone line, 3 km away from Güroymak station; frame-relay modem unit and the digitizer of the seismometer were damaged (Fig. 4.2). This event tragically ended the data flow from the Güroymak station and stopped the hypocenter solutions for the network. Consequently, analyses only performed before this date (between October 2003 and October 2005) will be presented here. Efficiency of the network between October 2003 and October 2005 is 77%, 62% and 67% for Tatvan, Ahlat and Güroymak stations respectively. Still, there is a loss of 23% - 38% of data in this period. These losses are mainly because of the infrastructure of the local telecommunication system. Note that the efficiency of Tatvan station is higher than other two stations. This is because the telecommunication system infrastructure in Tatvan town is better than the other towns (Ahlat and Güroymak).

Upgrades and Scheduled upgrades in the system

To overcome the lost of data because of the telecommunication system and to increase the efficiency of the network, precautions were necessary. The first of the cautions was to strengthen the stations with additional surge protectors. Second change was the replacement of the computers at the stations in September 2007. These new computers are equipped with hard disc drives with high storage

capacities. Now data are both recorded at the stations and send to Ankara. Third scheduled upgrade will be in the data transfer protocol. At the end of 2007, local telecom added ADSL (Asymmetric Digital Subscriber Line) data transfer protocol to Tatvan, Güroymak and Ahlat towns. Teleprocessing with frame-relay system will be ended and will be changed to ADSL system before the end of 2008. This change in teleprocessing will be a quantum leap for Nemrut monitoring network: (1) continuous data flow will be more stable, (2) recording of 100 SPS data will be possible and (3) the digitizer units of the seismometers will be controlled and their software will be updated daily by the manufacturer of the seismometers.

4.2 Data Processing

Three codes were written in LabView environment to analyse the data. The first code “Nemtrig” (Nemrut trigger) is used to trigger the possible events (Fig. 4.3). The code and its short user guide is presented in e-Appendix-4. The code uses a two-level STA/LTA (Short-term average/Long term average ratio) filter to trigger and save possible events. Here, using two-level term, we mean that there are two synchronous STA/LTA algorithms running backwards. The first is running as usual STA/LTA trigger algorithm (Trnkoczy, 2002) while the second one searches the small amplitude events in the background and/or noise. Second STA/LTA algorithm uses a low triggering threshold and triggers if all the seismometers pass the low threshold level. One of the simplest and most successful methods is to bandpass filtering of the data before applying the STA/LTA detector (Blandford, 1982; Ruud and Husebye, 1992). Nemtrig optionally allows the bandpass filtering before the STA/LTA triggering.

Nemtrig accepts data in GCF (Güralp compressed file) format analyses data, cuts and saves triggered data in SAC (Seismic analysis code) file format.

In process, raw data are band-pass filtered between 1-9 Hz, the STA value is set to 1 second and the LTA value is set to 30 seconds. STA/LTA threshold values for the first and the second triggering algorithms are set as 4 and 1.5 respectively. The triggered events are then analyzed and localization is then performed using another program: PickEv2000 (Frechet and Thouvenot, 1990; Thouvenot et al., 1990), the seismic analysis software of Grenoble seismic network.

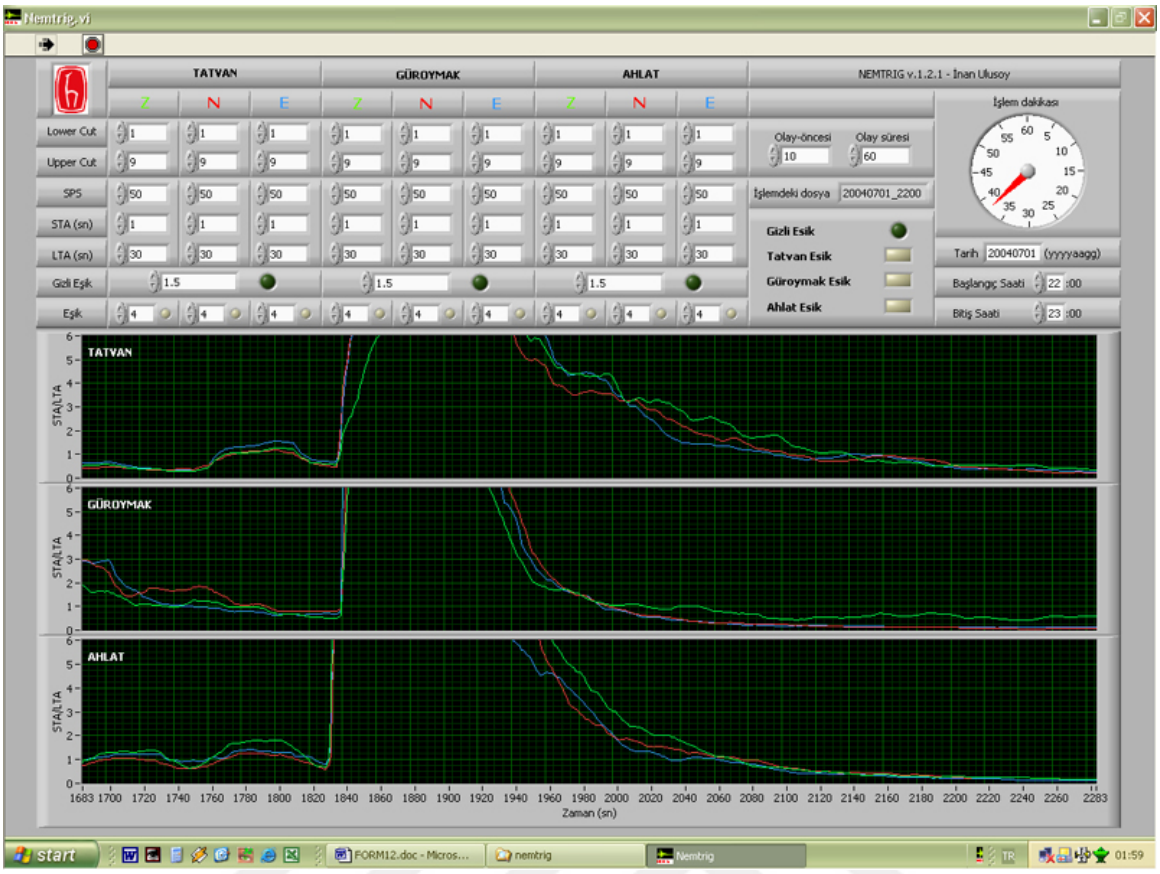

Figure 4.3. Screenshot of Nemtrig code in progress. In the signal charts STA/LTA signal flow for Tatvan, Güroymak and Ahlat stations are continuously visible during filtering process. Different colored lines are assigned to two horizontal and one vertical component channels of the seismometers.

The second code we wrote, “Nemtract” (Nemrut extract) is supporting “Nemtrig” and is used to cut data (Fig. 4.4). Depending on the magnitude or the relative location of the triggered event, the event is not always triggered by all the three seismometers. During STA/LTA triggering process, when a possible event is triggered only by one or two seismometers, we use Nemtract to cut the related data portion using “Nemtrig” for the missing (untriggered) station(s).

Our third code, “Nemspec” (Nemrut spectrogram), visualize the spectrogram of the event to determine the type of seismic event (Fig. 4.5).

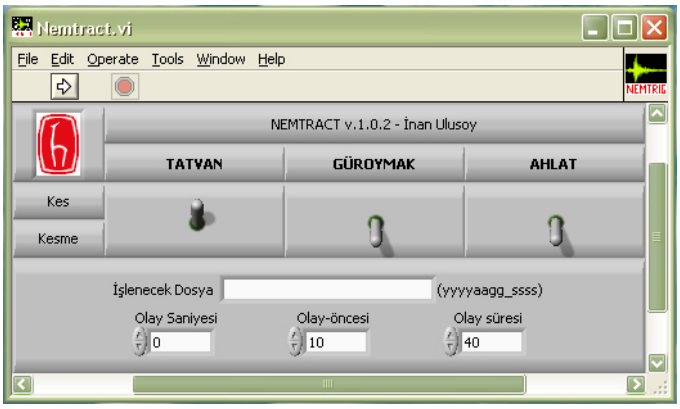

Figure 4.4. Screenshot of Nemtract. For the defined pre-set time, event time and duration, Nemtract cuts the desired dataset and saves the cut file in SAC file format.

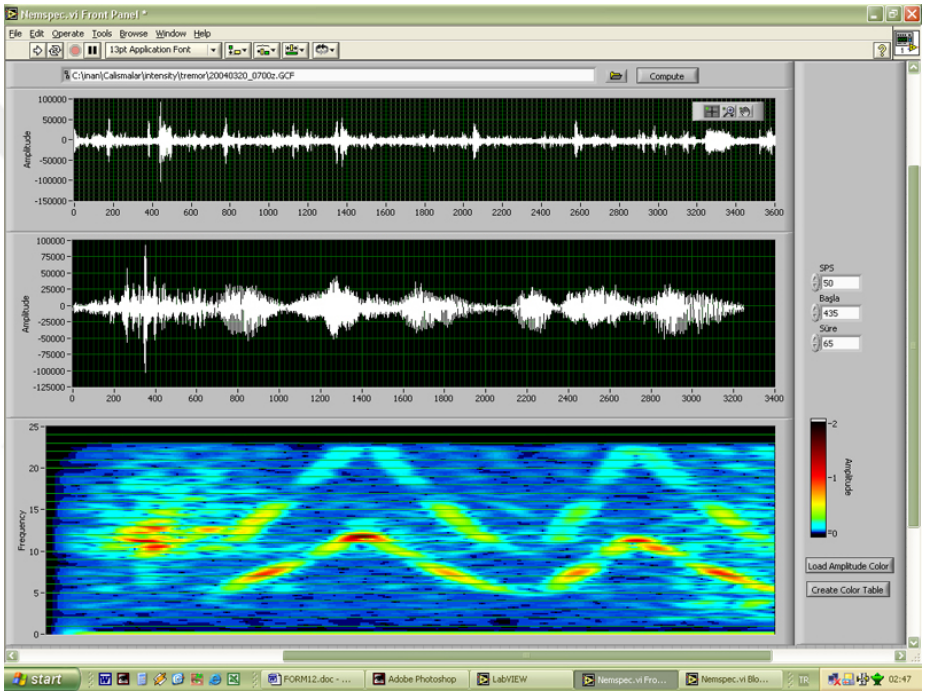

Figure 4.5. Screenshot of Nemspec code in progress. For a given portion of the seismic signal, Nemspec draws the spectrum of the signal in terms of time, frequency and amplitude.

4.3. Seismicity of the volcano

Previous seismic activity around the volcano is reported by Boğaziçi University, Kandilli Observatory and Earthquake Research Institute, National center of earthquake monitoring (Fig. 4.6). The seismic activity around the volcano is being observed since November 2003 by our network. This is the first seismic network for the purpose of volcano monitoring in Turkey.

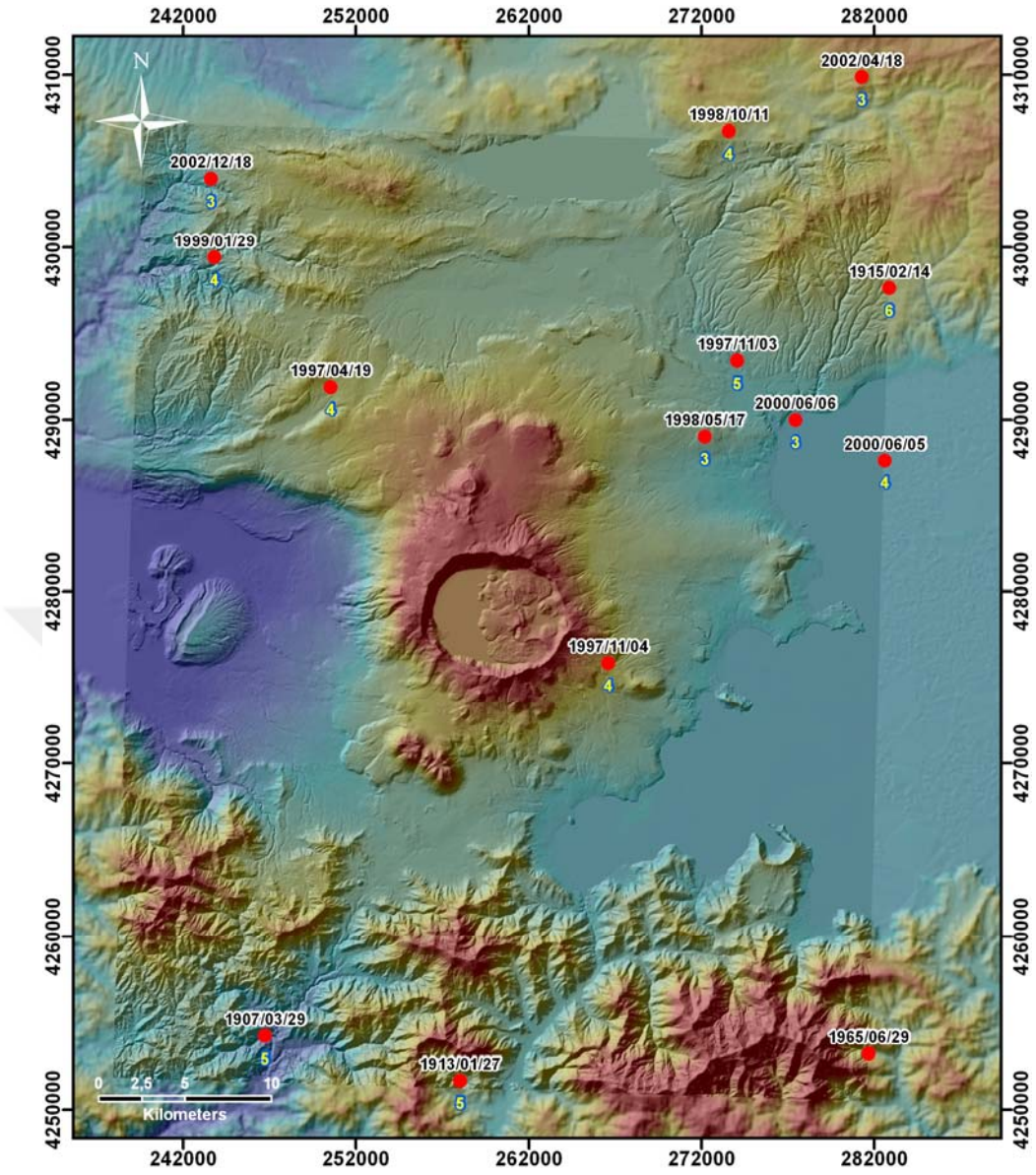

Figure 4.6. Seismic events (M>3) reported by Kandilli observatory and earthquake research institute in the last century (1900 - 2003). Magnitudes (under the point) and dates (over the point) of the events are indicated (Magnitude of the 1965 event is unknown). Projection: UTM, European Datum 1950.

Event types

Raw data are triggered by our code in near real-time. Following the hypocenter solutions of the seismic events, event types are determined by frequency and depth spectrum analyses. While classifying the events according to their spectral characteristics, we used the generally agreed features defined in the works of McNutt (1996a, 1996b, 2000), Chouet (1996) and Wassermann (2002). General characteristics of volcanic event types compiled from McNutt (2000) and Wassermann (2002) are presented in Table 4.1. Additionally, typical waveforms of volcanic earthquakes are shown in Figure 4.7.

Type		Depth	P - S waves	Frequency spectra	Frequency class	Sample	Remarks
Volcano-Tectonic events	VT-A	Deep ~>2 km	Clear P and S wave arrivals	>5 Hz 5-15 Hz	HF	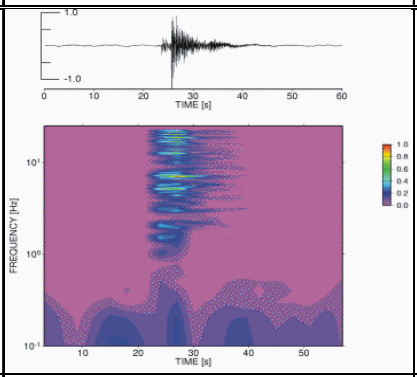	Most HF events are thought to be caused by shear failure or slip on faults.
	Low frequency - LP events	Shallow ~1-2 km	Clear P wave arrival, sometimes impossible to observe S wave arrival	1-5 Hz generally 2-3 Hz	LF	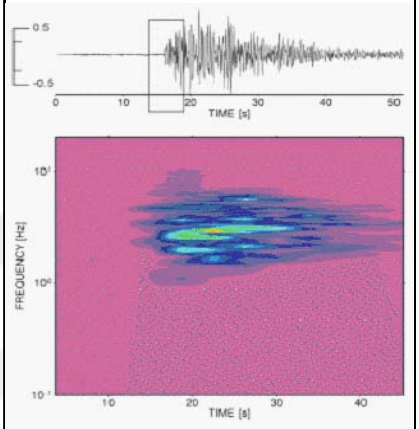	Most LF events are thought to be caused by fluid pressurization process such as bubble formation and collapse and also by shear failure, tensile failure, or nonlinear flow processes which occur at very shallow depths for which attenuation and path effects play an important role.
Hybrid events		Could share the attributes of both VT-A and VT-B type events and LF (ex. Tornillo) events.			LF	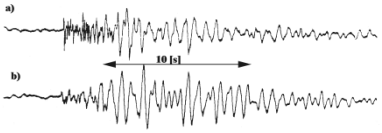 a) Hybrid, b) LF-LP events	A VT event that triggers LP event may cause such activity. An earthquake occuring adjacent to a fluid filled cavity that setting it into oscillation may be an example.

Table 4.1. Volcanic event types and their common attributes. HF: High-frequency, LF: Low-frequency.

Type	Depth	P - S waves	Frequency spectra	Frequency class	Sample	Remarks
Multi-Phase events	Could share the attributes of both VT-A and VT-B type events and LF (ex. Tornillo) events.		> than Hybrid events, 3-8 Hz	LF	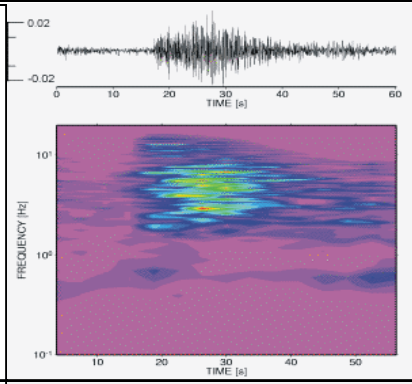	Frequency content of this type of event is higher than Hybrid events but are related as well to energetic dome growth at a very shallow level.
Long-Period or Long-Coda events (Tornillo)	Generally <2 km	Very emergent signal onset and no S wave arrivals	1-3 Hz	LF	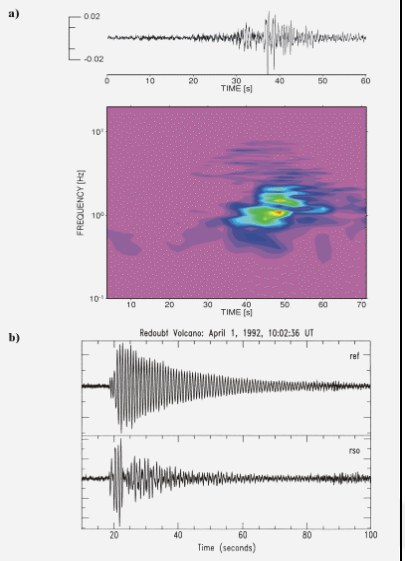	Locations are deduced mainly by amplitude distance curves, Hypocenter solutions could rarely be made by using broadband networks
Volcanic Tremor	Volcanic tremor is a continuous signal with a duration of minutes to days or longer. Tremor is a seies of LF events occuring at intervals of a few seconds.		1-5 Hz generally 2-3 Hz	LF	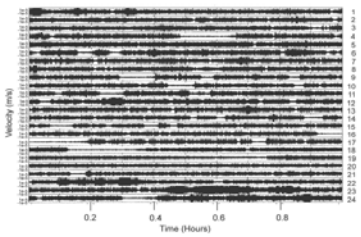	
Harmonic Tremor	Harmonic tremor is a LF, often single-frequency sine-wave with smoothly varying amplitude, or sometimes consists of a fundamental frequency with many overtones.			LF	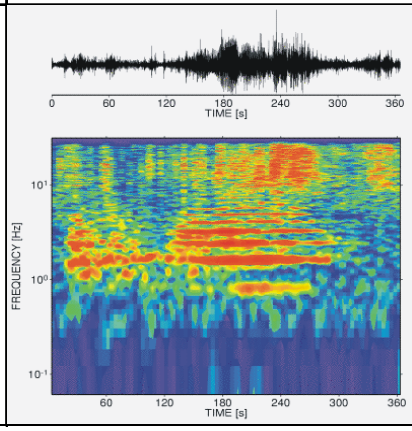	They are thought to be caused by the resonating bodies because of gases and inside the magma channels

Table 4.1.cont. Volcanic event types and their common attributes.

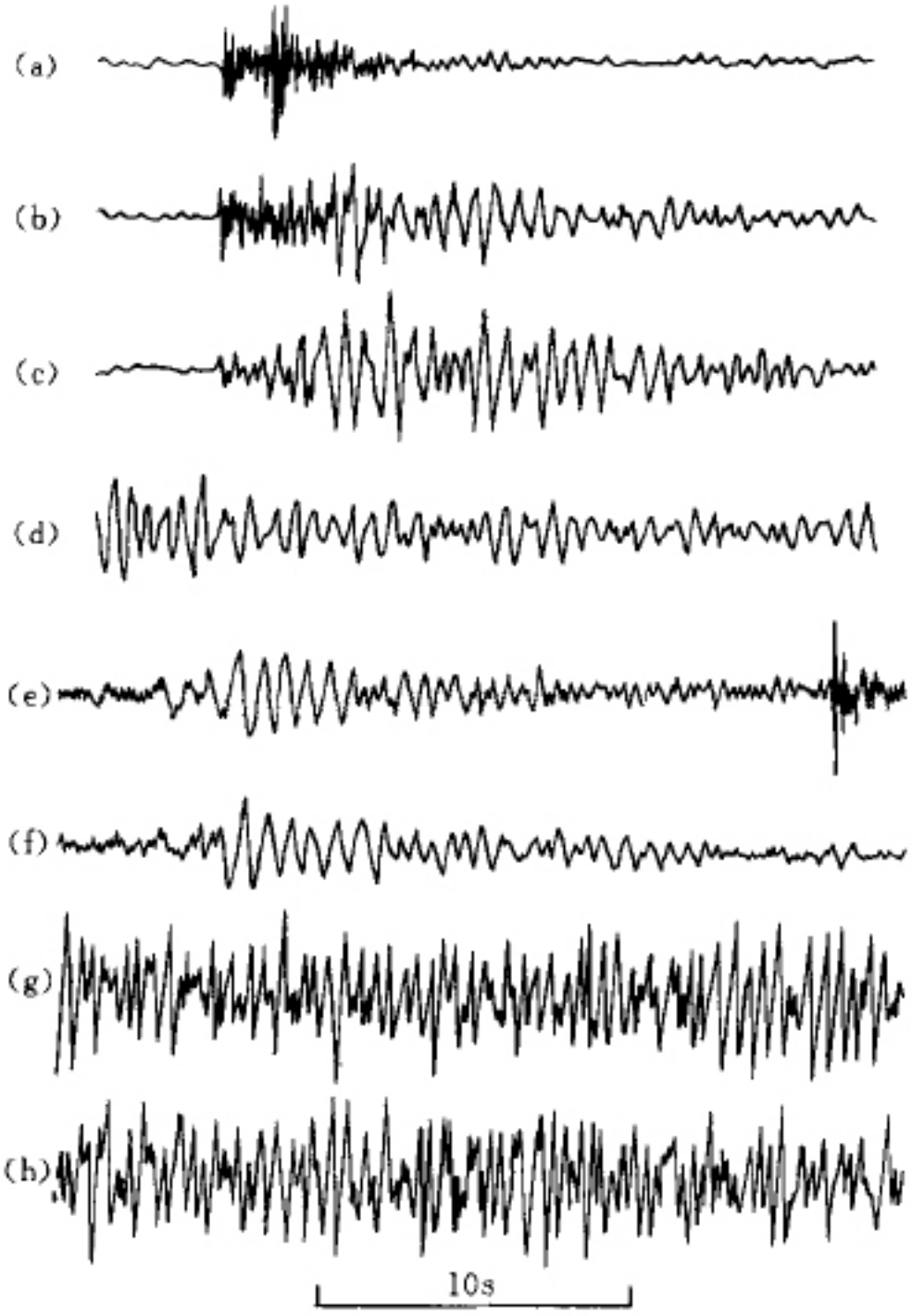

Figure 4.7. Typical waveforms of volcanic earthquakes: (a) High frequency or type A volcano structural earthquake, Redoubt volcano, 6.8 km deep, RED recorded, 8 km away from crater; (b) Mixed frequency event, 0.6 km deep (0.61 m above sea level), Redoubt volcano, RED recorded; (c) Low frequency or long-periodic event, 4 km deep, RED recorded; (d) Volcanic tremor, Redoubt Volcano, RED recorded; (e) Explosive shock, Pavlof Volcano, PVV recorded, 8.5 km away from the volcano (note: arrival of abrupt air wave); (f) Low frequency or type B event, Pavlof volcano, PVV recorded; (g) Volcanic tremor before eruption, Spurr volcano, CRP recorded, 4.8 km away from the volcano; (h) Tremor in the eruption, Pavlof volcano, PVV recorded (after McNutt, 1996b).

Examples of volcano-seismic events observed by our network beneath the Nemrut volcano are presented in Figure 4.8. A-type volcano tectonic event with its high frequency content (Figure 4.8a), LF event with 2-3 Hz dominant frequency (Figure 4.8b) and the hybrid type event covering a large range of frequency spectrum (Figure 4.8c) is obvious in these three samples.

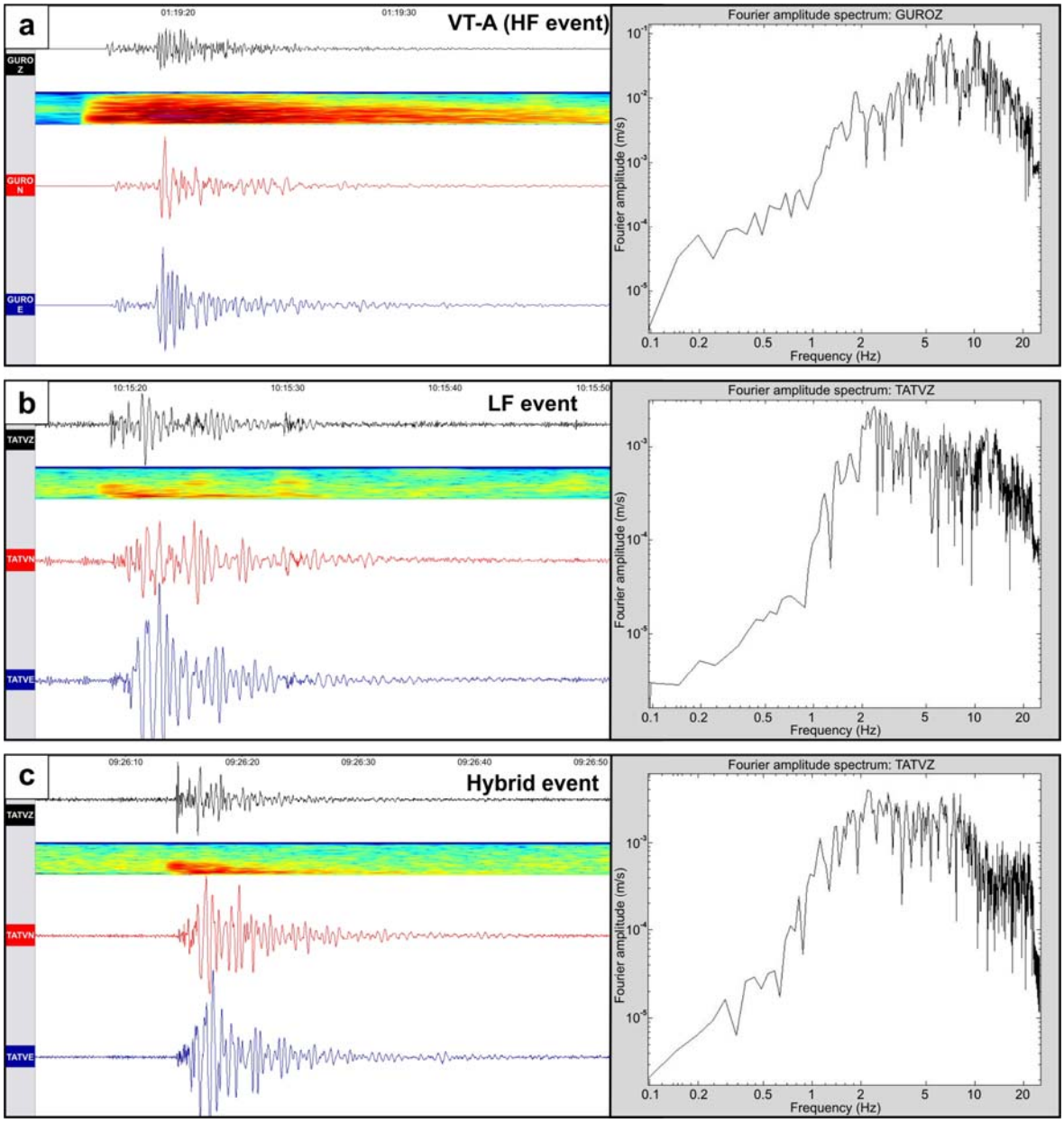

Figure 4.8. Z-N-E components and Fourier amplitude spectrum (S-wave, Z-component) of the Seismic events of volcanic origin recorded by Hacettepe University Nemrut Monitoring Network between October 2003 and October 2005. **a)** A-type volcanic event recorded in 29.05.2005 at 01:199:13.72 (UTC), **b)** LF-LP event recorded in 06.06.2005 at 10:15:16.20 (UTC), and **c)** Hybrid event recorded in 16.10.2003 at 09:26:11.83 (UTC).

Magnitudes

Duration dependent magnitude (Md) equations of the three seismic stations were derived using a regression method (Kalafat, 1989a,b; Ayhan et al., 1988). Local magnitude equations of recorded events were calculated using the magnitudes of the events reported by National center of earthquake monitoring (Kandilli observatory). In order to determine the duration dependent magnitude equation for Nemrut seismic monitoring network, we used the following equation:

$Md = a + bLogT + cD$ (Kalafat, 1989b),

Where "Md" is the duration dependent magnitude of the earthquake, "T" is the total signal duration, "D" is the epicentral distance in km, and "a", "b" and "c" are the coefficients of regression. Using the least squares method, coefficients of regression for the Nemrut seismic monitoring network are calculated as: a = 0.40, b = 2.001 and c = -0.0016.

4.3.1. Seismicity between October 2003 and October 2005

Within a two years period, between October 2003 and October 2005, 219 events including regional Long-Period tectonic events and 89 low magnitude local and regional earthquakes have been recorded (Fig. 4.9). A total of 133 events were observed in the vicinity of the volcano, with magnitudes (Md) ranging from 1.3 to 4.0 (Table 4.2, Fig. 4.9). 32 events that are thought to be of volcanic origin have been observed with a frequency of 1.3 events per month (Fig. 4.10). This is a considerable value for a dormant volcano. Occurrence frequency of events is an important precursor to determine an upcoming eruption, as the rates of seismicity before and during eruptions are typically several tens to several hundreds or more events per day, and include larger-magnitude events (McNutt, 2000). Events of volcanic origin were observed in three types: VT-A (volcano-tectonic, type A), LF-LP (Low frequency – long period) and Hybrid events (Table 4.1). 18 VT-A type (Md: 1.7-3.8), 3 LF-LP type (Md: 2.4-3.0) and 12 Hybrid type (Md: 1.3-3.4) events were located in the close vicinity of the volcano (Fig. 4.10).

Depths of the volcanic events range between 4 and 25.5 km. Under the Nemrut caldera, depth of the volcanic events could be grouped in two main swarms: first group events are localized between 3.9 and 8.5 km with an average of 5.8 km, second group is defined by only two events at 14.3 and 16.6 km depth (Fig. 4.10). Other than the events under the Nemrut volcano, volcanic events also occurred

under the Mazik dome with a depth ranging between 4.9 and 25.6 km (Fig. 4.10). Hypocenters of these events are slightly parallel to the N57ºE directed fault system which is located on the Mazik dome.

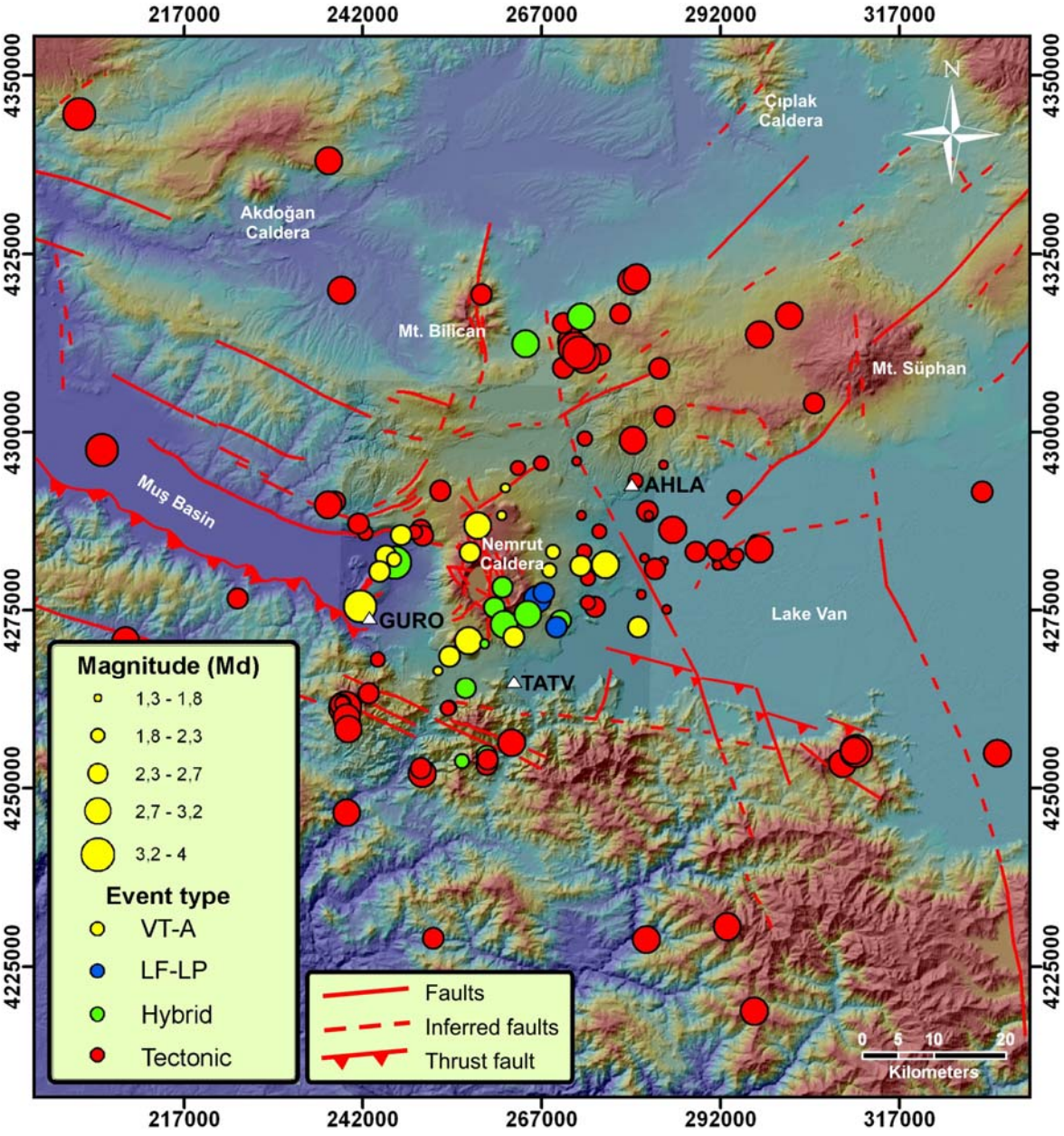

Figure 4.9. Seismic events recorded by Hacettepe University Nemrut Monitoring Network between October 2003 and October 2005. White triangles indicate the station locations. Projection: UTM, European Datum 1950.

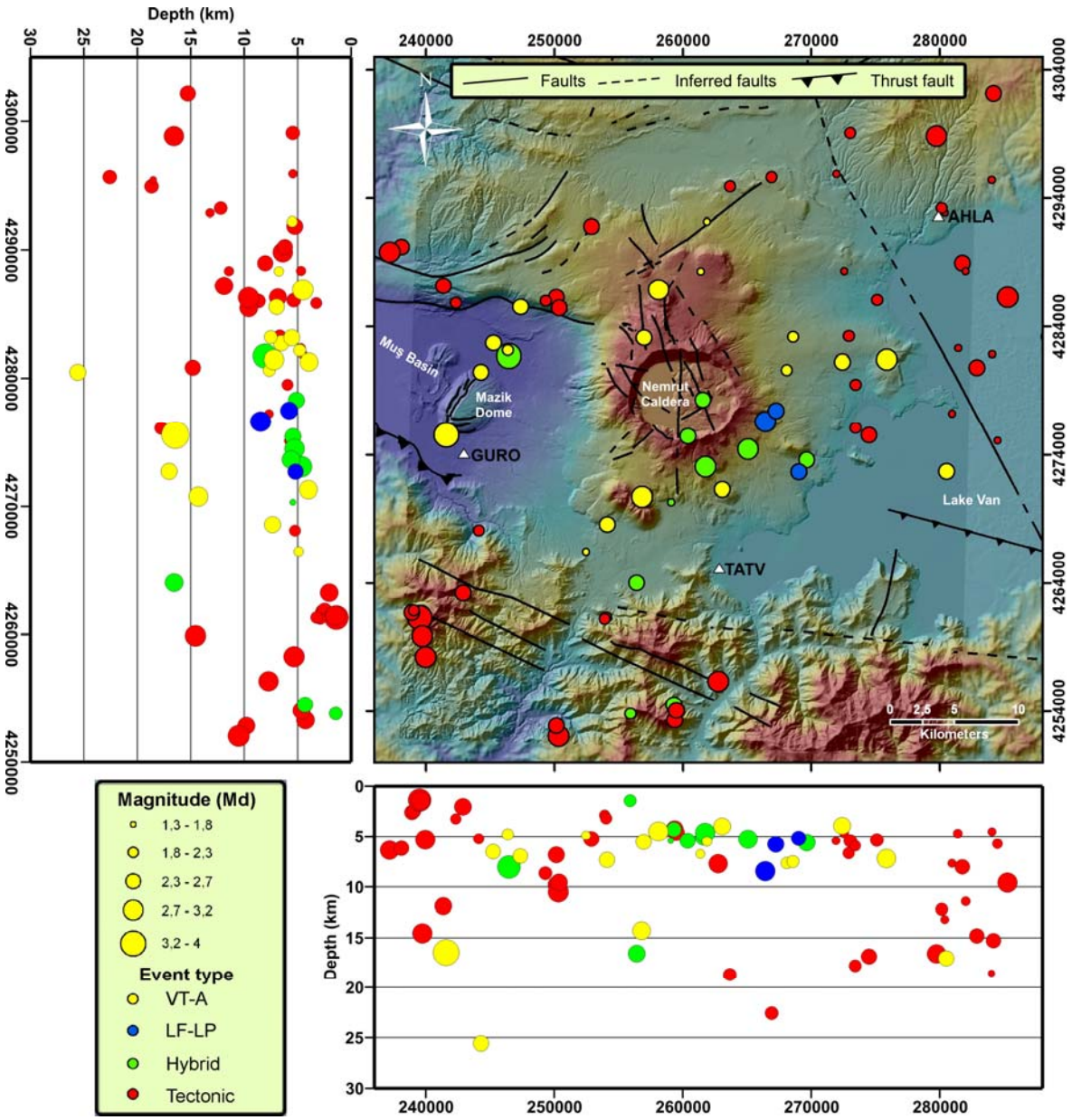

Figure 4.10. Seismic events recorded by Hacettepe University Nemrut Monitoring Network between October 2003 and October 2005 in the immediate area of Nemrut volcano. White triangles indicate the station locations. Projection: UTM, European Datum 1950.

Shallow emplacements of the volcanic events occurred under Nemrut volcano (Fig. 4.10) are the indicative evidence of a shallow magma chamber at 4-5 km depth. According to his research on the phase equilibria among mineral species, Çubukçu (2008) also suggested that the crystallization takes place in a shallow magmatic reservoir.

NO	DATE	ORIGIN_(UTC)	LAT	LONG	X	Y	Depth	Md	DMIN	RMS	T_(S)	FC	Pon	Son	ET
1	22.09.2003	03:07:11.23	38,3357	41,8590	225446,14	4247803,94	4,93	2,4	30,10	0,02	10,92	HF	c	c	T
2	01.10.2003	13:13:59.96	38,0935	42,6818	296704,45	4218797,19	27,38	2,8	56,50	0,09	17,36	HF	c	c	T
4	05.10.2003	14:46:58.34	39,0118	42,4542	279566,21	4321242,65	5,36	3,1	28,70	0,01	23,35	HF	c	c	T
5	06.10.2003	17:57:18.80	39,0155	42,4628	280322,42	4321632,53	5,01	2,9	29,10	0,03	17,75	HF	c	c	T
6	13.10.2003	13:50:50.64	39,1988	41,5540	202391,79	4344571,46	2,46	3,3	81,50	0,00	34,36	HF	c	c	T
7	14.10.2003	20:49:51.45	38,6432	42,3355	268093,00	4280623,66	7,66	2,0	17,10	0,01	6,30	HF	c	c	A-VT
8	15.10.2003	12:20:41.49	38,6860	42,6665	297026,59	4284588,69	9,30	2,1	17,30	0,00	7,24	HF	c	c	T
9	16.10.2003	09:26:11.83	38,4057	42,2437	259311,29	4254498,80	4,31	2,4	10,50	0,01	10,24	MF	c	uc	H
10	16.10.2003	18:13:38.83	38,5952	41,8373	224538,98	4276673,89	2,75	2,5	17,60	0,01	12,01	HF	c	c	T
14	24.10.2003	15:58:14.95	38,9020	42,5027	283432,06	4308938,90	1,13	2,4	16,40	0,01	10,22	HF	c	c	T
20	28.10.2003	22:06:9.22	38,7457	42,2603	261887,18	4292193,71	5,51	1,8	19,80	0,01	5,16	HF	c	c	A-VT
22	03.11.2003	02:58:59.28	38,4253	43,0608	330716,37	4254856,43	5,60	3,0	61,90	0,03	22,29	LF	c	c	T
23	03.11.2003	22:09:42.68	38,8108	42,3863	273046,38	4299099,01	5,46	2,2	10,80	0,01	7,88	LF	c	c	T
24	10.11.2003	20:45:15.04	38,6583	42,5185	284068,22	4281852,59	4,53	1,6	11,00	0,03	4,06	LF	c	c	T
25	12.11.2003	12:34:50.95	38,7140	42,3843	272565,37	4288359,68	4,69	1,7	10,10	0,00	4,79	LF	c	c	T
26	20.11.2003	03:02:34.86	38,6645	42,6127	292284,18	4282323,00	5,57	2,7	14,70	0,05	13,94	LF	c	c	T
27	26.11.2003	12:41:51.16	38,6557	42,6045	291545,09	4281364,92	7,35	1,7	14,90	0,02	4,62	LF	c	c	T
28	15.01.2004	22:58:01.93	38,5512	42,2093	256796,66	4270738,87	14,29	2,8	9,10	0,06	16,17	HF	c	c	A-VT
29	17.01.2004	21:23:45.35	38,6488	42,5053	282890,75	4280829,36	14,81	2,4	11,80	0,19	10,10	HF	c	c	T
31	31.01.2004	18:54:40.14	38,8990	42,3480	270004,67	4308984,80	7,64	2,5	20,10	0,11	11,70	HF	c	c	T
32	06.02.2004	05:27:42.90	38,6982	42,5310	285275,41	4286251,75	9,60	3,0	7,30	0,05	19,41	MF	c	c	T
33	07.02.2004	03:19:31.34	38,7217	42,4898	281763,33	4288957,47	8,04	2,4	3,70	0,21	10,50	HF	c	c	T
34	09.02.2004	19:09:01.49	38,7400	42,1570	252887,92	4291835,03	5,27	2,5	21,70	0,09	12,34	HF	c	c	T
35	18.02.2004	00:53:57.99	38,4088	42,8135	309082,45	4253508,55	22,84	3,2	47,10	0,09	26,71	HF	c	c	T
36	21.02.2004	00:24:42.80	38,7418	42,6300	294011,65	4290863,41	2,44	2,0	12,40	0,27	6,55	MF	c	c	T
37	27.02.2004	03:07:41.91	38,1988	42,6353	292924,14	4230586,32	29,67	3,0	44,90	0,22	21,41	HF	c	c	T
38	29.02.2004	00:43:01.56	38,6938	42,4143	275110,95	4286043,50	5,37	2,2	9,30	0,02	8,41	HF	c	c	T
39	04.03.2004	01:01:52.22	38,6472	42,0870	246474,74	4281725,69	8,06	3,4	9,80	0,21	32,03	MF	c	uc	H
40	07.03.2004	20:03:41.82	38,6967	42,3143	258105,74	4286863,96	4,52	3,0	31,80	0,00	20,32	MF	c	c	A-VT
41	11.03.2004	02:38:09.06	38,6892	42,1277	250163,77	4286275,83	6,85	2,6	15,60	0,05	12,99	HF	c	c	T
42	18.03.2004	00:42:07.08	38,9475	42,6623	297403,93	4313622,05	9,16	3,0	26,20	0,27	21,04	HF	c	c	T
43	23.03.2004	22:39:12.57	38,5748	42,4805	280506,61	4272675,08	17,03	2,5	19,20	0,02	12,14	HF	c	c	A-VT
47	09.04.2004	21:16:42.61	38,7107	42,2557	261370,81	4288320,80	6,76	1,7	20,80	0,21	4,69	HF	c	uc	A-VT
48	09.04.2004	22:29:21.59	38,4655	42,1810	254038,30	4261301,90	3,21	2,0	9,60	0,02	6,21	HF	c	c	T
49	09.04.2004	22:31:16.56	38,4645	42,1797	253921,45	4261194,38	2,88	1,9	9,80	0,03	5,48	HF	c	c	T
50	10.04.2004	19:55:56.10	38,4628	42,0155	239585,58	4261457,60	1,47	2,9	11,90	0,06	17,69	LF	c	c	T
56	22.04.2004	21:47:52.61	38,4243	42,8348	310982,91	4255184,85	25,58	3,4	47,50	0,07	35,67	LF	c	c	T
57	22.04.2004	23:43:03.61	38,4250	42,8317	310714,09	4255268,91	27,68	3,1	47,30	0,11	25,66	LF	c	c	T
58	25.04.2004	23:28:38.00	38,8103	42,4635	279749,26	4298854,53	16,58	2,9	6,60	0,25	18,57	HF	c	c	T
59	26.04.2004	11:40:46.09	38,4613	42,0148	239519,09	4261293,09	1,38	3,4	12,10	0,06	32,37	LF	c	c	T
60	01.05.2004	00:28:25.01	38,6557	42,0725	245242,67	4282709,40	6,53	2,4	10,20	0,03	9,98	HF	c	c	A-VT
61	01.05.2004	19:49:24.08	37,5068	41,9518	230548,63	4155530,34	0,10	4,0	113,50	15,20	100,30	LF	c	c	T
62	09.05.2004	15:13:19.07	38,4650	42,0078	238921,51	4261723,62	2,61	2,4	11,80	0,10	9,69	MF	c	c	T
64	17.05.2004	00:57:11.04	38,9888	42,2127	258573,86	4319302,75	32,38	2,7	35,30	0,18	15,42	HF	c	c	T
65	18.05.2004	10:40:38.09	38,6682	42,3900	272916,20	4283262,03	6,68	2,0	12,80	0,21	6,21	MF	c	c	T
66	19.05.2004	02:07:32.92	38,7818	42,3745	271929,12	4295909,53	5,45	1,6	10,30	0,08	4,07	HF	c	c	T
67	25.05.2004	06:12:56.01	38,6510	42,0858	246383,70	4282150,81	4,81	2,0	10,10	0,04	6,10	MF	c	c	A-VT
68	30.05.2004	18:36:42.93	38,8413	42,5135	284185,16	4302175,96	15,28	2,4	9,90	0,35	10,23	HF	c	c	T
69	31.05.2004	00:51:42.07	38,6715	42,5690	288502,01	4283199,89	5,25	2,4	11,60	0,03	10,22	HF	c	c	T
70	02.06.2004	12:09:40.58	38,6345	42,3972	273436,53	4279503,74	5,95	1,9	15,50	0,20	5,97	HF	c	c	T
71	03.06.2004	07:37:14.26	38,3948	42,2448	259371,20	4253286,12	4,27	2,7	11,60	0,06	14,58	LF	c	c	T
72	05.06.2004	07:07:24.95	38,4663	42,0095	239074,56	4261863,10	2,48	2,3	11,60	0,06	9,07	HF	c	c	T
73	07.06.2004	12:29:10.38	38,4487	42,0178	239735,60	4259886,02	14,56	3,0	13,40	0,04	21,54	HF	c	c	T
74	09.06.2004	00:49:10.76	38,6630	42,6258	293419,83	4282126,91	8,86	2,5	15,70	0,02	11,40	HF	c	c	T
75	23.06.2004	01:55:01.94	38,1798	42,5070	281630,55	4228772,37	6,68	3,1	40,00	0,09	23,02	LF	c	c	T
78	24.07.2004	15:09:44.22	38,9177	42,4067	275155,24	4310913,99	17,01	2,5	19,50	0,02	11,65	HF	c	c	T
81	29.07.2004	14:47:22.11	38,5372	41,6598	208841,23	4270783,42	5,68	3,1	33,00	0,01	22,80	LF	c	c	T
87	13.08.2004	22:52:49.34	38,5942	42,2488	260382,60	4275407,80	5,44	2,5	11,50	0,05	11,67	LF	c	c?	H
91	20.08.2004	13:03:58.71	38,9327	42,3605	271197,23	4312693,96	12,85	3,0	22,70	0,02	20,83	MF	c	c	T
92	20.08.2004	23:49:37.90	38,7708	42,2798	263665,11	4294929,14	18,67	2,2	18,20	0,06	8,13	HF	c	c	T
93	21.08.2004	05:32:15.73	38,9555	42,3462	270031,19	4315260,73	4,84	2,5	25,50	0,08	11,33	HF	c	c	T
94	21.08.2004	07:24:25.50	38,9697	42,4380	278031,74	4316609,05	5,05	2,4	24,30	0,07	10,53	HF	c	c	T
95	21.08.2004	16:26:34.73	38,9210	42,3683	271835,96	4311375,73	16,03	3,0	21,20	0,02	20,98	HF	c	c	T
96	21.08.2004	17:15:04.30	38,9140	42,3825	273044,95	4310563,28	18,59	3,3	19,90	0,00	29,89	HF	c	c	T
97	21.08.2004	17:34:05.28	38,9243	42,3653	271586,42	4311749,53	11,39	3,3	21,70	0,01	29,03	HF	c	c	T

Table 4.2. Datasheet of recorded seismic events. Md: duration dependent magnitude, Dmin: minimum distance to the closest station in km, T(s): coda duration, FC: frequency class, HF: high freq., LF: low freq., MF: middle freq., Pon and Son: P and S wave onset, c: clear, uc: unclear, ET: event types, Art.: Artificial expolsions.

NO	DATE	ORIGIN_(UTC)	LAT	LONG	X	Y	Depth	Md	DMIN	RMS	T_(S)	FC	Pon	Son	ET
98	22.08.2004	10:17:56.80	38,9192	42,3727	272211,73	4311164,92	18,63	3,4	20,90	0,06	32,18	LF	c	c	T
99	23.08.2004	21:44:14.96	38,4343	42,0210	239963,22	4258278,61	5,34	3,0	15,00	0,13	20,16	HF	c	c	T
100	28.08.2004	08:48:28.65	38,4015	42,2460	259498,24	4254026,63	4,64	2,6	10,90	0,01	12,14	HF	c	c	T
101	05.09.2004	23:05:48.82	38,4798	42,0527	242892,58	4263239,94	2,05	2,7	10,00	0,05	13,69	HF	c	c	T
102	06.09.2004	06:21:00.02	38,4233	42,2825	262757,63	4256351,62	7,73	2,9	7,90	0,06	18,67	HF	c	c	T
105	29.09.2004	23:03:01.70	38,7212	41,9878	238109,56	4290218,94	6,20	2,4	17,50	0,01	10,46	HF	c	c	T
106	30.09.2004	00:24:18.73	38,7173	41,9773	237182,17	4289816,14	6,39	2,9	17,30	0,04	18,64	HF	c	c	T
107	12.10.2004	08:41:27.49	38,6065	42,3177	266424,39	4276595,36	8,47	3,0	12,80	0,02	19,59	LF	c	c	LF-LP
108	17.10.2004	16:59:50.99	38,6768	42,6708	297374,71	4283558,07	10,59	2,9	18,10	0,03	18,92	HF	c	c	T
109	19.10.2004	03:01:52.47	38,6628	42,2068	256955,86	4283132,66	5,55	2,5	18,20	0,03	11,18	HF	c	c	A-VT
110	22.10.2004	19:52:24.30	38,1742	42,1675	251868,29	4229005,88	5,00	2,7	37,00	0,30	15,15	MF	c	c	T
111	24.10.2004	18:43:26.41	38,6663	42,3402	268576,54	4283175,74	7,52	2,1	16,20	0,30	7,12	HF	c	c	A-VT
113	25.10.2004	04:14:45.45	38,6743	42,6038	291538,14	4283430,91	5,01	2,6	13,40	0,09	13,33	MF	c	c	T
116	14.11.2004	02:09:27.10	38,9285	42,2865	264767,72	4312416,23	9,73	3,0	45,50	0,01	22,79	MF	c	uc	H
117	14.11.2004	04:00:58.58	38,9642	42,3743	272494,45	4316155,82	8,58	2,9	52,70	0,02	20,20	LF	c	uc	H
120	23.11.2004	23:38:53.99	38,6818	42,1303	250364,23	4285447,35	9,58	2,7	15,00	0,34	13,84	HF	c	c	T
123	07.12.2004	02:18:51.52	38,7162	42,4930	282024,86	4288339,39	11,43	1,7	4,30	0,06	4,68	HF	c	c	T
124	09.12.2004	12:53:36.95	38,6683	42,6345	294192,09	4282695,57	6,77	2,2	15,90	0,00	8,30	HF	c	c	T
125	09.12.2004	16:12:23.91	38,6160	42,4842	280954,33	4277239,04	7,68	1,6	15,40	0,02	4,25	HF	c	c	T
126	09.12.2004	20:33:02.66	38,5973	42,5255	284494,77	4275065,73	5,75	1,8	17,70	0,05	5,18	HF	c	c	T
127	22.12.2004	00:06:39.16	38,7562	43,0272	328572,00	4291642,33	13,46	2,7	46,90	0,10	15,88	HF	c	c	T
130	03.01.2005	18:38:51.31	38,5117	42,1612	252468,66	4266483,00	4,91	1,7	11,00	0,16	4,50	HF	c	c	A-VT
131	03.01.2005	18:38:59.24	38,5310	42,1792	254104,21	4268576,90	7,35	2,5	10,10	0,12	11,41	HF	c	c	A-VT
132	17.01.2005	04:40:40.12	38,8625	42,7540	305119,58	4303987,90	5,00	2,5	26,00	0,19	11,88	HF	c	c	T
160	01.03.2005	00:43:22.11	38,7763	41,6110	205568,16	4297481,90	0,49	3,4	43,60	0,18	34,34	LF	c	c	T
163	21.03.2005	12:43:57.09	38,7782	42,3170	266921,72	4295655,00	22,58	2,2	15,10	0,05	8,33	HF	c	c	T
175	07.04.2005	01:30:43.87	38,3287	42,0228	239741,86	4246552,25	5,25	2,8	26,70	0,13	16,26	HF	c	c	T
176	18.04.2005	11:01:26.94	38,5803	42,3557	269650,19	4273591,29	5,62	2,7	11,40	0,00	15,13	LF	c	uc	H
178	05.05.2005	09:46:05.62	38,5480	42,2355	259069,65	4270314,64	5,45	1,3	7,30	0,17	2,75	HF	c	uc	H
179	05.05.2005	09:46:17.35	38,6147	42,3268	267243,47	4277482,38	5,80	2,6	13,80	0,25	13,20	LF	c	uc	LF-LP
180	19.05.2005	04:05:38.01	38,5240	42,0650	244122,38	4268111,72	5,25	1,9	5,50	0,07	5,95	LF	c	uc	T
181	19.05.2005	04:08:36.04	38,6828	42,0380	242337,07	4285814,00	3,26	1,9	12,70	0,13	5,77	HF	c	uc	T
182	29.05.2005	01:19:13.72	38,5900	42,0332	241586,11	4275526,70	16,45	3,8	2,40	0,03	47,80	HF	c	c	A-VT
184	30.05.2005	14:28:39.29	38,5733	42,2652	261742,11	4273045,31	4,64	3,0	8,90	0,35	20,51	LF	c	uc	H
187	06.06.2005	10:15:16.20	38,5717	42,3488	269021,46	4272654,08	5,20	2,4	10,20	0,01	10,33	LF	c	uc	LF-LP
190	14.06.2005	13:55:53.46	38,5577	42,2810	263067,58	4271272,92	4,00	2,7	7,00	0,02	14,06	LF	c	c	A-VT
191	21.06.2005	12:21:28.79	38,6205	42,2615	261576,03	4278293,88	5,12	2,5	14,10	0,00	11,16	LF	c	uc	H
192	23.06.2005	13:47:32.17	38,5867	42,3030	265079,51	4274435,21	5,29	2,9	10,30	0,01	17,59	MF	c	uc	H
193	25.06.2005	17:28:17.67	38,6525	42,4243	275851,96	4281434,99	7,22	2,9	21,30	0,01	19,48	LF	c	c	A-VT
194	26.06.2005	02:42:37.87	38,6500	42,3848	272406,07	4281254,85	3,94	2,7	19,30	0,01	14,36	HF	c	c	A-VT
197	09.07.2005	01:18:33.41	38,7565	42,4728	280391,82	4292860,70	13,20	1,6	1,30	0,01	3,93	HF	c	c	T
198	09.07.2005	01:18:34.80	38,7805	42,5138	284027,55	4295426,86	18,52	1,4	3,70	0,01	3,33	HF	c	c	T
199	09.07.2005	01:20:08.66	38,7598	42,4700	280158,61	4293233,70	12,20	2,1	1,70	0,02	7,32	HF	c	c	T
200	09.07.2005	11:32:27.09	38,3922	42,2602	260707,84	4252957,44	4,62	2,7	11,60	0,00	13,95	LF	c	uc	Art.
201	09.07.2005	14:51:26.86	38,3812	42,1417	250318,34	4252050,82	10,52	3,1	17,70	0,02	23,58	HF	c	c	T
202	09.07.2005	14:52:28.64	38,3883	42,1395	250150,58	4252844,84	9,80	2,6	17,30	0,01	12,42	MF	c	c	T
204	13.07.2005	15:02:48.12	38,3982	42,2497	259810,48	4253650,71	3,88	2,3	11,10	0,01	9,62	LF	c	uc	Art.
205	15.07.2005	09:44:48.16	38,3810	42,2327	258268,27	4251786,08	8,25	2,0	13,40	0,00	6,12	MF	c	uc	Art.
206	20.07.2005	15:37:46.06	38,4127	42,1995	255474,52	4255392,14	4,58	2,6	11,70	0,04	12,91	LF	c	uc	Art.
207	23.07.2005	23:58:44.44	38,9885	41,9872	239037,10	4319892,12	15,26	3,2	46,80	0,01	27,13	HF	c	c	T
208	24.07.2005	01:05:33.52	39,1518	41,9598	237270,12	4338098,67	5,64	2,9	63,60	0,07	20,70	HF	c	c	T
209	02.08.2005	10:08:18.72	38,3910	42,2347	258476,30	4252890,76	4,75	2,6	12,30	0,04	12,20	LF	c	uc	Art.
210	03.08.2005	14:52:45.51	38,3900	42,2048	255860,96	4252858,54	2,70	2,6	13,50	0,04	12,88	LF	c	uc	Art.
211	06.08.2005	15:23:03.69	38,4198	42,2358	258668,27	4256084,47	4,80	2,9	9,30	0,05	17,34	LF	c	uc	Art.
212	07.08.2005	11:37:57.63	38,9723	42,7102	301624,85	4316269,21	11,82	3,2	30,90	0,02	27,38	HF	c	c	T
214	10.08.2005	16:34:43.45	38,4280	42,2460	259586,16	4256967,93	0,05	2,4	8,10	0,02	10,31	MF	c	uc	Art.
215	12.08.2005	03:49:59.98	38,5987	42,4107	274499,69	4275496,96	16,85	2,5	15,90	0,02	11,02	HF	c	c	T
217	13.08.2005	15:46:55.39	38,4178	42,2437	259351,47	4255841,81	4,36	2,4	9,20	0,07	9,63	MF	c	uc	Art.
218	14.08.2005	19:53:12.05	38,6863	42,1180	249309,77	4285980,45	8,67	2,2	14,90	0,00	8,33	HF	c	c	T
219	16.08.2005	03:28:40.86	38,6947	42,0263	241361,98	4287167,90	11,89	2,7	14,00	0,01	14,65	HF	c	c	T
221	23.08.2005	17:43:04.20	38,6035	42,3982	273426,01	4276060,51	17,77	2,1	15,60	0,00	7,26	HF	c	c	T
222	25.08.2005	09:36:35.44	38,3985	42,2050	255907,04	4253801,46	1,44	2,1	12,70	0,01	7,32	MF	c	uc	H
223	30.08.2005	11:57:27.78	38,6353	42,0625	244299,71	4280472,86	25,57	2,5	7,70	0,04	10,79	HF	c	c	A-VT
227	02.09.2005	23:55:24.38	38,6817	42,0958	247362,15	4285530,86	6,97	2,4	13,60	0,03	10,45	HF	c	c	A-VT
228	03.09.2005	08:12:10.37	38,6618	42,4878	281407,08	4282313,84	4,71	1,7	10,30	0,06	4,38	HF	c	c	T
229	11.09.2005	05:53:07.96	38,4082	42,2612	260847,96	4254730,72	23,32	2,6	9,80	0,06	12,25	HF	c	c	Art.
230	11.09.2005	05:57:58.71	38,4132	42,2402	259030,54	4255340,40	24,97	2,3	9,80	0,24	9,44	HF	c	c	Art.
231	11.09.2005	15:09:15.52	38,4907	42,2073	256418,32	4264028,99	16,56	2,7	6,80	0,11	13,96	MF	c	c	H

Table 4.2.cont. Datasheet of recorded seismic events.

Frequency of Occurrences

Some anomalies in frequency of occurrence of seismic events in daily and monthly periods were observed (Fig. 4.11). A data collection of two years is not satisfactory for a healthy analysis. However, slight increase starting with spring time and ending in autumn (Fig. 4.11a, dashed line) must not be disregarded in the future monitoring of the volcano. Furthermore, masking of the signals by city noise is visible during day time (between 06:00 and 17:00 in local time, Fig. 10b).

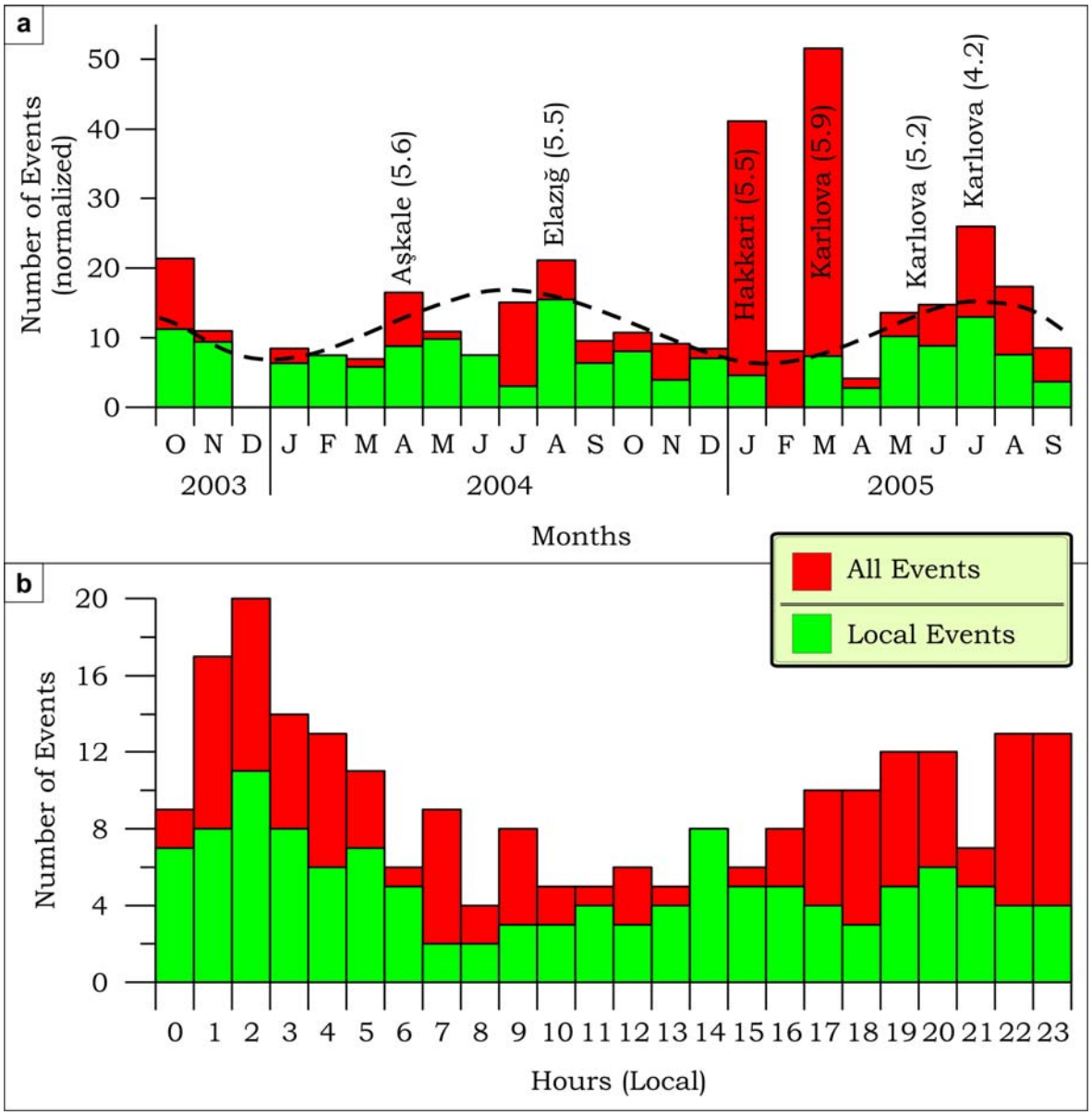

Figure 4.11. Temporal frequency of occurrence of events observed by Nemrut Network for **a)** monthly and **b)** hourly periods. (Some important earthquakes that affect the monthly histogram and their magnitudes are indicated. Monthly frequencies were normalized using the efficiency (Figure 4.2) data).

The small magnitude events located under the Lake Van are interpreted as tectonic events (Fig. 4.10). However, they have nearly the same spectra with the VT-A type events. Kipfer et al. (1994) applied helium isotope analysis from a location near these events, and they emphasized the injection of mantle type helium into Lake Van. Kipfer et al. (1994) pointed out that this injection is possibly related to the local extensional tectonics and the associated magmatic activity. Liability of volcanic origin for those small magnitude events must not be disregarded. Additionally, Toker et al. (2007), and Horasan and Boztepe-Güney (2006), indicated that the seismic events of volcanic origin have been recorded in the Lake Van.

Frequency – Magnitude distrubution

Some of the heterogeneities in the Earth crust can be mapped by variations in the frequency-magnitude distribution of earthquakes (Wiemer and Benoit, 1996; Wiemer and McNutt, 1997; Wiemer and Wyss, 1997). The "b-value" is the slope of the straight line that usually fits magnitude and logarithm of frequency distribution of the observed data. We calculated the b-values for the recorded event by using the frequency-magnitude distribution equation (Gutenberg and Richter, 1944):

$$Log_{10}N = a - bM$$

Where "N" is the cumulative number of earthquakes having magnitude larger or equal to "M", and "a" and "b" are constants.

General trend of calculated b-values is 0.69 ± 0.06 for all the recorded events; trends below and over a magnitude of 2.4 are 0.15 ± 0.0002 and 1.34 ± 0.02 respectively (Fig. 4.12). Generally, b-value does not vary much from its usual value of b = 1 (e.g. Froehlich and Davis., 1994), except for volcanic areas where high values, up to b = 2, are commonly reported (Wiemer and McNutt, 1997; Wyss et al., 1997, Warren and Latham, 1970). However, in all seismogenic areas, it is possible to observe b-values with significant variations (Wiemer and Wyss, 2002). Wiemer and Mcnutt (1997) reported that in volcanic areas, most of the crust shows normal or even low b-values (b<1), with rather small volumes of anomalously high b-values (b>1.3).

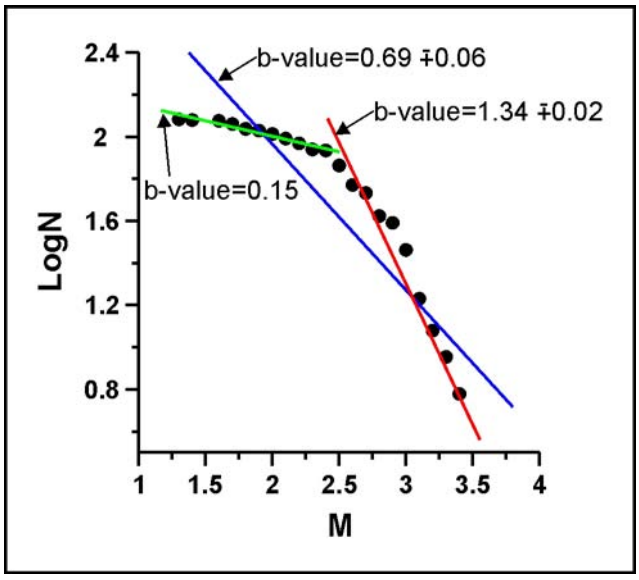

Figure 4.12. Calculated b-values of seismic events recorded by Hacettepe University Nemrut Monitoring Network between October 2003 and October 2005 in the vicinity of Nemrut volcano.

An increase in material heterogeneity (Mogi, 1962) and in geothermal gradient (Warren and Latham, 1970) results in high b-values, whereas an increase in applied shear stress or effective stress (Wyss, 1973) induces a decrease of the b-values (Horasan and Boztepe-Güney, 2007).

By mapping the b-values in detail on a fine scale, gathering the information contained in the variation of b, or the mean earthquake size, as a function of space is possible (Wiemer and Wyss, 1997).

The frequency-magnitude distribution of the earthquakes associated with the epicenters was analyzed to get a spatial distribution of the b-value (Fig. 4.13). Calculated b-values were evaluated by gathering the fit equations by manual fitting and then, b-values were interpolated using inverse distance weighting method. Number of events used to calculate the b-values and b-value map is very limited (133). Consequently, reliability of the map is controversial. Still, it is possible to note that the high b-values are concentrated around Nemrut volcano, Mazik dome and tectonically active zones (Fig. 4.13). Instead of using all values, with the accrual of data in time, use of frequency-magnitude distribution for specific depths and profiles will surely purvey important information on the volcano and the underlying magma chamber.

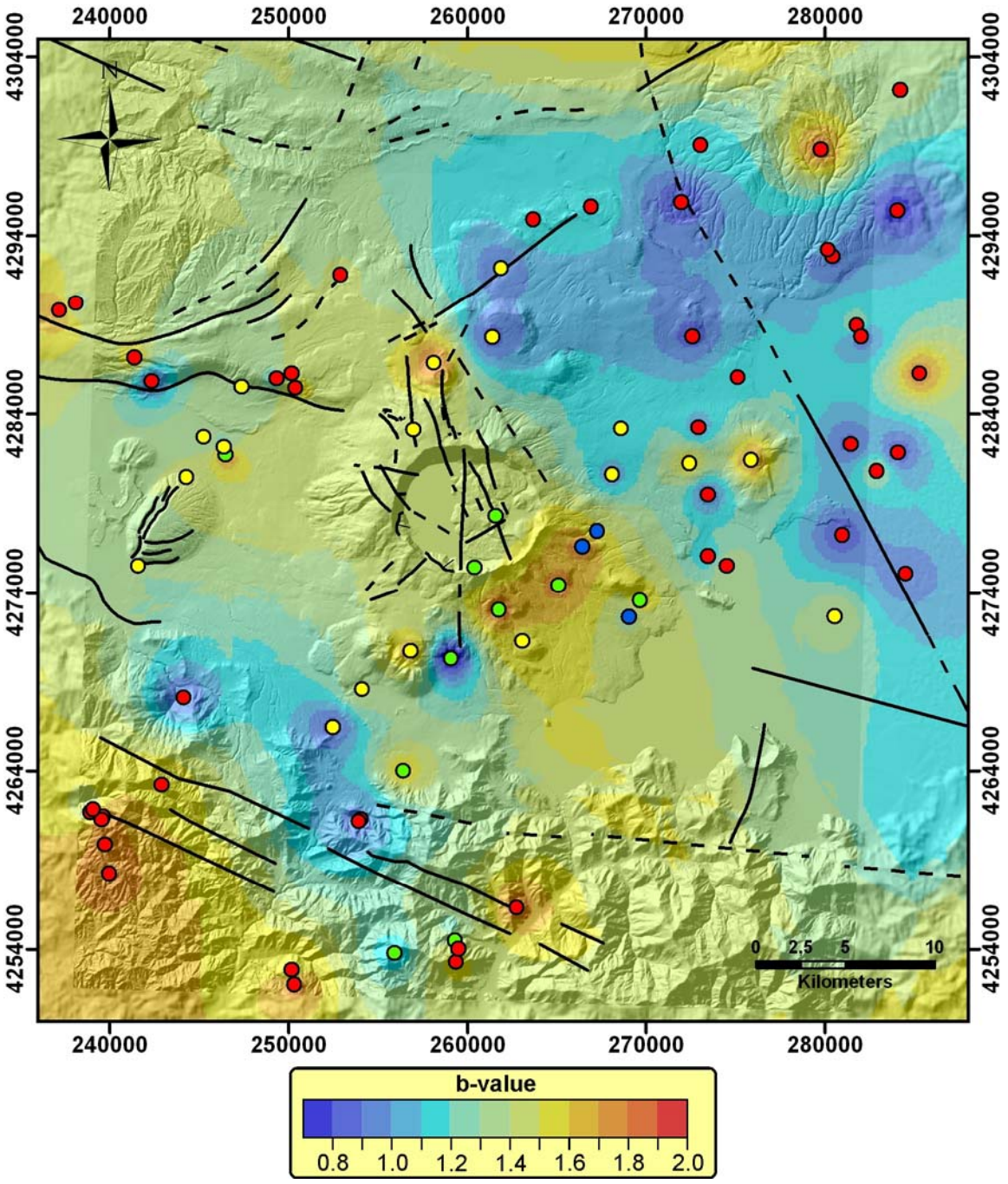

Figure 4.13. b-value map of seismic events recorded by Hacettepe University Nemrut Monitoring Network between October 2003 and October 2005. It is possible to observe the higher b-values around the volcano and tectonically active zones. Yellow points: epicenters of VT-A type events; Blue points: epicenters of VT-B type events; Green points: epicenters of Hybrid events; Red points: epicenters of tectonic events; Black lines: faults; Dashed black lines: inferred faults. Projection: UTM, European Datum 1950.

4.4. Synthesis

Mt. Nemrut, probably the most hazardous for its vicinity, amongst the Anatolian volcanoes is being seismically monitored since October 2003. The seismic network (composed of three 3-component seismometers, a broadband and two short-period sensors) is the first and yet the only volcano-monitoring network on an Anatolian volcano.

Raw data, digitally recorded by the stations are being collected in our laboratory with a Frame-Relay data communication link since October 2003. Raw data are being processed with a two-level STA/LTA triggering system and the triggered possible events are then analyzed.

Mount Nemrut is an active dormant volcano which is threatening 135,000 habitants living nearby (Aydar et al., 2003). In addition to the hydrothermal signature of the volcano, it is now clear that the volcanic signals beneath the volcano refer an active magma chamber at around 4-5 km depth.

Identification of the seismic character of the Nemrut volcano, seasonal and long term effects on this character and more knowledge is possible by long term monitoring of the volcano. Measurements of at least a few years duration are necessary to characterize and understand the background seismicity (McNutt, 2000). Long-term observation of Mt. Nemrut which is thought to be an active-quiescent volcano will yield more knowledge about this volcano.

Chapter 05

Discussion and conclusions

5. Discussion and Conclusions

5.1. Structure of Nemrut Caldera

Recent structural frame of the Nemrut volcano is undoubtedly marked by the spectacular summit caldera, which is 8.5 x 7 km in diameter and slightly elongated in the east-west direction. Western half of the caldera is filled with a half-bowl shaped lake (Nemrut Lake) with a maximum depth of 176 m and 1.264 km^3 volume. The average depth is around 140 m over the majority of the lake. At the northern section of the caldera, ~500 m east of Nemrut Lake, there is a second, smaller hot lake. The deepest point of this lake is 11 m.

Within the spectrum of new data, the structural elements of the Nemrut caldera (Fig. 5.1) have been calculated as (Chapter 3): topographic diameter: 8.5 x 7 km (maximum diameter of the topographic rim of the caldera); structural diameter: 6.7 x 5.3 km (maximum diameter of the structural boundary of the caldera, Fig. 5.1); topographic area: 46.7 km^2; structural area: 27.9 km^2; maximum collapse on the eastern part: 600 m; maximum collapse from the bottom of the lake: 650 m; topographic volume: 32.9 km^3 (volume calculated using topographic diameter); structural volume: 18.14 km^3 (volume calculated using structural diameter); northern collar angle (on land): 29.2°, western collar angle (from lake bottom): 27.9°. The lower collar angle value computed from the bottom of the lake reflects a higher collar slide mechanism due to the existence of Nemrut Lake (Ulusoy et al., 2008). Definitions of the structural elements we used here are literally as defined by Lipman (1997).

Within the scope of our surveys and analyses, an innovative structural model of the Nemrut caldera was presented (Fig. 5.1), stating that it collapsed by a piecemeal mechanism (Ulusoy et al., 2008). It consists of three main blocks, namely P_1, P_2 and P_3 (Fig. 5.1). The displacement between blocks P2 and P3 is topographically evident. Piecemeal caldera subsidence refers to a caldera with numerous floor blocks, and/or multiple collapse centers (Lipman, 1997, 2000; Cole et al., 2005). Small-displacement piecemeal faulting of subsiding caldera floors is probably common (Lipman, 1987).

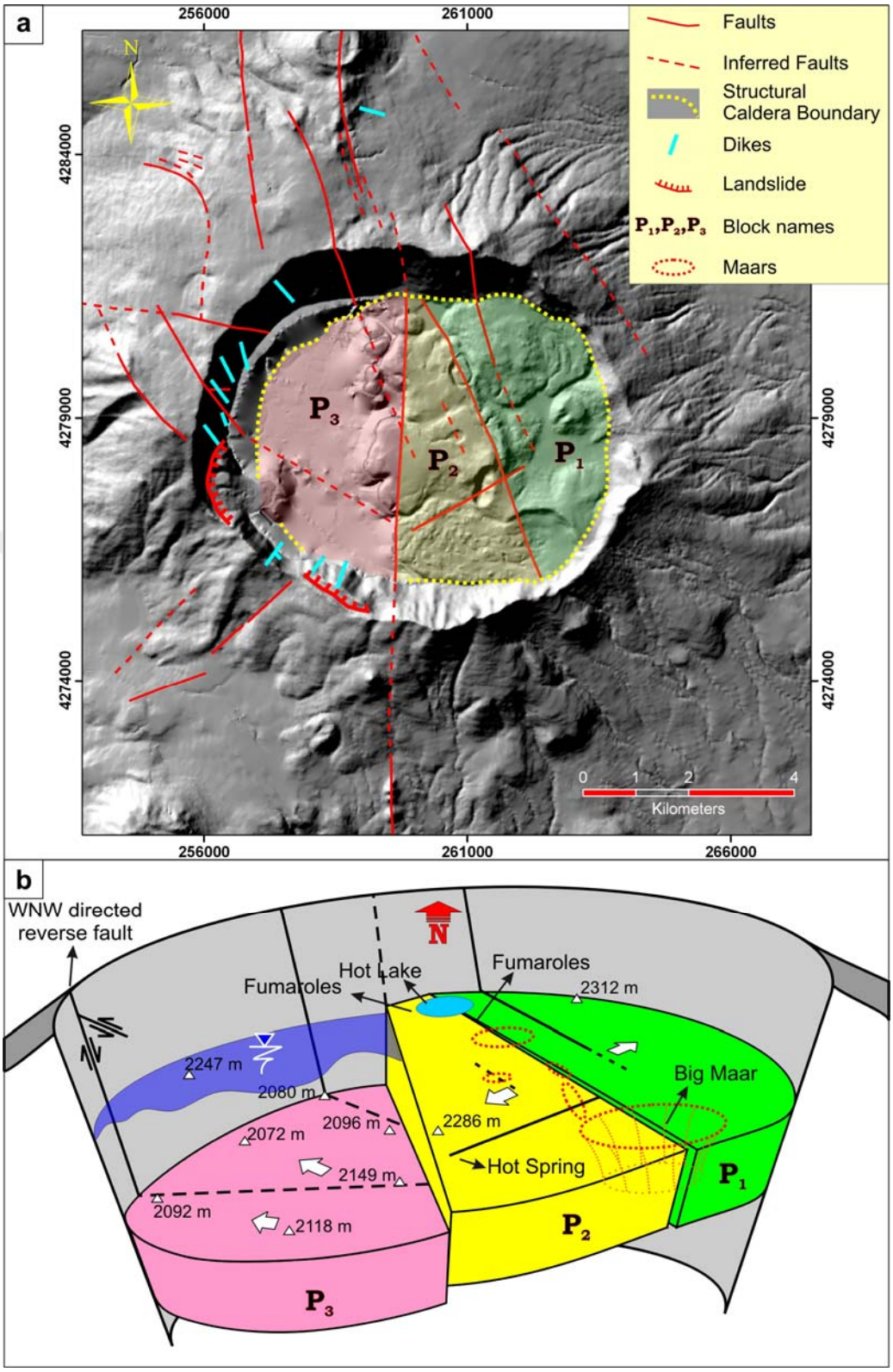

Figure 5.1. Structure of Nemrut caldera **(a)** Structural map of Nemrut Caldera and the blocks responsible for the piecemeal collapse of the caldera. **(b)** Simplified structural model of the Nemrut Caldera. The faults and collapsed blocks are indicated. White arrows: general slope direction of the block; white triangles: altitude points; dashed red circles: maars; black lines: known and observed faults; dashed black lines: inferred faults; "P_1, P_2, P_3": caldera blocks. To simplify the visualization, caldera fill is discarded; note that there are approximately 280 meters of caldera infilling products according to drill logs of Atasoy et al., 1988. Projection: UTM, European Datum 1950.

Collapse of such calderas may be due to (1) multiple magma chambers with overlapping eruption times in which eruption of one may trigger eruption of the other (e.g., Scafell Caldera; Branney and Kokelaar, 1994) or (2) where tectonically controlled faults break the caldera floor into numerous blocks prior to the (main) eruption and control the collapse location (e.g. Glencoe Caldera; Moore and Kokelaar, 1997), or (3) where the entire caldera floor has been rendered a megabreccia (Branney and Kokelaar, 1994), inducing a chaotic subsidence (Lipman, 1997) in some cases (Cole et al., 2005). In Nemrut case, it is inessential to discuss the megabreccia and chaotic type subsidence. Çubukçu (2008) petrologically indicates that a single shallow magma chamber is stratified compositionally and physically on the basis of the intensive crystallization and reservoir parameters. Both petrologically and geologically, clues of multiple collapses following multiphase eruptions are absent. Eruption of Nemrut and Kantaşı ignimbrite series has led to the collapse of the edifice. Faults controlled by regional tectonic stress and discontinuities generated during the evolution and at the late stage of inflation, present the most consistent structural elements for the collapse mechanism of Nemrut caldera.

Actual hydrothermal fluid circulation quantified by SP analyses and the intra-caldera eruption centers are mostly located on the structural discontinuities limiting these blocks and on the caldera boundary faults. Blocks "P_1" and "P_2" (Fig. 5.1) form the eastern part of the caldera. The structural boundary between these blocks controls the main hydrothermal fluid flow in the caldera and is supposed to be responsible for the major explosive intra-caldera activity. Complexities in caldera-floor geometry may be indicated by scattered or transverse distributions of post-caldera, post-collapse vents that are commonly present within recurrently subsided calderas, as at Campi Flegrei, Aso, Santorini (Walker, 1984; Lipman, 1997) or Nemrut as proposed on the schematic structural map of the caldera system (Fig. 5.1).

According to their orientations, intra-caldera faults are grouped in three main groups (Fig. 5.1): N-S directed fault(s) separating blocks P2 and P3; NW-SE-directed faults and NE-SW directed fault systems (Chapter 3). Intra-caldera hydrothermal activity seems to be mainly controlled by the internal structure of the caldera (Ulusoy et al., 2008). Faults and structural boundaries of the caldera floor are the main pathways for the circulation of hydrothermal fluids. Positive SP and

Ce anomalies mainly appear on these structures (Ulusoy et al., 2008). Thermal anomalies detected on the night thermal image reinforce that these zones are hydrothermally active and have been active as visualized by the hydrothermal alteration image defining clay mineralizations (Ulusoy et al., 2008).

Two major slides were observed on the southwestern section of the caldera wall (Fig. 5.1a: slip faults). Both slide events are marked with a brecciated zone between the sliding material/block and inner topographic wall of the caldera (Figs. 5.2 and 5.3).

Figure 5.2. Panoramic photographs of slided block and underlying brecciated zone at the western sector collapse, **a)** upper and, **b)** lower section of the outcrop. Please note the size of the panorama with the scale of two members of our team indicated by red arrows.

Dikes located at north of the slip fault southeast of Zerihuli hill (Fig. 5.3) are slightly rotated clockwise due to the small-scale collapse of the caldera rim. Collapse situated northwest of Zerihuli hill may be initiated and/or syn-generated with the effusive lava flow activity originating from the caldera wall and extending into the Nemrut Lake. This activity may be related with the caldera boundary fault and/or co-radial faulting on the caldera wall.

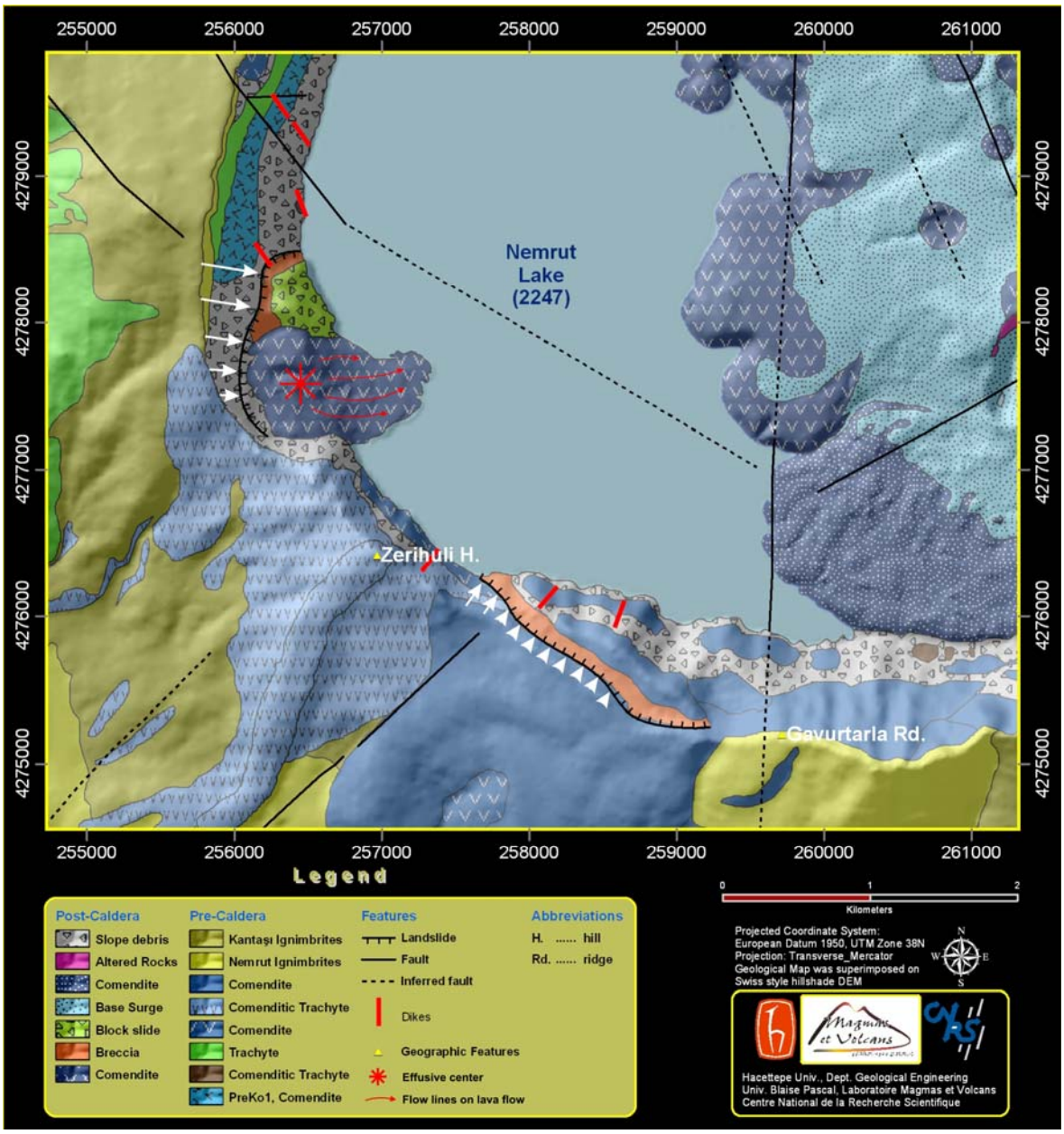

Figure 5.3. Geology and small scale caldera-rim collapses on the southwestern part of the caldera. White arrows are indicating the slide direction.

Dikes are mostly observed on the western portion of the caldera wall (Fig. 5.1a). These dikes are pre-caldera injections and it is evident that some of these were acted as feeder-dikes (Figs. 2.28: trachytic dyke, and 5.4a). Physical properties of these dikes are summarized in Table 5.1. It was possible to observe furcation on one of these dikes (Fig. 5.4b); as well, jointing due to cooling is common (Fig. 5.4c,d).

No	X	Y	Orientation	Azimuth	Thickness (m)
1	259199	4284793	N75W/90	105	5
2	256455	4278815	N20W/82NE	160	4,47
3	257329	4276382	N36E/75NW	36	3,53
4	258125	4276127	N40E/71NW	40	11,6
5	258614	4276012	N20E/87NW	20	7,1
6	256318	4279476	N35W	145	
7	256781	4280155	N15W/90	165	8
8	256488	4279922	N25W	155	
9	256200	4278468	N35W	145	
10	257585	4281275	N40W	140	

Table 5.1. Physical properties of dikes observed on the caldera wall. Coordinates are given in UTM, European Datum 1950 projection.

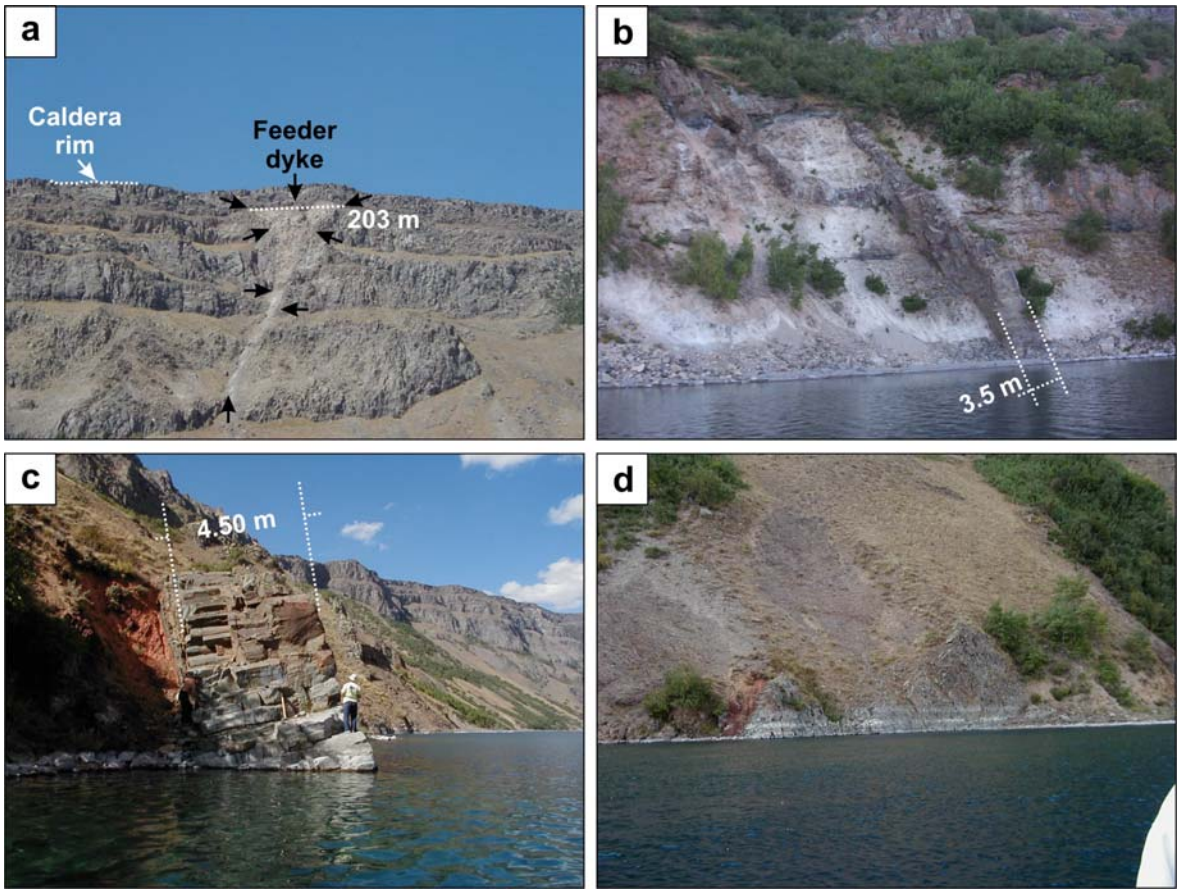

Figure 5.4. Dikes on the caldera wall. **a)** Feeder dyke on the NW caldera wall, **b)** branched dyke on the SW caldera wall, **c)** columnary jointed dyke at the western caldera wall and **d)** its side view.

Faults out of the caldera are mainly grouped in NW-SE and NE-SW directions. Kale hills and Kalekirana hill (Fig. 2.6b) are aligned on a fault paralleling the N-S directed fault separating caldera blocks P_2 and P_3 (Figs. 2.28 and 5.1a). Additionally, WNW-ESE directed reverse fault on the western caldera rim (Fig.

5.1b; Ulusoy et al., 2008) and arc shaped fault (and its en-échelon couples) on the northwestern flank of the volcano draw attention on the western side. This fault is best visualized by the high resolution imagery for example by Google™ Earth® (Fig. 5.5). N-S directed rifting on the northern zone must not be disregarded in the structural context of the volcano (Fig. 5.5).

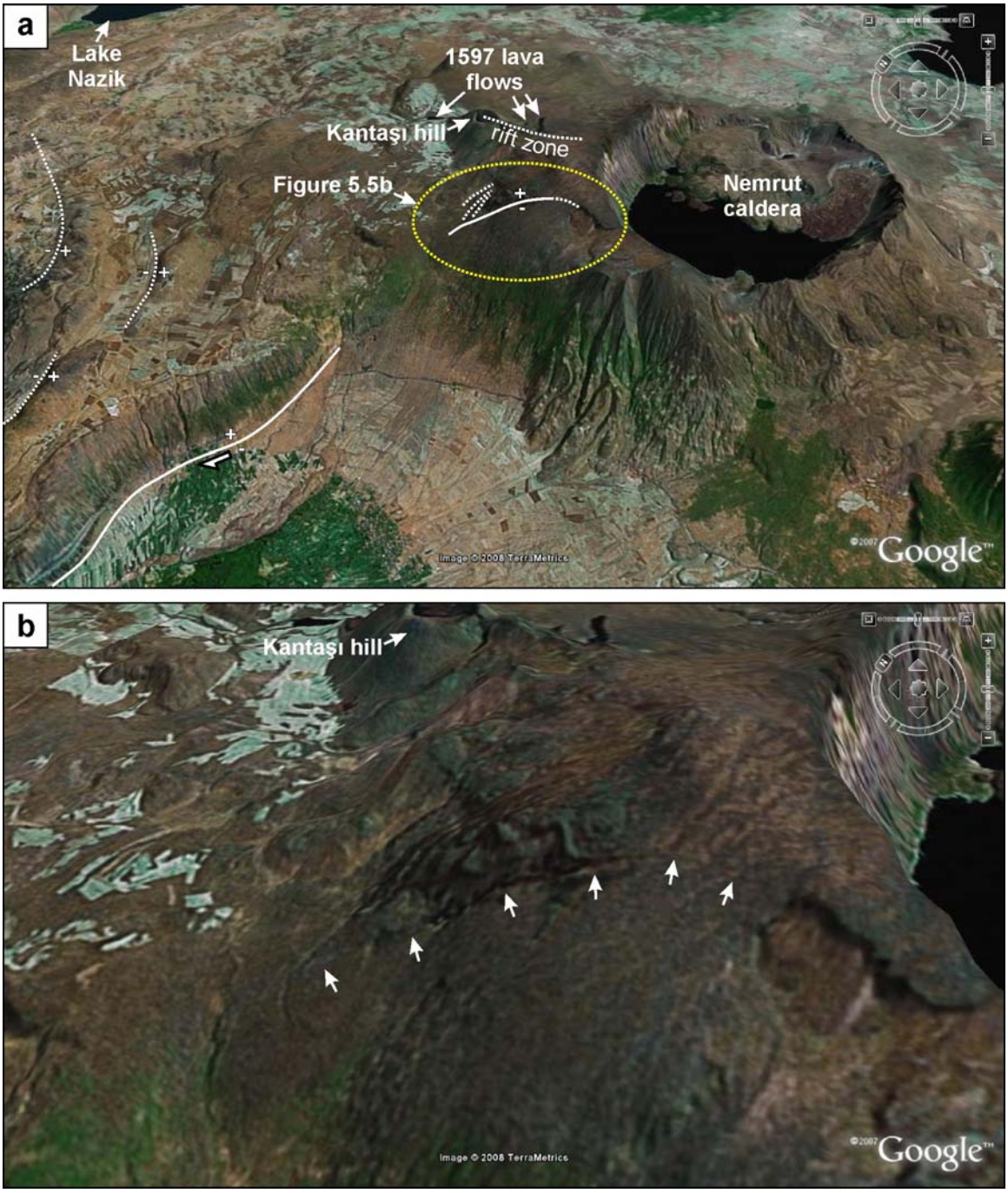

Figure 5.5. High resolution Google™ Earth® imagery, view of the caldera from SW corner. **a)** General view of the area and some of the major structural and volcanological features. White lines: faults; White, pointed lines: inferred faults. **b)** Closer view of the arc shaped fault (white arrows) on the NW flank of the volcano.

5.1.1. Tectonic evolution and initiation of Nemrut volcanism

Several tectonic models have been proposed to explain the style of deformation in Eastern Turkey (Keskin, 2003). Pınar et al. (2007) summarized these models as follows: (1) Tectonic escape of the microplates to the east and the west along the NAFZ (North Anatolian Fault Zone), EAFZ (East Anatolian Fault Zone) and NEAFZ (Northeast Anatolian Fault Zone) transform faults (Fig. 1.1) has been proposed by McKenzie (1972), Şengör & Kidd (1979) and Jackson & McKenzie (1988). Most of the focal mechanisms (e.g. McClusky et al., 2000; Reilinger et al., 2006) support this model because they are dominantly of a strike-slip type, including a little component of reverse and normal faulting (Pınar et al., 2007). (2) The second model based on subcrustal earthquake activity is the subduction of the Arabian plate beneath Eurasia (Rotstein & Kafka 1982). (3) Another model proposed by Dewey et al. (1986), suggests that the Arabian-Eurasian collision results in thickening of the lithosphere in Eastern Anatolia.

Researches on the crustal and tectonic evolution and recent tectonics of Eastern Anatolia continues (e.g. McClusky et al., 2000; Sandvol et al., 2003; Şengör et al., 2003; Zor et al., 2003; Angus et al., 2006; Faccenna et al., 2006; Reilinger et al., 2006); evidently, the complexity of the system is indisputable.

On the other hand, large-scale effect of tectonics on volcano structures was previously discussed (e.g. in Eastern Anatolia: Adiyaman et al., 1998; Dhont and Chorowicz, 2006; in Cordón Caulle-Puyehue, Southern Andes: Lara et al., 2006). Regional effect on volcanic fracturing was also documented by actual observations. Dominiguez et al. (2001) studied the source characteristics of earthquakes that occurred during June-July 1998, that have been interpreted as a volcanic swarm within the edifice of Volcan de Colima. They introduced that the fracturing of the volcanic edifice occurred within a system of fractures coinciding with the general trend of regional fault Tamazula which intersect the volcanic structure.

Relations between regional tectonics and caldera structure/geometry have also been presented geologically (e.g. Marti et al., 1994; Moore and Kokelaar, 1997; Accocella et al., 1999, 2003; Beresford and Cole, 2000; Ulusoy et al., 2004; Dhont et al., 2008) and experimentally (Lagmay et al, 2000; Holohan et al., 2005, 2008; Tibaldi, 2008). Regional and local structures have a profound affect on the morphology of calderas (Cole et al., 2005).

To introduce the relationship of local and regional tectonics and structure of Nemrut caldera is momentous. Structural, geometrical and morphological context of Nemrut caldera may shed light on the numerous questions arising: Is there a relationship between local and regional tectonics and the structure of the caldera? What is the effect of tectonics in the initiation and evolution of the volcanism? What produces the peralkaline volcanism (Çubukçu, 2008) in front of a contractional / collisional zone? What is the role of Muş basin (Chapter 1, Pg. 15; Fig. 1.6) in the general frame? Were the eruptions of Nemrut lead or played a role in the formation of Lake Van?

To answer these questions, detailed definition of the general tectonic frame and state of Nemrut caldera in this frame is essential. We mapped the faults in the region using literature data (Koçyiğit et al., 2001; Bozkurt, 2001; Dhont and Chorowics, 2006) and SRTM DEM obtained from Earth Science Data Interface (Fig. 5.6). Faults in the region exhibit the general trends observed in Eastern Anatolia. WNW-ESE-directed faults are generally dextral or oblique with dextral component. Varto fault system (VF), Otluk fault (Otf), Kavakbaşı fault (KBF), Korkut faults (Ko1F, Ko2F) and Northern Bitlis Thrust fault (NBTF) exemplify this system (Fig. 5.6). Besides, NE-SW-trending faults represent sinistral strike-slip component; Malazgirt (MF), Süphan (SF) and Erciş (EF) faults are the examples for this type of movement.

Muş Basin and Otluk fault

In detail, Muş - Van basins (Lake Van), and Bitlis suture zone play an important role in the regional tectonic system. Dhont and Chorowicz (2006), denote that these basins have been regarded as ramp basins of compressional origin on the basis of interpretations of seismic sounding, earthquake focal mechanisms, photographs, and satellite images (McKenzie, 1972; Şengör and Kidd, 1979; Şengör et al., 1985).

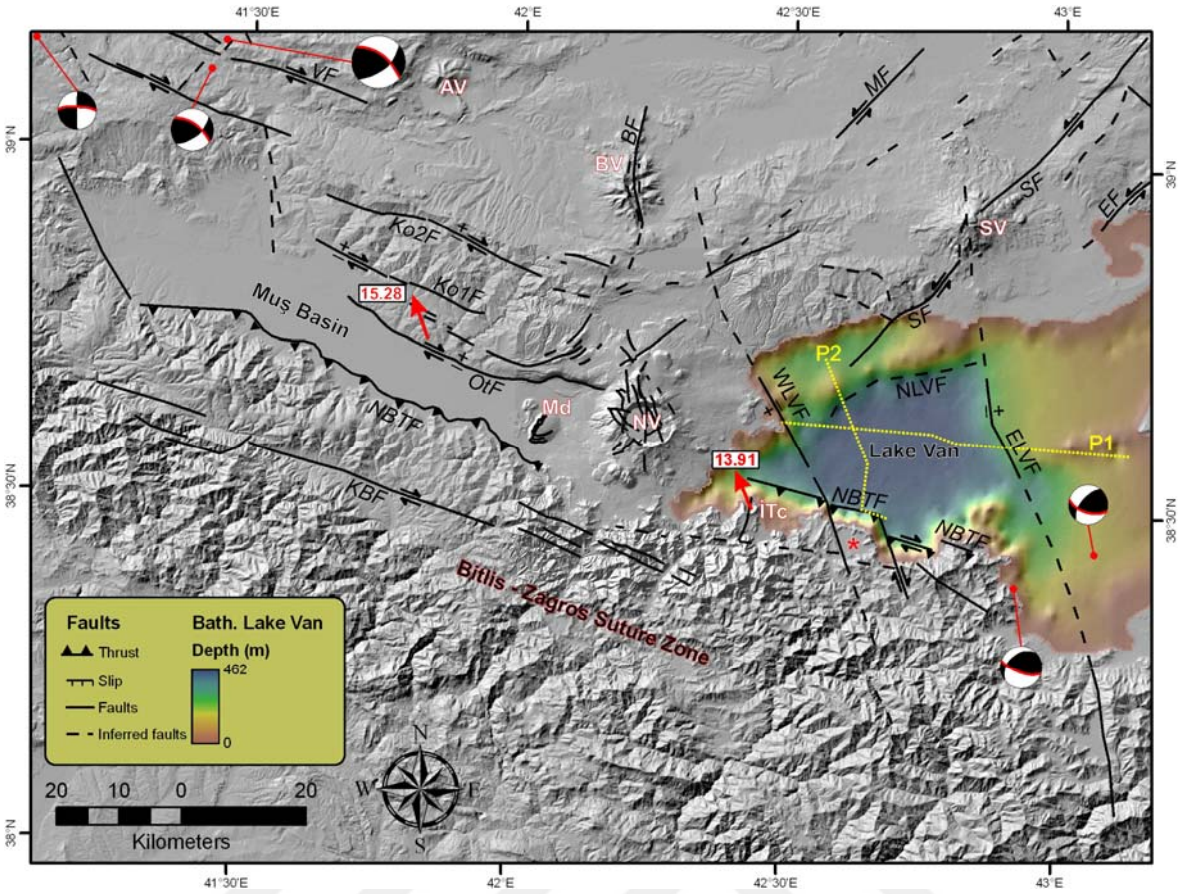

Figure 5.6. Structural map of Nemrut volcano and its vicinity. Black, filled triangles on the thrust fault indicate the thrusting block. Beachball representations of fault-plane solutions are from Dhont and Chorowics (2006); Pınar et al., 2007 and Harvard Global Centroid Moment Tensor Catalog. Red lines on the beachballs represent the fault plane. Red arrows indicate the plate motions relative to Eurasia (values are in mm/yr; data from McCluscy et al., 2000; Reilinger et al., 2006). Volcanic centers: AV: Akdoğan volcano; BV: bilican volcano; İTc: İncekaya Tuff cone; Md: Mazik dome; NV: Nemrut volcano; SV: Süphan volcano. Faults: BF: Bilican fault; EF: Ecemiş fault; ELVF: Eastern Lake Van fault; KBF: Kavakbaşı fault; Korkut faults (Ko1F, Ko2F); MF: Malazgirt fault; NBTF: Northern bitlis Thrust fault; NLVF: Northern Lake Van fault; OtF: Otluk fault; SF: Süphan fault; VF: Varto fault; WLVF: Western Lake Van fault. Yellow pointed lines, P1 and P2 are the seismic reflection profiles of Toker et al. (2007). Red star: circular topographic feature. Projection: Geographic Lat / Long, European Datum 1950.

Conversely, Dewey et al. (1986) noticed that Quaternary volcanic deposits around Lake Van remain unfolded (Dhont and Chorowixz, 2006). Gülen (1984), re-interpreting seismic profiles of Wong and Finckh (1978), concluded that there are no major thrusts in these basins but mainly oblique-slip normal faults associated with subsidence (Dhont and Chorowixz, 2006). Muş basin is bounded to the north by the Otluk fault (OtF) and to the south by the Bitlis Thrust fault (NBTF). Dhont and Chorowicz (2006), specified the Otluk fault does not have the morphology of a reverse fault with a trace slightly curved rather than sinuous, and concluded that it forms the southern boundary of a tilted block represented by a planar erosion

surface dipping to the north. That tilted block is elongated up to Varto fault to the north, in an en-échelon manner, including Koruk faults (Fig. 5.6). Dhont and Chorowicz (2006) suggested that the Muş basin is an oblique-slip half-ramp basin and the Otluk fault is a transtensional dextral oblique-slip fault. Koçyiğit et al. (2001), defined the Otluk fault as a reverse fault, but also specified the considerable dextral component of the Otluk fault, and indicated that, this dextral movement was started with the inversion in the nature of tectonic regime in Pliocene.

Localized extension on Nemrut caldera

Focusing on the structure of Nemrut caldera will clarify its state in the general tectonic framework. On a volcanic edifice growing in relation to an extensional regime, the vents on its flanks are expected to be aligned perpendicular to the extension axes (Nakamura, 1977; Adiyaman, 2000). The elongation of the edifice is also expected to be parallel to the extension direction and perpendicular to the compression axis (e.g. Adıyaman et al., 1998; Nakamura, 1977). Holohan et al. (2005) well documented this phenomenon experimentally (Fig. 5.7); they concluded that elliptical calderas are formed above circular magma chambers when subjected to regional stress during formation. In the absence of regional forces, the local stress field due to a deflating (or inflating) oblate or spherical magma chamber will produce a circular caldera (Holohan et al., 2005). Acocella et al. (2005), also experimentally showed that the elongation of the calderas is parallel to the extension direction.

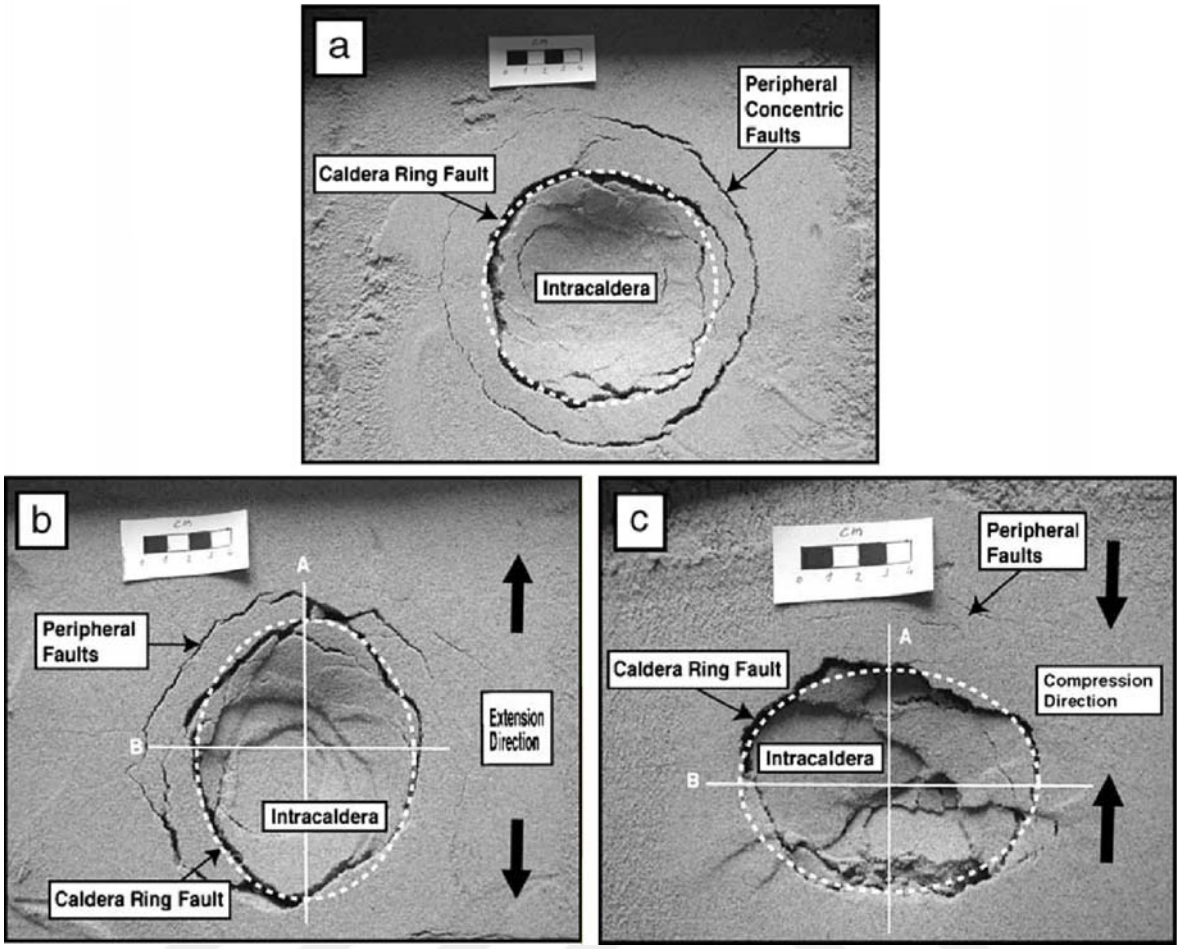

Figure 5.7. Plan view photographs of experimental caldera models made in sand under **a)** stress-free conditions, **b)** regional extension and **c)** regional compression. The major axes of calderas in compression/extension experiments were denoted the A- and B-axes (From Holohan et al., 2005).

Nemrut caldera is a semi-circular caldera with an aspect ratio of 0.85 (Fig. 5.8: B/A), and slightly elongated in E-W direction. In their experimental study, Holohan et al. (2005), stated that aspect ratio of the calderas in stress-free conditions is equal to 1. Under the extensional conditions they resulted that the average aspect ratio is 0.81 and 0.83 for deeper and shallower magma chambers, respectively. On the contrary, under compressional conditions, the average aspect ratio is 1.15 for both deeper and shallower magma chambers. Theoretically, for Nemrut caldera, such an elongation may be governed either by N-S compression or E-W extension. For the region both tectonic regimes are effective; but locally, the N-S directed extensional rift zone at north and N-S alignment of domes (Kale hills) at south highlights the dominant effect of extension (Fig. 5.8).

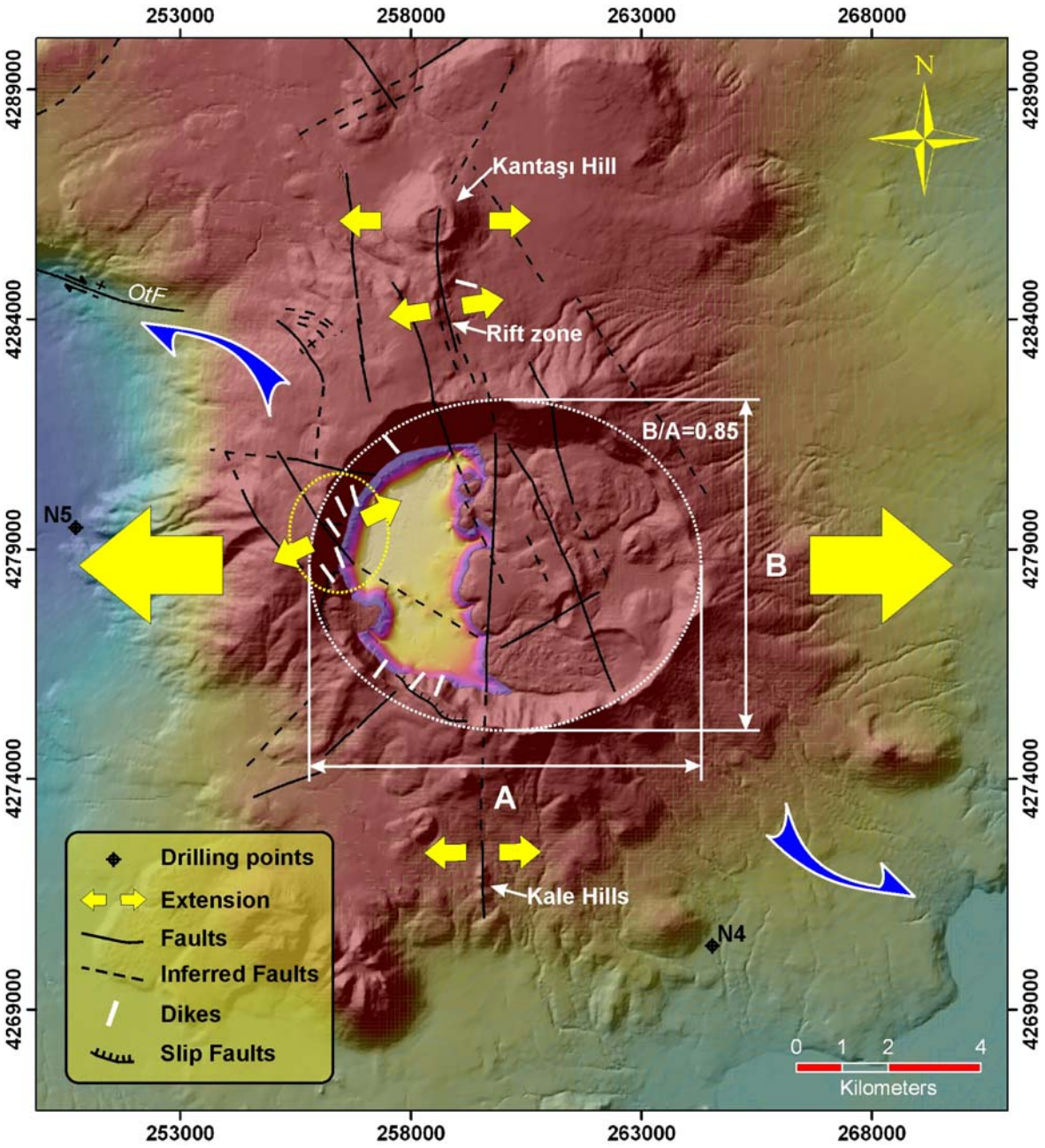

Figure 5.8. Tectonic effect on the structure of Nemrut caldera. Blue arrows indicate the shear stress forming the localized extension.

Peralkaline calderas are associated with areas of high extension (Cole et al., 2005). They are common in the East African Rift (e.g., Ethiopia; Acocella et al., 2003), but also occur in areas of unusually high rates of localized extension in convergent margin (e.g., Mayor Island, New Zealand; Houghton et al., 1992) or intra-plate oceanic islands (e.g., Canary Islands; Schmincke, 1967; Marti and Gudmundsson, 2000) (Cole et al., 2005). The genesis of Nemrut peralkaline magmatism in this collisional context has been ascribed to the localized extensions where the volcano has been located (Çubukçu, 2008).

Structural evidence of this localized extension appears on the western and northwestern sections of the caldera. Arc shaped fault on the northwestern flank of Nemrut caldera is most probably a track of a horsetail crack formed due to the oblique character of the Otluk fault. Same conclusion led Dhont and Chorowicz (2006), to interpret the Otluk fault as a transtensional dextral oblique-slip fault. Additionally, except the dikes on the western wall (Yellow pointed circle, Fig.5.8), radial emplacement of the dikes is evident on the caldera wall (Fig. 5.8). Dikes on the western wall, however, lie with an average angle of 64º, relative to the expected radial axis on the western flank of the volcano. Sheet intrusions are normally emplaced along planes perpendicular to the direction of the minimum principal compressive stress (σ_3) (Anderson, 1936; Pollard, 1987; Marinoni, 2001). Though, concerning these dikes, we can conclude an intrusion, where σ_3 is N26ºE (Fig. 5.8), favoring the effect of the shear force producing the arc-shaped fault on the northwestern flank. Generally, sheet intrusions produce the fracture, in which they propagate, although, given favorable boundary conditions, they may intrude suitably oriented pre-existing fractures (Delaney et al., 1986; Marinoni, 2001).

Structure of Lake Van Basin

Koçyiğit et al. (2001) defines Muş basin as the deformed and dissected remnant of the WNW-ESE-trending Oligo-Miocene Muş-Van basin located at the northern foot of the Bitlis suture zone (Fig. 5.6). This dissection, however, is of great importance on the initiation of Nemrut volcanism; it is best observed at north of the two basins. While the faults north of the Muş basin including the Otluk fault trend in WNW-ESE direction, the faults north of the Van basin trends in NE-SW direction (Fig. 5.6). In addition to this directional change, a change is also clear on the sense of the fault systems, dextral to sinistral. Moreover, paralleling the direction of faults, a bending of the topographic features, centered at north of Nemrut volcano is obvious (Fig. 5.6).

Following the initial bathymetric, geologic and geophysical studies (e.g. Wong and Degens, 1978; Wong and Finckh, 1978; Degens et al., 1984; Landmann, 1996; Landmann et al., 1996), recent geophysical studies provided a better approach on the nature of Lake Van. Seismic reflection profiles published by Toker et al. (2007) reveal that eastern and western edges of the basin are bounded by normal faults (Fig. 5.9a). Toker et al. (2007) interpreted the fault at the southern portion of

Tatvan basin (NBTF, Fig. 5.6) as a transtensive fault. However, this southern fault system defined as a thrust fault with a right-lateral strike-slip component (Pınar et al., 2007 and references therein).

Toker et al. (2007) also interpreted the circular topographic feature located at the southern end of the Profile 2 (red star in fig. 5.6) as a collapsed volcanic center; however, volcanic nature of this feature is debatable for us. Any type of volcanic feature at this location was never referred before, in the literature or in the geological maps. According to our limited observations based on remote sensing, this depression rather represents the characteristics of a sedimentary plain bounded by hills. On the other hand, Toker et al., (2007), and Horasan and Boztepe-Güney (2006), pointed out the seismic events of volcanic origin, which have been recorded in the Lake Van. At this point, it would be helpful to remind the mantle originated Helium contribution to Lake Van, using the ratio $^{3}He/^{4}He$, calculated as 75 % (Güleç et al., 2002; Kipfer et al., 1994). Moreover, Toker et al. (2007) indicated volcanic activity in their seismic reflection profiles under the lake (Fig. 5.9b). We also located seismic events of volcanic origin and events that present similar characteristics with VT-A events under Lake Van. In addition to the activity of Nemrut volcano, evidence of volcanic activity (gaseous activities and/or intrusions) are present under the Lake Van.

Pınar et al. (2007) specified that source mechanism of 15 November 2000 event (Fig. 5.6) that took place on the southern boundary fault of Lake Van (NBTF, Fig. 5.6) and its aftershocks, and concluded for an oblique component of the fault. In hence, dextral component of this fault and tensional faults at the western and eastern edge of Lake Van are in accordance with the E-W directed extension.

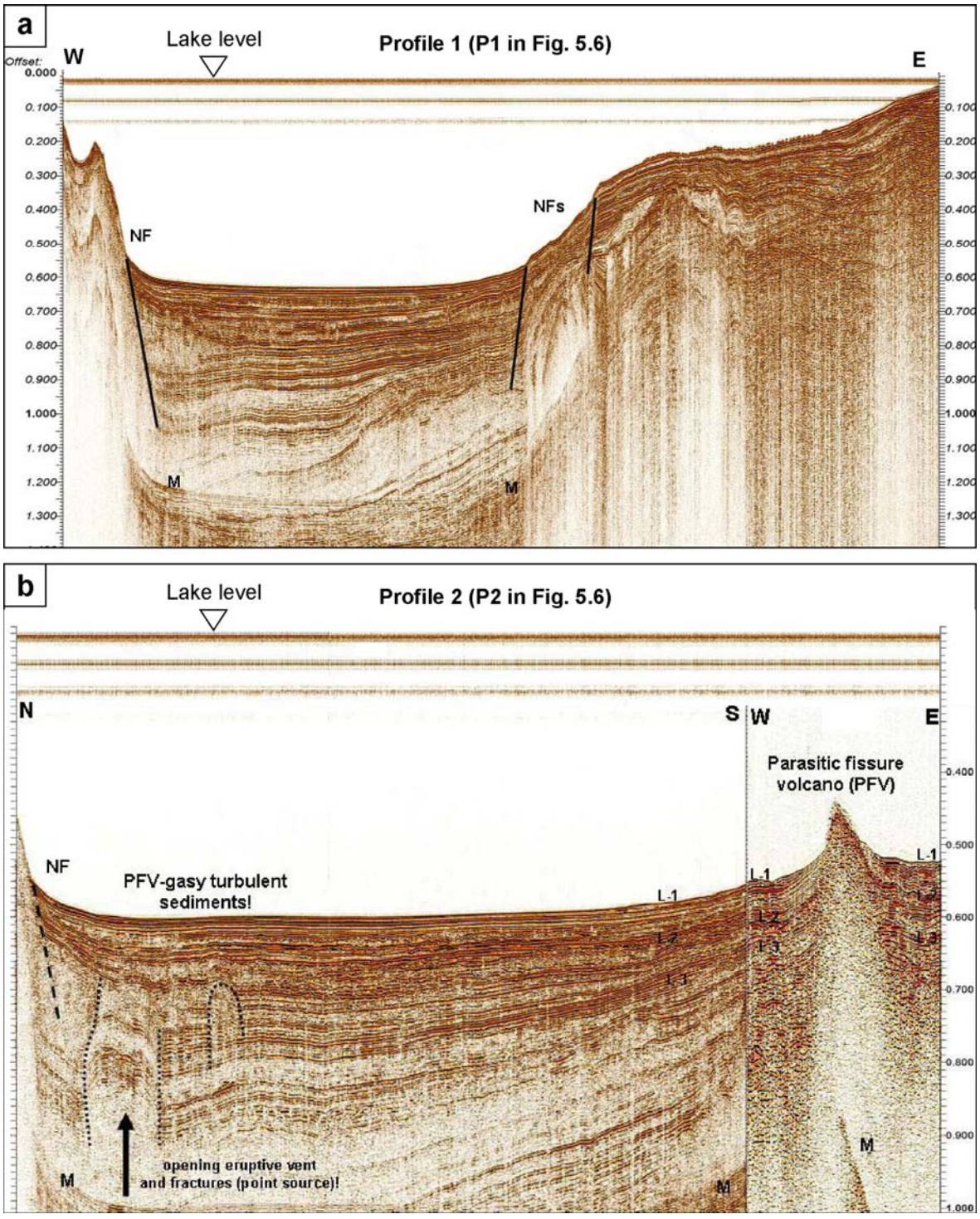

Figure 5.9. Seismic reflection profiles at Lake Van (From Toker et al., 2007; with their original interpretations). **a)** E-W profile; P1, as indicated in Fig. 5.6. Western and Eastern Lake Van boundary faults are clearly visible. **b)** N-S profile; P2, as indicated in Fig. 5.6. Inferred Norhtern Lake Van boundary fault is indicated.

Consequently, the inversion of tectonic regime in Pliocene (Koçyiğit et al., 2001; Bozkurt, 2001), and the initiation of strike-slip regime, structurally rooted and initiated the volcanism of Mt. Nemrut. Addition of strike-slip component to the preexisting structures have led localized extensions where Nemrut volcanic system has been preferentially emplaced (Blue arrow couple, Figs. 5.6 and 5.10). General tectonic frame based on our regional volcano-tectonic interpretation is presented in Figures 5.10 and 5.11.

N-S directed tensional fault system that shaped the edifice strongly suggests that Bilican volcano has also been shaped under the same extensional system (Fig. 5.10). However, lack of geochemical, geophysical, geological and structural data on the Bilican volcano limits us for a firm interpretation on the nature of this volcano.

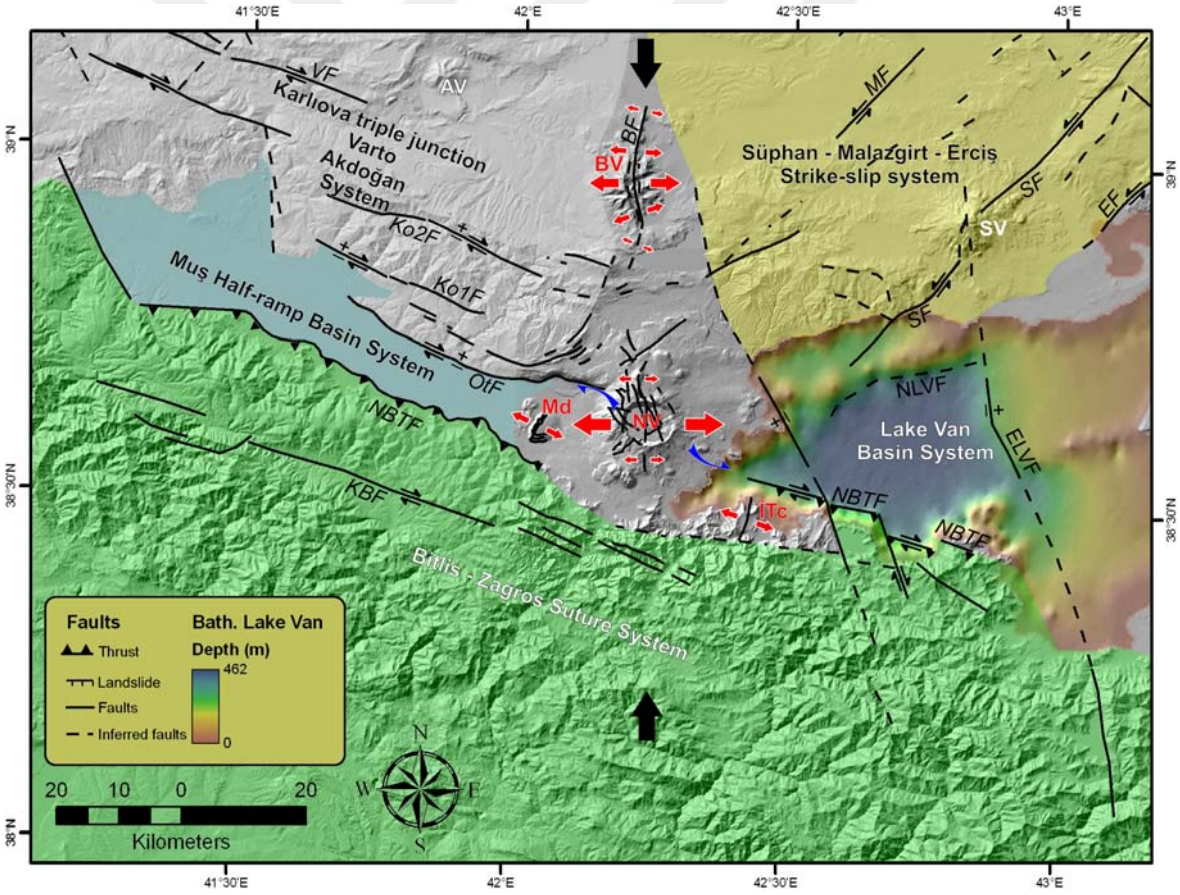

Figure 5.10. General tectonic frame around Nemrut volcano based on volcano-tectonic interpretations (Please refer to Fig. 5.6 for abbreviations). Projection: Geographic Lat / Long, European Datum 1950.

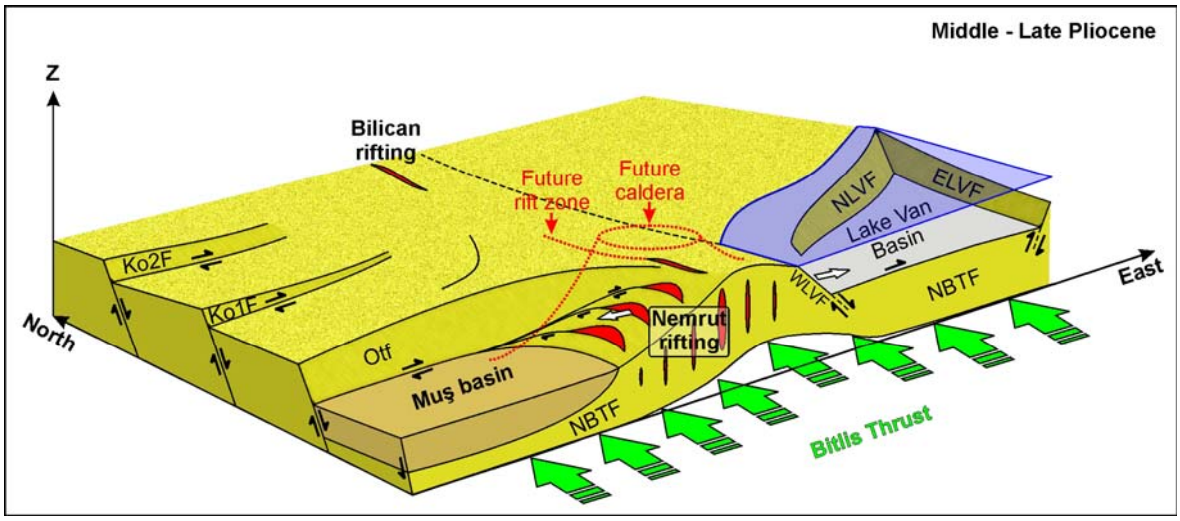

Figure 5.11. Simplified, hypothetic block model representing the role of tectonics in the initiation of Nemrut Volcanism (not in scale). ELVF: Eastern Lake Van Fault; Ko1F, Ko2F: Koruk Faults; NBTF: Northern Bitlis Thrust Fault; NLVF: Northern Lake Van Fault; OtF: Otluk Fault; WLVF: Western Lake Van Fault.

5.1.2. On the formation of Lake Van

Formation of Lake Van has often been ascribed to the eruptions of Nemrut volcano (e.g. Maxson, 1936; Blumenthal et al., 1964; Degens et al., 1984; Güner, 1984; Yılmaz et al., 1998). It has been said that the lava flows and/or pyroclastic eruptions of Nemrut would have blocked the discharge path of a river (older Murat valley) and rapidly formed the Lake Van. This hypothesis was first proposed by Maxson (1936), and has been accepted by following researchers, except Özpeker (1973b). One of the most important argument proposed by Özpeker (1973b), is the fossil rich (ostracoda) lacustrine sediments found at an altitude 86 m higher than the current lake-level (1773 m, Fig. 5.12a), suggesting a similar lake-level long before the Nemrut eruptions. Besides, during the latest 20 ka, fluctuations in the lake-level were documented by Landmann and Kempe (2005) (Fig. 5.12a, b). At north of Lake Van, at İnce cape (see Fig. 2.1 for the exact location), products of İncekaya Tuff cone are overlain by Nemrut Ignimbrites, suggesting that the tuff cone was present before the ignimbritic eruptions. High water influx is necessary to construct tuff cones (e.g. Fisher and Schmincke, 1984). Formation of İncekaya Tuff cone favors that the Lake Van was reached its current lake-level even before the Nemrut ignimbrites.

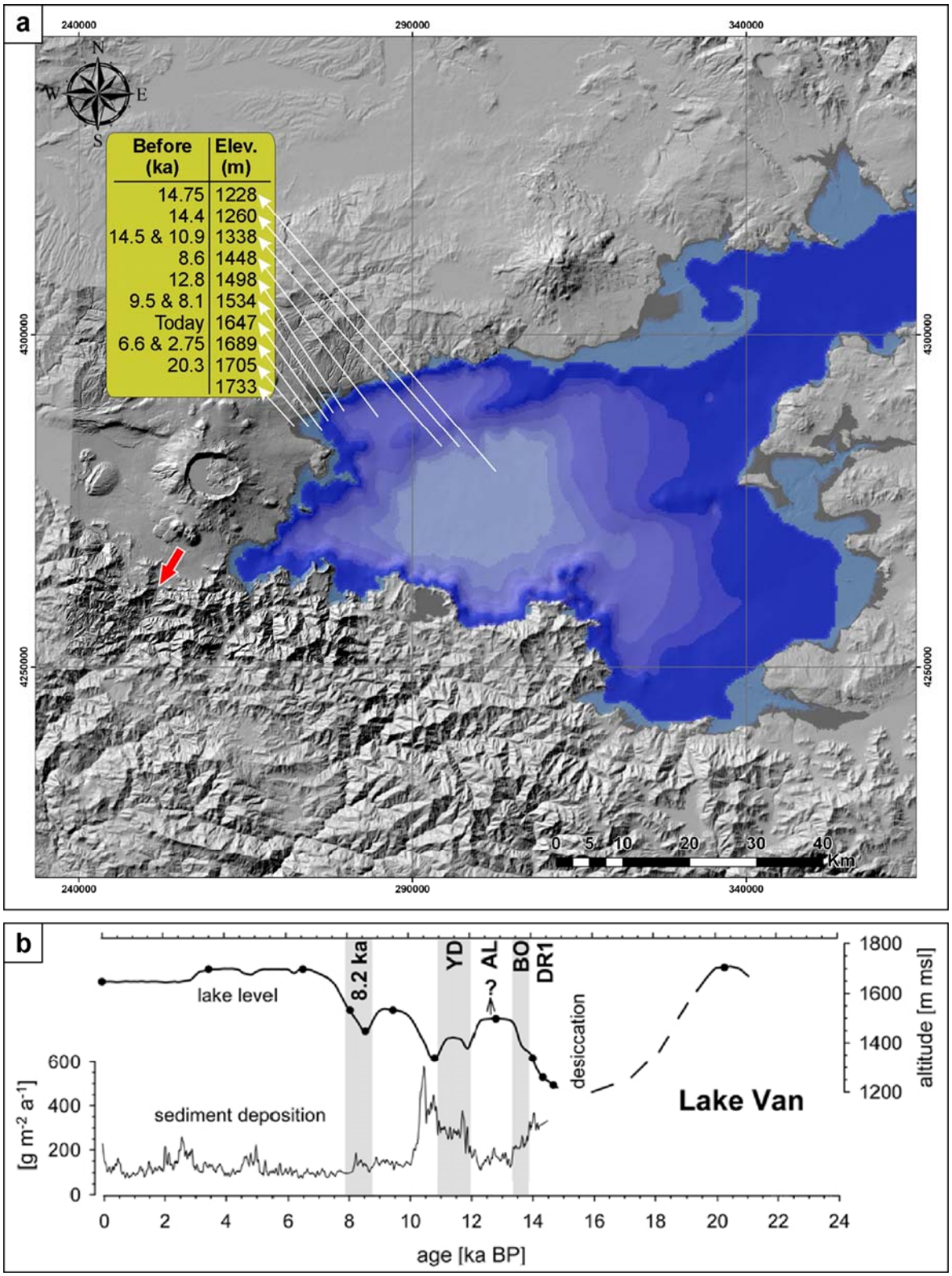

Figure 5.12. Lake Van, lake-level changes (data from Landmann and Kempe, 2005; Özpeker, 1073b). **a)** Map of lake-level change, **b)** change of lake-level in the last 20 ka (from Landmann and Kempe, 2005).

If we consider the topography before the emplacement of Nemrut ignimbrites, between Lake Van and Bitlis valley, it is possible to argue that, Bitlis valley might have been a discharge route of Lake Van as proposed by Özpeker (1973b). Özpeker (1973b) indicated that the older terraces of Bitlis river were 15-20 m higher than its current level. In the direction of Lake Van, the basement metamorphics were met at 65 m depth (Fig. 5.12: Red arrow) in a drilling point (Table 2.5, PID: 51). To crest this barrier, the lake level should have been at least 1713 m high.

5.2. Natural Risk potential of Nemrut volcano

Hydrothermal activity of Nemrut volcano has been previously discussed (e.g. Özpeker, 1973a; Güner, 1984; Atasoy et al., 1988); geochemical analysis of hydrothermal sources and fumaroles showed that the mantle derived "He" contribution to the hydrothermal sources is evident (e.g. Nagao et al., 1989; Kipfer et al.; 1994). Moreover, highest magmatic originated "He" contribution to the hydrothermal sources in Anatolia is observed on Nemrut volcano (Güleç et al., 2002). We also made temperature measurements of the sources; some with a daily period during one month (see Ulusoy et al., 2008). Hot sources around Ilığ Lake and Nemrut lake (Fig. 2 of Chapter 3.2) reach to ~60ºC and ~30 ºC, respectively. Hydrothermal activity of the Nemrut caldera has been mapped by Self-Potential measurements and TIR satellite imagery (Chapter 3; Ulusoy et al., 2008). Historical descriptions of Şerefhan (1597), show that, in addition to the hydrothermal activity he observed, northern rift zone was active during 1590's. Besides, volcano is seismically active too. During our monitoring between October, 2003 and October, 2005, volcanic originated events were observed and classified (Chapter 4).

Nemrut volcano is an active, quiescent volcano, and it is potentially hazardous for its vicinity. Monitoring of the volcano should be continued and improved. We reported our geological, geophysical and seismological results to the local authorities every two years with unpublished reports during our works, and attended to a local symposium to present our findings (Ulusoy et al., 2007). A topographic risk map was also presented to the local authorities after the publication of Aydar et al. (2003).

As we specified in Ulusoy et al. (2008), very large volume of Nemrut Lake (1.264 km^3) is a potential danger for southwestern settlements, especially for Güroymak town (see Chapter 3.2). We mapped two large landslides which took place on the SW caldera wall (Fig. 5.3). Flank landslide is one of the most important and common hazards that can happen in volcanic terrains (Merle et al., 2008). Triggering factors of such flank landslides include dyke or magma emplacement, earthquakes, a weak decollement horizon within the edifice, excess pore pressures due to intrusion, regional faulting, cryptodome emplacement, volcano spreading, changing sea levels and hydrothermal alteration (Merle et al., 2008 and references therein). It is highly possible for Nemrut Caldera to meet one or more of these conditions. The area is tectonically and seismically active and faults defined on the western and northwestern flanks (Ulusoy et al., 2008; Fig. 5.5) increases the possibility of such a cataclysmic event. In addition to the flank landslide, large volume of the Nemrut Lake doubles the danger. To face such cataclysmic events, there is no way to protect civilians but to evacuate the entire population from the area at risk, before the collapse occurs (McGuire, 2003, Merle et al., 2008). Land planning and settlement in the area must be organized considering the danger.

5.2.1. Small scale cold lahars

On 19.07.2007 and 11.03.2008, two small scaled cold lahar flows occurred on the flanks of the Nemrut volcano. First event was observed on the northeastern and southeastern flanks of the volcano and occurred just after a heavy rain. At the northeastern flank, near Serinbayır village (Fig. 2.28), the road to the mountain and some agricultural fields were destroyed and the lahar filled its flow channel (older stream channel) with ~1.5 m thick pyroclastic material (Fig. 5.13a,b). Same day, another relatively large flow occurred at the southeastern flank of the volcano. The flow totally destroyed the road between Yumurtatepe village (Fig. 2.28) and the Caldera rim, channeled in the drainage channels, filled them and reached to the Lake Van (Fig. 5.13c). The flow formed 50-60 m long fans in the shoreline of the Lake Van (Fig. 5.13c). Drainage channels prevented possible mud floods that might effect the settlement and the agricultural areas at the lower altitudes. On the other hand, agricultural areas at higher altitudes were partially affected and the bridges on the drainage channels were damaged.

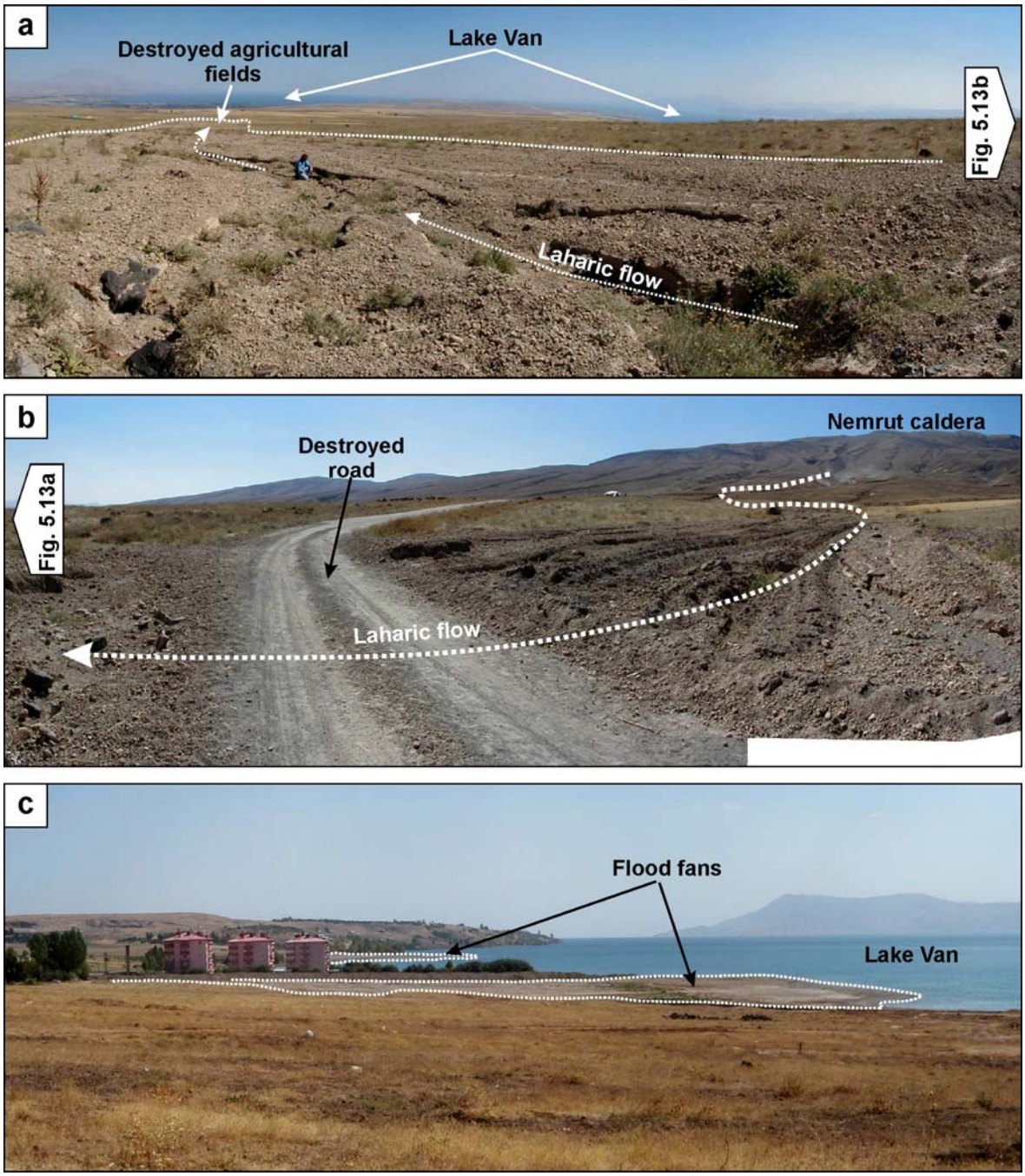

Figure 5.13. 19.07.2007 Lahar flows. **a,b)** Lahar flows originated from the northeastern flank of the caldera (destroyed road was bored by the villagers) and, **b)** Flood fans of the cold lahar flows in the Lake Van. These flows were originated from the southeastern flank of the caldera.

Second event (11.03.2008) happened on the northwestern flank of the volcano, and it was possible to observe this event on the satellite imagery (Fig. 5.14). News services reported that the event was caused by melting of the snow due to the rising air-temperature. Gölbaşı Town was highly affected from the flow. Agricultural fields were destroyed, ~100 houses were highly damaged; drains and sewers were totally filled.

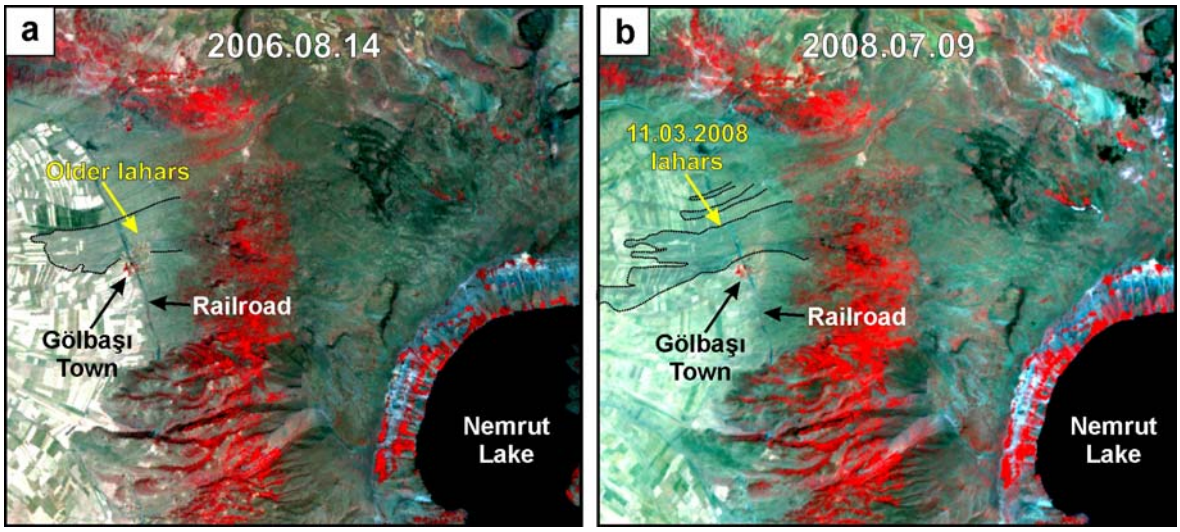

Figure 5.14. Two ASTER false color composite images demonstrating the difference before and after 11.03.2008 lahar flow event(images are from ASTER image database of volcanoes - Geological survey of Japan). **a)** ASTER VNIR image acquired on 14.08.2006, traces of older lahar flows are evident in the image. **b)** ASTER VNIR image acquired on 09.07.2008, Traces of lahar flows occurred on 11.03.2008 are visible with their darker colors.

5.3. Suggestions

Beyond doubt, our first and most important suggestion is the sustainable continuance of the monitoring of the volcano. Regarding the performance of the new data transfer protocol which will be installed till the end of 2008, installation of a new seismometer should be considered. The best location for the new instrument is the new ski-center constructed (in 2007) at the southern flank. It is the most closest, and secure place to install the equipment. Energy and data transfer issues may easily be solved at this location. The broadband seismometer located at Tatvan station may be transferred here, and a new short-period seismometer may be replaced at Tatvan station. Installation of a new station at the flank of the volcano where the artificial noise is low will surely provide precious data; and a fourth station will support the other three stations in case of a failure in one of them. A sustainable budget for the travel and maintenance expenses is essential. A local contributor may surely provide and improve the sustainability of the network. Newly founded Bitlis Eren University may be a possible address for this contribution.

With the change of the data transfer protocol, software system used in the analysis must be revised and adopted to the new system. Digitizers of the seismometers have the capability of applying STA/LTA triggering in-situ and the new protocol

have the capability to provide the necessary data flow velocity to send both triggered and raw 100 SPS data. Consequently, the code “Nemtrig” is going to be out of usage. Instead, a new, easy code that will convert triggered data from GCF format to SAC format will be required. Güralp Systems provide an executable single file which does this conversion; we used this converter at the background of Nemtrig code. The new data acquisition protocol will surely simplify the duty of the network manager. Other present codes such as “Nemtract” and “Nemspec” may still be used in the analysis workflow without any problems.

Risk and Hazard modelling is essential for the volcano. The modelling should primarily include the modelling of the impact areas of lahar risk, as well, pyroclastic activity risk should also be considered. High resolution imagery will provide tremendous amount of data and informations for the hazard modelling. During this study a large GIS database was constituted. All further research may be added on this large information database.

Further geophysical surveys will also provide valuable information on the volcano. During this study, Self-Potential map of the caldera was completed. Two additional profiles were measured out of the caldera. A new Self-potential survey covering the area out of the caldera will quantify the hydrothermal system precisely. Total profiles length for this type of survey is roughly estimated as 170 km. The northern rift zone may be mapped in high resolution.

Intra-caldera topography is very suitable for a multi-electrode resistivity survey. Multiple, parallel resistivity imaging profiles which may be set in NE-SW direction will precisely demonstrate the intra-caldera structural system. Together with the Self-potential data, resistivity imaging will provide valuable information on the shallow structure of the calderas. Finally, deep resistivity survey may provide a noteworthy contribution.

5.4. Ongoing works

5.4.1. On the calculation method of Ce Map

SP/elevation gradient (Ce-gradient) calculation method proposed by Lénat (2007), which was used to produce Ce-gradient map of Nemrut volcano (Ulusoy et al., 2008) calculates the gradient in four directions (N-S, E-W, NW-SE and NE-SW). Using an array-type operator could overcome the limitations of calculations with

four directional operators. For this purpose, a computer code using an array-based operator was designed and tested. The code uses a procedure that may be named as “Swirl procedure”. Swirl procedure depends on swirling two (in this case PS-PS or DEM-DEM) images (arrays) and applying a mathematical operation to overlapped pixels during swirling (Fig. 5.15a). Using PS image and DEM, this operation allows calculating ΔV or Δz between two points in image array (Fig 5.15a).

In swirl operation, the duplicate of the image array is shifted on the same image by predefined number of pixels. This predefined “number of pixels” can be called as “swirl degree”. A duplicate (red) of a 5x5 array (yellow) is shifted over the same image by 2 pixels in Figure 5.15b; therefore swirl degree is “2”. Using this condition of the shifted images (Fig. 5.15b), a mathematical operation between points A and B (or C and D) can be made (Fig. 5.15c). When the duplicate image is swirled on the original image, depending on the swirl degree, a mathematical operation can be applied on certain angles. These specific angles according to swirl degree are listed in Table 5.2. With the change of swirl degree, the lateral difference between pixels (dx) also changes for every point calculated.

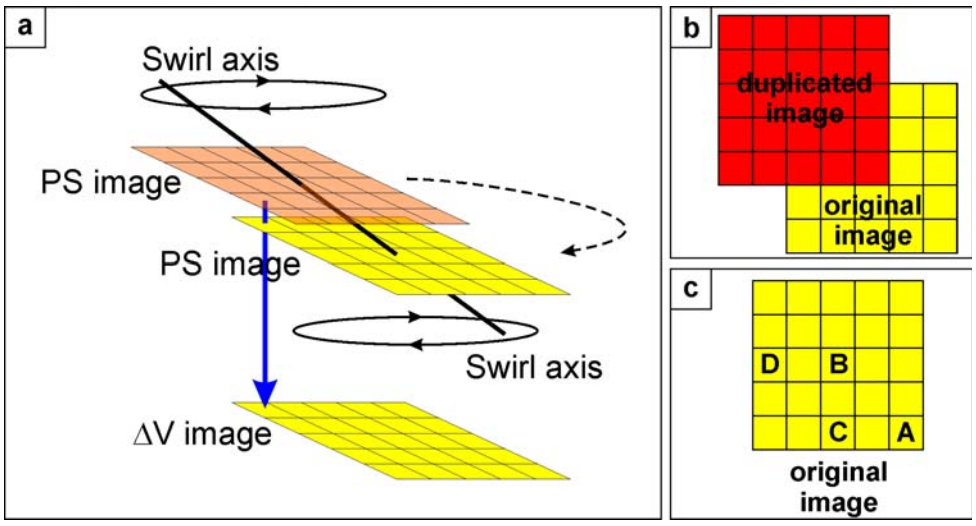

Figure 5.15. Principles of Swirl operation **a)** Swirl procedure using a duplicated Self-Potential (PS) image pair, to produce ΔV image. **b)** Image pairs shifted with a swirl degree of 2. **c)** Sample Pixel pairs (A-B and C-D) that the calculation will be based on with a swirl degree of 2.

Swirl degree	1	2	3	4	5	6	7	8	9	10
Operation angle	45.00	22.50	11.25	5.63	2.81	1.41	0.70	0.35	0.18	0.09

Table 5.2. Swirl degree and the corresponding angle between calculated pixels.

Two ways of calculation can be applied using swirl procedure: “Full-swirl” and “limited-swirl”. In the full-swirl calculation, all the neighboring pixels up to swirl degree are taken into account and final value of center pixel is calculated upon these neighboring pixels. On the other hand, limited-swirl operator uses only the pixel values defined by the swirl degree for the calculation. The contribution of pixels to the operation in full-swirl procedure (Fig. 5.16a), and in limited-swirl procedure (Fig. 5.16b), when the swirl degree = 2 is shown in Figure 5.16. Red point symbolizes the calculated center value and the black points symbolize the contributing neighboring pixels. Desired mathematical operation could be applied for all the pixels in the image. If the swirl degree = 1 there is no difference between full-swirl and limited-swirl procedures (Fig. 5.16c).

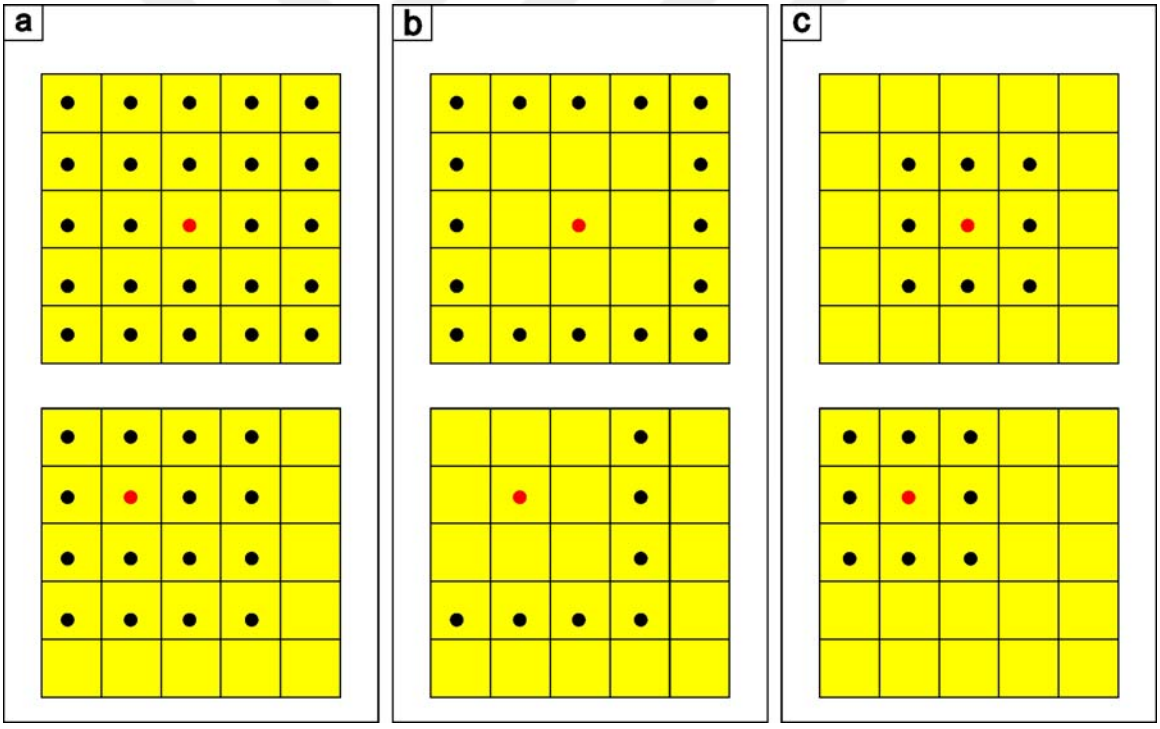

Figure 5.16. Principles of Full-swirl and Limited-swirl procedures. Contributions of pixels in, **a)** Full-swirl procedure **b)** Limited-swirl procedure, for swirl degree = 2 and, **c)** for swirl-degree =1.

Ce gradient calculation

PS-altitude gradient (Ce) can be calculated using swirl procedure. A copy of PS image can be swirled on itself to calculate ΔV between two pixels (Fig. 5.17). Similarly, when swirl procedure is applied to a DEM covering the same area and resolution with PS image, Δz for same points used in PS swirl procedure can be calculated (Fig. 5.17). Using ΔV and Δz values four different methods can be applied to calculate Ce values:

Method 1: Ce-mean calculation using full-swirl procedure,
Method 2: Ce-mean calculation using limited-swirl procedure,
Method 3: Ce-max calculation using full-swirl procedure,
Method 4: Ce-max calculation using limited-swirl procedure.

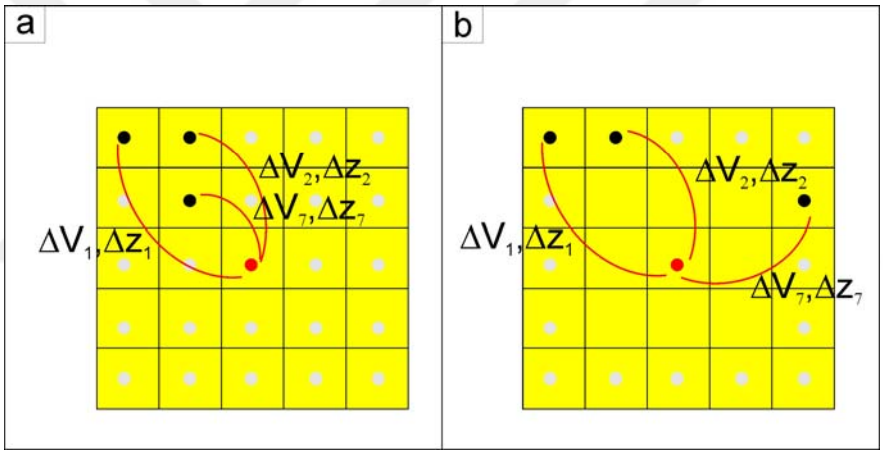

Figure 5.17. Swirl procedures used to calculate Ce-gradient. Black and grey points are representing the contributing pixel values to calculate final (red) value. **a)** Calculation of ΔV and Δz in full-swirl procedure for swirl degree = 2, **b)** Calculation of ΔV and Δz in limited-swirl procedure for swirl degree = 2.

We wrote an IDL code to calculate the Ce-gradient map, which is using the following equations for the four methods described above:

Method 1 and 2:

$$f(Ce-mean)=\left(\frac{\frac{\Delta V_1}{\Delta z_1}+\frac{\Delta V_2}{\Delta z_2}+\ldots+\frac{\Delta V_7}{\Delta z_7}+\ldots+\frac{\Delta V_n}{\Delta z_n}}{n}\right)$$

Method 3 and 4:

$$f(Ce-\max)=MAX\left(\frac{\Delta V_1}{\Delta z_1},\frac{\Delta V_2}{\Delta z_2},...,\frac{\Delta V_7}{\Delta z_7},...,\frac{\Delta V_n}{\Delta z_n}\right)$$

At the end of the calculation Ce_calc code can filter the final image using median filter of selected kernel size. Advantages of this method are: 1) array based code can make the calculations rapidly, 2) Ce gradient calculations can be made using wide range of neighboring values (and more then 4 directions) which increases the reliability of the result. Where Δz values are very low (i.e. <1m for a dataset with 25 m spatial resolution), resulting Ce-gradient is relatively more reliable than a calculation in 4-direction. Still, where Ce values are abnormally high due to low Δz values, it is possible to eliminate this effect by blinding low Δz values, using a NaN (not a number) definition in the code. Finally, when the code ran, due to the calculation method, a cropping related to the swirl degree is occurred on the final Ce-gradient image.

Artificial dataset test run

We have produced an artificial dataset (Fig. 5.18) which consists of PS and DEM sets (each set is an array of 90x58 pixels and have 16 m resolution). Using this dataset, Ce maps were calculated by our code with four methods described above (Fig. 5.19a,b,c,d). Calculation of Ce-mean, using Method 1 gave the most reliable output. Both positive and negative Ce-value ranges and the anomalies of Ce are consistent with the PS dataset. Ce-max calculators failed because: a) they don't enclose the maximums in the negative range; b) maximum values are abnormally high. Code may be changed in an appropriate way to recalculate the negative maximum values (minimums), but the resulting positive and negative range of values will be still too high.

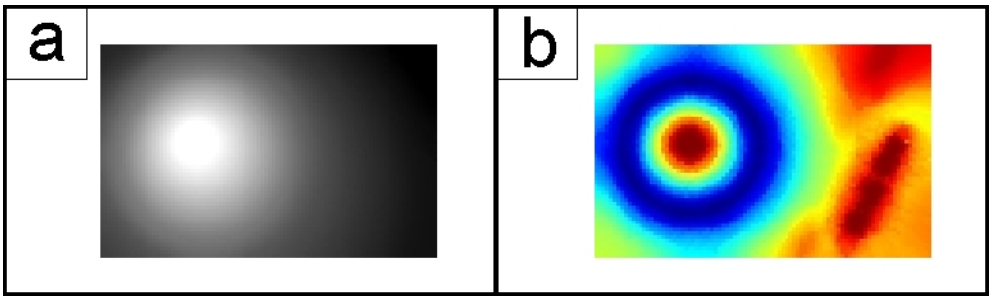

Figure 5.18. Artificial dataset to calculate Ce-gradient image. Artificial **a)** DEM and **b)** PS images.

Real dataset test run

The code was also used to produce Ce-gradient from Nemrut datasets and the output is given in Figure 5.20a. The old Ce map produced by code of Lénat is given in Figure 5.20b. Note that, identical color ramps were used for Ce-gradient images for a better comparison.

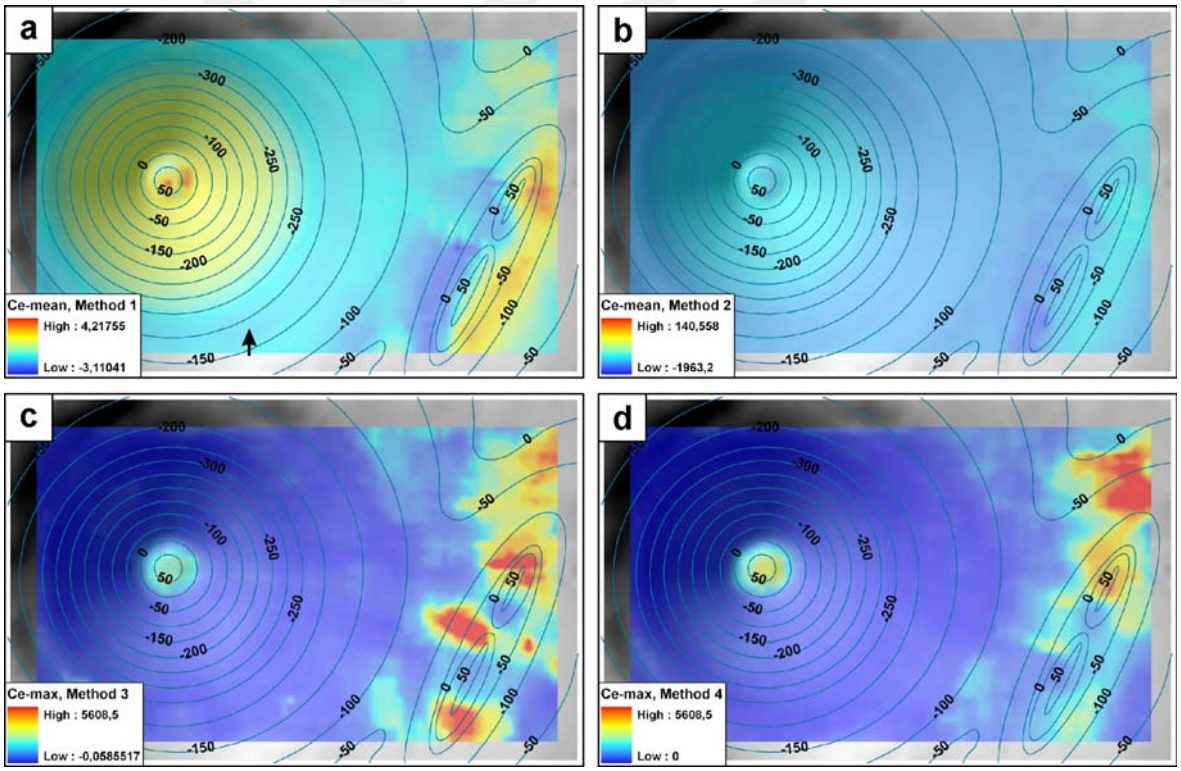

Figure 5.19. Ce-gradient maps produced with Swirl method, using artificial dataset. Swirl degree = 5, median filter size = 5x5. Final Ce-gradient image is overlapped on hillshade of artificial DEM. Contour lines show the artificial PS data. **a)** Ce-mean calculated with method 1, **b)** Ce-mean calculated with method 2, **c)** Ce-max calculated with method 3 and **d)** Ce-max calculated with method 4.

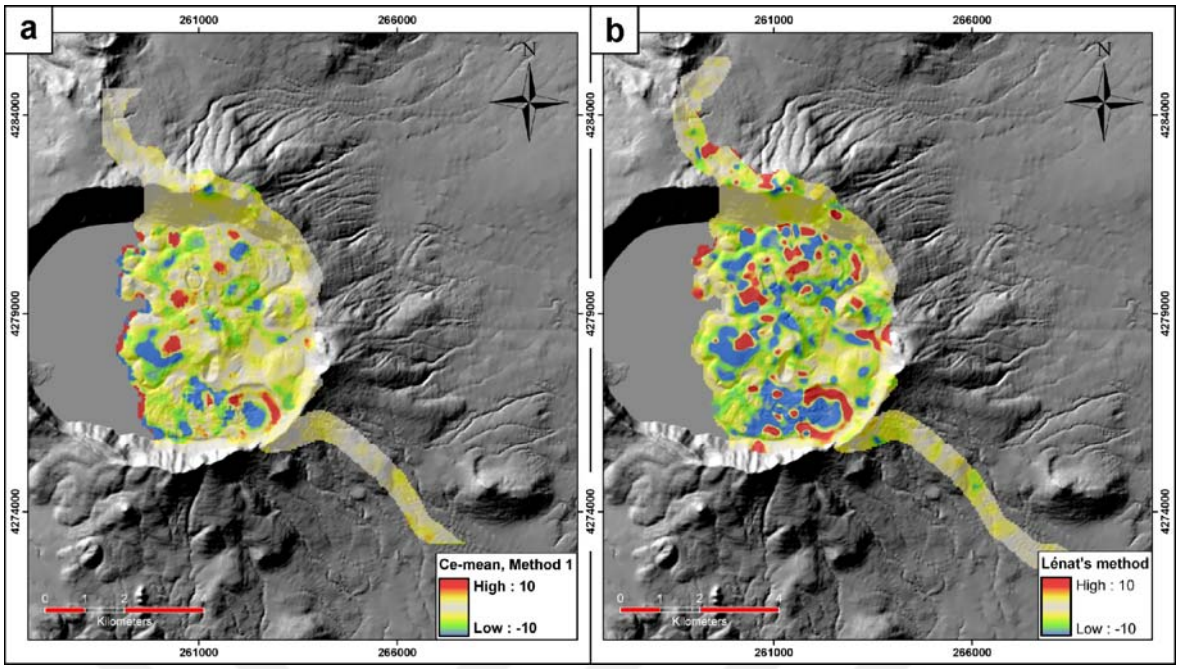

Figure 5.20. Ce-gradient maps of Nemrut caldera. Both gradient images were filtered with a 5x5 median filter. **a)** Ce-gradient (Ce-mean) calculated with swirl procedure (swirl degree = 5), method 1, **b)** Ce-gradient calculated using the method defined by Lénat (2007).

Swirl procedure could be used in various applications (e.g. ΔT calculations with Thermal satellite imagery, topographic corrections in geophysics). Our studies on various uses of swirl procedure continue; a short paper describing the procedure and its applications will soon be prepared for publishing.

5.4.2. Lightweight multi-electrode resistivity cabling system

Computer-controlled data acquisition systems of DC resistivity imaging techniques generally consists of a resistivity instrument, a relay switching unit, a computer, electrode cables, various connectors and electrodes (e.g. Overmeeren and Ritsema, 1988; Dahlin, 1993, 2001). In some cases two or more components are housed in the same box, e.g. a computer integrated with the instrument (Dahlin, 2001). Some systems employ intelligent switches at each electrode take-out instead of a central switching unit (Dahlin, 2001). Commercially available resistivity imaging systems, especially the ones for long surveys are expensive and equipment (especially the cable) is heavy. We are currently developing a new resistivity cabling system which is reducing the cable weight to a considerable value and which is cheaper than the convenient systems (The work was carried out with Prof. Erkan Aydar and Assist. Prof. Harun Artuner). The system is using intelligent switch nodes which are connected to every electrode of the profile (Fig. 5.21a). The difference of the system from the other intelligent switching systems is the number of wires in the main cable. The system uses 6 wires in the main cable, 4 of them are used to measure the resistivity and the other 2 wires are used to control the switching system. We adopted a resistivity-meter to our cabling system which is capable of providing digital output (Fig. 5.21b). The resistivity-meter is connected to a controlling device which is used to communicate with the computer and intelligent switch nodes (Fig. 5.21b). In the operation, switching nodes connected to the electrodes are automatically recognized and a number is assigned to each of them by the control device. Then using a predefined dataset, multi-electrode resistivity measurement is applied. The system must be improved to test the connectivity of the electrodes layout; it is preconfigured with a capability to make the connectivity test. The weight of the new cabling system is 75% less than the convenient resistivity systems which are using a central relay switching unit. The cost of the new cabling system is 2500 Euros. A patent application will soon be made for the new system. The most recently patented similar system (Abdelhadi, 2007) uses 10 cables and more complex relay units.

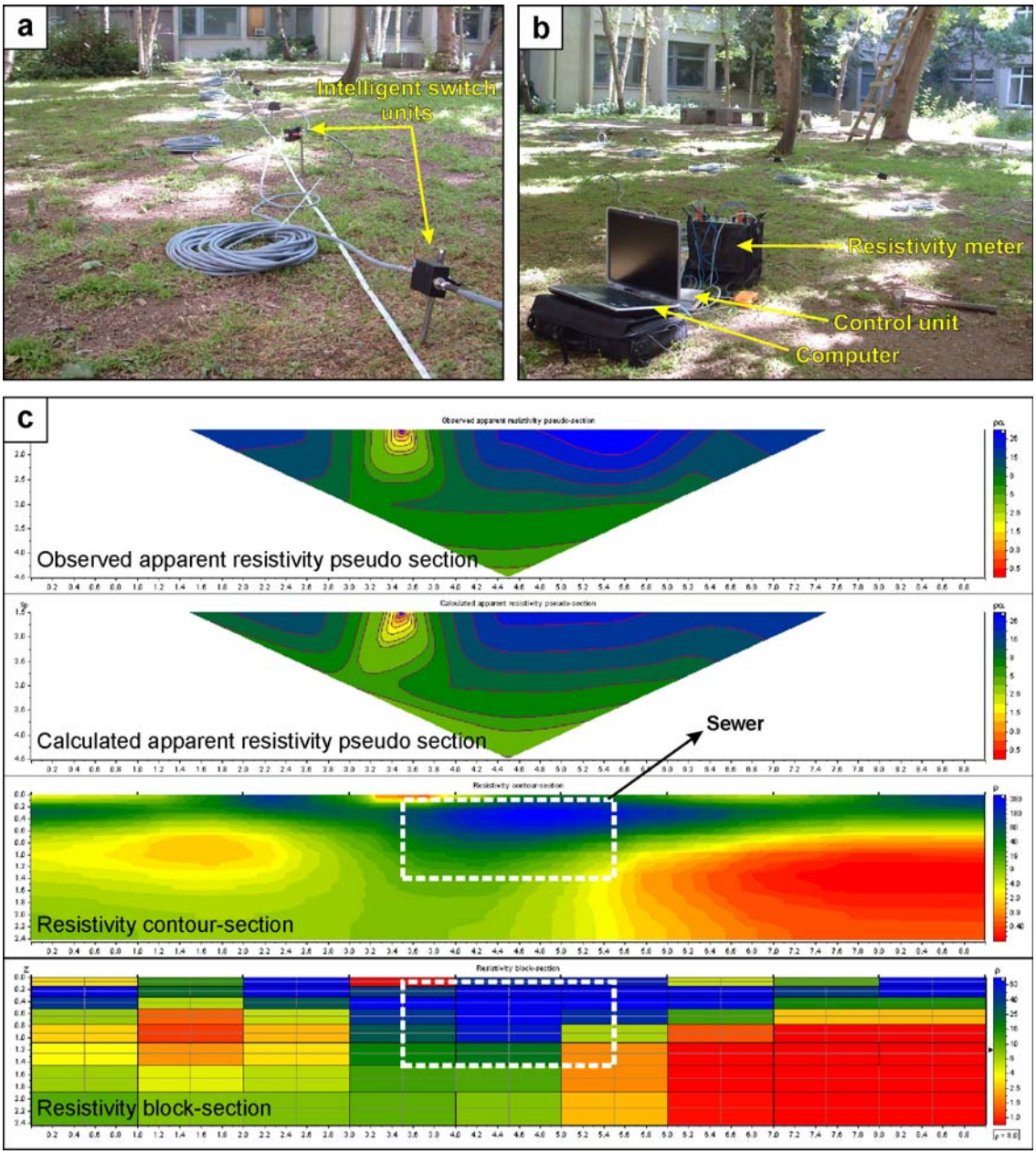

Figure 5.21. Resistivity imaging cabling system. **a)** Intelligent switching nodes connected to the new cabling system in a test array. **b)** Photograph introducing the cabling system. **c)** Result of a 1 meter spaced test profile (20 itterations, Final RMS fit: 1.15). Data inversion was made using Prof. Andrew Binley's ProfileR software.

References cited

Şerefhan (1543-1604)

A

Abrams, M., and Hook, S., 2002. ASTER user handbook. Pasadena, CA: Jet Propulsion Laboratory. 135 pp.

Abdelhadi, A., 2007. Identically programmed intelligent electrodes for use in geoelectrical surveys. United States Patent, US7158048-B2.

Acocella, V. and Funiciello, R., 1999. The interaction between regional and local tectonics during resurgent doming: the case of the island of Ischia, Italy. J. Volcanol. Geotherm. Res. 88: 109-123.

Acocella, V., Korme, T. and Salvini, F., 2003. Elliptic calderas in the Ethiopian Rift: control of the pre-existing structures. J. Volcanol. Geotherm. Res. 119: 189-203.

Adıyaman, Ö., Chorowicz, J. and Köse, O., 1998. Relationships between volcanic patterns and neotectonics in Eastern Anatolia from satellite images and DEM, J. Volcanol. Geotherm. Res., 85: 17-32.

Adiyaman, Ö., 2000. Relations entre volcanisme et tectonique en contextes de collision et de deécrochement (Turquie). Approche par analyse structurale, géochimie, imagerie spatiale, modeles numériques de terrain et systemes d'information geographique. PhD thesis, Univ. P. et M. Curie Paris VI, Paris, France.

Anderson, E.M., 1936. The dynamics of formation of cone-sheets, ring-dykes and cauldron-subsidences. Proc. R. Soc. Edinburgh, 56: 128-163.

Angus, D.A., Wilson, D.C., Sandvol, E. and Ni, J.F., 2006. Litospheric structure of the Arabian Eurasian collision zone in eastern Turkey from S-wave receiver functions, Geophys. J. Int., 166: 1335-1346.

Atasoy, E., Terzioğlu, N., and Mumcuoğlu, H.Ç., 1988. Nemrut volkanı jeolojisi ve jeotermal olanakları. T.P.A.O. Research group Report. pp. 109.

Aydar, E., 1992. Etude volcano-structurale et magmatologique du strato-volcan Hasan Dagi (Anatolie centrale-Turquie). These de Doctorat. Univ. Blaise Pascal-France, 200p.

Aydar, E., Gourgaud, A., Ulusoy, I., Digonnet, F., Labazuy, P., Sen, E., Bayhan, H., Kurttas, T. and Tolluoglu, A.U., 2003. Morphological analysis of active Mount Nemrut stratovolcano, eastern Turkey: evidences and possible impact areas of future eruptions. J. Volcanol. Geotherm. Res., 123: 301-312.

Ayhan, E., Kalafat, D., İnce, Ş. and Öğütçü, Z., 1988. İstasyon Sayısı ile Magnitüd ilişkisi kullanılarak 1976-1989 Batı Türkiye Depremlerine Magnitüd Verilmesi, Deprem Araştırma Bülteni, 63, 99-130.

B

Bal, S., 1986. Bitlis-Tatvan-Nemrut sahası Jeotermal Manyetik etüdü, MTA report, 8p.

Barka, A.A., 1992. The North Anatolian Fault zone, Annales Tecton., 6: 164-195.

Barka, A.A. and Reilinger, R., 1997. Active tectonics of the Mediterranean region: deduced from GPS, neotectonic and seismicity data, Annali di Geophis., XI: 587-610.

Beresford, S.W. and Cole, J.W., 2000. Kaingaroa Ignimbrite, Taupo Volcanic Zone, New Zealand: evidence for asymmetric caldera subsidence of the Reporoa Caldera. N.Z. J. Geol. Geophys 43: 471-481.

Black, J. and Green, A., 1992. Gods, Demons and Symbols of Ancient Mesopotamia: An Illustrated Dictionary, ISBN: 978-0-292-70794-8, British Museum Press.

Black, J.A., Cunningham, G., Robson, E., and Zólyomi, G., 1998. The Electronic Text Corpus of Sumerian Literature, (http://etcsl.orinst.ox.ac.uk/) Oxford.

Blendford, R.R., 1982. Seismic event discrimination. Bull. Seism. Soc. Am., 72: S69-S87.

Blumenthal, M.M., van der Kaaden, G. and Vlodavetz, V.I., 1964. Catalogue of the active volcanoes of the world including solfatara fields, Part XVII, Turkey and the Caucasus, Internat. Assoc. Volcanology, pp. 23.

Bozkurt, E., 2001. Neotectonics of Turkey - a synthesis. Geodinamica Acta, 14/1-3: 3-30.

Branney, M.J. and Kokelaar, B.P., 1994. Volcanotectonic faulting, softstate deformation and rheomorphism of tuffs during development of a piecemeal caldera, English Lake District. Geol. Soc. Am. Bull. 106, 507– 530.

C

Chouet, B.A., 1996. Long-Period volcano seismicity: Its source and use in eruption forecasting. Nature, 380, 309-316.

Civco, D.L., 1989. Topographic normalization of Landsat thematic mapper digital imagery. Photogrammetric Engineering and Remote Sensing 55, 1303-1309.

Cole, J.W., Milner, D.M. and Spinks, K.D., 2005. Calderas and caldera structures: a review. Earth-Science Reviews, 69: 1-26.

Coolbaugh, M.F., Kratt, C., Fallarco, A., Calvin, W.M. and Taranik, J.V., 2007. Detection of geothermal anomalies using Advanced Spaceborne Thermal Emission and Reflection Radiometer (ASTER) thermal infrared images at Bradys Hot Springs, Nevada, USA. Remote Sensing of Environment 106, 350-359.

Craig H, Clarke W B, Beg M A. 1975. Excess ^{3}He in deep water on the East Pacific Rise, Earth Planet. Sci Lett., 26: 125-132.

Ç

Çilingiroğlu, A., Urartu Krallığı Tarihi ve Sanatı, İzmir 1997.

Çubukçu, E., Aydar, E. and Gourgaud, A., 2007. Comment on "Volcanostratigraphy and petrogenesis of the Nemrut stratovolcano (East Anatolian High Plateau): The most recent post-collisional volcanism in Turkey" by Ozdemir et al., 226 (2006) 189-211, Chemical Geology.

Çubukçu, H. E., (2008). Petrologic evolution of Nemrut Stratovolcano (Turkiye): Peralkaline magmatism in a collisional domain, PhD Thesis, Hacettepe University, Turkey and Univ. Blaise Pascal-France,, 223pp.

D

Dahlin, T., 1993. On the automation of 2D resistivity surveying for engineering and environmental applications. PhD Thesis, ISRN LUTVDG/TVDG–1007–SE, ISBN 91-628- 1032-4, Lund University, 187pp.

Dahlin, T., 2001. The development of DC resistivity imaging techniques, Computers and Geosciences, 27(9), 1019-1029.

Degens, E.T., Wong, H.K., Kempe, S. and Kurtman, F., 1984. A geological study of Lake Van, eastern Turkey. International Journal of Earth Sciences, 73(2): 701-734, doi:10.1007/BF01824978.

Delaney, P.T., Pollard, D.D., Ziony, J.I. and McKee, E.H., 1986. Field relations between dykes and joints: emplacement processes and paleostress analysiss. J. Geophys. Res., 91: 4920-4938.

Dewey, J.F., Hempton, M.R., Kidd, W.S.F., Şaroğlu, F. and Şengör, A.M.C., 1986. Shortening of continental lithosphere: the neotectonics of Eastern Anatolia—a young collision zone, in Collision Tectonics, 19 (R. M. Sheckleton volume), pp. 3–36, eds. M.P. Coward & A.C. Ries, Geol. Soc. London Spec. Pub.

Dewey J.F. and Şengör, A.M.C., 1979. Agean and surrounding regions: Complex multiplate and continuum tectonics in a convergent zone, Geol. Soc. America Bull., Part 1., 90: 84-92.

Dhont, D. and Chorowicz, J., 2006. Review of the neotectonics of the Eastern Turkish – Armenian Plateau by geomorphic analysis of digital elevation model imagery. Int. J. Earth Sci., 95: 34-49.

Dhont D., Yanev, Y., Bardintzeff, J.-M. and Jean Chorowicz, J., 2008. Evolution and relationships between volcanism and tectonics in the central-eastern part of the Oligocene Borovitsa caldera (Eastern Rhodopes, Bulgaria). J. Volcanol. and Geotherm. Res., 171: 269-286.

Dominguez, T., Zobin, V.M. and Reyes-Davila, G.A., 2001. The fracturing in volcanic edifice before an eruption: the June-July 1998 high-frequency earthquake swarm at Volcan de Colima, Mexico. J. Volcanol. and Geotherm. Res., 105: 65-75.

E

Elachi, C., 1987. Introduction to the Physics and Techniques of Remote Sensing, New York: John Wiley and Sons. 432 pp.

Ercan, T., Fujitani, T., Matsuda, J.I., Notsu, K., Tokel, S., Ui, T., 1990. Doğu ve Güneydoğu Anadolu Neojen-Kuvaterner volkaniklerine ilişkin yeni jeokimyasal, radyometrik ve izotopik verilerin yorumu. MTA Dergisi, 110, 143-164.

Ersoy O., Chinga G., Aydar E., Gourgaud A., Cubukcu H.E., Ulusoy I., 2006. Texture discrimination of volcanic ashes from different fragmentation mechanisms: a case study, Mount Nemrut stratovolcano, eastern Turkey. Computers and Geosciences, 32: 936-946.

F

Faccenna, C., Bellier., O., Martinod, J., Piromallo, C. and Regard, V., 2006. Slab detachement beneath eastern Anatolia: A possible cause for the formation of the North Anatolian fault, Earth and Pla. Sci. Lett., 242: 85-97.

Feraud J. and Özkocak Ö., 1993. Les volcans actifs de Turquie: guide geologique et itineraires de'excursions. L'Assoc Volc Europeenne (LAVE), 2: 1-82.

Fisher, R.V. and Schmincke, H.-U., 1984. Pyroclastic Rocks, Springer, Heidelberg 474 pp.

Foster, K.P., 2000. Volcanic Landscapes in LUGAL-E in L, Milano, L. et al., 1997. Landscapes XLIV RAI, Part III: Landscape in Ideology, Religion, Literature and Art, Paduna, 23-39.

Frechet, J., and Thouvenot, F., 1990. SISMALP Library: Seismic Data Acquisition and Processing, in 'Applications of Personal Computers in Seismology', XXII ESC Gen. Ass., Geol. Survey of Catalunya, Barcelona, p 35-38.

G

Gadjimuradov, I. and Schmoeckel, R., 2005. Das Geheimnis des anatolischen Meeres. Der Garten Eden, die Sintflut und die Hölle, ISBN 3-8334-2692-6, Herstellung und Verlag, Bonn.

Garfunkel, Z., 1998. Constrains on the origin and history of the Eastern Meditarrenean basin, Tectonophysics, 298: 5-35.

Gunderson, R. 1988. Geological summary of Nemrut volcano, Eastern Turkey: UNOCAL Geothermal Geology Report, 8p.

Gutenberg, B. and Richter, R.F., 1944. Frequency of earthquakes in California. Bull. Seismol. Soc. Am., 34: 185-188.

Güleç, N., Hilton, D.R. and Mutlu, H., 2002. Helium isotope variations in Turkey: relationship to tectonics, volcanism and recent seismic activities. Chemical Geology. 187, 129-142.

Gülen, L., 1984. Sr, Nd, Pd isotope and trace elements geochemistry of calc-alkaline and alkaline volcanics, eastern Turkey. PhD Thesis, Massachussets Inst Tech.

Güner, Y., 1984. Doğu Anadolu Kuvaterner volkanizması (Nemrut Yanardağı), MTA Genel Müdürlüğü, Temel Araştırmalar Dairesi, Ankara, pp. 77.

H

Hapke, 1963; A theoretical photometric function for the lunar surface. Journal of Geophysical Research 68(15), 4571-4586.

Haroutiunian, R.A., 2004. On the article of A. Karakhanyan et al. on the Holocene-historical volcanism and active faults as natural risk factors for Armenia and neighboring countries. Izvestia NAN RA, Yerevan LVII (1), 62-65 (in Russian).

Hejmanowska, B., 1998. Removal of topographical effect from remote sensing data for thermal inertia modeling. International Archives of Photogrammetry and Remote Sensing 32, part 4, 238-245.

Hugli, H. and Frei, W., 1983. Understanding Anisotropic Reflectance in Mountainous Terrain. Photogrammetric Engineering and Remote Sensing 49(5), 671-683.

Holben, B.N. and Justice, C.O., 1980. The topographic effect on spectral response from nadir-pointing sensors. Photogrammetric Engineering and Remote Sensing 46, 1191-1200.

Holohan, E.P., Troll, V.R., Walter, T.R., Münn, S., McDonnell, S. and Shipton, Z.K., 2005. Elliptical calderas in active tectonic settings: an experimental approach. J. Volcanol. Geotherm. Res., 144: 119-136.

Holohan, E.P., van Wyk de Vries, B. and Troll, V.R., 2008. Analogue models of caldera collapse in strike-slip tectonic regimes. Bull. Volcanol., 70: 773-796, DOI 10.1007/s00445-007-0166-x.

Hook, S.J., Gabell, A.R., Green, A.A. and Kealy, P.S., 1992. A comparison of techniques for extracting emissivity information from thermal infrared data for geologic studies. Remote Sensing of Environment, Vol. 42, pp. 123-135.

Hook, S.J., Abbott, E.A., Grove, C., Kahle, A.B. and Palluconi, F., 1999. Use of multispectral thermal infrared data in geological studies. In: A.N. Renez (Ed.), Manual of Remote Sensing, 3rd Edition Remote Sensing for Earth Sciences, New York: John Wiley and Sons. 3, pp. 59-110.

Horasan, G. and Boztepe-Güney, A., 2007. Observation and analysis of low-frequency crustal earthquakes in Lake Van and its vicinity, eastern Turkey. J. Seismol. 11: 1-13, doi: 10.1007/s10950-006-9022-2.

Houghton, B.F., Weaver, S.D., Wilson, C.J.N. and Lanphere, M.A., 1992. Evolution of a Quaternary peralkaline volcano: Mayor Island, New Zealand. J. Volcanol. Geotherm. Res., 51: 217-236.

I

Innocenti, F., Mazzzouli, R., Pasquare, G., Radicati di Brozolo, F. and Villari, L., 1976. Evolution of the volcanism in the area of interaction between the Arabian, Anatolian and Iranian plates (Lake Van, Eastern Turkey), J. Volcanol. and Geotherm. Res., 1: 103-112.

J

Jackson, J.A. and McKenzie, D.P., 1988. The relationship between plate motions and seismic moment tensors, and the rates of active deformation in the Mediterranean and Middle East, Geophys. J., 93, 45-73.

K

Kahle, A.B., 1977. A simple thermal model of the Earth's surface for geologic mapping by remote sensing. Journal of Geophysical Research, 82, 1637-1680.

Kalafat, D., 1989a. Batı Anadolu'da Yeralan Sismik istasyonların Süreye Bağlı Yerel Magnitüd Denklemlerinin Çıkartılması, Deprem Araştırma Bülteni, 65, 83-94.

Kalafat, D., 1989b. İznik Deprem İstasyonu için Yerel Magnitüd Denkleminin Saptanması, Deprem Araştırma Bülteni, 65, 57-68.

Karakhanian, A., Djrbashian, R., Trifonov, V., Philip, H., Arakelian,S., Avagian, A., 2002. Holocene-historical volcanism and active faults as natural risk factors for Armenia and adjacent countries. J. Volcanol. Geotherm. Res., 113, 319-344.

Karakhanian, A., Jrbashyan, R., Trifonov, V., Philip, H., Arakelian, S., Avagyan, A., Baghdassaryan, H. and Davtian V., 2006. Historical volcanoes of Armenia and adjacent areas: What is revisited?. J. Volcanol. Geotherm. Res., 155(3-4): 338-345.

Karaoğlu, Ö., Özdemir, Y., Tolluoğlu, A.Ü., Karabıyıkoğlu, M., Köse, O. and Froger, J.L., 2005. Stratigraphy of the Volcanic Products around Nemrut Caldera: Implications for Reconstruction of the Caldera Formation. Turkish J. Earth Sci., vol. 14, 123–143.

Kealy, P.S. and Hook, S.J., 1993. Separating temperature and emissivity in thermal infrared multispectral scanner data: Implications for recovering land surface temperatures. IEEE Transactions on Geoscience and Remote Sensing, Vol. 31, No. 6, pp.1155-1164.

Keskin, M., 2003. Magma generated by slab steepening and breakoff beneath a subduction-accretion complex: an alternative model for collision-related volcanism in Eastern Anatolia, Turkey, Geophys. Res. Lett., 30(24), 8046 doi:10.1029/2003GL018019.

Kipfer, R., Aeschbach-Hertig, W., Baur, H., Hofer, M., Imboden, D.M. and Signer, P., 1994. Injection of mantle-type helium into Lake Van (Turkey): the clue for quantifying deep water renewal. Earth Planet. Sci. Lett. 125, 357-370.

Koçyiğit, A., Yılmaz, A., Adamiac, S. and Kuloshvili, S., 2001. Neotectonics of East Anatolian Plateau (Turkey) and Lesser Caucasus: implication for transition from thrusting to strike-slip faulting. Geodinamica Acta, 14: 177–195.

L

Lagmay, A.M.F., van Wyk de Vries, B., Kerle, N., and Pyle, D.M., 2000. Volcano instability induced by strike-slip faulting, Bulletin of Volcanology 62: 331-346, DOI 10.1007/s004450000103.

Landmann, G., 1996. Van See/Turkei: Sedimentologie, Warvenchronologie und regionale Klimageschichte seit dem Spätpleistozän. PhD-Thesis, Fac. Geosci. Univ. Hamburg, Germany, 123 pp.

Landmann, G., Reimer, A., Lemcke, G., and Kempe, S., 1996. Dating Late Glacial abrupt climate changes in the 14570 yr long continuous varve record of Lake Van, Turkey. Paleogeography, Paleoclimatology, Paleoecology, 122: 107-118.

Landmann and Kempe, 2005; Annual deposition signal versus lake dynamics: Microprobe analysis of Lake Van (Turkey) sediments reveals missing varves in the period 11.2 -10.2 ka BP. Facies, 51: 135-145.

Lara, L.E., Lavenu, A., Cembrano, J. and Rodríguez, C., 2006. Structural controls of volcanism in transversal chains: Resheared faults and neotectonics in the Cordón Caulle–Puyehue area (40.5°S), Southern Andes Journal of Volcanology and Geothermal Research 158 (2006) 70-86.

Law, K.H. and Nichol, J., 2004. Topographic correction for differential illumination effects on Ikonos satellite imagery. In proceedings: XXth congress of International Society for Photogrammetry and Remote Sensing, Istanbul, Turkey vol. XXXV, part B3, 6 pp.

Lénat, J.F., 2007. Retrieving self-potential anomalies in a complex volcanic environment: an SP/elevation gradient approach. Near Surf. Geophys. 5, 161–172.

Le Pichon, X. and Gaulier, J,-M., 1988. The rotation of Arabia and the Levant fault system. In. Le Pichon, X., Cochran, J.R. (Eds.), The Gulf of Suez and Red Sea Rifting. Tectonophysics, 153: 271-294.

Lipman, P.W., 1997. Subsidance of ash flow calderas: relation to caldera size and magma chamber geometry. Bull. Volcanol., 59: 198-218.

Lipman, P.W., 2000. Calderas. In: Sigurdsson, H. (Ed.), Encyclopedia of Volcanoes. Academic Press, San Fransisco, pp. 643-662.

Lombardo, V. and Buongiorno, M.F., 2006. Lava flow thermal analysis using three infrared bands of remote-sensing imagery: A study case from Mount Etna 2001 eruption. Remote Sensing of Environment, 101(2), 141-149.

M

Marinoni, L.B., 2001. Crustal extension from exposed sheet intrusions: review and method proposal. J. Volcanol. Geotherm. Res., 107: 27-46.

Marti, J., Ablay, G.J., Redshaw, L.T. and Sparks, R.S.J., 1994. Experimental studies of caldera collapse. J. Geol. Soc. (Lond) 151: 919-929.

Marti, J. and Gudmundsson, A., 2000. The Las Canadas caldera (Tenerife, Canary Islands): an overlapping collapse caldera generated by magma-chamber migration. J. Volcanol. Geotherm. Res., 103: 161-173.

Maxson, J.H., 1936. Nemrut Gölü, M.T.A. Institute Publ. no: 5, pp. 49-57.

McClusky, S., Balassanian, S., Barka, A., Demir, C., Ergintav, S., Georgiev, I., Gurkan, O., Hamburger, M., Hurst, K., Kahle, H., Kastens, K., Kekelidze, G., King, R., Kotzev, V., Lenk, O., Mahmoud, S., Mishin, A., Nadariya, M., Ouzounis, A., Paradissis, D., Peter, Y., Prilepin, M., Reilinger, R., Sanli, I., Seeger, H., Tealeb, A., Toksöz, M.N. and Veis, G., 2000. Global Positioning System constraints on plate kinematics and dynamics in the eastern Mediterranean and Caucasus. J. Geophys. Res., 105, B3: 5695-5719.

McGuire, W.J., 2003, Volcano instability and lateral collapse. Revista 1, 33-45.

McKenzie, D.P., 1970. Plate tectonics of the Mediterranean region, Nature, 226: 239-243.

McKenzie, D.P., 1972. Active tectonics of the Mediterranean region, Geophys. J. R. Astron. Soc, 30, 109-185.

McKenzie, D. and Yılmaz, Y., 1991. Deformation and volcanism in western Turkey and the Aegean, Bull. Tech. Univ. Istanbul, 44: 345-373.

McNutt, S.R., 1996a. Seismic monitoring of volcanoes: A review of the state-of-the-art and recent trends. in: Scarpa, R. and Tilling, R.I. (eds), Monitoring and Mitigation of Volcanic Hazards, Springer-Verlag, Berlin, p. 99-146.

McNutt, S.R., 1996b. Earthquake monitoring and eruption prediction of volcanoes: Review on newest development and historical events [A]. in: Scarpa, R. and Tiling, R.I. (eds), Monitoring and Mitigation of Volcano Hazards, Springer-Verlag, Berlin, p. 79-112.

McNutt, S.R., 2000. Volcanic Seismicity, Chapter 63 of Encyclopedia of Volcanoes, Sigurdsson, H., B. Houghton, S.R. McNutt, H. Rymer, and J. Stix (eds.), Academic Press, San Diego, CA, 1015-1033.

McPhie, J., Doyle M. & Allen, R. (1993). Volcanic Textures: a guide to the interpretation of textures in volcanic rocks. CODES SRC. University of Tasmania. 198 p.

Merle, O., Michon, L. and Bachelery, P., 2008. Caldera rim collapse: A hidden volcanic hazard. J. Volcanol. Geotherm. Res., (in press).

Michael, J., 1993. Encyclopedia of Gods, New York, Facts On File, Inc. p. 186-187.

Minneart, M., 1941. The reciprocity principle in lunar Photogrammetry. Astrophysics Journal 93, 403-410.

Mogi, K., 1962. Study of elastic shocks caused by the fracture of heterogeneous materials and its relation to earthquake phenomena. Bull. Earthquake. Res. Inst. Univ. Tokyo., 40: 125-173.

Moore, I. and Kokelaar, P., 1997. Tectonic influences in piecemeal caldera collapse and Glencoe volcano, Scotland. J. Geol. Soc. (Lond) 154, 765– 768.

MTA, 1964. Geological Map of Turkey (1:500,000), MTA, (Institute of Mineral Research and Exploration), Ankara, Turkey.

N

Nagao, K., Matsuda, J.I., Kita, I. and Ercan, T., 1989. Noble gas and carbon isotopic compositions in Quaternary volcanic area in Turkey. Bull. Geomorphol. 17, 101–110.

Nakamura, K., 1977. Volcanoes as possible indicators of tectonic stress orientation - Principle and proposal. J. Volcanol. Geotherm. Res., 2: 1-16.

Nichol, J., Law, K.H. and Wong, M.S., 2006. Emprical correction of low Sun angle images in steeply sloping terrain: a slope-matching technique. International Journal of Remote Sensing 27(3), 629-635.

Notsu, K., Fujitani, T., Ui, T., Matsuda, J. and Ercan, T., 1995. Geochemichal features of collision-related volcanic rocks in central and Eastern Anatolia, Turkey. J. Volcanol. Geotherm. Res., 64, 171-192.

O

Oral, M.B., Reilinger, R.E., Toksöz, M.N., Kong, R.W., Barka, A.A., Kınık, İ. and Lenk, O., 1995. Global positioning system offers evidence of plate motions in eastern Mediterranean, EOS Transac., 76 (9).

Overmeeren, R.A. and van Ritsema, I.L., 1988. Continuous vertical electrical sounding. First Break 6 (10), 313–324.

Ö

Özdemir, Y., Karaoğlu, Ö., Tolluoğlu, A.Ü. and Güleç, N., 2006. Volcanostratigraphy and petrogenesis of the Nemrut stratovolcano (East Anatolian High Plateau): The most recent post-collisional volcanism in Turkey. Chemical Geology, 226(3-4), 189-211.

Özpeker, I., 1973a. Nemrut yanardaginin petrojenezi. ITU Mad. Fak., Y-No:3-14, 70 p.

Özpeker, I., 1973b. Nemrut yanardağının volkanolojik incelenmesi. Tübitak 4. Bilim Kongresi, Yerbilimleri Seksiyonu Tebliğler Kitabı, pp. 1-17.

P

Pawlewicz, M.J., Steinshouer, D.W. and Gautier, D.L., 1997. Map showing geology, oil and gas fields, and geologic provinces of Europe including Turkey. USGS Open file Report, 97-470-I.

Pearce, J.A., Bender, J.F., De Long, S.E., Kidd, W.S.F., Low, P.J., Güner, Y., Saroglu, F., Yilmaz, Y., Moorbath, S. and Mitchell, J.G., 1990. Genesis of collision volcanism in Eastern Anatolia, Turkey. J. Volcanol. Geotherm. Res., 44(1-2), 189-229.

Pınar, A., Honkura, Y., Kuge, K., Matsushima, M., Sezgin, N., Yılmazer, M. and Öğütçü, Z., 2007. Source mechanism of the 2000 November 15 Lake Van earthquake (Mw = 5.6) in eastern Turkey and its seismotectonic implications. Geophys. J. Int., 170: 749-763.

Pieri, D. and Abrams, M., 2004. ASTER watches the world's volcanoes: a new paradigm for volcanological observations from orbit. Journal of Volcanology and Geothermal Research 135, 13-28.

Pieri, D. and Abrams, M., 2005. ASTER observations of thermal anomalies preceding the April 2003 eruption of Chikurachki volcano, Kurile Islands, Russia. Remote Sensing of Environment, 99, 84-94.

Pollard, D.D., 1987. Elementary fracture mechanics applied to the structural interpretation of dykes. In: Halls, H.C., Fahrig, W.F. (Eds.), Mafic dyke swarms. Geol. Assoc. Canada Spec. Pap., 34: 5-24.

Pugnaghi, S., Gangale, G., Corradini, S. and Buongiorno, M.F., 2006. Mt. Etna sulfur dioxide flux monitoring using ASTER-TIR data and atmospheric observations. Journal of Volcanology and Geothermal Research 152, 74-90.

R

Reilinger, R.E., McClusky, S.C., Oral, M.B., King, W., and Toksöz, M.N. 1997. Global Positioning System measurements of present-day crustal movements in the Arabian-Africa-Eurasia plate collision zone, J. Geophy. Res., 102: 9983-9999.

Reilinger, R., McClusky, S., Vernant, P., Lawrence, S., Ergintav, S., Cakmak, R., Ozener, H., Kadirov, F., Guliev, I., Stepanyan, R., Nadariya, M., Hahubia, G., Mahmoud, S., Sakr, K., ArRajehi, A., Paradissis, D., Al-Aydrus, A., Prilepin, M., Guseva, T., Evren, E., Dmitrotsa, A., S. V. Filikov, S.V., Gomez, F., Al-Ghazzi, R. and Karam, G., 2006. GPS constraints on continental deformation in the Africa-Arabia-Eurasia continental collision zone and implications for the dynamics of plate interactions, J. Geophys. Res., 111: B05411, doi:10.1029/2005JB004051.

Rotstein, Y. and Kafka, A.L., 1982. Seismotectonics of the southern boundary of Anatolia, Eastern Mediterranean region: subduction, collision, and arc jumping, J. Geophys. Res., 87, 7694-7706.

Rowan, L.C., Schmidt, R.G. and Mars, J.C., 2006. Distribution of hydrothermally altered rocks in the Reko Diq, Pakistan mineralized area based on spectral analysis of ASTER data. Remote Sensing of Environment 104(1), 74-87.

Ruud, B.O. and Husebye, E.S., 1992. A new three-component detector and automatic single-station bulletin production. Bulletin of the seismological society of America, 82/1: 221-237.

S

Sandvol, E., Türkelli, N. and Barazangi, M., 2003. The Eastern Turkey Seismic Experiment: the study of a young continent-continent collision. Geophys. Res. Lett., 30(24), 8038, doi:10.1029/2003GL018912.

Schmincke, H.-U., 1967. Cone sheet warm, resurgence of Tejeda caldera, and early geologic history of Gran Canaria. Bull. Volcanol., 31: 153-162.

Simkin, T. and Siebert, L., 2002-. Global Volcanism Program. Smithsonian Institution, Global Volcanism Program Digital Information Series, GVP-5 (http://www.volcano.si.edu/) access date: 2008.

Smith, J.A., Lin, T.L. and Ranson, K.J., 1980. The Lambertian assumption and Landsat data. Photogrammetric Engineering and Remote Sensing 46, 1183-1189.

Straub, C. and Kahle, H.G., 1995. Active crustal deformation in the Marmara Sea region, NW Anatolia, inferred from GPS measurements, Geophys. Res. Lett., 22: 2533-2536.

Songsheng, J. and Ming, H.E., 2008. Evidence for the tritium production in the Earth's interior. Chinese Science Bulletin, 53/4: 540-547.

Ş

Şengör, A.M.C. and Kidd, W.S.F., 1979. The post-collisional tectonics of the Turkish-IranianPlateau and a comparison with Tibet: Tectonophysics, 55, 361-376.

Şengör, A.M.C. and Yılmaz, Y., 1981. Tethyan evolution of Turkey: a plate tectonic approach , Tectonophysics, 75: 181-241.

Şengör, A.M.C., Görür, N. and Şaroğlu, F., 1985. Strike-slip faulting and related basin formation in zones of tectonic escape: Turkey as a case study. In Strike-slip Faulting and Basin Formation, Soc. Econ. Paleontol. Mineral. Sp. Pub. 37, pp. 227-264.

Şengör, A.M.C. and Natal'In, B.A., 1996. Turkic-type orogeny and its role in the making of the continental crust, Ann. Rev. Earth Sci., 24: 263-337.

Şengör, A.M.C., Özeren, S., Genç, T. and Zor, E., 2003. East Anatolian high plateau as a mantle-supported, north-south shortened domal structure, Geophys. Res. Lett., vol. 30, no. 24, 8045.

Şerefhan, 1597. Şerefname: Kürt tarihi (translated from Arabic to Turkish by M. Emin Bozarslan), 4th ed. (1990). Hasat yayınları, 544 pp.

T

Teillet, P.M., Guindon, B. and Goodenough, D.G., 1982. On the slope-aspect correction of multispectral scanner data. Canadian Journal of Remote Sensing 8, 1537-1540.

Thouvenot, F., Frechet, J.,Guyoton, F., Guiguet, R., and Jenatton, L., 1990. SISMALP: an Automatic Phone-Interrogated Seismic Network for the Western Alps, in 'Seismic Networks & Rapid Digital Transmission and Exchange', Cahiers du Centre Europeen de Geodynamique et de Seismologie, 1, 1-10, Luxemburg.

Tibaldi, A., 2008. Contractional tectonics and magma paths in volcanoes. J. Volcanol. Geotherm. Res., (in press).

Trnkoczy, A., 2002. Understanding and parameter settings of STA/LTA trigger algorithm, in: P. Bormann (Ed.), IASPEI New Manual of Seismological Observatory Practice, vol. 2, GeoForschungsZentrum Potsdam, pp. 1-19.

Toker, M., Krastel, S., Demirel-Schlueter, F., Demirbağ, E. and Imren, C., 2007. Volcano-seismicity of Lake Van (Eastern Turkey): A comparative analysis of seismic reflection and three component velocity seismogram data and new insights into volcanic lake seismicity. International Earthquake Symposium, Kocaeli, p 103-109.

U

Ulusoy, I., Cubukcu, E., Aydar, E., Labazuy, P., Gourgaud, A. and Vincent, P.M., 2004. Volcanic and deformation history of the Bodrum resurgent caldera system (southwestern Turkey). J. Volcanol. Geotherm. Res. 136: 71:96.

Ulusoy, I., Ersoy, O., Labazuy, P., Aydar, E., Cubukcu, E., Bayhan, H., Gourgaud, A., and Kurttas, T., 2006a. Self-Potential and image analysis of Mount Nemrut (Eastern Turkey): An approach to the hydrothermal system. Fourth Conference of Cities on Volcanoes, Abstracts Volume. pg. 76.

Ulusoy, I., Labazuy, P., Aydar, E., Ersoy, O., Cubukcu, E., Bayhan, H., Gourgaud, A., Tezcan, L. and Kurttas, T., 2006b. Pioneer Seismic Network installed on an Anatolian volcano: Mount Nemrut (Eastern Turkey). Fourth Conference of Cities on Volcanoes, Abstracts Volume. pg. 113.

Ulusoy, İ., Aydar, E. and Labazuy, P. 2007. Evolution, historical activity and monitoring of Nemrut Volcano. International Tatvan Symposium, Tatvan, Bitlis, Turkey.

Ulusoy, İ., Labazuy, P., Aydar, E., Ersoy, O. and Çubukçu, E., 2008. Structure of the Nemrut caldera (Eastern Anatolia, Turkey) and associated hydrothermal fluid circulation. J. Volcanol. Geotherm. Res., 174(4): 269-283.

Ulusoy, İ., Labazuy, P., Aydar, E. (submitted). STcorr: An IDL code for the image based retrieval of altitude and aspect effects on night time TIR imagery. Computers and Geosciences.

Ü

Ünlü, M.R. and Can, A.R., 1983. Nemrut Kalderası (Bitlis) ve çevresinin jeolojisi, jeotermal enerji olanakları, Bulletin of the Geological Congress of Turkey, 4: 141-146.

V

Vaughan, R.G., Hook, S.J., Calvin, W.M. and Taranik, J.V., 2005. Surface mineral mapping at Streamboat Springs, Nevada, USA, with multi-wavelenght thermal infrared images. Remote Sensing of Environment 99, 140-158.

W

Walker, G.P.L., 1984. Downsag calderas, ring faults, caldera sizes, and incremental caldera growth. J. Geophys. Res., 89: 8407-8416.

Warren, N.M. and Latham, G.V., 1970. An experiment study of thermal induced microfracturing and its relation to volcanic seismicity. J. Geophys. Res., 75: 4455-4464.

Wassermann, J., 2002. IASPEI New manual of seismological observatory practice, P. Bormann (ed), GeoForschungsZentrum Potsdam, pp. 42.

Watson, K., 1973. Periodic heating of a layer over a semi-infinite solid. Journal of Geophysical Research 78, 5904-5910.

Wentz, J. and Schabel, M., 2000. Precise climate monitoring using complementary satellite data sets. Nature 403, 414-416.

Westaway, R., 1994. Present-day kinematics of the Middle East and Eastern Mediterranean. J. Geophys. Res., 99: 12071-12090.

Wiemer, S., and Benoit, J., 1996. Mapping the b-value anomaly at 100 km depth in the Alaska and New Zealand subduction zones. Geoph. Res. Lett., 23: 1557-1560.

Wiemer, S., and McNutt, S., 1997. Variations in frequency-magnitude distribution with depth in two volcanic areas: Mount St. Helens, Washington, and Mt. Spurr, Alaska. Geoph. Res. Lett., 24: 189-192.

Wiemer, S., and Wyss, M., 1997. Mapping the frequency-magnitude distribution in asperities: An improved technique to calculate recurrence times? J. Geophy. Res., 102: 15115-15128.

Wiemer, S., and Wyss, M., 2002. Spatial and temporal variability of the b-value in seismogenic volumes: An overview. Advances in Geophysics, 45: 259-302.

Wong, H.K. and Finckh, P., 1978. Shallow structures in Lake Van In: Degens ET, Kurtman F (Eds) The Geology of Lake Van, Publ. N_ 169. Miner. Res. Explor. Inst., Ankara, pp 6-10.

Wong, H.K. and Degens, E.T., 1978. The bathymetry of Lake Van, eastern Turkey. In: Degens ET, Kurtman F (Eds) The Geology of Lake Van, Publ. N_ 169. Miner. Res. Explor. Inst., Ankara, pp 6-10.

Wyss, M., 1973. Toward a physical understanding of earthquake frequency distribution. Geophys. J.R. Astron. Soc. 31: 341-359.

Wyss, M., Shimazaki, K. and Wiemer, S., 1997. Mapping active magma chambers by b-value beneath the off-Ito volcano, Japan. J. Geophy. Res., 102: 20413-20422.

Y

Yılmaz, Y., 1990; Comparison of young volcanic associations of the western and eastern Anatolia formed under a compressional regime: a review. In: P. Le Fort, J.A. Pearce and A. Pecher (Editors), Collision Magmatism. J. Volcanol. Geotherm. Res., 44: 69-87.

Yılmaz, Y., Güner, Y., Şaroğlu, F., 1998. Geology of the quaternary volcanic centers of the east Anatolia. J. Volcanol. Geotherm. Res., 85, 173-210.

Z

Zor, E., Sandvol, E., Gürbüz, C., Türkelli, N., Seber, D. and Barazangi, M., 2003. The crustal structure of the East Anatolian plateau (Turkey) from receiver functions, Geophysical Research Letters., 30(24), 8044, doi: 10.1029/2003GL018192.

Appendix – A

History, myths and speculations…

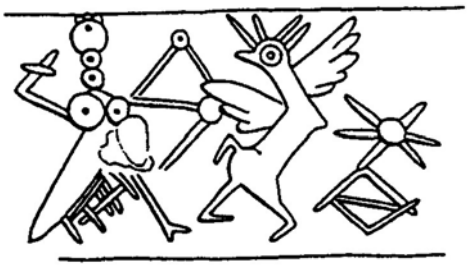

Battle of Ninurta and Anzu

Armenian chronicles

In their paper, which describes the historical volcanic eruptions in Anatolia and Armenia, Karakhanian et al. (2002) quote three historical events related to Mount Nemrut:

1) 1441 AD:

"In the year of 1441, Nemrut Mount between the towns of Ahlat and Baghesh (**Tatvan**) thundered suddenly as a terrific thunder-storm; the entire country shuddered since they saw how a wide crack split the mountain and misty smoke and fetid flame was coming out of the crack. Children fell sick of that smell, and stones boiled of the burning flame, huge stones five kangoun (**?**) in weight were thrown into sky; the fire was seen from the two-day travel distance. The town of Ahlat was trembling from that thunder. The mountain split and opened a huge abyss, and stones on the summit boiled and melted, and glued each other, and so this continued for years."

This event seems to be related with the eruptions located on the Nemrut fissure zone (Fig. A.1) and probably with the formation of the fissure. From the Şerefhan's (1597) observations, we understand that the activity of the fissure zone continued until 1590's. Other than the lava flows originating from the fissure zone, significant lava and dome activity were also generated in the fissure zone (Fig. A.1).

2) April 13, 1692 AD:

"In the town of Baghesh (**Tatvan**), on April 13, summer 1692, sunlight dimmed ever since the morning and colored plumbeous; darkness shrouded the earth so that people could not see each other. Till the very evening, red dust had fallen to the ground and there was an earthquake, many settlements were ruined and many people died."

Event described by here, has been a matter of debate between Karakhanian et al. (2006), and Haroutiunian (2004). A volcanic activity could still be suggested as proposed by (Karakhanian et al. (2002 and 2006), rather then a sandstorm mentioned by Haroutiunian (2004).

3) May 18, 1881 AD:

"On May 18, 1881, there was a strong earthquake in Van; everything was destroyed in Terzour Village. A day before the earthquake, one of the villagers heard terrible underground boom on Mount Nemrut. The village of Terzour is built on a lava flow from the Nemrut crater 400 years ago."

This event, however, qualified as a weak volcanic activity by Karakhanian et al. (2002), is of question. The lava flow defined as “400 years old” could not be other than the lava flows on the Nemrut fissure; and there are no traces of remnants of any village along these flows and no village nearby exist. Moreover, the name Terzour is not found in literature; it is totally unknown or forgotten.

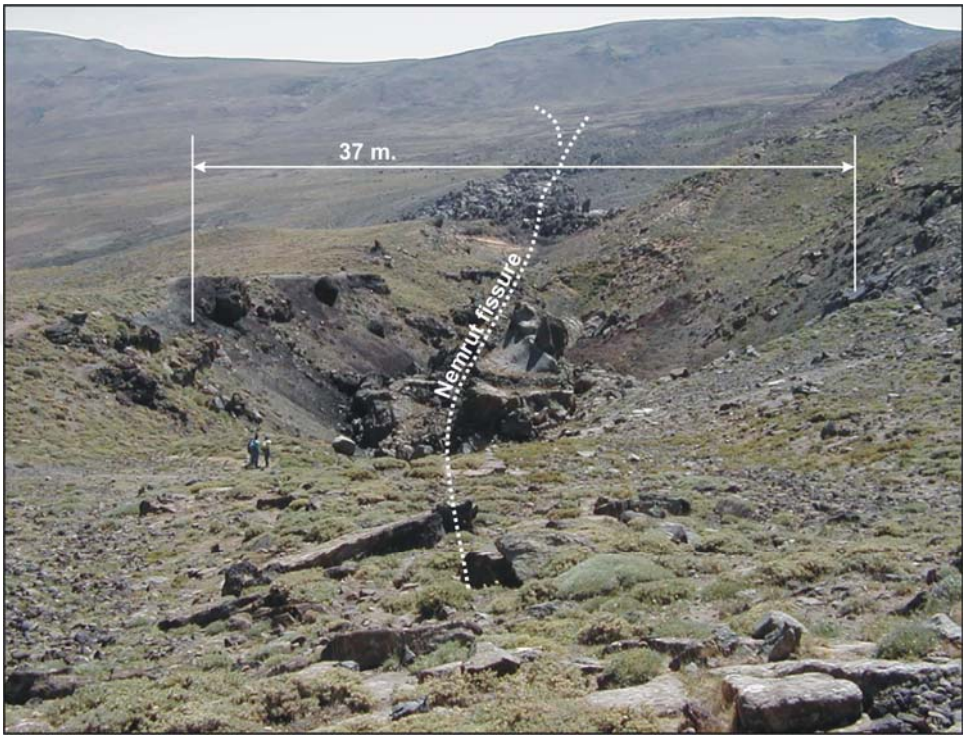

Figure A.1. Nemrut fissure zone. Photograph was taken from south of Nemrutbaşı cone. For the scale please note the presence of three members of our team.

Şerefhan’s observations

Most detailed description of Mount Nemrut and its eruption was made by Şerefhan (1597); his “length” descriptions agree with the actual values. Mythological description given in the entrance of the text is still known as a folkloric tale (with small variations) in Anatolia. Live expression of the eruption at the north of Nemrut describes the lava flows and fountains at the northern fissure zone. Aydar et al. (2003) give the translation of the text with their remarks in parenthesis:

“ (**Mythological description**) To the north of Bedlis (**actual Bitlis City**), between the cities of Muş and Ahlat, there is a high mountain called ‘Nemruz’ (**actual Nemrut**). Natives believe that Nemruz (**the king**) used to spend the winters around and the summers on this mountain. For this purpose, he had a castle and a palace built on the summit. He used to live and spend lots of time

there. He fell victim to God's wrath and got caught. Consequently, the god let this mountain, the height of which was not less than 2000 zira (**ancient length unit: 1 zira = 0.757738 m**), collapse and sink 1500 zira (**caldera collapse**).

(**Live description of Nemrut**) This sinking created a lake of 5000 zira wide. Its water is crystal clear and extremely cool. It is strange that when digging a pit on its banks hot water spouts upward. The land is stony. There is neither much soil nor much mud. Because the black rocks (**obsidian flows**) lay next to each other. Some of these rocks are of a kind called camel's eye by Turks. They are hard and do resemble filled honeycombs (**spherulitic obsidian**). In addition, there is another kind of stone which is softer than the others, like dark rocks (**dark-colored ignimbrites**).

(**Live description of the eruption**) In the northern part of this location there is a canal (**fissure**) through which flows a dark water (**basaltic magma**). It resembles the dark water which flows of the blacksmith's bellows and its weight is heavier than iron. It spouts upward and quickly flows down to the gorge. According to me, each year this water increases and decreases. It jets more than 30 zira (**lava fountain**), and spreads around longer than 100 zira (**ejecta**). And here it spouts out from several points (**rift zone**). Whoever has the intention to separate part of this water will face great difficulties (**hard basaltic rock**)".

Mythology

Gadjimuradov and Schmoeckel (2005), etymologically resembles the word "Nemrut" with old Assyrian king "Ninurta" (Ninurda, Nimurda, Nimrud and Nemrut). "Nin" (or "nine"), in many Middle Eastern languages means mother and/or grandmother (grandmother in Turkish) and "urda" is "erde" in German, "earth" in English, "yurt" in Turkish (Gadjimuradov and Schmoeckel, 2005). Thus "ninurta" is the mother of earth. In present day Turkish language, the word "Nemrut" is literally "merciless, cruel, and sulky".

Urartian civilization that reined the area between 13^{th} cc – 6^{th} cc BC was repeatedly attacked by the Assyrians. Two Urartian towns were under the control of Tukulti-Ninurta I and Tukulti-Ninurta II (Çilingiroğlu, 1997). Assyrian kings Tukulti-Ninurta I (reigned 1244 BC to 1208 BC) and Tukulti-Ninurta II (reigned 890 BC to 884 BC) may be related with the mythological tale given in Şerefhan (1597).

An older tale

Gadjimuradov and Schmoeckel (2005), note that, other than Assyrian king, Ninurta is the hero god in Mesopotamian civilizations (as Ninurta in Akkadians and Nimmah or Ninhursag in Sumerians) and generally illustrated with a bow or spear (of flames). Ninhursag is the “goddess of earth” or “goddess of mountain ranges” and referred as the mother of Ninurta. Michael (1993) describes Ninurta as: “Ninurta (Babylonian-Akkadian), lord of plough, is god of thunderstorms and the plough. He was worshipped from around 3500 BC to 200 BC. Ninurta was the Sumerian god of the farmers and identified with the plough. Also being the god of thunder and a hero in the Sumerian pantheon he was closely linked with confrontation battles between good and evil which comprise much of Mesopotamian literature. He is one of the several challengers of the malignant dragon or serpent *Kur,* said to inhabit the empty space between the earth's crust and the primeval sea beneath.”

An older myth describing the battle of Ninurta and the mountain (Karahashi, 2004) is also noteworthy. In the Sumerian mythological poem “Ninurta Lugal-e” (Exploits of Ninurta), Asag (or Anzu) is a monstrous demon (Black and Green, 1992). He was said to be accompanied into battle by an army of rock demon offspring - born of his union with the mountains themselves and was defeated by the god Ninurta. Asag, whose name means "demon that causes sickness", was often associated with the serpent or dragon mythological archetype by historians (Black and Green, 1992). There are various descriptions of Asag, who was sometimes symbolized as a dragon (Fig. A.2; Karahashi, 2004). Foster (2000) and Karahashi (2004) suggest that “Asag” is “a demonically personified volcano and its associated phenomena”.

Black et al. (1998), give the full translation of the Ninurta’s battle with the mountain (Karahashi, 2004) from Summerian:

“The Lord cried "Alas!" so that Heaven trembled, and Earth huddled at his feet and was terrified (?) at his strength. Enlil **(Father of Ninurta)** became confused and went out of the E-kur. The Mountains were devastated. That day the earth became dark, the Anuna trembled. The Hero beat his thighs with his fists. The gods dispersed; the Anuna disappeared over the horizon like sheep. The Lord arose, touching the sky; Ninurta went to battle, with one step (?) he covered a league, he was an alarming storm, and rode on the eight winds towards the rebel lands. His arms grasped the lance. The mace snarled at the Mountains, the club began to

devour the entire enemy. He fitted the evil wind and the sirocco on a pole (?); he placed the quiver on its hook (?). An enormous hurricane, irresistible, went before the Hero, stirred up the dust, caused the dust to settle, leveled high and low, and filled the holes. It caused a rain of coals and flaming fires; the fire consumed men. It overturned tall trees by their trunks, reducing the forests to heaps, Earth put her hands on her heart and cried harrowingly; the Tigris[1] was muddied, disturbed, cloudy, stirred up. He hurried to battle on the boat Ma-kar-nunta-eda; the people there did not know where to turn, they bumped into (?) the walls. The birds there tried to lift their heads to fly away, but their wings trailed on the ground. The storm flooded out the fish there in the subterranean waters, their mouths snapped at the air. It reduced the animals of the open country to firewood, roasting them like locusts. It was a deluge rising and disastrously ruining the Mountains."

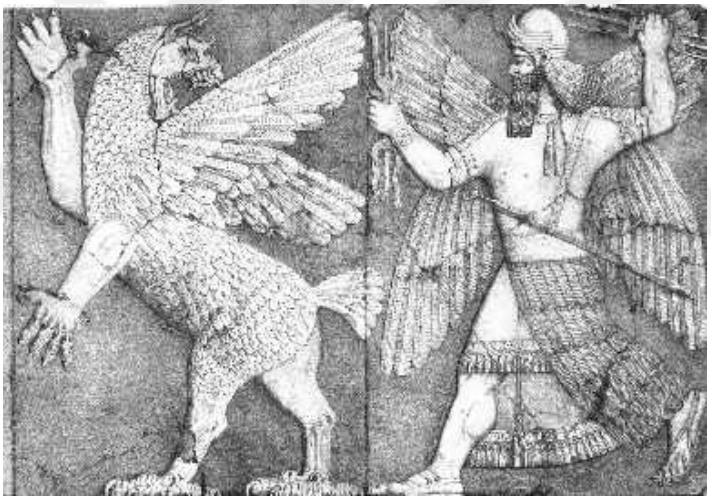

Figure A.2. Battle of Ninurta and Asag

[1] *Dicle river; Bitlis steam that sourced in the Bitlis valley (~19 km southeast of Mt. Nemrut) joins with Botan steam and then Dicle river.*

Appendix – B

Morphological analysis of active Mount Nemrut stratovolcano, eastern Turkey: evidences and possible impact areas of future eruption

Available online at www.sciencedirect.com
SCIENCE DIRECT®
Journal of volcanology and geothermal research
ELSEVIER
Journal of Volcanology and Geothermal Research 123 (2003) 301–312
www.elsevier.com/locate/jvolgeores

Morphological analysis of active Mount Nemrut stratovolcano, eastern Turkey: evidences and possible impact areas of future eruption

Erkan Aydar [a,*], Alain Gourgaud [b,**], Inan Ulusoy [a], Fabrice Digonnet [b], Philippe Labazuy [b], Erdal Sen [a], Hasan Bayhan [a], Turker Kurttas [a], Arif Umit Tolluoglu [c]

[a] *Department of Geological Engineering, Hacettepe University, 06532, Beytepe-Ankara, Turkey*
[b] *Université Blaise Pascal, UMR–CNRS 6524, 5 rue Kessler, 63038 Clermont-Ferrand, France*
[c] *Department of Geological Engineering, Yuzuncuyil University, Van, Turkey*

Received 1 February 2002; accepted 13 December 2002

Abstract

Mount Nemrut, an active stratovolcano in eastern Turkey, is a great danger for its vicinity. The volcano possesses a summit caldera which cuts the volcano into two stages, i.e. pre- and post-caldera. Wisps of smoke and hot springs are to be found within the caldera. Although the last recorded volcanic activity is known to have been in 1441, we consider here that the last eruption of Nemrut occurred more recently, probably just before 1597. The present active tectonic regime, historical eruptions, occurrence of mantle-derived magmatic gases and the fumarole and hot spring activities on the caldera floor make Nemrut Volcano a real danger for its vicinity. According to the volcanological past of Nemrut, the styles of expected eruptions are well-focused on two types: (1) occurrence of water within the caldera leads to phreatomagmatic (highly energetic) eruptions, subsequently followed by lava extrusions, and (2) effusions–extrusions (non-explosive or weakly energetic eruptions) on the flanks from fissures. To predict the impact area of future eruptions, a series of morphological analyses based on field observations, Digital Elevation Model and satellite images were realized. Twenty-two valleys (main transport pathways) were classified according to their importance, and the physical parameters related to the valleys were determined. The slope values in each point of the flanks and the Heim parameters H/L were calculated. In the light of morphological analysis the possible impact areas around the volcano and danger zones were proposed. The possible transport pathways of the products of expected volcanic events are unified in three main directions: Bitlis, Guroymak, Tatvan and Ahlat cities, the about 135 000 inhabitants of which could be threatened by future eruptions of this poorly known and unsurveyed volcano.
© 2003 Elsevier Science B.V. All rights reserved.

Keywords: Turkey; Nemrut; volcano; morphology; image analysis; impact area

1. Introduction

Eastern Turkey hosts several poorly known sub-active/active volcanoes like Mount Ararat,

* Corresponding author.
** Corresponding author.
E-mail addresses: eaydar@hacettepe.edu.tr (E. Aydar), gourgaud@opgc.univ-bpclermont.fr (A. Gourgaud).

0377-0273/03/$ – see front matter © 2003 Elsevier Science B.V. All rights reserved.
doi:10.1016/S0377-0273(03)00002-7

Mount Tendurek, Mount Suphan and Mount Nemrut (Yilmaz et al., 1998). All witnessed volcanic activity during the Late Pleistocene and/or Holocene. The area still experiences tectonic deformations related to the collision of the Arabian and Eurasian plates (Dewey et al., 1986). In this active tectonic context, Nemrut Volcano is located at the eastern end of the Mus Basin (Yilmaz et al., 1987) (Fig. 1a). However, radiometric ages collected from the literature show that the volcano has been active for the last 1.2 Ma; most of the volcanics are younger than 500 ka. Although the last volcanic activity is known to have occurred in 1441 (Oswalt, 1912; Pfaffengolz, 1950), we found a live description of the last eruption of Nemrut in an Arabic book written in 1597 (Serefhan, 1597). The Turkish translator of the mentioned book provides a note stating that the original version of this book called 'Serefname' is in the Bodleian Library of Oxford University, UK (registration number 312). We decided to quote the text as it is in the Turkish translation of the mentioned book. Remarks in parentheses are our own comments.

'(Mythological description) *To the north of Bedlis* (actual Bitlis City)*, between the cities of Mus and Ahlat, there is a high mountain called 'Nemruz'* (actual Nemrut). *Natives believe that Nemruz* (the king) *used to spend the winters around and the summers on this mountain. For this purpose, he had a castle and a palace built on the summit. He used to live and spend lots of time there. He fell victim to God's wrath and got caught. Consequently, the god let this mountain, the height of which was not less than 2000 zira* (ancient length unit: 1 zira = 0.757738 m)*, collapse and sink 1500 zira* (caldera collapse).

(Live description of Nemrut) *This sinking created a lake of 5000 zira wide. Its water is crystal clear and extremely cool. It is strange that when digging a pit on its banks hot water spouts upward.*

The land is stony. There is neither much soil nor much mud. Because the black rocks (obsidian flows) *lay next to each other. Some of these rocks are of a kind called camel's eye by Turks. They are hard and do resemble filled honeycombs* (spherulitic obsidian; Fig. 1e)*. In addition, there is another kind of stone which is softer than the others, like dark rocks* (dark-colored ignimbrites).

(Live description of the eruption) *In the northern part of this location there is a canal* (fissure) *through which flows a dark water* (basaltic magma). *It resembles the dark water which flows off the blacksmith's bellows and its weight is heavier than iron. It spouts upward and quickly flows down to the gorge. According to me, each year this water increases and decreases. It jets more than 30 zira* (lava fountain), *and spreads around longer than 100 zira* (ejecta). *And here it spouts out from several points* (rift zone)*. Whoever has the intention to separate part of this water will face great difficulties* (hard basaltic rock)'.

As Nemrut represents historical volcanism as well as current fumarole activity, we aim to investigate the volcanological and morphological features of Mount Nemrut in this paper. A scenario of possible volcanic events expected to occur in future and their impact areas will be discussed.

2. Volcanological past of Mount Nemrut

Mount Nemrut stratovolcano, which culminates at 2948 m, is situated on the western shore of Lake Van (1648 m above sea level), a soda lake covering a surface of 3574 km^2 (Fig. 1). The volcano exhibits a summit caldera, the surface area of which is 8.5×7 km. The eastern half of the caldera is filled by pyroclastic deposits related to maar-like explosion craters (Fig. 1b), lava domes and flows. The western half is filled by a freshwater lake covering a surface area of 5.3×3 km and a small lake with hot springs (Fig. 1). The average depth of the larger lake is estimated to be 100 m, although the maximum depth is close to 156 m (Ozpeker, 1973). The fumarole activity is

Fig. 1. Georeferenced SPOT image. (a) DEM of Turkey and the location of Mount Nemrut Volcano. (b) Field view of intracaldera phreatomagmatic products. (c) Fumarole activity at the caldera floor. (d) A view of the caldera interior with obsidian flow and lake. (e) Spherulite occurrences on the obsidian flow. (f) A general view of Bitlis valley.

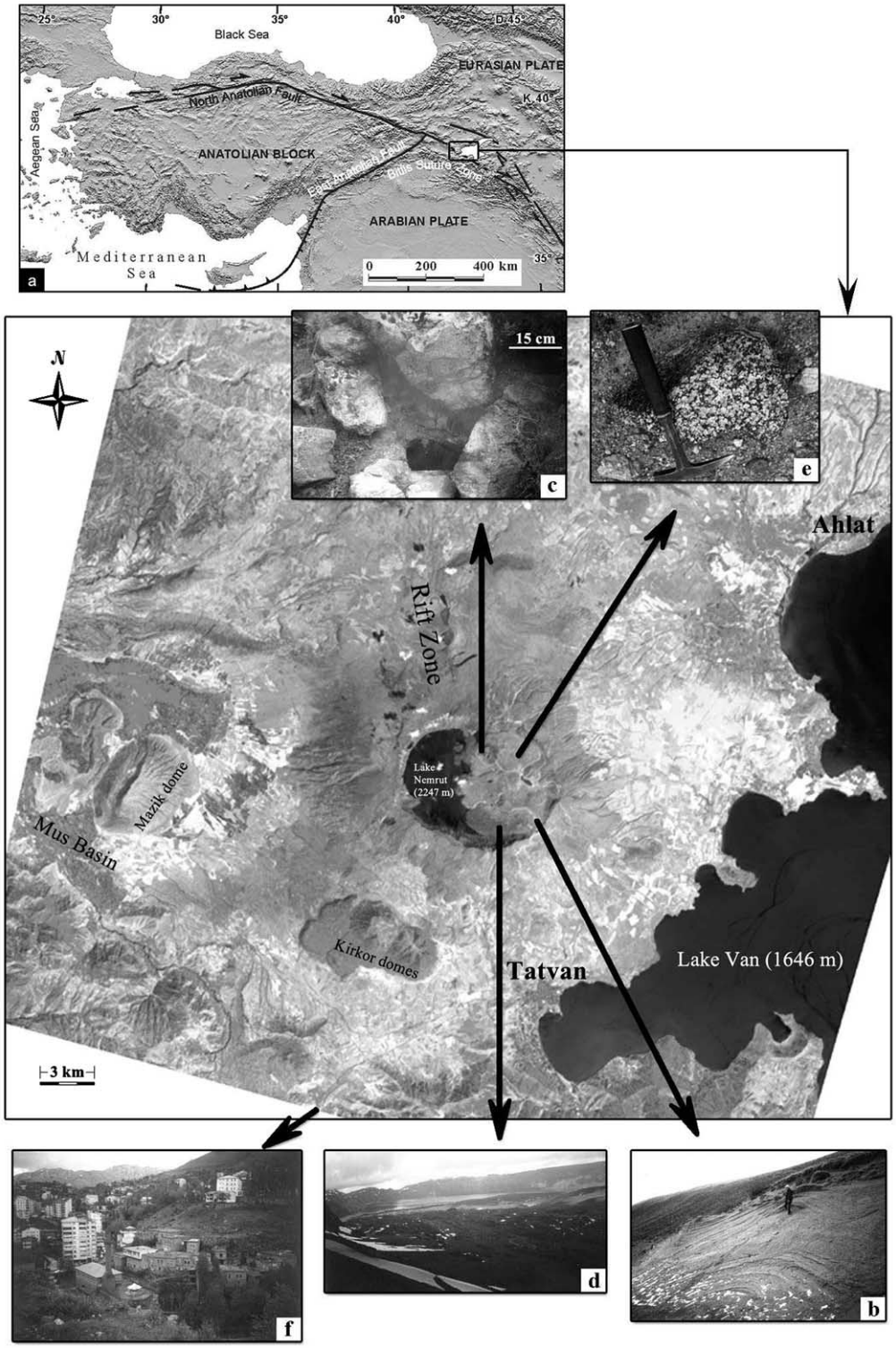
25°
30°
35°
40°
45°
Black Sea
EURASIAN PLATE
North Anatolian Fault
40°
Aegean Sea
ANATOLIAN BLOCK
Bitlis Suture Zone
ARABIAN PLATE
Mediterranean Sea
0 200 400 km
35°
a
N
15 cm
c
e
Ahlat
Rift Zone
Lake Nemrut (2247 m)
Mazik dome
Mus Basin
Kirkor domes
Tatvan
Lake Van (1646 m)
3 km
f
d
b

also present over a dome situated at the northern part of the caldera (Fig. 1c). A $^{3}He/^{4}He$ isotopic ratio measurement on the hot spring indicates that the gases are actually released directly from the mantle-derived magma (Nagao et al., 1989). Mount Nemrut, however, is poorly known in the literature, but was previously investigated in Yilmaz et al. (1998), who proposed five evolutionary phases for all East Anatolian volcanoes (the stratovolcanoes of Mount Ararat, Mount Suphan, Mount Nemrut and the shield volcano of Mount Tendurek) as pre-cone, cone building, climactic, post-caldera and late phase. Our stratigraphy and evolutionary stage distinctions are different and we defined two main evolutionary stages in the history of this active volcano, cut by the paroxysmal eruption leading to the caldera collapse (Fig. 2): the pre-caldera and post-caldera stages.

2.1. Pre-caldera stage

It can be subdivided into two phases: construction and destruction phases.

2.1.1. Construction phase

This is characterized predominantly by basaltic, trachytic, rhyolitic lava flows, lava dome emplacements and associated block-and-ash flows (Fig. 1). The oldest lavas are fissure-fed basalts related to scoria cones, dated to 1.18 ± 0.23 Ma (Pearce et al., 1990). At the southwest and west of the caldera, the dome complex of Kirkor (dated to 0.31 Ma by Ercan et al., 1990) and Mazik were emplaced within the Mus Basin. Measured flanks and slope values lead us to suppose that the summit of this primitive volcano reached about 4500 m high.

2.1.2. Destruction phase

During the destruction phase, the eruption style of the volcano became paroxysmal with important pumiceous plinian-style air-falls which were subsequently followed by welded ignimbrite emplacement. Near Tatvan city, 10 km from the source, the thickness of plinian fall deposits is some tens of meters. The ignimbrites are dark brown colored and exhibit a fiamme texture. They are thin on the slopes of the volcano, only several meters thick, while the thickness increases drastically within the valleys, reaching several tens of meters in the Bitlis valley. The volume of the ignimbrite and its related products is estimated as 40 km^3, over an area of 860 km^2. Following this paroxysmal event, the caldera collapsed. The surface area of collapse, representing an ellipsoidal shape, corresponds to 45 km^2. The volumes of caldera and total collapse are estimated to be 40 km^3 and 65 km^3, respectively. Although the age of this major event is unknown, we observed the ignimbrites over the Kirkor domes dated to 0.31 Ma by Ercan et al. (1990).

2.2. Post-caldera stage

This stage witnessed intracaldera and flank eruptions. The eastern half of the caldera is occupied by phreatomagmatic craters, lava dome and flows (Fig. 1d). At least three explosion craters are recognized. Their tuff-rings exhibit base surge deposits with dune and anti-dune structures, bomb-sags and pool structures, bread-crust bombs and cross-bedding. Trachytic and rhyolitic lavas were extruded within the explosion craters in the forms of either lava flows, dominantly obsidian flows sometimes spherulitic (Fig. 1e), or lava-domes. The radiometric ages of intracaldera volcanism are very young, ranging from 0.02 ± 0.01 Ma to < 10 ka (Nagao et al., 1989). Fumarole activity and hot springs are still present on the caldera floor.

Basalts and trachytes are dominant among the flank eruption products. Beside the scattered basaltic and trachytic lavas on the flanks, the most spectacular eruptive event is that of the northern flank, where there is a ‘rift zone’, supposed to have occurred in 1441 (Fig. 1). It is composed of fissural basaltic and trachytic lavas.

3. Morphological analysis of Mount Nemrut

Because of present active tectonics, young ages, historical eruptions, occurrence of mantle-derived magmatic gases and fumarole and hot spring activities on the caldera floor, Nemrut Volcano is considered dangerous for its vicinity. According

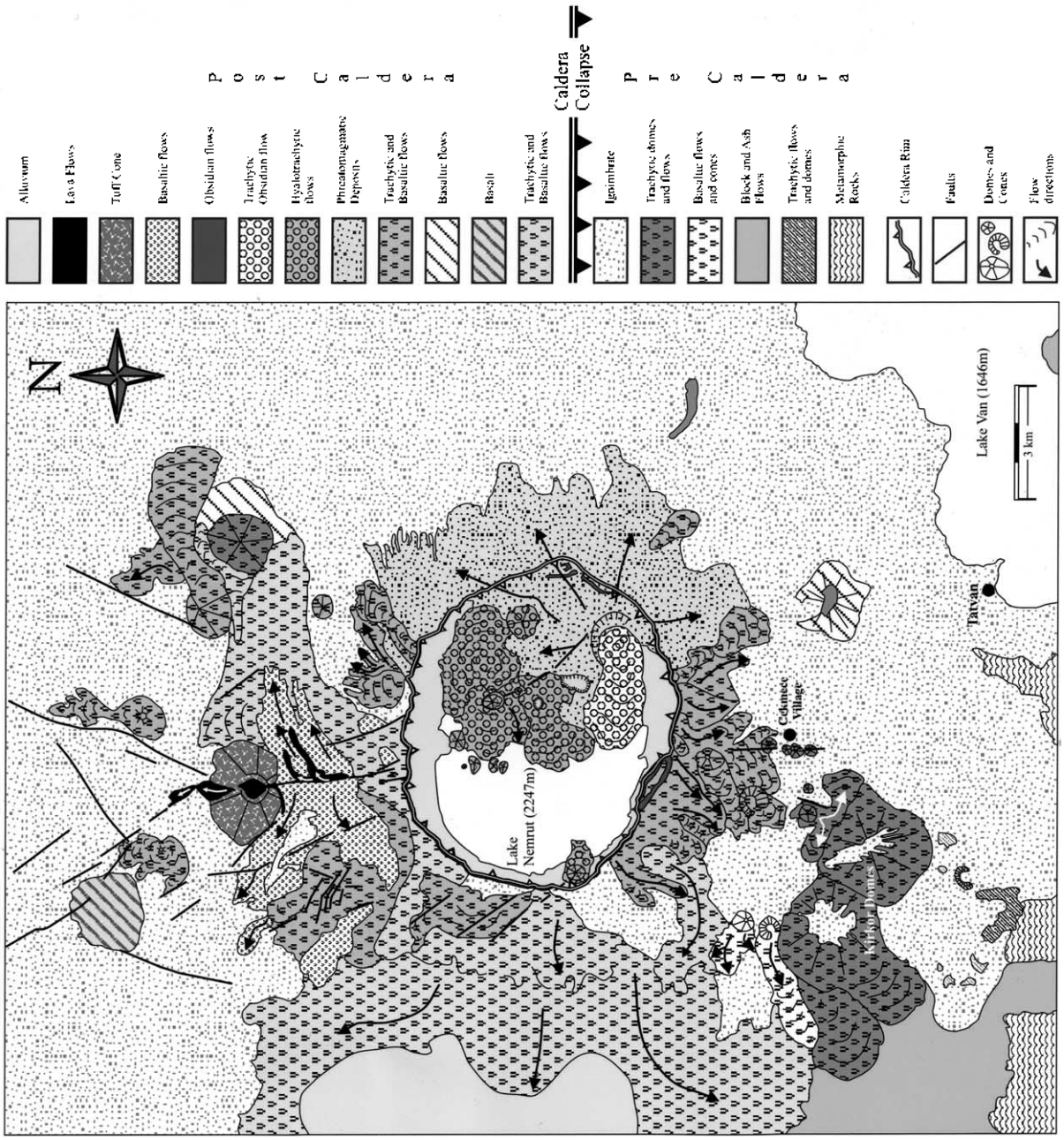

Fig. 2. Geological sketch map of Mount Nemrut (modified from Yilmaz et al., 1998).

to the volcanological past of Nemrut, the styles of expected eruptions are of two types: (1) occurrence of water within the caldera leads to phreatomagmatic (high energy) eruptions, subsequently followed by lava extrusions, and (2) lava effusions or extrusions (non-explosive or low energy eruptions) from the fissures on the flanks. The expected future eruptions could have a great impact on Tatvan city (Fig. 1) (10 km from the summit of the volcano), where the population is 66 000 inhabitants according to the results of Turkey's 1997 census. The other impact areas are Bitlis

Fig. 3. Risk analysis based on DEM of Mount Nemrut. (a) Slope visualization of Mount Nemrut. Dark areas correspond to high slope values. (b) Drainage pattern of volcano. (c) Classification of the steep valleys obtained by overlapping of slope image and valley visualization.

city (Fig. 1f) (to the SSW of the volcano, population: 52 000 inhabitants), Guroymak town (to the SW of the volcano, population: 14 868) and Ahlat city (to the NE of the volcano, population: 22 000). Around Nemrut Volcano, about 135 000 inhabitants could be affected by future eruptions of this poorly known and unsurveyed volcano. For that reason, we undertook image analysis, combined with field work observations, of the possible impact areas and described transport pathways of volcanic materials of future eruptions.

3.1. Methodology

We used three-band SPOT images, taken by the SPOT-2 satellite with the HRV instrument on 8/9/1997 (Fig. 1). Then, we constituted the image in RGB format using the third, second and first bands, respectively. The image was georeferenced using 49 ground control points and then the method of LUT (Look Up Table detailed in Richards, 1993) was applied using linear stretching.

In addition to the satellite image, a DEM (Digital Elevation Model), which covers 22×28 km of surface area and has a resolution of 40 m, was produced by digitizing 1/25 000 scaled topographic maps of the relevant area. Then, the digitized map was linearly interpolated to have a defect-free surface of the volcano. Finally, a raster image of the DEM was generated for geomorphological analysis.

Hierarchical cluster analysis was applied as geostatistical method to Nemrut Volcano. This procedure attempts to identify relatively homogeneous groups of cases (or variables) based on selected characteristics, using an algorithm that starts with each case (or variable) in a separate cluster and combines clusters until only one is left. This procedure was applied in two steps. In the first step, each valley was grouped with respect to its topographic elevations and slope values in each processed point. Then, the average slope values of groups and the slope values of the transition points between the groups (break points) were computed. As a second step, cluster analysis was applied to the groups of the first step to have homogeneous areal groups of slope values. Then, the valley groups were interpolated using kriging methods and the flanks of Nemrut Volcano were divided into four zones (green, yellow, pink and red).

3.2. Application and interpretation

First we realized a slope visualization (Fig. 3a) (the method used is detailed in Wood, 1996). The western flank of Nemrut is steeper than the others, and this flank hosts predominantly lava facies. The other flanks, especially the southern and eastern ones, mostly occupied by pyroclastics, represent irregular surfaces due to erosional factors. The drainage pattern of the volcano (Fig. 3b) shows that the valleys are radially distributed from the center. The deepest and longest ravines are situated on the western and southern flanks, and continue to Tatvan city.

To classify the steep valleys, the slope image

Fig. 4. Visualization of risk factors and the impact areas of future eruptions. (a) Illustration of deepest and longest valleys as the most dangerous pathways. Contour map based on calculated H/L values. (b) Estimation for each slope value of valleys and valley classification according to their importance. (c) Overlapped spot image and DEM of Mount Nemrut, creating 3D near-real visualization. The risk zones and possible impact areas, during a volcanic event related to Mount Nemrut, deduced by morphological analysis (slope values and H/L parameters): green zone, high slope values which will be mantled by the products if an eruption occurs; yellow zone, transitional zone from topography mantling to channeling; pink zone, smaller slope values where the fan-style behavior of transported material will be expected; red zone, the possible deposition field of transported mass. Note that the settlements are located within the pink and red zones.

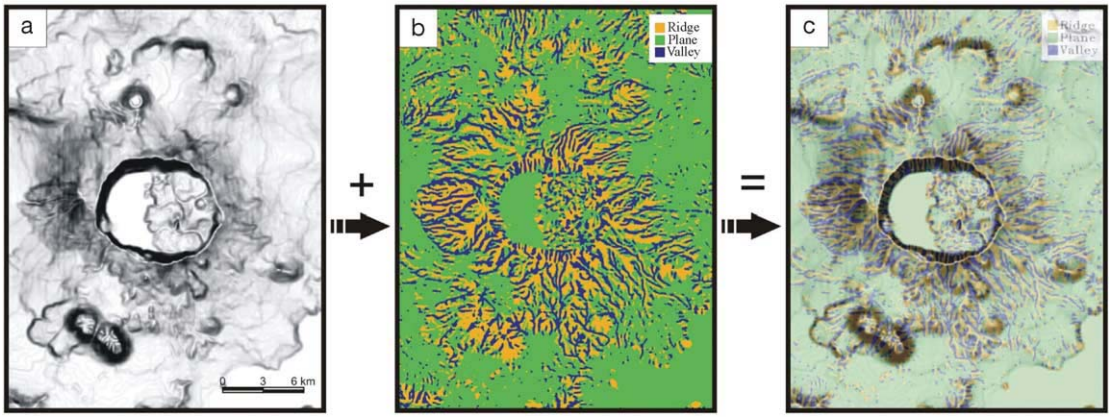
a
b
c
Ridge
Plane
Valley
0 3 6 km
+
=

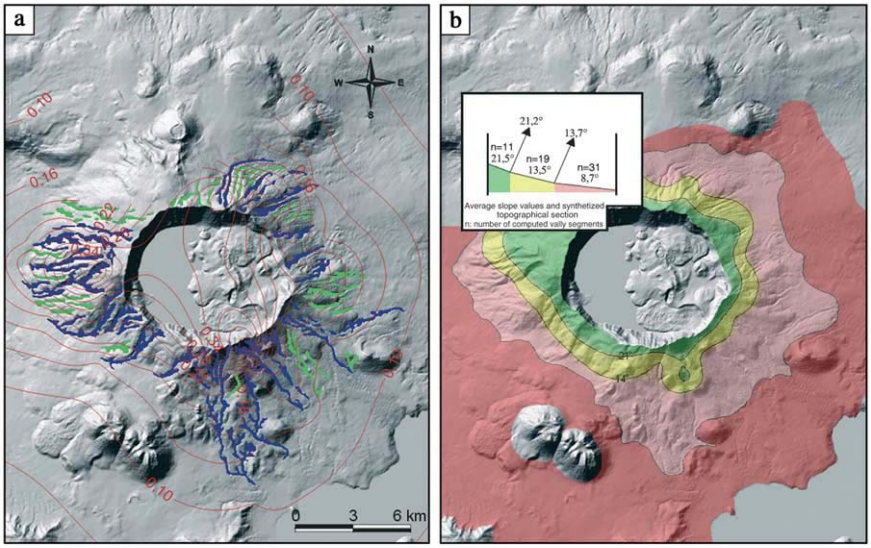
a
b
N
W
E
S
0 3 6 km
21.2°
13.7°
n=11
21.5°
n=19
13.5°
n=31
8,7°
Average slope values and synthetized topographical section
n: number of computed vally segments

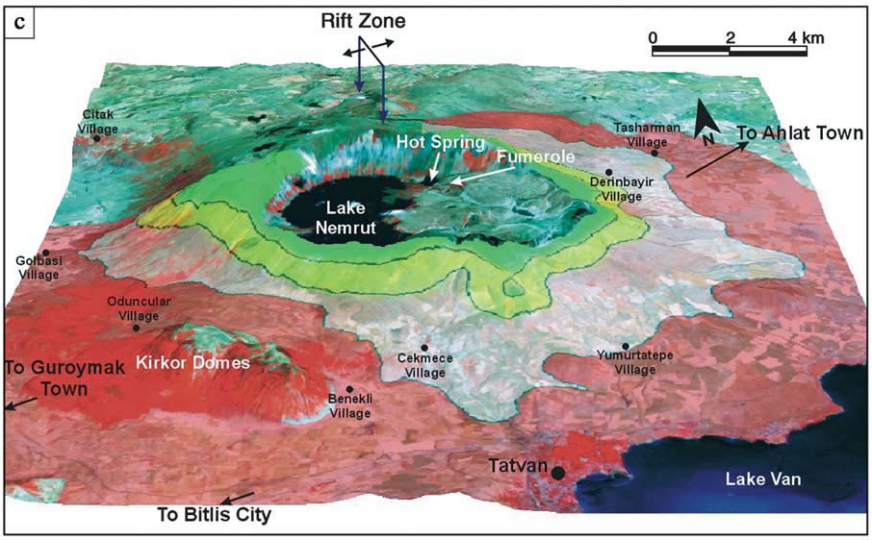
c
Rift Zone
0 2 4 km
Citak Village
Hot Spring
Fumerole
Tasharman Village
N
To Ahlat Town
Derinbayir Village
Lake Nemrut
Gorbasi Village
Oduncular Village
To Guroymak Town
Kirkor Domes
Cekmece Village
Yumurtatepe Village
Benekli Village
Tatvan
Lake Van
To Bitlis City

Table 1
Physical characteristics of selected valleys and the results of geostatistical classification

Valley	Processed data points	Length of valley (m)	Max. depth (m)	First cluster analysis	Mean slope values of first cluster analysis groups	Breaking point slope value between first and second groups	Breaking point slope value between second and third groups	Second cluster analysis
Western and southwestern flanks								
v1	140	5895	36	1	17.4	16.2		y
				2	9.8			p
v2	160	4958	144	1	16.9	26.26	15.55	y
				2	17.8			y
				3	6.2			p
v3	151	4301	133	1	24.1	22.14	23.4	g
				2	15.7			y
				3	8.3			p
v4	190	5235	204	1	24.9	25.57	12.03	g
				2	19.6			y
				3	7.4			p
v5	219	6009	65	1	14.5	18.88	14.57	y
				2	14.7			y
				3	7.8			p
v6	132	3834	94	1	11.9	18.95	7.11	y
				2	6.5			p
				3	4.7			p
v7	111	3054	100	1	13.1	10.6	15.99	y
				2	8.1			p
				3	7.2			p
Southern and southeastern flanks								
v8	313	9114	127	1	17.3	12.62	7.39	y
				2	8.9			p
				3	3.3			p
v9	209	7119	121	1	23.9	23.59	8.64	g
				2	10.4			p
				3	4.5			p
v10	287	7680	135	1	25.7	23.92	9.68	g
				2	9.4			p
				3	4.0			p
v11	180	4513	135	1	13.1	10.68	7.91	y
				2	8.1			p
				3	5.5			p
v12	155	4306	142	1	14.1	16.75	8.26	y
				2	7.8			p
				3	4.9			p
v13	123	3445	20	1	9.6	11.11	11.68	p
				2	8.2			p
				3	4.9			p
v14	192	5278	80	1	10.2	7.31	10.72	p
				2	6.3			p
				3	5.1			p
v15	251	7153	17	1	11.4	12.46	6.08	y
				2	6.5			p
				3	3.9			p
Northern and northeastern flanks								
v16	97	2591	23	1	13.5	18.97	11.34	y
				2	12.7			y
				3	7.2			p
v17	107	2692	36	1	11.3	16.03	9.87	y

Table 1 (*Continued*).

Valley	Processed data points	Length of valley (m)	Max. depth (m)	First cluster analysis	Mean slope values of first cluster analysis groups	Breaking point slope value between first and second groups	Breaking point slope value between second and third groups	Second cluster analysis
				2	10.0			p
				3	4.9			p
v18	94	2722	47	1	12.1	24.08		y
				2	7.3			p
v19	99	2646	35	1	27.7	18.18		g
				2	10.4			p
v20	94	3229	40	1	22.0	12.98		g
				2	7.1			p
v21	132	3576	40	1	18.6	21.31		y
				2	7.2			p
v22	136	3556	44	1	24.4	20.91	7.5	g
				2	13.5			y
				3	6.0			p

Abbreviations: g, green; y, yellow; p, pink.

and valley visualization were overlapped (Fig. 3c). In the case of an eruptive event or a debris flow, transported materials will probably travel down these valleys. The risk factors were estimated for each slope value of the valleys and were classified as first degree and second degree according to their importance (Fig. 4a). Twenty-two valleys were selected between the deepest and longest ones as the most dangerous pathways. Although they are numerous, the channels are unified in three main directions: to Tatvan, Bitlis–Guroymak and Ahlat cities. The slope values were classified in four groups (Fig. 4b) using the statistical method of Hierarchical Cluster Analysis (realized by 3572 slope and altitude values) based on 'between-groups linkage and squared Euclidean distance' parameters. The results, except the lowlands, are summarized in Table 1. To complete the morphological analysis, we computed for 22 selected valleys and for each settlement the Heim parameters H/L (vertical drop/runout distance between the source and the deposition area of possible debris flows). For those calculations, the end of each valley and also each settlement were considered as depositional areas for expected flood flow. Although the values obtained do not correspond to the mobility of any product, we evaluated the mobility character of possible floods under topographical influences. In their works on hazard estimation of the possible pyroclastic flow disasters, Itoh et al. (2000) also suggest that topography and starting direction of flood strongly influence the impact area more than the volume of pyroclastics and discharge rate. The contour map of those calculations presented in Fig. 4a confirms the role of topographical influences on possible impact areas. The contours are condensed in three directions (WSW, SSE, NNE) and show clearly that if any volcanic debris occurs, these products will probably travel in those directions. The sectoral average values obtained from each valley are 0.202 for the WSW flank, 0.115 for the SSE flank and 0.185 for the NNE flank. The details are given in Table 2. Thouret et al. (2000) plot H vs. L on a diagram for the small-volume pyroclastic flows, large-volume pyroclastic flows, debris flows and cold rock avalanches of Merapi and Unzen volcanoes. They clearly show that most of the large-volume pyroclastic flows and debris flows generated by Merapi and Unzen have H/L ratios between 0.1–0.02, while H/L values of small-volume pyroclastic flows and cold rock avalanches range between 0.5 and 0.1. On the other hand, Capra et al. (2002) also calculate H/L ratios of debris flows and debris avalanches for Mexican volcanoes and point out that H/L ratios are 0.03–0.05 for debris flows and H/L values of less mobile debris avalanches are between 0.13 and 0.09. Comparing those values with Mount Nemrut data, the flanks of Nemrut and

Table 2
Calculated Heim parameters H/L for the valleys and settlements around the volcano

Valley	H/L ratio for the flanks			Settlement	H/L
	Green–yellow transition	Yellow–pink transition	Pink–red transition		
Western and southwestern flanks					
v1	0.200	0.242	0.214	Golbasi	0.155
v2	0.240	0.264	0.228	Oduncular	0.104
v3	0.380	0.421	0.276	Citak	0.086
v4	0.466	0.397	0.230	Guroymak	0.058
v5	0.238	0.241	0.179		
v6	0.201	0.207	0.133		
v7	0.251	0.183	0.154		
Southern and southeastern flanks					
v8	0.282	0.187	0.114	Yumurtatepe	0.158
v9	0.129	0.151	0.101	Cekmece	0.150
v10	0.472	0.179	0.109	Benekli	0.130
v11	0.229	0.178	0.145	Tatvan	0.101
v12	0.240	0.156	0.124	Bitlis	0.049
v13	0.168	0.159	0.122		
v14	0.178	0.134	0.110		
v15	0.203	0.138	0.102		
Northern and northeastern flanks					
v16	0.249	0.234	0.193	Derinbayir	0.125
v17	0.196	0.185	0.151	Tasharman	0.079
v18	0.169	0.208	0.166	Ahlat	0.033
v19	0.307	0.298	0.213		
v20	0.191	0.269	0.191		
v21	0.301	0.317	0.204		
v22	0.402	0.267	0.181		

most of the settlements around the volcano have H/L values >0.1. It means that considering the literature data on Merapi, Unzen and Mexican volcanoes, the flanks of Mount Nemrut will be affected by the future volcanic event. Some settlements like Ahlat, Tasharman, Bitlis, Guroymak, Citak have H/L values less than 0.1. According to an assumption based on literature data, we can suggest that those settlements will be threatened only by large-volume, highly mobile pyroclastic flows and/or air-falls if they occur. On the other hand, Ahlat town will probably be less threatened from an event, because it is located in the flatland. It is difficult to consider that the surge or flow products could reach Ahlat city if a future eruption will occur as a hydrovolcanic one or cold debris generated by strong rainfalls.

Transported volcanic materials (erupted or cold debris) could reach the city center of either Tatvan or Bitlis and Guroymak or both. We emphasize that the altitude of the SW part of the Kirkor domes, in the direction of Bitlis valley, is topographically 100 m below Lake Van (1646 m).

Finally, the spot image and DEM of Nemrut were overlapped, creating 3D near-real visualization (Fig. 4c). On this image, cluster classification is shown with different colors as potential risk zones as a function of their average slope and H/L values which may affect the mobility of transported material. The expected behavior of transported material which would be produced during the next volcanic event on different zones of Mount Nemrut is summarized as follows.

A green color corresponds to high slope values and this area could be mantled by eruptive deposits. There are no settlements in the green zone, so the expected impact of the next event will only affect the environment rather than the human life in this zone. The average H/L ratio of this zone is 0.26. The yellow zone is a transitional zone from topography mantling to channeling. Its average H/L ratio is close to 0.22. The average

slope values and H/L ratios of the green and yellow zones lead us to suppose that those zones will be affected even from small-scale rock falls and less mobile, highly viscous transported material. The pink zone, where slope values are relatively smaller than in the previous zones ($< 14°$), will witness the fan-style behavior of transported material which could probably destroy mainly Tatvan and/or Bitlis city. The red zone is the possible deposition field of transported mass. The settlements like the villages, town and cities are mainly situated in the pink and the red zones (Fig. 4c) where the slope values are gentle and most of those settlements are located at the end of the valleys. Cole et al. (1999) pointed out that the settlements within valleys or at valley mouths are particularly vulnerable to damage from tephra remobilization both during and after an explosive eruption of Furnas Volcano, Azores. In addition, Hall et al. (1999) emphasized how the valleys drain pyroclastic flows and debris flows on Tungurahua Volcano (Ecuador) and their role in the risk over Banos. In the light of our morphological analysis, we conclude that the volcano flanks are open to risks generated from all kinds of volcanic events, while some settlements which have H/L values less than 0.1 will be threatened if a debris flow is triggered.

4. Discussion and conclusion

Mount Nemrut stratovolcano is located in an active tectonic context and releases mantle-derived gases. However, the last eruption of Mount Nemrut is known to have occurred in 1441 (Oswalt, 1912; Pfaffengolz, 1950; Ozpeker, 1973; Féraud, 1994; Yilmaz et al., 1998), but the live description of the last eruption of Nemrut in a book written in 1597 proves that the volcano was very active about 400 years ago. Additionally, the recent publication of Karakhanian et al. (2002), based on the Armenian Chronicles, shows that Mount Nemrut has had some historical volcanic activities. On the other hand, a study on Lake Van varve records for the past 10 420 years (Kempe and Degens, 1978) described the volcanic products of the 1441 AD eruption based on the sediment core sections as light-colored volcanic tuff rather than the dark-colored products emitted from the rift zone in 1441. So, in 1441, Mount Nemrut probably produced the light-colored tuffs which are actually present on the southern flank and within the caldera, and were related to a phreatomagmatic eruption.

According to the volcanological past of Mount Nemrut, two major hypotheses may be proposed for the expected eruption: intracaldera volcanism or flank eruption.

If the eruption occurs within the caldera, it will be phreatomagmatic and destructive because of the presence of water (about 1 km^3) within the caldera. The hot water mixed with pyroclastics will form mud flows, as occurred in the eruption of Nevado del Ruiz (Colombia) where about 25 000 people were killed in 1985. On the other hand, the region is high enough to have lots of snow during winter. This is also very dangerous, because if the magmatic gases heat snow by several degrees, debris flows can be generated.

The other possibility is a flank eruption. If an eruption occurs during winter, the same danger mentioned above could be produced. If not, the lava effusions could destroy the lands, as far as the city of Tatvan. Or, the rift zone could be reactivated, producing some lava flows.

As summarized above, the major risk for Mount Nemrut is its capability to produce small or large-volume pyroclastic flows and/or debris flows. This poorly known active volcano has been morphologically analyzed and the results are speculative. Twenty-two important valleys were distinguished. The maximum depth of some valleys reaches 200 m. The valleys are localized in three zones: the WSW flank where the deeper valleys are present, the SSE flank where the longest valleys are located, and the NNE flank where the valley depths and lengths are less important. Based on the morphological analysis we propose that Mount Nemrut Volcano has four danger zones, illustrated in Fig. 4c. The green and yellow zones will be affected by all types of event such as small or large-volume pyroclastic flows, cold or hot debris flows, surges or cold rock avalanches. The settlements are situated in the pink and red zones, which will probably be

threatened by channeled products. Considering the water presence within the caldera, debris flows may be generated during the next volcanic activity. Debris flows normally fill depressions and may attain their maximum thickness some distance from the edifice, where valleys widen and gradients become lower, as observed at Nevado de Toluca Volcano by Capra and Macias (2000). In this case those debris flows will use the valleys, be deposited in lowlands and probably destroy settlements.

Finally, Mount Nemrut represents a real danger for 135 000 people that live in the area and it is necessary to survey this volcano. So, a seismic survey combined with periodical water and gas sampling and analyzing will be proposed. An alert code system and civil evacuation plans need to be established.

Acknowledgements

This work benefited from a research grant of Hacettepe University Research Foundation (Project No. 01 01 602 020). It was also financially supported by UMR-CNRS 6524. Prof. L. Wilson (Editor), Dr. Marta Calvache and an anonymous reviewer provided useful comments and ideas to the manuscript.

References

Capra, L., Macias, J.L., 2000. Pleistocene cohesive debris flows at Nevado de Toluca volcano, Central Mexico. J. Volcanol. Geotherm. Res. 102, 149–168.

Capra, L., Macias, J.L., Scott, K.M., Abrams, M., Garduno-Monroy, V.H., 2002. Debris avalanches and debris flows transformed from collapses in the Trans-Mexican Volcanic Belt, Mexico – behavior, and implications for hazard assessment. J. Volcanol. Geotherm. Res. 113, 81–110.

Cole, P.D., Guest, J.E., Queiroz, G., Wallestein, N., Pacheco, J.M., Gaspar, J.L., Ferreira, T., Duncan, A.M., 1999. Styles of volcanism and volcanic hazards on Furnas volcano, Sao Miguel, Azores. J. Volcanol. Geotherm. Res. 92, 39–53.

Dewey, J.F., Hempton, M.R., Kidd, W.S.F., Saroglu, F., Sengor, A.M.C., 1986. Shortening of continental lithosphere: the neotectonics of Eastern Anatolia – a young collision zone. In: Coward, M.P., Ries, A.C. (Eds.), Collision Tectonics. Geol. Soc. Spec. Publ. 19, pp. 3–36.

Ercan, T., Fujitani, T., Matsuda, J.I., Notsu, K., Tokel, S., Ui, T., 1990. Dogu ve Guneydogu Anadolu Neojen–Kuvaterner volkaniklerine iliskin yeni jeokimyasal, radyometrik ve izotopik verilerin yorumu. MTA Dergisi 110, 143–164.

Féraud, J., 1994. Les volcans actifs de Turquie. Guide Géologique et itinéraires d'excursions. Mémoire de l'Association Volcanologique Européenne (LAVE), pp. 85–101.

Hall, M.L., Robin, C., Beate, B., Mothes, P., Monzier, M., 1999. Tungurahua Volcano, Ecuador: structure, eruptive history and hazards. J. Volcanol. Geotherm. Res. 91, 1–21.

Itoh, H., Takahama, J., Takahashi, M., Miyamoto, K., 2000. Hazard estimation of the possible pyroclastic flow disasters using numerical simulation related to the 1994 activity at Merapi Volcano. J. Volcanol. Geotherm. Res. 100, 503–516.

Karakhanian, A., Djrbashian, R., Trifonov, V., Philip, H., Arakelian, S., Avagian, A., 2002. Holocene-historical volcanism and active faults as natural risk factors for Armenia and adjacent countries. J. Volcanol. Geotherm. Res. 113, 319–344.

Kempe, S., Degens, E.T., 1978. Lake Van varve record: The past 10,420 years. In: Degens, Kurtman (Eds.), The Geology of Lake Van. MTA yayinlari 169, pp. 56–63.

Nagao, K., Matsuda, J.I., Kita, I., Ercan, T., 1989. Noble gas and carbon isotopic composition in Quaternary volcanic area in Turkey. Jeomorfoloji Dergisi 17, 101–110.

Oswalt, F., 1912. Armenian. Handbuch der regionalen Geologie, vol. 10. Heidelberg.

Ozpeker, I., 1973. Nemrut yanardaginin petrojenezi. ITU Mad. Fak. 3–14, 70 pp.

Pearce, J.A., Bender, J.F., De Long, S.E., Kidd, W.S.F., Low, P.J., Guner, Y., Saroglu, F., Yilmaz, Y., Moorbath, S., Mitchell, J.J., 1990. Genesis of collision volcanism in eastern Anatolia, Turkey. J. Volcanol. Geotherm. Res. 44, 189–229.

Pfaffengolz, K.N., 1950. Über die Entstehung der Seen: Sewan (Armenien), Wan (Anatolien) und Urmia (Iran). Mitteilungen der Akademie der Wissenschaften USSR, Geol. Serie, pp. 125–138.

Richards, J.A., 1993. Remote Sensing Digital Image Analyis: An Introduction. Springer, Berlin, 340 pp.

Serefhan, 1597. Serefname: Kurt tarihi (translated from arabic to turkish by M. Emin Bozarslan), 4th edn. (1990). Hasat yayinlari, 544 pp.

Thouret, J.C., Lavigne, F., Kelfoun, K., Bronto, S., 2000. Toward a revised hazard assessment at Merapi volcano, Central Java. J. Volcanol. Geotherm. Res. 100, 479–502.

Wood, J., 1996. The geomorphological characterization of digital elevation models. Ph.D. Thesis, Univ. of Leicester.

Yilmaz, Y., Saroglu, F., Guner, F., 1987. Initiation of the neomagmatism in East Anatolia. Tectonophysics 134, 177–199.

Yilmaz, Y., Guner, Y., Saroglu, F., 1998. Geology of the Quaternary volcanic centers of the east Anatolia. J. Volcanol. Geotherm. Res. 85, 173–210.

e-Appendix – 1 (in CD) *Evolution of Nemrut volcano (movie file).*

e-Appendix – 2 (in CD) *Stratigraphical sections (image file).*

e-Appendix – 3 (in CD) *"STcorr" and short user guide (code and pdf).*

e-Appendix – 4 (in CD) *"Nemtrig" and short user guide (code and pdf).*

CURRICULUM VITAE

Adı Soyadı : İnan Ulusoy

Doğum Yeri : Ankara
Doğum Yılı : 1976
Medeni Hali : Evli

Eğitim ve Akademik Durumu:
Lise 1991 – 1994, Özel Arı Lisesi
Lisans 1994 – 1999, Hacettepe Üniversitesi, Jeoloji Mühendisliği Bölümü
Y. Lisans 1999 – 2002, Hacettepe Üniversitesi, Jeoloji Mühendisliği Bölümü

Yabancı Dil:
İngilizce, Fransızca

İş Tecrübesi:
2000 – 2008, Araştırma Görevlisi, Hacettepe Üniversitesi, Jeoloji Müh. Bölümü
2008 - ....., Doktora sonrası Araştırmacı, Lund Üniversitesi, Jeoloji Bölümü